

Northumbria Research Link

Citation: Liu, Lei (2013) Investigation of Aperture Coupled Microstrip Antenna to Obtain a High Efficient Active Integrated Antenna by Using Class F and Inverse Class F Power Amplifiers. Doctoral thesis, University of Northumbria.

This version was downloaded from Northumbria Research Link:
<http://nrl.northumbria.ac.uk/id/eprint/21425/>

Northumbria University has developed Northumbria Research Link (NRL) to enable users to access the University's research output. Copyright © and moral rights for items on NRL are retained by the individual author(s) and/or other copyright owners. Single copies of full items can be reproduced, displayed or performed, and given to third parties in any format or medium for personal research or study, educational, or not-for-profit purposes without prior permission or charge, provided the authors, title and full bibliographic details are given, as well as a hyperlink and/or URL to the original metadata page. The content must not be changed in any way. Full items must not be sold commercially in any format or medium without formal permission of the copyright holder. The full policy is available online: <http://nrl.northumbria.ac.uk/policies.html>

Investigation of Aperture Coupled Microstrip
Antenna to Obtain a High Efficient Active
Integrated Antenna by Using Class F and
Inverse Class F Power Amplifiers

Lei Liu

PhD

2013

Investigation of Aperture Coupled Microstrip
Antenna to Obtain a High Efficient Active
Integrated Antenna by Using Class F and
Inverse Class F Power Amplifiers

Lei Liu

A thesis submitted in partial fulfilment of the
requirements of the University of
Northumbria at Newcastle for the degree of
Doctor of Philosophy

Research undertaken in the Faculty of
Engineering and Environment

October 2013

Abstract

In wireless communications and radar systems, there are requirements for high efficiency, small size, low cost, and wide bandwidth of transmitter front –end usage for commercial and also military applications. Active integrated antenna (AIA) could satisfy almost all the requirements. The overall objective of the proposed research is to model, optimise, and design a compact and high efficient AIA using an aperture coupled microstrip antenna (ACMA) by integrating with a power amplifier (PA). Research on ACMA has been focused on the transmissions line (TL) model (TLM) and full wave electromagnetic (EM) model analysis. The full wave investigation is rigorous and elegant but because the dimension of the physical model and the value of the circuit elements are interdependent, the design of the antenna is still difficult. TLM analysis has lower accuracy but easier to analysis and optimise than full wave EM model analysis. To increase the accuracy, the challenge is the coupling ratios between feed/slot, and slot/patch where no unique solution at the moment exists. In this thesis, a novel and simplified method has been produced to investigate these ratios using Scattering (S) parameters. A dual frequency ACMA has been designed to verify these results. Research on the class F and inverse class F PAs is carried out by a novel and simplified load/pull method. A new design method of harmonic load matching network has been presented using lump elements and TLs. Both linear and nonlinear modelling has been investigated. High power added efficiency (PAE) and high gain which are up to 60% and 12dB have been obtained. Finally AIAs have been produced based on previous investigation on class F, inverse class F PAs and a broadband circular polarized ACMA design with 350 MHz bandwidth and 8.5 dB gain at 2 GHz.

Table of Contents

Abstract.....	II
List of Figures	VIII
List of Tables.....	XIV
Glossary of Symbols	XV
Glossary of Acronyms.....	XX
Acknowledgements.....	XXII
Declaration.....	XXIII
Chapter 1 Introduction and Overview.....	1
1.1 Introduction.....	1
1.2 Motivations and Objectives of the Research	3
1.3 Contributions of Research	5
1.4 Outline of Thesis	6
1.5 List of Publications	10
Chapter 2 Review of Transmission Line and Microstrip Antenna Theory.....	12
2.1 Introduction.....	12
2.2 Review of TL Theory	13
2.2.1 Primary Constants	13
2.2.2 Secondary TL Parameters.....	14
2.3 Review of the ML Theory.....	17

2.3.1 Effective Relative Permittivity.....	18
2.3.2 Characteristic Impedance	18
2.3.3 Loss Investigation of a ML	19
2.3.4 Review of S Parameters	21
2.4 Characteristics of Microstrip Patch Antennas	24
2.4.1 Radiation Elements.....	24
2.4.2 Different Feed Methods of Microstrip Patch Antenna	26
2.5 Summary	31
Chapter 3 Investigation of Aperture Coupled Microstrip Antenna using Transmission Line Model	33
3.1 Introduction.....	33
3.2 Analysis of the Equivalent Circuit of the Radiation Patch	36
3.3 Review of Slot Lines	40
3.4 Investigation of Microstrip/Slot Structure and Coupling Ratio between Microstrip Feed and Slot n_f	47
3.5 A Novel Method to Determine the Coupling Ratio of Feed/Slot and Slot/Patch using the S Parameter	53
3.5.1 Determine Turns Ratio n_f using S_{21} Parameter	54
3.5.2 Determine Turns Ratio n_f using S_{11} Parameter	58
3.6 Investigation of the End Effects of the Slot.....	63
3.7 Investigation of the Coupling Ratio between the Slot and the Patch	66

3.8 Design Procedure of an ACMA	69
3.9 Design of Broadband Dual Frequency ACMA	73
3.10 Summary	80
Chapter 4 Review and Theoretical Analysis of Power Amplifier using Linear Model	81
4.1 Introduction.....	81
4.2 Reviews of PAs	82
4.3 Design Parameters of PAs	83
4.4 Types of PAs.....	85
4.4.1 Classical PAs.....	85
4.4.2 High Efficiency PAs.....	88
4.5 Theoretical Analysis and Comparison of Class F and Inverse Class F PAs	91
4.6 Linear Switch Model Analysis of Class F and Inverse Class F PAs	98
4.6.1 Linear Switch Model Analysis with Infinite Harmonics Conditions	99
4.6.2 Linear Switch Model Analysis with up to Third Harmonics Conditions using Lump Element.....	102
4.6.3 Novel Methods of Harmonic Load Matching Network Design using TL	107
4.7 Summary	109
Chapter 5 Investigation and Design of Non-linear Class F and Inverse Class F Power Amplifiers	110
5.1 Introduction.....	110

5.2 Loss Investigation of Harmonic Matching Network using S Parameter	110
5.2.1 Loss Investigation of Impedance Effects of Shunt Stub using S_{21} Parameter	111
5.2.2 Practical Measurement for Shunt and Series Connected Lines	115
5.3 Characteristics of Nonlinear Device Model	118
5.4 Classical Load Pull Method	121
5.5 A Simplified Design Method of Class F PA	122
5.6 A Simplified Design of Inverse Class F PA	130
5.7 Practical Design and Test of Class F PA	136
5.8 Practical Design and Test of Inverse Class F PA	144
5.9 Summary	151
Chapter 6 Review and Design of Active Integrated Antenna	152
6.1 Introduction	152
6.2 Literature Review of AIA	152
6.3 Design of AIA	154
6.3.1 Introduction	154
6.3.2 Design of a Circular Polarized ACMA for AIA Design	155
6.3.3 Simulation and Practical Design of AIA using Class F PA	162
6.3.4 Simulation and Practical Design of AIA using Inverse Class F PA	165
6.4 Summary	169
Chapter 7 Conclusions and Future Work	170

7.1 Conclusions.....	170
7.2 Future Work.....	172
7.2.1 Investigation of an AIA without Harmonic Load Matching Networks ...	173
7.2.2 Optimisation of ACMA using GA.....	174
Reference	178

List of Figures

Fig. 1. 1 Summary of the issues, effects, current solutions and original contributions in AIA research.	9
Fig. 2. 1 Elementary components of a TL.....	14
Fig. 2. 2 Geometry of TL.	17
Fig. 2. 3 Signal flow diagram of a two port network.	22
Fig. 2. 4 The schematic of patch shapes.	25
Fig. 2. 5 Schematic of edge fed microstrip patch antenna.	26
Fig. 2. 6 Schematic of an inset fed microstrip patch antenna.	27
Fig. 2. 7 Schematic of probe fed microstrip patch antenna.....	28
Fig. 2. 8 Schematic of proximity coupled patch antenna.....	29
Fig. 2. 9 Schematic of ACMA.	30
Fig. 3. 1 Geometry of an ACMA.	33
Fig. 3. 2 Equivalent circuit of an ACMA.....	35
Fig. 3. 3 Structure of radiation patch and fringing field (a) top view (b) side view.	36
Fig. 3. 4 Equivalent circuit of radiation patch.....	38
Fig. 3. 5 Simplified equivalent circuit of radiation patch.	39
Fig. 3. 6 Physical structure of SL.....	41
Fig. 3. 7 Electric and magnetic field propagate around slot.	41
Fig. 3. 8 Frequency response of characteristic impedance for substrates PCB FR4, Duroid 5870 and Duroid6010 with height: (a) 1.575 mm, and (b) 0.7875 mm.	44
Fig. 3. 9 Frequency response of wave length for PCB FR4, Duroid 5870 and Duroid6010 with different height of substrate: (a) 1.575 mm, and (b) 0.7875 mm.....	46
Fig. 3. 10 Physical structure of microstrip/slot structure.	47
Fig. 3. 11 Electric field propagation of microstrip/slot structure: (a) even model, and (b) odd model.....	48
Fig. 3. 12 Equivalent circuit of the slot/microstrip structure.	48
Fig. 3. 13 Frequency response of n_f using Knorr and Das's equations with different substrate: (a) PCB FR4, (b) Duroid 5870, and (c) Duroid 6010.....	51

Fig. 3. 14 n_f as a function of slot length for Jaisson and Himdi equations using PCB FR4, Duroid 5870 and Duroid 6010.	52
Fig. 3. 15 Equivalent impedance of slot after coupling into microstrip feed line.....	54
Fig. 3. 16 Geometries of: (a) feed and slot lines, and (b) calibration line.....	54
Fig. 3. 17 Signal flow graphs: (a) the feed line with coupling slot effects, and (b) the calibration line.....	55
Fig. 3. 18 n_f as a function of slot length with PCB FR4, Duroid 5870 and 6010 substrate..	56
Fig. 3. 19 Microstrip feed lines on one side, and five slot lines on the other, of a fabricated PCB board.	57
Fig. 3. 20 Measured and simulation results for n_f as a function of slot length.	57
Fig. 3. 21 Structure of model established for S_{11} test: (a) ML with slot, and (b) open circuit microstrip calibration line.	59
Fig. 3. 22 Signal flow graphs: (a) ML with coupling slot impedance Z , and (b) microstrip open circuit calibration line.....	60
Fig. 3. 23 Microstrip feed lines with slot lines (0 – 50 mm) and open circuit microstrip calibration line.....	61
Fig. 3. 24 Measured and simulation results for the turn ratio n_f as a function slot line lengths.	62
Fig. 3. 25 Fabricated boards with (a) feed and open circuit side, and (b) slot line side.....	62
Fig. 3. 26 Frequency response of the series impedance Z	63
Fig. 3. 27 Two port network of feed slot structure used for S_{21} test: (a) physical structure, and (b) circuit structure.	64
Fig. 3. 28 Extended end effect slot length in terms of physical slot length using substrate PCB FR4, Duroid 5870 and Duroid 6010.....	65
Fig. 3. 29 R_s varies in terms of the physical slot length with the effects of substrate PCB FR4, Duroid 5870 and Duroid 6010.	66
Fig. 3. 30 Equivalent circuit of slot/patch structure.	66
Fig. 3. 31 n_p as a function of slot length and the patch width of: (a) 50 mm, and (b) 60 mm.	68
Fig. 3. 32 n_p as a function of L_s and W_p with the comparison of simulation and Jaisson's results.	69
Fig. 3. 33 Equivalent structure of the parallel patch and slot.....	70
Fig. 3. 34 Input admittance of the patch.....	70
Fig. 3. 35 Input admittance of SL.	71
Fig. 3. 36 Frequency response of the return loss.....	73

Fig. 3. 37 (a) Physical structure of the antenna, and (b) equivalent circuits of the antenna at the two frequencies.	74
Fig. 3. 38 Length of the fringing field ΔL as a function of the height of air substrate obtained from simulation and equation (3.1).	75
Fig. 3. 39 Frequency response of the return loss of the two matched antenna.	77
Fig. 3. 40 Circuit diagram of 1.9 GHz and 2.4 GHz antennas connected by feed arms.	78
Fig. 3. 41 Photograph of the fabricated antenna (a) radiation element, and (b) feed line....	78
Fig. 3. 42 Simulated and practical frequency responses: (a) reflection coefficient, and (b) gain of the antenna.	79
Fig. 4. 1 Block diagram of PA.	83
Fig. 4. 2 Circuit model of PA.....	83
Fig. 4. 3 Load line, voltage and current waveform of class A PA.	86
Fig. 4. 4 Load line, voltage and current waveform of class B PA.	87
Fig. 4. 5 Load line, voltage and current waveform of class AB PA.	87
Fig. 4. 6 Load line, voltage and current waveform of class C PA.	88
Fig. 4. 7 Class D PA.....	89
Fig. 4. 8 Voltage and current waveform of class D PA.	89
Fig. 4. 9 Class E power amplifier.....	90
Fig. 4. 10 Voltage and current waveform of class E PA.....	90
Fig. 4. 11 Circuit model for class F and inverse class F PA.	91
Fig. 4. 12 Voltage and current waveform: (a) class F PA, and (b) inverse class F PA.....	92
Fig. 4. 13 Output characteristic of the active device.....	96
Fig. 4. 14 Effects of R_{on} on: (a) power output, (b) DC to AC power conversion efficiency, and (c) load resistance.	98
Fig. 4. 15 Ideal linear switch model of class F PA.	100
Fig. 4. 16 Voltage and current drain waveforms of ideal linear switch model of class F PA.	101
Fig. 4. 17 Ideal linear switch model of inverse class F PA.....	101
Fig. 4. 18 Voltage and current drain waveforms of ideal linear switch model of inverse class F PA.....	102
Fig. 4. 19 Lumped elements harmonic load design for class F PA.....	103
Fig. 4. 20 Frequency response of impedance produced by LC circuit.....	104

Fig. 4. 21 Voltage and current drain waveforms of class F PA with up to third harmonics condition.....	105
Fig. 4. 22 Lump elements harmonic load design for inverse class F PA.....	105
Fig. 4. 23 Voltage and current drain waveforms of inverse class F PA with up to third harmonics.	106
Fig. 4. 24 Harmonic load matching network of class F PA using TLM.	108
Fig. 4. 25 Harmonic load matching network of inverse class F PA using TLM.	108
Fig. 5. 1 Microstrip open/short shunt stub network and equivalent model.....	111
Fig. 5. 2 Ratio of power dissipated over power available P_{dissPa} in terms of electrical length.....	114
Fig. 5. 3 Resistance R varies with shunt stub length.....	115
Fig. 5. 4 (a) Theoretical circuit model used to calculate shunt connected loss of ML, and (b) a practical board.	116
Fig. 5. 5 (a) Practical design of 0 – 80 mm ML, and (b) power dissipation ratio vs. the physical length.	117
Fig. 5. 6 Nonlinear model of low noise pHEMT ATF 33143.....	119
Fig. 5. 7 $I_{ds} - V_g$ characteristics of ATF33143.	120
Fig. 5. 8 $I_{ds} - V_{ds}$ characteristic of ATF 33143.....	120
Fig. 5. 9 Classical block diagram of load/source pull setup [194].....	121
Fig. 5. 10 Vector-receiver load pull block diagram [194].....	122
Fig. 5. 11 Schematic of load and source pull method based on nonlinear simulation.	123
Fig. 5. 12 Schematic of nonlinear model class F PA with up to third harmonic load control.	124
Fig. 5. 13 PAE and gain in terms of input power: (a) no input harmonic control, (b) with second harmonic control at input termination.....	125
Fig. 5. 14 PAE and gain in terms of frequency: (a) no input harmonic control, (b) with second harmonic control at input termination.....	126
Fig. 5. 15 Schematic of class F PA with even harmonic short circuit of load matching network.....	127
Fig. 5. 16 PAE and gain in terms of input power: (a) no input harmonic control, (b) with second harmonic control at input termination.....	128
Fig. 5. 17 PAE and gain in terms of frequency: (a) no input harmonic control, (b) with second harmonic control at input termination.....	129
Fig. 5. 18 Nonlinear model of inverse class F PA.	130

Fig. 5. 19 Simulated PAE and gain of the inverse class F PA design without source harmonic control in terms of: (a) input power, and (b) frequency.....	131
Fig. 5. 20 Nonlinear model of inverse class F PA with source harmonics control.....	132
Fig. 5. 21 Simulated PAE and gain of the inverse class F PA design with source impedance second harmonic control in terms of: (a) input power, and (b) frequency.....	133
Fig. 5. 22 Source matching network of nonlinear model of the inverse class F PA with source control up to third harmonics.....	134
Fig. 5. 23 Simulated PAE and gain of the inverse class F PA design with source impedance second and third harmonic control in terms of: (a) input power, (b) frequency.	135
Fig. 5. 24 ML model of class F PA design.	137
Fig. 5. 25 PAE and gain of the class F PA design with the ML model in terms of: (a) input power, and (b) frequency.	138
Fig. 5. 26 The V_{ds} and I_{ds} waveform over active device.....	138
Fig. 5. 27 Schematic of the ML model for the class F PA with T-junction.....	139
Fig. 5. 28 The V_{ds} and I_{ds} waveform over active device.	140
Fig. 5. 29 Footprint mirror layout of class F PA.....	140
Fig. 5. 30 Fabricated board of the class F PA.	141
Fig. 5. 31 Measured and simulated PAE for the class F PA in terms of: (a) input power, and (b) frequency.	142
Fig. 5. 32 Measured and simulated gain for the class F PA in terms of: (a) input power, and (b) frequency.	143
Fig. 5. 33 Schematic of ML model of inverse class F PA.	144
Fig. 5. 34 PAE and gain of the inverse class F PA design with the ML model in terms of: (a) input power, and (b) frequency.	145
Fig. 5. 35 The V_{ds} and I_{ds} waveforms over active device.....	146
Fig. 5. 36 Schematic of ML model inverse class F PA with T-junction.....	147
Fig. 5. 37 The V_{ds} and I_{ds} waveforms over active device.	147
Fig. 5. 38 Printed circuit layouts of the inverse class F PA.	148
Fig. 5. 39 Fabricated board of the inverse class F PA.	148
Fig. 5. 40 Measured and simulated PAE for the inverse class F PA in terms of: (a) input power, and (b) frequency.	149
Fig. 5. 41 Measured and simulated gain for the inverse class F PA in terms of: (a) input power, and (b) frequency.	150
Fig. 6. 1 Block diagram of AIA.	155

Fig. 6. 2 Schematic of broad band circular polarized aperture coupled microstrip antenna.	156
Fig. 6. 3 Equivalent circuit of broad band circular polarized aperture coupled microstrip antenna.	157
Fig. 6. 4 Practical fabricated boards of the broadband circular polarized ACMA: (a) radiation element, (b) slot, and (c) feed and matching stub.	157
Fig. 6. 5 Agilent Network Analyser N5230A.	158
Fig. 6. 6 Simulated and measured results for S_{11}	158
Fig. 6. 7 Conical log spiral antenna model 3102.	159
Fig. 6. 8 Equipments setup for antenna testing (a) antennas under test in anechoic chamber (b) signal generator and power meter.	160
Fig. 6. 9 Simulated and measured results for: (a) gain, and (b) AR.	161
Fig. 6. 10 Schematic of AIA by using class F PA.	162
Fig. 6. 11 V_{ds} and I_{ds} waveforms for Fig. 6.10.	163
Fig. 6. 12 Printed circuits for AIA.	164
Fig. 6. 13 Simulation and measured results for PAE and the gain in terms of: (a) the input power, and (b) the frequency.	165
Fig. 6. 14 Schematic circuit diagram of AIA using the inverse class F PA.	166
Fig. 6. 15 V_{ds} and I_{ds} waveforms for Fig. 6.14.	166
Fig. 6. 16 Printed circuit for AIA.	167
Fig. 6. 17 Simulation and measured PAE and gain plots in terms of: (a) the input power, and (b) the frequency.	168
Fig. 7. 1 Schematic of an AIA without harmonic load matching network.	173
Fig. 7. 2 GA implementation flow chart diagram.	175

List of Tables

Table 3. 1 Dimension of an ACMA.	72
Table 3. 2 Dimension of a broadband dual frequency ACMA.	76
Table 4. 1 Efficiency comparison of class F and inverse class F PAs with R_{on} and harmonics effects	107
Table 5. 1 Comparison data of theoretical and practical results.	118
Table 5. 2 Dimension of fabricated board of class F PA.	141
Table 5. 3 Dimensions of fabricated board of inverse class F PA.	148
Table 6. 1 Load and source impedances (Unit: Ω).	163
Table 6. 2 Load and source impedances (Unit: Ω).	167

Glossary of Symbols

a	Incident power
b	Reflected power
C	Capacitance
E	Source power
ϵ_r	Relative permittivity
ϵ_{reff}	Effective relative permittivity
f	Frequency
f_0	Fundamental frequency
G	Conductance
G_p	Power gain
H	Height
h	Height of substrate between feed and slot
I_{dc}	DC current
I_{ds}	Current flow over transistor
I_{Fun}	Current at fundamental frequency
I_I	Input current
i_{max}	Peak current of transistor
i_p	Peak current of active device
I_R	Reflected current

k_0	Wave propagation constant in air
L	Inductance
L_c	Length of conductor
L_{eff}	Effective length
L_{os}	Length of open circuit line
L_p	Length of patch
L_s	Length of slot
L_{st}	Length of stub
n_f	Turns ratio between feed and slot
n_p	Turns ratio between slot and patch
P_a	Power available
P_{AC}	AC power
P_{DC}	DC power
P_{diss}	Power dissipation
P_{Fun}	Power at fundamental frequency
P_L	Power obtained by the load
P_{out}	Power output
R	Resistance
R_L	Load resistance
R_{on}	Internal resistance of transistor
R_s	Surface resistance

$S_{11(22)}$	Reflection coefficient
$S_{21(12)}$	Transmission coefficient
T	Tallness
V_{DD}	DC voltage
V_{ds}	Voltage flow over transistor
V_{Fun}	Voltage at fundamental frequency
V_I	Input voltage
v_k	Knee voltage
v_{max}	Peak voltage of active device
V_p	Pinch off voltage
V_R	Reflected voltage
W	Width
W_f	Width of feed
W_p	Width of patch
W_s	Width of slot
W_{st}	Width of stub
Z_0	Characteristic impedance
Z_{0p}	Characteristic impedance of patch
Z_{0s}	Characteristic impedance of slot
Z_{2n}	Impedance at even harmonic frequency
Z_{2n+1}	Impedance at odd harmonic frequency

Z_{Fun}	Impedance at fundamental frequency
Z_{in}	Input impedance
Z_p	Impedance of patch
Z_s	Impedance of slot
α	Attenuation constant
α_c	Conductor loss
α_d	Dielectric loss
β	Phase constant
γ	Propagation constant
δ	Skin depth
ΔL	Extended length of fringing field
ΔL_s	Extended length of slot
η	Power converted efficiency
η_A	Average efficiency
θ	Electrical length
θ_p	Electrical length of patch
θ_s	Electrical length of slot
λ	Wavelength
λ_p	Wavelength of patch
λ_s	Wavelength of slot
μ	Absolute magnetic permeability of the conductor

ρ	Bulk resistivity
ω	Angular frequency
$f(\theta, \phi)$	Magnitude of field

Glossary of Acronyms

AC	Alternating Current
ACMA	Aperture coupled microstrip antenna
ADS	Advanced Design System
AIA	Active Integrated Antenna
AlGaAs	Aluminium Gallium Arsenide
AM	Amplitude Modulation
AR	Axial Ratio
CST	Computer Simulation Technology
dB	Decibel
DC	Direct Current
EM	Electromagnetic
GA	Genetic Algorithm
GaN	Gallium Nitride
Ge	Germanium
GHz	Gigahertz
GPS	Global Positioning Satellite
HB	Harmonic balance
HBT	Heterojunction Bipolar Transistor
HEMT	High Electron Mobility Transistor

HF	High frequency
HFET	Heterojunction Field Effect Transistor
InGaAs	Indium Gallium Arsenide
InP	Indium Phosphide
LF	Low frequency
MHz	Megahertz
ML	Microstrip Line
mW	Milliwatt
PA	Power Amplifier
PAE	Power Added Efficiency
PCB	Printed Circuit Board
pHEMT	pseudomorphic High Electron Mobility Transistor
RF identification	RFID
RF	Radio Frequency
SiC	Silicon Carbide
SL	Slot line
TE	Telegrapher's Equation
TL	Transmission Line
TLM	Transmission Line Model
UHF	Ultra high frequency
VHF	Very high frequency

Acknowledgements

I would like to express my deep gratitude to my supervisors Professor Fary Ghassemlooy, Professor Alistair Sambell, Prof. Sean Danaher, and also Professor Edward Korolkiewicz for their invaluable advice, support, and also patient guidance during the years. The project has been successfully accomplished with their supervision and professional assistance.

I am grateful to Dr Wai Pang Ng, Dr Hoa Le Minh, and also other OCRG group members for their kind advice and support at weekly group meetings and EBE 409 members for the daily help. Many thanks to Ed Holmes and David Johnston for their technical supports in fabrication of antenna and power amplifiers. I also would like to give thanks to Professor Krishna Busawon and Professor David Smith for the support of paper publication.

Finally, I am indebted to my family members Baozhang Liu, Jinhuan Zhang, Lily Zhang, and also my lovely cat Gouzi who have been giving me inspiration, support and positive influence in my life. I could not accomplish this work without any of them.

Lei Liu

Northumbria University at Newcastle upon Tyne, UK

October, 2013

Declaration

I declare that the work contained in this thesis has not been submitted for any other award and that it is all my own work.

Lei Liu

October 2013

Chapter 1 Introduction and Overview

1.1 Introduction

In wireless communications and radar systems, there are requirements for high efficiency, small size, low cost, and wide bandwidth transmitter at the front-end usage for commercial and also military applications. AIA [1, 2] could satisfy almost all the requirements, which could be regarded as an active microwave circuit by replacing the output and input ports using wireless components instead of a conventional interface [3]. In order to reduce the power consumption at the transmitter and receiver, it is important to reduce the power dissipation or improve the power conversion efficiency from DC to the AC signal for the PA. To reduce the size, the radiation element could be directly integrated with the active device with matching networks or alternatively for additional size reduction, the radiation element could be used as the optimum load for the PA section. The cost of AIA could be reduced by using different integration methods, transistors, or suitable materials for different applications [4]. A wide bandwidth is quite essential when designing AIA for radio frequency (RF) wireless technologies with multimedia capabilities. AIA applications have been extended to the area of quasi-optical power combiners in the past ten years [2, 5-7]. In this thesis, analysis of TLM of the ACMAs is carried out to obtain a broad band and a high gain as the radiation element, as well as an optimum load for the PA. The thesis shows comprehensive investigation of PAs with the aim of improving the efficiency, gain and increasing the bandwidth by means of using the switch mode active device and novel designed harmonic matching networks.

As the radiation element, the traditional microstrip based patch antennas offer small size, low cost, ease of integration at the cost of a narrow bandwidth, poor gain, and limited

applications. In order to overcome these problems, the ACMA [8, 9] was proposed and utilized to obtain a wide bandwidth and high gain. Due to its separate feed and radiation element structure, it is easy to use different feed methods [10-12], substrates and many patch shapes [13, 14] in order to obtain the optimum performance. The circular polarized antenna and arrays [15-22] were introduced to increase the gain for satellite communication applications. The EM simulation method for the antenna design is accurate and rigorous. However, the dimension of physical model and parameters of circuit elements are interdependent and the antenna design is still difficult. Hence, the simplified TLM analysis is used for investigation and design which is relatively straight forward for further optimization using the genetic algorithms (GAs) [23-25], stochastic algorithms [26, 27], and conjugate gradients [28, 29], etc. The key problem in circuit modelling is the two turns ratios between feed/slot n_f and slot/patch n_p , which are reported in numerous research publications, however with no single approach or technique. In this thesis a simplified theoretical method for analysing the turn ratios by means of S parameter is presented. To verify the mathematical theory, simulation is carried out and the results are compared with the measured data. Equations are derived by means of curve fitting methods for n_f and fringing field using the large gap between slot/patch with the air substrate. A broadband dual frequency linear polarized ACMA is subsequently designed to verify the obtained results.

In order to achieve high power conversion efficiency for DC-to-AC signal, switching model class F and inverse class F PAs are used, where the active device is driven by a large input signal to ensure that the active device functions as a switch. The power dissipation from the active device is due to the internal resistance of transistor which causes the overlap of voltage and current. In order to overcome this problem, the harmonic load matching networks are proposed in order to shape the voltage and current

waveforms by the lumped elements and the TLM. The ideal linear switch models are developed for the simulation purpose and mathematical expressions are derived for the output power, optimum load impedance, and efficiency in order to investigate the system performance. For non-linear simulation, based on Statz model, a simplified load/source pull method is proposed for the harmonic source and the load matching network in order to obtain maximum PAE as well as the gain. The thesis outlines detailed comparison of class F and inverse class F PAs with lossless TL, and microstrip line (ML) model. Source and load matching network designs and also harmonics effects have been presented.

For the AIA design, a broadband circular polarized ACMA is designed at 2 GHz to integrate with the class F and inverse class F PAs. Simulation methods are also adopted to predict the PAE and gain by replacing the load of PAs with an antenna. Based on these results, two practical AIAs using class F PA and inverse class F PAs are designed, fabricated and tested. In the advanced AIA design, the harmonic load matching network of PA can be eliminated and directly integrated with the antenna as the harmonic load. In this case, the antenna acts both as the radiating element and the optimum load. However, the design procedure is rather complex, which could lead to a more compact module.

1.2 Motivations and Objectives of the Research

Based on the defence and space applications, the demand for both the microstrip antennas and AIAs have increased with emphasis on the performance rather than the cost. However, for commercial civilian applications such as global positioning satellite (GPS), cellular phone, RF identification systems (RFID), personal communication systems, automatic toll collection, wide area computer networks, and RF energy harvesting systems, the reduction of cost has the priority by comparing with high-quality performance. In order to have the

best of two worlds (i.e. performance and reduced costs) broadband, high gain, dual frequency, or circularly polarized microstrip antennas are the way forward. Adopting the circuit design method can lead to reduced simulation time and utilising GA or other optimization methods could assist in more accurate. Research based on either the cavity method [14] or the full wave EM analyses [9] are rigorous but complex and with conflicting results. Hence, TLM analysis has been carried out which is simple structured but low accuracy. To improve this, the challenges of TLM focus on the turns ratio between feed/slot, and slot/patch. The PA is the most costly element in RF circuits [30]. To minimize the cost, and enhance the efficiency and gain, research has been mainly focused on the power dissipation analysis of transistor, harmonics control and also the low cost material used by MLs. To obtain maximize the PAE and the gain, the switch model class F and inverse class F PAs are investigated and compared using a novel design for harmonic load matching networks. The objectives of this research are summarized as follows:

- To develop a novel and simplified topology for calculating, simulating, and measuring n_f and n_p using the S_{21} and S_{11} parameters.
- To verify the turns ratio produced by designing an ACMA using the TLM.
- To produce a simplified design procedure to produce an ACMA using the TLM.
- To develop a logical and novel method to design harmonic load matching networks of class F and inverse class F PAs using the lump elements and TLM.
- To predict the power converted efficiency, PAE and gain using linear and nonlinear models of transistor for the class F and inverse class F PAs.
- To produce AIAs based on the designed classes F and inverse class F PAs integrated with the circular polarized antenna.

1.3 Contributions of Research

- A simplified and novel method has been developed to produce the turns ratio between feed and slot using S_{21} and S_{11} parameters which has been verified by simulation and practically measurement, see Chapter 3. Additionally an expression is derived for this turns ratio in terms of the slot length and height of the substrate using the curve fitting method.
- A dual frequency broad band aperture coupled antenna has been designed using the TLM to approve the validity of turns ratio between the feed and slot produced by means of simulation and practical measurement, which is presented in Chapter 3.
- A novel and simplified design approach has been developed by using the TLM for the design of an ACMA, which is shown in Chapter 3.
- Novel topologies have been developed to produce harmonic load matching networks using the lumped element and the TLM to satisfy the conditions of class F PA and inverse class F PAs with accurate numerical calculation and also simulation validation by ADS software, which is presented in Chapter 4.
- Power converted efficiency investigation has been systematically carried out by simulation using the linear model of transistor under the conditions of varying internal loss of the active device, infinity harmonics of the load matching network, up to third harmonics matching network using the ideal TL and the lossy ML, which is shown in Chapter 4.
- Novel load/source pull methods have been developed based on the new harmonic load matching network design methods. Performances of the PAE and gain have been compared by means of simulation using ADS software for the nonlinear model class F and inverse class F PAs, which is presented in Chapter 5.

1.4 Outline of Thesis

This thesis presents a simplified method of investigation into ACMA by using circuit and TLMs, which focus on the turns ratio analysis. Also the performance of class F and inverse class F PAs are investigated by linear and non linear models.

Chapter 2 reviews the primary and secondary parameters of the TL theory, which is based on Maxwell's equations indicating that the TLs are equivalent to the lumped circuit of a resistor, inductor, conductor and capacitor. The characteristic impedance is indicated by the ratio of voltage to current when signal is applied to an infinite long line. The propagation constant is expressed by the attenuation constant and the propagation constant. The ML is one type of electrical TL, which is fabricated in printed circuit board (PCB). For practical usage, the ML is easy to be used as an integrated circuit design. However, power will be dissipated due to the loss factors, which are the conductor and dielectric losses. To minimize this problem, low loss materials are normally chosen for the design but at a high cost. Equations are derived for the reflection and transmission coefficients in terms of source, load impedance and also the voltage and current, which are utilized for further analysis. Microstrip patch antennas are introduced with different patch shapes and feed methods. In this work the ACMA is selected for the further analysis due to its characteristics of flexible structure, wide bandwidth and high gain.

Chapter 3 investigates the TL model of a rectangular patch ACMA. By comparing with the full wave EM model, which is more accurate but difficult to analyse requiring complex equations, the TLM can be easily analysed using circuits to save simulation and also optimization time. The key challenge of the circuit model is the coupling ratios between feed/slot, and slot/patch, which has been investigated by number of researchers using

different rigorous methods. However, there are non-unique and simple solutions for the TLM analysis. This work outlines a simplified method to calculate, simulate and also measure the turns ratio using the S parameters for different substrates. Equations are derived in terms of the height of substrates and the length of slot. Based on these results, a wide bandwidth dual frequency dual polarized ACMA is designed to verify the theoretical analysis.

In Chapter 4, the PA histories and theories are reviewed. The PAs are analysed for the class A to class F and the inverse class F. In this thesis, class F and inverse F PAs are selected for analysis due to their high performance and low profile. The active device ideally works as a switch to minimize the voltage and current overlap and also the power dissipation from transistor. Hence, an ideal switch connected with a resistor is used to model the active device. The harmonic load matching networks are designed for both PAs to shape the voltage and current waveforms using the lump elements model and also the TLM. A novel and logical method is also proposed to design the harmonic load matching network with accurate calculations.

In Chapter 5, loss investigation is carried out for the shunt stub of harmonic matching networks using S parameters. A circuit model is proposed to indicate the power dissipation in terms of the resistor and transmission length. To investigate the nonlinear model, the transistor is modelled by Statz model based on the data sheet from ATF 33143. Based on the designed harmonic matching networks, the performance of class F PA and inverse class F PA are investigated and compared in terms of a range of input power levels and frequencies. The source harmonic terminations are also analysed by the second and third harmonic controls and comparisons are carried out for both PAs.

Chapter 6 presents the concepts of AIA, which can integrate circuit functions such as filter, mixer, and power amplifier, thus saving the space and reducing the power dissipation. A broadband circular polarized ACMA is designed, which is based on the analysis in Chapter 3, to replace the load of PA. The comparison is carried out using class F and inverse F PAs based on Chapter 5 with simulation and also practical measurement.

Chapter 7 concludes the work that has been done. A further design method of AIA to obtain a smaller size and a higher efficiency is presented. An ACMA can be used as the optimum harmonic load of active device by eliminating the matching network to improve the efficiency. GA is introduced to optimise the bandwidth of antenna, enhance the efficiency and the gain of AIA.

The issues, effects, solutions, and original contributions are listed in the road map in Fig. 1.1.

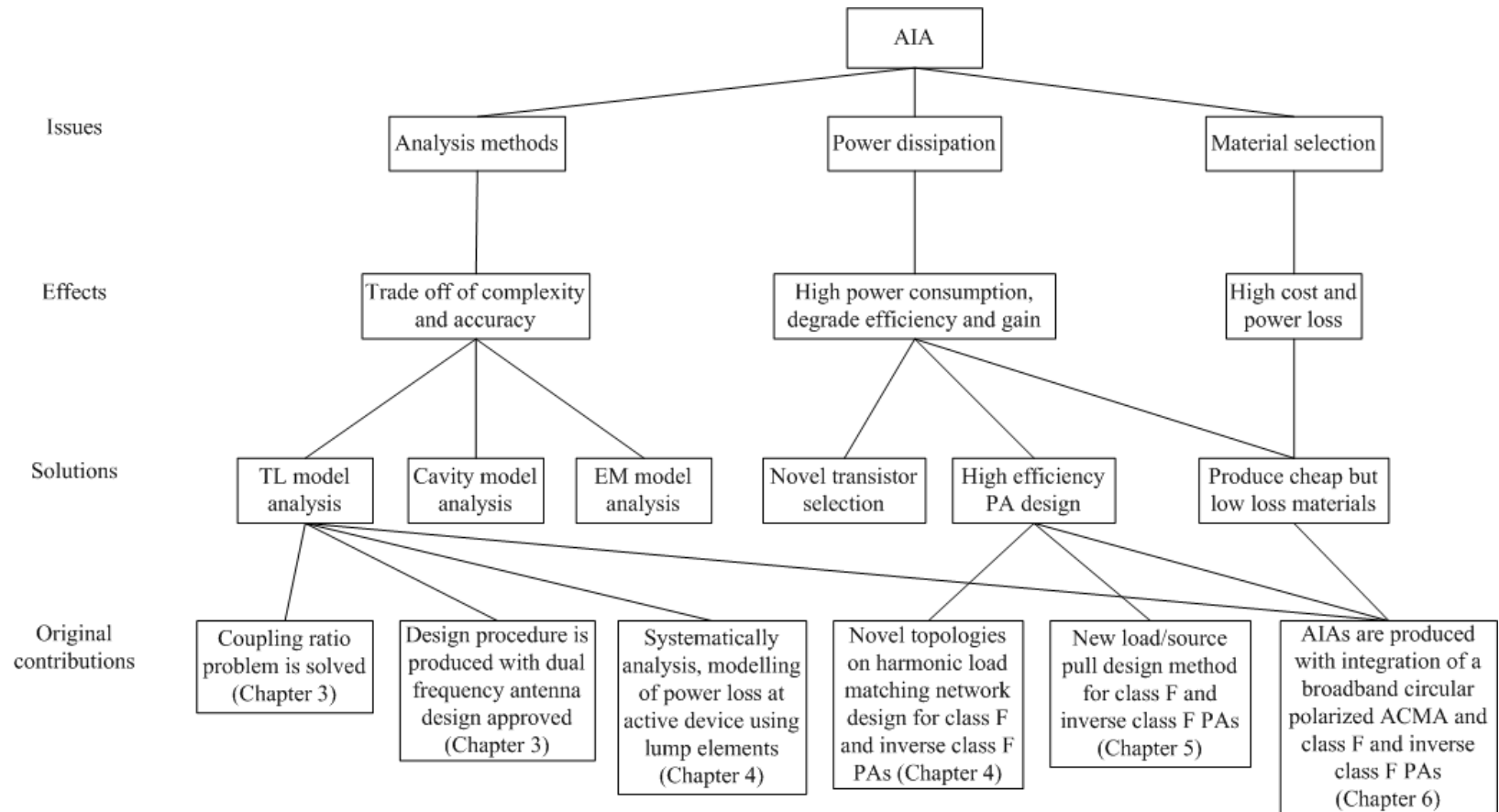


Fig. 1.1 Summary of the issues, effects, current solutions and original contributions in AIA research.

1.5 List of Publications

Journals

- [1]. L. Liu, E. Korolkiewicz, Z. Ghassemlooy, A. Sambell, S. Danaher, and K. Busawon, "Investigation of the equivalent circuit parameters and design of a dual polarised dual frequency aperture coupled microstrip antenna" *Antennas and Propagation, IEEE Transactions on*, vol. 61, pp. 2304-2308, 2013.
- [2]. L. Liu, Z. Ghassemlooy, A. Sambell, S. Danaher, and D. Smith, "Investigation of Transformer Turns Ratio between Feed and Slot of Aperture Coupled Slot Antenna by using S_{11} Parameter " *Antennas and Propagation, IEEE Transactions on*, vol. 61, NO. 11, 2013.

Conferences

- [1]. W. Dehao, E. Korolkiewicz, Q. Lu, and L. Liu, "To design and model a class F amplifier and investigate the effect of losses on the efficiency of dc to ac power conversion," in *Communication Systems Networks and Digital Signal Processing (CSNDSP), 7th International Symposium on*, pp. 119-122, 2010.
- [2]. L. Liu, L. Qing, W. Dehao, A. Sambell, and E. Korolkiewicz, "Determination of the transformers turn ratios and design of a circular polarised cross slot coupled antenna," in *Communication Systems Networks and Digital Signal Processing (CSNDSP), 7th International Symposium on*, pp. 115-118, 2010.

- [3]. Q. Lu, L. Liu, A. Sambell, Z. Ghassemlooy, and S. Danaher, "Comparison of the Return Loss and Axial Ratio for Circular Polarised Square Patch Antenna using Two Branch and Ring Coupler Feeds," in *PG NET*, Liverpool, UK, 2010.
- [4]. L. Qing, A. Sambell, S. Danaher, E. Korolkiewicz, Z. Ghassemlooy, L. Liu, and W. Dehao, "The effect of the turn on resistance of an active device and the Q factor of the load harmonic network on the efficiency and efficiency bandwidth of a class E amplifier," in *Communication Systems Networks and Digital Signal Processing (CSNDSP), 7th International Symposium on*, pp. 106-110, 2010.
- [5]. L. Liu, Z. Ghassemlooy, A. Sambell, S. Danaher, Q. Lu, and E. Korolkiewicz, "Investigation of transformers' turn ratios and design procedure for an aperture coupled slot antenna," in *Active RF Devices, Circuits and Systems Seminar*, pp. 61-65, 2011.
- [6]. Q. Lu, L. Liu, S. Danaher, E. Korolkiewicz, and Z. Ghassemlooy, "Modelling of losses in load harmonic networks of high efficiency class E power amplifiers," in *Active RF Devices, Circuits and Systems Seminar*, pp. 75-79, 2011.
- [7]. L. Liu, E. Korolkiewicz, Z. Ghassemlooy, A. Sambell, S. Danaher, and Q. Lu, "Effect of Losses in an Active Device and Harmonic Network on the Efficiency of Class F and Inverse Class F Power Amplifiers," in *2nd International Symposium on Environment Friendly Energies and Applications (EFEA 2012)*, Northumbria University, Newcastle upon Tyne, UK., 2012.
- [8]. V. Nimbark, Q. Lu, E. Korolkiewicz, and L. Liu, "Design of a Three Port Feed Matching Network for a Dual- Band and Dual -Polarized Rectangular Patch Antenna," in *International Conference on Signal Processing and Communications*, India, 2012.

Chapter 2 Review of Transmission Line and Microstrip Antenna Theory

2.1 Introduction

This chapter introduces the concept of TL, which is a material medium that forms a path for transmitting energy from one place to another. Each elementary element of TL can be represented by a series resistance connect with an inductance; parallel connect with a leakage conductance and a capacitance. These four parameters are called primary constants. The secondary constants - characteristic impedance and propagation constant are constrained by these primary constants and will be used in the ML analysis. A ML is an electrical TL with metal and ground printed on two sides of dielectric substrate. A ML can be used in integrated circuits and combine multi-functional elements using PCB technology. When a signal propagates along the TL, there will be power reflected back and power that goes through which can be analysed by a two port network. Electrical properties of networks can be expressed by scattering parameters (S parameters) such as gain, return loss, voltage standing wave ratio, reflection coefficient, etc[9]. In antenna design field, the power reflected back can be represented by S_{11} which is called input port voltage reflection coefficient. For a two port network as used in designing of a power amplifier, the forward voltage gain can be indicated by S_{21} . At the end of this chapter, this author introduces the characteristics of microstrip patch antenna which consist of radiation element, substrate, and also ground plane. Different shapes of radiation elements are introduced with the performance of bandwidth and gain. Five feed methods are also

presented which are used to connect the antennas with integrated circuits or other RF components.

2.2 Review of TL Theory

In an electronic system, the delivery of power requires the connection of two wires between the source and the load. At low frequencies, power is considered to be delivered to the load through the wire. In the microwave frequency region, power is considered to be propagating in electric and magnetic fields that are guided through a channel. Any physical structure that guides an electromagnetic wave is known as the TL [9, 14]. TLs are normally in the forms of two wire lines, coaxial cable, wave guide and planar TL, with the latter being widely adopted in this thesis. Planar TLs mainly include strip line, ML, slot line, fin line, coplanar waveguide and coplanar slot line [31, 32]. In the following section primary and secondary parameters of TLs will be discussed.

2.2.1 Primary Constants

The relationship of voltage and current on an electrical TL as a function of the distance and time was described by the Telegrapher's Equations (TEs) [33] developed by Oliver Heaviside who created the transmission model based on Maxwell's equations [34, 35]. This model represents the TL as an infinite series of two-port elementary components, each representing an infinitesimally short segment of the TL, with the equivalent elementary section shown in Fig. 2.1 [36-38] .

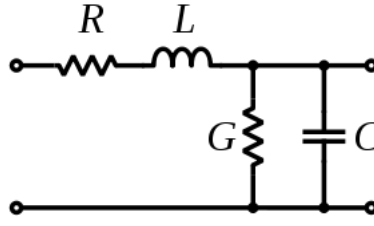


Fig. 2.1 Elementary components of a TL.

where,

R (unit: Ω): Resistance per unit length, which is due to finite resistivity of conductors.

G (unit: S): Leakage conductance per unit length, which is due to losses in an imperfect insulator.

C (unit: F): Capacitance per unit length, which is due to the potential difference between conductors generating the electric field.

L (unit: H): Inductance per unit length, which is due to the magnetic field generated by the AC current.

2.2.2 Secondary TL Parameters

When the signal is applied to an infinitely long line, the ratio of voltage to current implied on any distance from the source is defined as the line characteristic impedance Z_0 . When the wave reaches the end of the line, in general, there will be a reflected wave that travels back along the line in the opposite direction towards the source. Based on the TEs, using the TLM, the characteristic impedance could be represented by [14]:

$$Z_0 = \sqrt{\frac{R + j\omega L}{G + j\omega C}}, \quad (2.1)$$

where ω is the angular frequency.

The main properties of transmission lines are:

1. Independent of the length of the line,
2. Independent of the termination of the line,
3. Not the impedance that a line itself possesses,
4. Determined only by the parameters of the line per unit length.

At high frequencies or low losses $R \ll \omega L$, $G \ll \omega C$, Z_0 can be approximated from the binomial expansion:

$$\begin{aligned} Z_0 &= \sqrt{\frac{R + j\omega L}{G + j\omega C}} \\ &= \sqrt{\frac{L}{C}} * \left(1 + \frac{1}{2} * \left(\frac{R}{j\omega L} - \frac{G}{j\omega C} \right) \right) \\ &= \sqrt{\frac{L}{C}} \quad \text{Lossless } (R = G = 0). \end{aligned} \quad (2.2)$$

The propagation constant γ of an electromagnetic wave is a measure of the change undergone by the amplitude of the wave as it propagates in a given direction. The quantity being measured can be the voltage or current in a circuit or a field vector such as the electric field strength or the flux density. The propagation constant itself measures change per metre but is otherwise dimensionless. The relationship between the propagation constant and the primary constant is given by (2.3):

$$\gamma = \sqrt{(R + j\omega L) * (G + j\omega C)} . \quad (2.3)$$

The propagation constant is a complex quantity, which is given by $\gamma = \alpha + j\beta$, where α is the attenuation constant and β is the phase constant.

The propagation constant is separated into two components that have very different effects on signals. The real part of the propagation constant is the attenuation constant, which causes the signal amplitude to decrease along the TL. The natural unit of the attenuation constant is Nepers/meter, but is often converted into dB/meter in microwave engineering. The phase constant determines the sinusoidal amplitude/phase of the signal along a TL. In a lossless TL, the wave propagates as a perfect sine wave. For a TLM, the propagation constant can be determined from the primary line coefficients as given by [14]:

$$\begin{aligned} \gamma &= \sqrt{(R + j\omega L) * (G + j\omega C)} \\ &= j\omega\sqrt{LC} + \frac{R}{2}\sqrt{\frac{C}{L}} + \frac{G}{2}\sqrt{\frac{L}{C}} . \end{aligned} \quad (2.4)$$

Hence,

$$\alpha = \frac{R}{2}\sqrt{\frac{C}{L}} + \frac{G}{2}\sqrt{\frac{L}{C}} = \alpha_c + \alpha_d, \quad (2.5)$$

where

$$\alpha_c = \frac{R}{2}\sqrt{\frac{C}{L}} \text{ (Conductor loss)}, \quad (2.6)$$

$$\alpha_d = \frac{G}{2}\sqrt{\frac{L}{C}} \text{ (Dielectric loss)}, \quad (2.7)$$

$$\beta = \omega\sqrt{LC}. \quad (2.8)$$

For a lossless TL, $\alpha = 0$, $\gamma = j\beta$.

2.3 Review of the ML Theory

ML is a type of electrical TL and is used to convey microwave-frequency signals. It consists of a conducting strip separated from a ground plane by a dielectric layer known as the substrate. Microwave components such as antennas, couplers, filters, power dividers etc. can be formed from ML with the entire device fabricated as a pattern of metallization on the substrate [9, 14]. ML is much less expensive than the traditional waveguide technology, as well as being far lighter and more compact. By comparing with other TLs like wave guide, the drawbacks of the MLs are the generally lower power handling capacity and higher losses. Also, unlike waveguide, microstrip is not enclosed, and is therefore susceptible to the cross-talk and un-intentional radiation [39, 40].

The geometry of ML is shown in Fig. 2.2.

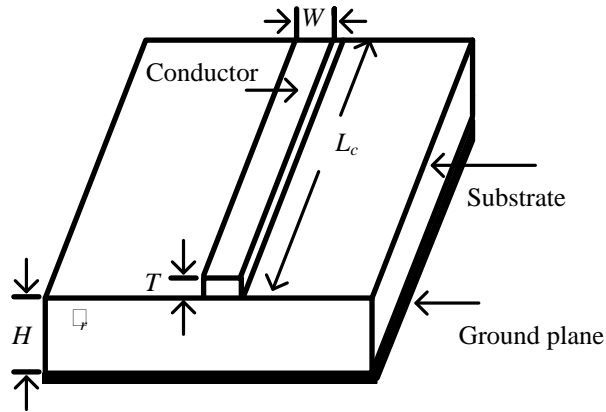


Fig. 2.2 Geometry of TL.

W and L_c are the width and length of the conductor, T is the conductor thickness, H and ϵ_r are the height, and dielectric constant of the substrate.

2.3.1 Effective Relative Permittivity

The effective relative permittivity (ϵ_{reff}) is the effective dielectric constant between the constant of air and the relative dielectric constant of the substrate. In a copper conductor, the electric current generates the electric and magnetic fields. The propagation of the electrical field is in and around the ML, which is produced in the substrate and air. The effective dielectric constant is defined as the function of relative permittivity and the ratio of W/H , as given in (2.9), and (2.10) [9]:

$$\epsilon_{reff} = \frac{\epsilon_r + 1}{2} + \frac{(\epsilon_r - 1)}{2} * \left[\left(1 + \frac{12H}{W} \right)^{-\frac{1}{2}} + 0.04 \left(1 - \frac{W}{H} \right)^2 \right] \quad (W/H \leq 1), \quad (2.9)$$

$$\epsilon_{reff} = \frac{\epsilon_r + 1}{2} + \frac{(\epsilon_r - 1)}{2} * \left(1 + \frac{12H}{W} \right)^{-\frac{1}{2}} \quad (W/H > 1). \quad (2.10)$$

2.3.2 Characteristic Impedance

For a ML, Z_0 is a function of the relative permittivity and W/H ratio, which can be represented by [9]:

$$Z_0 = \frac{60}{\epsilon_{reff}^{\frac{1}{2}}} \ln \left(\frac{8H}{W} + \frac{0.25W}{H} \right) \quad (W/H \leq 1), \quad (2.11)$$

$$Z_0 = \frac{\frac{120\pi}{\epsilon_{reff}^{\frac{1}{2}}}}{\frac{W}{H} + 1.393 + 0.667 \ln \left(\frac{W}{H} + 1.444 \right)} \quad (W/H > 1). \quad (2.12)$$

In addition W/H is defined in terms of Z_0 and ϵ_r as:

$$\frac{W}{H} = \frac{8e^A}{e^{2A} - 2} \quad (W/H \leq 2), \quad (2.13)$$

$$\frac{W}{H} = \frac{2}{\pi} \left\{ B - 1 - \ln(2B - 1) + \frac{\epsilon_r - 1}{2\epsilon_r} \left[\ln(B - 1) + 0.39 - \frac{0.61}{\epsilon_r} \right] \right\} \quad (W/H \geq 2), \quad (2.14)$$

$$\text{where } A = \frac{Z_0}{60} \left(\frac{\epsilon_r + 1}{2} \right)^{\frac{1}{2}} + \frac{\epsilon_r - 1}{\epsilon_r + 1} (0.233 + \frac{0.11}{\epsilon_r}) \text{ and } B = \frac{377\pi}{2Z_0 \sqrt{\epsilon_r}}, \quad (2.15)$$

$$\lambda_g = \frac{c}{f \sqrt{\epsilon_{\text{reff}}}} \text{ and } \theta = \beta L = \frac{2\pi L}{\lambda_g}, \quad (2.16)$$

where λ_g is the wave length in substrate.

2.3.3 Loss Investigation of a ML

Due to the characteristics of the MLs, the loss cannot be ignored particularly when an ordinary low cost PCB FR4 substrate is used. The loss tangent of PCB FR4 is 0.025 which is higher than that of Duroid 5870 (0.0025) at microwave frequency range. The rest of this section will analyse the loss of MLs that can equally be applied to other materials in future designs especially using PCB FR4 substrate.

The major losses due to the MLs are (i) conductor loss α_c , (ii) dielectric loss α_d , and (iii) radiation loss α_r .

(i) Conductor loss - The resistance of any conductor is not zero. So when current is passed through the wire, the energy is lost in the form of heat. At high frequencies, the conductor losses are generally due to the skin effect. When a DC voltage (or current) is applied the distribution of electron movement is fairly uniform. When AC is applied, the flux density at the centre of the wire is greater than at the outer edge, thus the reactance is also greater. The current reduces with inversing the resistance. In other words, when AC is applied the current will flow faster on the outer edge of the conductor than through the centre [42]. For a ML, the surface resistance R_s is given by [43]:

$$R_s = \frac{\rho}{\delta} \Omega/\text{square}, \quad (2.17)$$

where ρ is the bulk resistivity and δ is the skin depth define by:

$$\delta = \sqrt{\frac{\rho}{\mu\pi f}} \text{ cm}, \quad (2.18)$$

where μ is the absolute magnetic permeability of the conductor, and f is the working frequency.

The conductor loss is therefore defined as:

$$\alpha_c = 8.86 * \frac{R_s}{Z_0 W}. \quad (2.19)$$

(ii) Dielectric loss - Different dielectric substrate material creates a different power loss at microwave frequencies. The loss in the dielectric is due to a high resistance and the movement of the dielectric molecules in the substrate. The movement of molecules in the dielectric substrate will contribute losses in the form of heat. The dielectric loss is defined by:

$$\alpha_d = 27.3 * q * \epsilon_r * \frac{\tan \delta}{\epsilon_{\text{reff}} * \lambda_g}, \quad (2.20)$$

where $q = \frac{\epsilon_{\text{reff}} - 1}{\epsilon_r - 1}$.

(iii) Radiation loss – The energy radiated is called radiation loss which depends on dielectric material conductor spacing and length of TL. If separation between conductors in

a metallic TL is appreciable fraction of wavelength, the electrostatic and electromagnetic fields that surround the conductor cause the line to transfer energy to nearby conductive material. Radiation losses can stem from numerous factors, including the type of dielectric material, its thickness, the shapes of TL structures in a microstrip circuit and also frequency. Radiation loss can significantly impact performance, resulting in increased insertion loss, changes in signal phase, and shifts in resonant frequency in certain microstrip circuits, such as filters and couplers. The shape of TL discontinuities could influence the amount of radiation loss with sharper edges on junctions cause higher radiation loss [9]. Substrate with low dielectric constants has often been used in microwave designs due to the low cost and versatility. However, less of the conducted EM energy is concentrated in the substrate and metal conductor which lead to higher radiation effects. The thickness of PCB material also impact the amount of radiation loss at higher frequency that it can be reduced by using thinner dielectric substrate for lower dielectric constant material and also higher dielectric constant material as well [9], [13].

Finally, the total loss is given by:

$$\alpha_t = \alpha_c + \alpha_d + \alpha_r \quad (2.21)$$

2.3.4 Review of S Parameters

This section introduces the basic concept of S parameters and the derivation of equations for unequal source and load impedance. This will be used in the rest of this thesis for patch antenna and power amplifier design and analysis. S parameters describe the input-output relationship between terminals in an electrical system and always a function of the frequency. For instance, for a two port network, S_{mn} represents the power transferred from

Port n to Port m . A block diagram of a two port system with the unequal source and load impedance is depicted in Fig. 2.3:

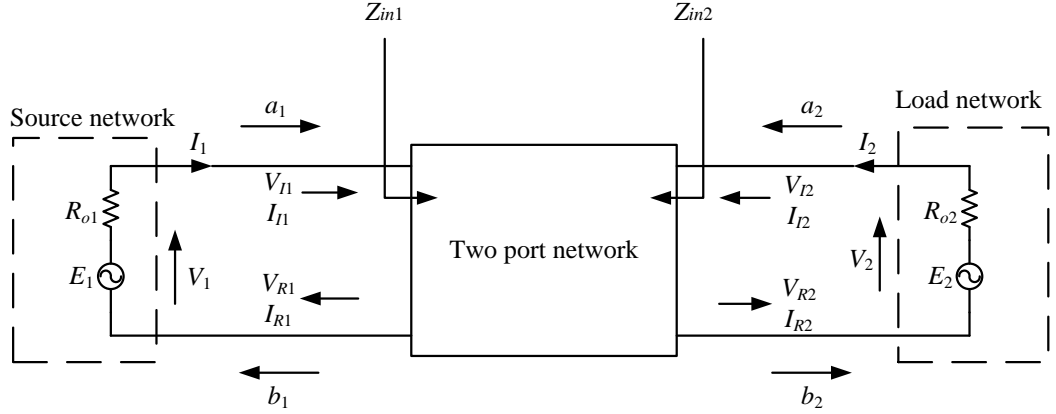


Fig. 2.3 Signal flow diagram of a two port network.

E_1, R_{01} (E_2, R_{02}) is the source (load) power and its internal resistance. V_1, I_1 (V_2, I_2) are the voltage and current across the source (load). V_{11}, I_{11} (V_{12}, I_{12}) are the input voltage and current flow into the two port network from the source (load) port, and the V_{R1}, I_{R1} (V_{R2}, I_{R2}) are the reflected voltage and current from the two port network. If considering an incident power wave a_1 (a_2) from source port (load port), it will lead to the reflected waves which exciting at both source port b_1 and load port b_2 . The source (load) port is represented by port 1 (port 2) in the rest of this chapter.

$S_{11} = \frac{b_1}{a_1} |_{a_2=0}$ represents the reflection coefficient at port 1 with port 2 terminated with a matched load.

$S_{21} = \frac{b_2}{a_1} |_{a_2=0}$ represents the transmission coefficient from port 1 to port 2 with port 2 terminated with a matched load.

The S parameters are defined as:

$$S_{11} = \frac{b_1}{a_1} \Big|_{a_2=0} = \frac{I_{R1}\sqrt{R_{01}}}{I_{I1}\sqrt{R_{01}}} = \frac{I_{R1}}{I_{I1}} \Big|_{I_{I2}=0} = \frac{V_{R1}}{V_{I1}}. \quad (2.22)$$

So

$$S_{11} = \frac{Z_{in1} - R_{01}}{Z_{in1} + R_{01}}, \quad (2.23)$$

similarly

$$S_{22} = \frac{b_2}{a_2} \Big|_{a_1=0} = \frac{Z_{in2} - R_{02}}{Z_{in2} + R_{02}}, \quad (2.24)$$

where Z_{in1} , and Z_{in2} are the input impedance flowing into the two port network when E_1 , and $E_2 = 0$.

$$S_{21} = \frac{b_2}{a_1} \Big|_{a_2=0} = \frac{I_{R2}\sqrt{R_{02}}}{I_{I1}\sqrt{R_{01}}} \Big|_{I_{I2}=0} = 0. \quad (2.25)$$

As $I_2 = I_{I2} - I_{R2}$ and $I_{I2} = 0$, $I_2 = -I_{R2}$.

So

$$S_{21} = \frac{-I_2\sqrt{R_{02}}}{\sqrt{R_{01}}E_1/R_{01}} = \frac{-2I_2\sqrt{R_{01}}\sqrt{R_{02}}}{E_1}. \quad (2.26)$$

$$S_{12} = \frac{-2I_1\sqrt{R_{01}}\sqrt{R_{02}}}{E_2}. \quad (2.27)$$

2.4 Characteristics of Microstrip Patch Antennas

Microstrip patch antennas are the most common form of printed antennas. They are popular for their low profile, geometry, low cost and easy to integrate with RF circuit functions. A microstrip device in the simplest form is a layered structure with two parallel conductors separated by a dielectric substrate. The lower conductor acts as a ground plane. The device becomes a radiating microstrip antenna when the upper conductor is a patch with a length that is an appreciable fraction of a wavelength, approximately half a wavelength [9]. The width of the patch controls the total input impedance which will be reduced with the increasing width [13]. The width further controls the radiation pattern, which is widely used in telecommunication field. The microstrip patch antenna can be designed as the radiation element and also as the optimum load of an active device which make the whole circuit compact. As in airplane and space industry requirement, patch antennas could be designed to be operated in harsh environment [44]. The following section will present the effects of different shapes of radiation elements and feed methods on the performance of microstrip antennas.

2.4.1 Radiation Elements

There are different conductor shapes proposed and investigated for a microstrip patch antenna. The schematics of these radiation elements are shown in Fig. 2.4 [45].

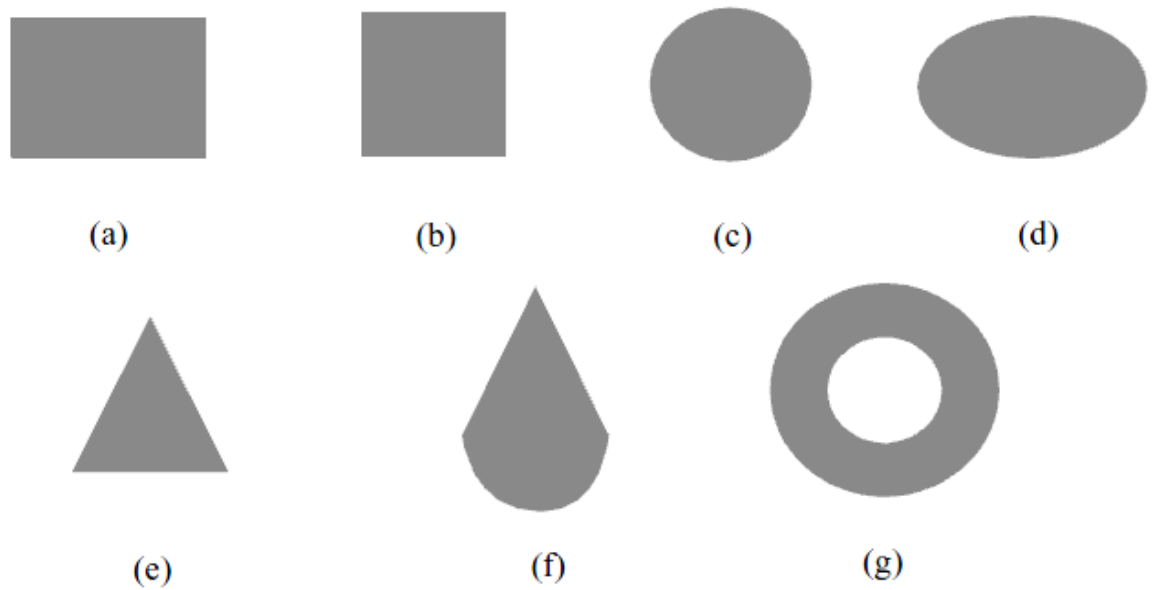


Fig. 2.4 The schematic of patch shapes.

The rectangular and square patches in Fig. 2.4(a) and Fig. 2.4(b) are mostly used, which can be easily to be modelled and analysed [46-48]. The square patch also could be used to obtain a circular polarized radiation antenna [49, 50]. The circular and elliptical patches (Figs. 2.4(c) and (d) [11, 51-53]) are slightly smaller than the corresponding rectangular patch with lower gain and bandwidth. The triangular and dish patches, Figs. 2.4(e) and (f), are smaller than corresponding rectangular and circular patch antennas with lower bandwidth and gain [45, 54]. Dual polarized radiation patterns can be produced using these geometries but with lower bandwidth and gain [54, 55]. Due to the lack of symmetry of the structure, higher cross polarization can be generated [45, 56]. An annular patch is demonstrated in Fig. 2.4(g) which has the smallest conductor shape but decreased bandwidth, gain, and also the symmetry issue as circular geometry patch [45]. Exciting the lowest order model and obtain a superior impedance bandwidth are not a simple process. Thus, the noncontact excitation form is normally used [57, 58]. Other shapes of microstrip

patches are well investigated as H, E shapes [59-62] due to their low profiles and a compact configuration. However, the bandwidths of such antennas are not wide enough for some applications including radar and broadband communications [63-65]. To compensate these drawbacks, new structures will be introduced in the following sections.

2.4.2 Different Feed Methods of Microstrip Patch Antenna

A feed line via direct or indirect contact is used to excite the antenna. Here six typical feed methods are presented, which are edge fed, inset fed, probe fed, coupled fed, proximity coupled, and aperture coupled. The first three types are classified as direct contact and the rest are defined as indirect contact.

(i) Edge fed

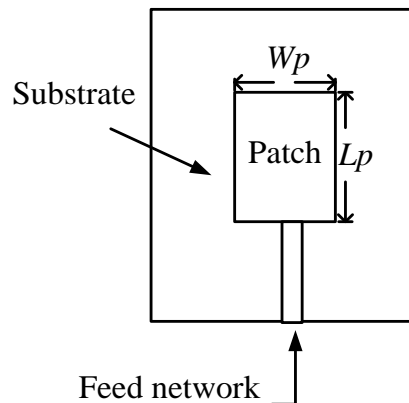


Fig. 2.5 Schematic of edge fed microstirp patch antenna.

The edge fed technique is one of the original feed methods for the microstrip patch antenna where a ML is in direct contact with patch as shown in Fig. 2.5. The width and length of patch is W_p and L_p , respectively. The input impedance can be easily matched by changing

the width and length of the feed using a quarter wave matching or other matching techniques [66, 67]. It is simple to fabricate this type of antenna because the feed and patch are in the same layer. Planar arrays could also be developed with higher gains [21, 68]. Transmission line models can be utilized to model the edge fed microstrip patch antenna, which will be covered in Chapter 3. Using large and thick substrate with a low value of dielectric constant could increase the bandwidth. However the surface wave efficiency will be reduced when using thick substrate with a high dielectric constant material [45, 54]. In addition, modelling of the performance of this type of antenna is not straightforward. The bandwidth and the gain of the microstrip patch antenna with this method are relatively narrow and low [14, 69].

(ii) Inset fed

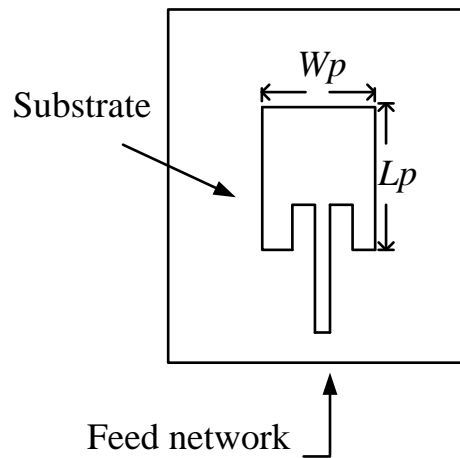


Fig. 2.6 Schematic of an inset fed microstrip patch antenna.

At the edge of the normal edge fed microstrip patch antenna, the input impedance is high. The impedance could be reduced by modifying the feed, where the current is low at the

ends of a half-wave patch and increasing in magnitude toward the centre. Also the voltage will decrease in the same amount when the feed moves to the centre of the patch. Hence the input impedance could be reduced if the feed line is closer to the centre of the patch with impedance matching achieved by changing the position of feed line [70-72]. The advantage and draw backs of this method are similar to the edge fed antenna.

(iii) Probe fed

The probe fed method for a microstrip patch antenna was proposed in 1970s, where a probe extends from the feed port at the ground plane and is connected to the patch is shown in Fig. 2.7.

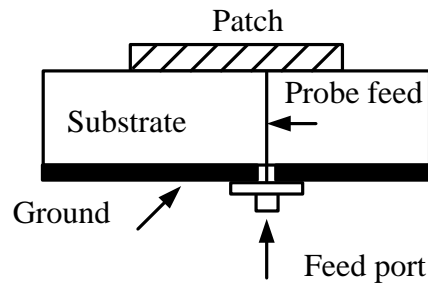


Fig. 2.7 Schematic of probe fed microstrip patch antenna.

The pin of the feeding probe is usually a coaxial line so it also called the coaxial feed. The position of the feed controls the input impedance [73-75], which has small value at the centre position and large value at the edge. The key advantage of this feed method is the independent optimization of each layer. This is due to the feed network being isolated by the ground plane, and the phase shifter and filter functions could be integrated with the feed network [48, 76, 77]. Because of direct contact between the feed and patch, higher

efficiency and a low spurious radiation are obtained. Problems of this feed method are similar to the edge fed method that a relatively wide bandwidth is still difficult to obtain.

(iv) Proximity coupled

In order to overcome the disadvantage of direct contact patch antennas, noncontact excitation methods are used such proximity coupled patch antennas and aperture coupled patch antennas [78, 79]. The proximity coupled patch antennas are shown in Fig. 2.8.

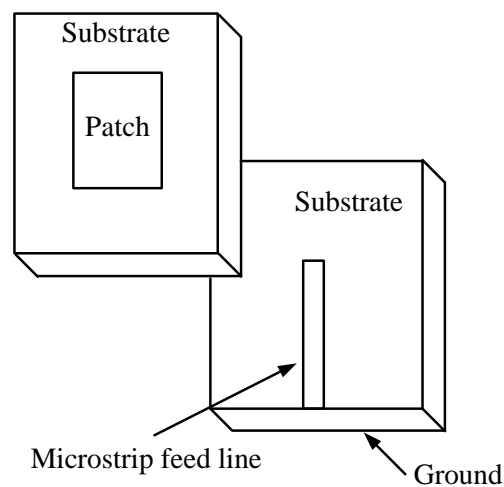


Fig. 2.8 Schematic of proximity coupled patch antenna.

This proximity coupled patch antenna consists of two parts where a substrate is located at the centre of a microstrip feed line and a ground plane at the base. Above the feed line there is another substrate with a radiating patch at the top. The power from the feed is coupled to the patch by means of electromagnetic radiation, thus it is also called the electromagnetic coupled patch antenna. Compared with the direct contact methods, which are predominantly inductive, the indirect contact of the proximity couple mechanism is

capacitive in nature. The important effect of this method is on the impedance bandwidth. The bandwidth of a proximity coupled microstrip patch antenna is inherently greater than that of the direct contact method patch antennas. This is because the substrate thickness of the direct contact structure is limited by the inductive coupling feature. Full wave EM analysis can be used to develop the proximity coupled patch antenna due to the lack of current discontinuity between the feed and radiating patch. However, because of the efficiency of power coupling, feed and radiating element are not fully independent, thus leading to creation of spurious feed radiation. From practical fabrication point of view, due to the multi-layer structure, the alignment procedure needs to be accurate in order to ensure accuracy in results [45].

(v) Aperture coupled

The structure of ACMA, which is a noncontact excitation structure, is illustrated in Fig. 2.9 [80].

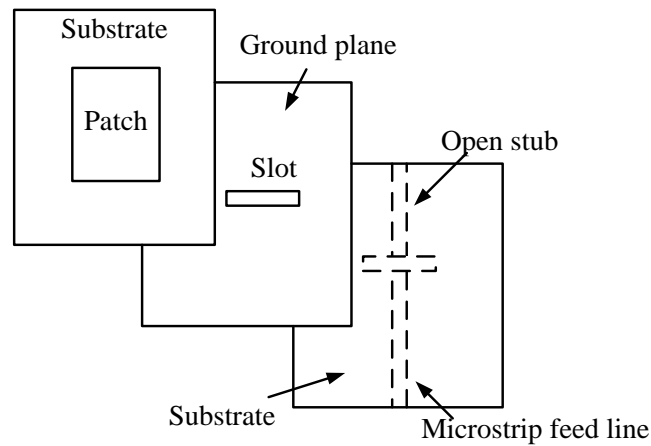


Fig. 2.9 Schematic of ACMA.

Unlike the proximity coupled patch, the feed and radiating elements of the aperture coupled structure are separated by a ground plane with the slot etched in. Comparing it with direct contact mechanisms like edge fed and probe fed structures, the feed and radiating elements of the ACMA can be optimized independently; no vertical interconnects are required, and also the spurious radiation is low. The ACMA has more design parameters than other types and therefore more flexibility for designers. The total input impedance is affected by the dimension of the patch, slot and substrate. The gain of the antenna will be influenced by the loss tangent and also height of substrate [9]. Unlike the direct contact fed methods, there are no abrupt current discontinuities. Therefore, relatively simple, TL model and full wave analysis are easy to be developed. Also due to its complex structure, it is easy to enhance the bandwidth up to 10% – 15% with a single layer, and up to 30% - 50% with a stacked patch configuration [81]. Other methods developed to optimise or increase the bandwidth, which produces dual or circular polarization for an ACMA were demonstrated in [24, 82, 83]. However, there are also problems with the ACMA such as alignment and multi-layer issues. Gap between layers of dielectric can change the impedance nature of this antenna. The next chapter will investigate the equivalent circuit of the ACMA.

2.5 Summary

This chapter introduced the basic concept of TL that was proposed to deliver power from the source to the load. The equations for the characteristic impedance and the propagation constant were shown using primary parameters. The ML theory also was reviewed. Equations of the effective dielectric constant and the characteristic impedance were given

which would be utilized in the future microstrip patch antenna analysis. A two port network with different source and load impedance was proposed for the analysis of S parameters which were derived to determine power reflected back and power passing through the circuit. Finally a number of microstrip patch antennas with different patch shapes and feed methods were presented. Advantage and draw backs of these antennas were reviewed and compared.

Chapter 3 Investigation of Aperture Coupled Microstrip Antenna using Transmission Line Model

3.1 Introduction

There is a requirement for light, low cost, wide bandwidth, multi-band, and high gain microwave antennas in applications such as automatic road tolling, ‘on the move’ satellite communication services and high-capacity data networks [21, 22, 64, 84-88]. These requirements can often be satisfied by an aperture coupled patch antenna [9, 89-92], see Fig. 3.1, and can also be used as a load with a high efficiency PA in the AIA design. W_p , L_p (W_s , L_s) are the width and length of patch (slot). W_f and L_{os} are the width of feed line and length of open stub.

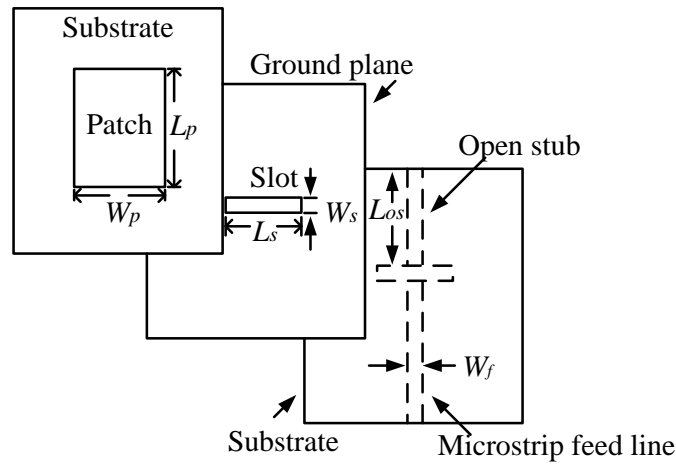


Fig. 3.1 Geometry of an ACMA.

An ACMA normally consists of a radiating patch and a microstrip feed line. A ground plane is used to separate the antenna substrate and the feed substrate with the slot etched in the ground plane. The shape of the slot is normally rectangular to improve coupling [14,

21, 78, 93,94]. Such an antenna has many parameters that could be exploited to improve its performance. In order to simplify the design procedure and to readily optimize the dimensions of an ACMA, the transmission line model analysis is still the best option for the speed and simplicity [69].

To obtain a wide bandwidth and a high gain, different substrate materials as well as a range of the stub length and size of coupling slot have been investigated [95-99]. Dual polarized antennas could be obtained by two orthogonal feeds with no overlapping slots and a rectangular patch element [78, 100-102]. To achieve circular polarization, a 90 degree phase offset hybrid coupler could be used but at the cost of limited isolation and polarization purity [48, 89, 103,104]. To solve this problem, a cross slot solution was suggested by [105] with different arrangement for the of feed lines [95], which resulted in a very wide bandwidth of return loss and also a 3 dB axial ratio up to 50% [81]. Due to flexible features of the aperture coupled patch antenna, sufficient space is allocated for arrays and feed networks to compensate for the limited power radiation by the single element [16, 106, 107]. It is not that simple to model the ACMA due to its complex structure. The cavity model initially developed in [80] was not rigorous enough, thus the development of full wave analysis reported in [8]. Pozar also derived the reciprocity theorem [108] to eliminate complex modelling of the feed and a stub applied to the mutual coupling between radiation elements for the array design. In this chapter, the equivalent circuits of the ACMA are reviewed and investigated with the aim of verifying and simplifying the model adopted for this antenna.

The equivalent circuit of the antenna is depicted in Fig. 3.2 where G and C are the parallel conductance and capacitance of the radiation of the patch. Z_{0p} and θ_p are the characteristic impedance and electrical length of the patch, respectively. Z_{0s} and θ_s are the characteristic

impedance and electrical length of the slot, respectively. Z_0 and θ are the characteristic impedance and electrical length of the open stub, respectively, and n_p and n_f are the coupling ratios between slot/patch and the feed/slot, respectively.

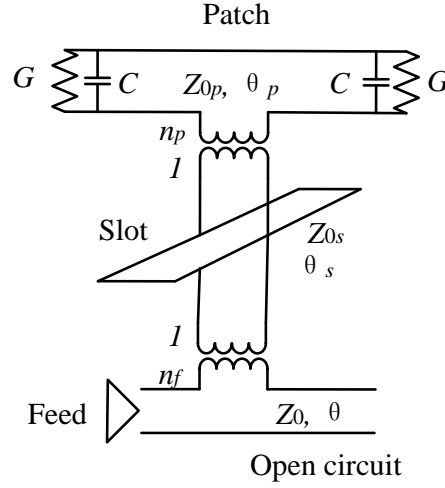
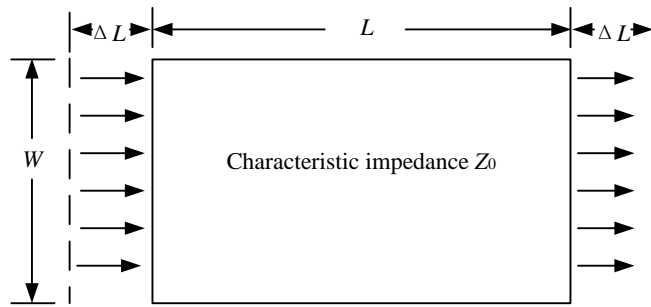


Fig. 3.2 Equivalent circuit of an ACMA.

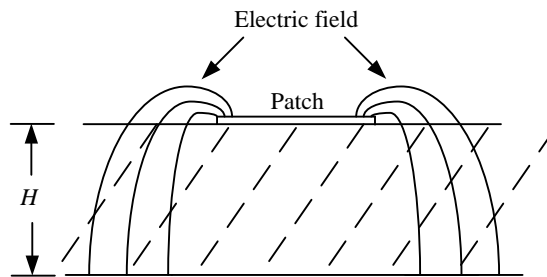
To investigate n_f , comparisons are carried out with previous works that used the spectral domain analysis and the spatial solutions [108-111]. The analysis carried out are rigorous and elegant but the dimensions of the physical model and values of the circuit elements of the equivalent circuit are interdependent thus making the design still more challenging. The n_p is a function of the width of the patch and length of the slot [112]. The patch is modelled as a TLM with the power radiation at the edge. The analysis of the equivalent circuit will be given in the following section.

3.2 Analysis of the Equivalent Circuit of the Radiation Patch

TLM is the simplest to be adopted for analysing this type of antenna compared to the cavity and full wave analysis [9]. Although TLM is less accurate and more difficult to model coupling [9] it gives a good physical insight, which will be adopted in investigation and design of the ACMA. This section will outline the TLM analysis of the radiation patch. A rectangular patch, which is straight forward to analyse and the most accurate for thin substrates, is adopted [45]. Because of the finite dimension of the patch, the field at the edge undergoes fringing. A rectangular microstrip antenna could be represented by an array of two radiation slots with the length ΔL and height H , separated by a transmission line with a distance L , see in Fig. 3.3:



(a)



(b)

Fig. 3.3 Structure of radiation patch and fringing field (a) top view (b) side view.

The amount of the fringing field is a function of the patch length [9]. Also the substrate affects the fringing field, see Fig. 3.3(b), which is a non homogeneous line of two dielectrics [80]. Because most of the electric field lines reside in the substrate and parts are in the air, an effective dielectric constant ϵ_{reff} is introduced for calculating the wave propagation. The effective dielectric constant has values between that of the air and the dielectric constant of substrate and is a function of frequency[14]. As frequency increases, most of the fields are concentrated in the substrate. Hence, the effective dielectric constant approaches the value of the dielectric constant of the substrate. For low frequency applications, the value of effective dielectric constant is referred to as the static value, see (2.10) [9]. Because of the fringing effects, the electrical length of the patch is greater than the physical length, which is extended by ΔL on each side. The length extension is given by (3.1) as a function of W/H and the effective dielectric constant ϵ_{reff} [9]:

$$\Delta L = 0.412H * \frac{(\epsilon_{\text{reff}} + 0.3) * (\frac{W}{H} + 0.264)}{(\epsilon_{\text{reff}} - 0.258) * (\frac{W}{H} + 0.8)} . \quad (3.1)$$

Thus the effective length of the patch is defined as:

$$L_{\text{eff}} = L + 2\Delta L . \quad (3.2)$$

Based on the derived equations, a simplified design procedure for the radiation patch is presented below.

- (i) The width of the patch for effective radiation is defined:

$$W = \frac{c}{2f} \sqrt{\frac{2}{\epsilon_r + 1}} , \quad (3.3)$$

where c is the free space speed of light and f is the working frequency.

- (ii) Obtain the extension length of patch ΔL using (3.1).
- (iii) Calculate the physical length of the patch from (3.2), where $L_{eff} = \lambda/2$, λ is the wavelength of propagated wave:

$$L = \frac{c}{2f\sqrt{\epsilon_{reff}}} - 2\Delta L. \quad (3.4)$$

The fringing fields store the energy in C which is grounded at the edge of the patch. The radiation power at each slot is represented by the conductance G_1 and the power losses due to the coupling between two slots are indicated by the conductance G_{12} . The equivalent circuit is illustrated in Fig. 3.4.

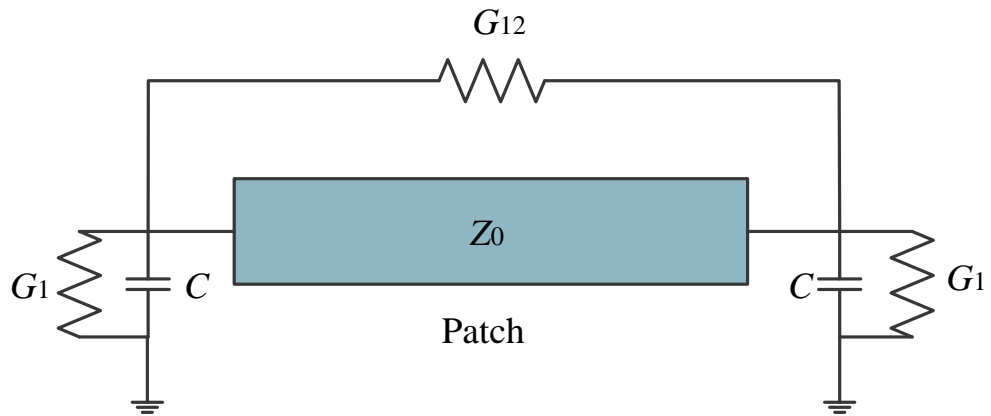


Fig. 3.4 Equivalent circuit of radiation patch.

G_{12} is seen as parallel with each side of the patch and therefore Fig. 3.4 can be simplified to Fig. 3.5.

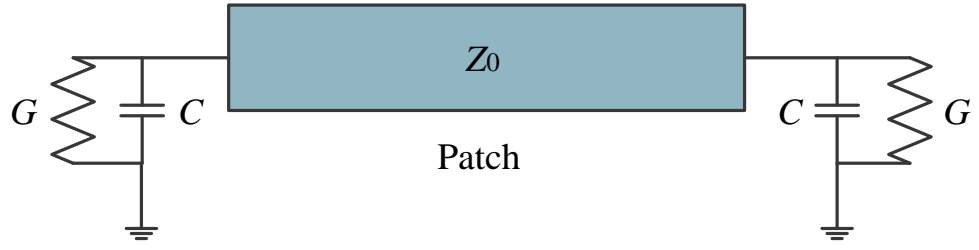


Fig. 3.5 Simplified equivalent circuit of radiation patch.

Where $G = G_1 + G_{12}$. So at each slot, G_1 for the finite width W and C is represented by the susceptance B as given by [9]:

$$G_1 = \frac{W}{120\lambda_0} \left[1 - \frac{1}{24} (k_0 H)^2 \right] \frac{H}{\lambda_0} < 0.1, \quad (3.5)$$

$$B = \frac{W}{120\lambda_0} [1 - 0.636 \ln(k_0 H)] \frac{H}{\lambda_0} < 0.1, \quad (3.6)$$

where λ_0 is the signal wavelength in the air, and k_0 is the wave propagation constant in air.

By using the field expression derived by the cavity model, G_1 and G_{12} could also be expressed as [9]:

$$G_1 = \frac{\int_0^\pi \left(\frac{\sin(k_0 * \frac{W}{2} * \cos \theta)}{\cos \theta} \right)^2 * (\sin \theta)^3 d\theta}{120 * \pi^2}, \quad (3.7)$$

$$G_{12} = \frac{1}{120\pi^2} * \int_0^\pi \left(\frac{\sin(k_0 * \frac{W}{2} * \cos \theta)}{\cos \theta} \right)^2 (\sin \theta)^3 * J_0 * (k_0 L \sin \theta) d\theta, \quad (3.8)$$

where J_0 is the Bessel's function of first kind of order zero.

The edge slots are connected by a TL of the characteristic impedance Z_0 given by:

$$Z_0 = \begin{cases} \frac{60}{\sqrt{\epsilon_{reff}}} \ln \left(\frac{8H}{W} + \frac{W}{4H} \right) \frac{W}{H} \leq 1, \\ \frac{120\pi}{\sqrt{\epsilon_{reff}} \left[\frac{W}{H} + 1.393 + 0.667 \ln \left(\frac{W}{H} + 1.444 \right) \right]} \frac{W}{H} > 1. \end{cases} \quad (3.9)$$

The normalized radiation pattern is approximately given by [14]:

$$E_\theta = \frac{\sin\left(\frac{kW}{2} \sin\theta \sin\phi\right)}{\frac{kW}{2} \sin\theta \sin\phi} \cos\left(\frac{kL}{2} \sin\theta \cos\phi\right) \cos\phi, \quad (3.10)$$

$$E_\phi = -\frac{\sin\left(\frac{kW}{2} \sin\theta \sin\phi\right)}{\frac{kW}{2} \sin\theta \sin\phi} \cos\left(\frac{kL}{2} \sin\theta \cos\phi\right) \cos\theta \sin\phi, \quad (3.11)$$

where $k = 2\pi/\lambda$, and the magnitude of the field is given by:

$$f(\theta, \phi) = \sqrt{E_\theta^2 + E_\phi^2}. \quad (3.12)$$

3.3 Review of Slot Lines

The slot line (SL) was proposed by Cohn in 1968 [113], which is a planar transmission structure. Cohn employed the transverse resonance approach, which converses SL into a waveguide configuration. The structure of SL is depicted in Fig. 3.6, which shows that a slot is etched in the metallization on one side of a dielectric substrate. This allows the SL to be included into microstrip circuits to produce a range of microwave subsystems.

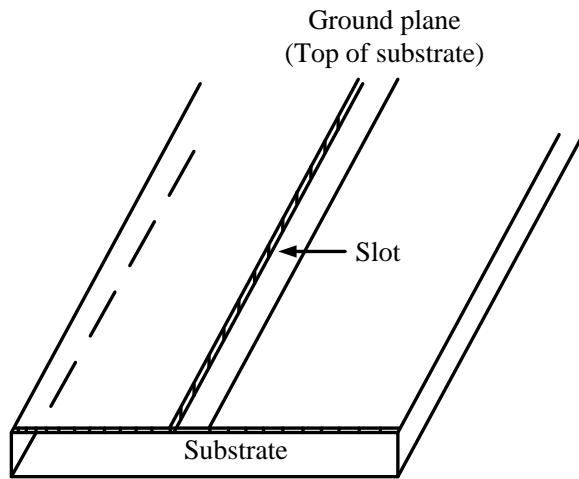


Fig. 3.6 Physical structure of SL.

In SL, a non-transverse electromagnetic (TEM) wave, which is almost transverse electric in nature, [113] propagates along SL with the major electric field oriented across the slot. The field distribution is shown in Fig. 3.7.

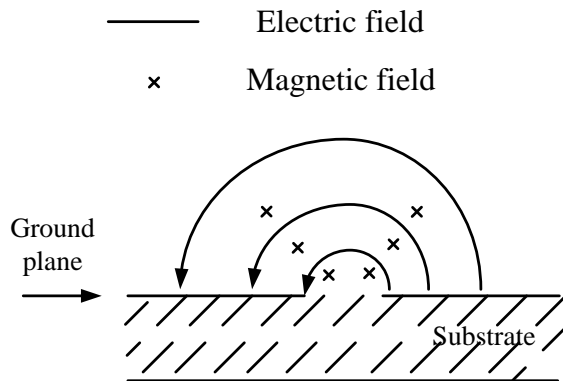


Fig. 3.7 Electric and magnetic field propagate around slot.

There are a number of mathematical methods that have been used to analyse SLs including the approximate analysis, transverse resonance approach [113], Galerkin's method in Fourier transform domain [114-117], and finite different time domain technique [118].

However, these methods do not lead to any closed form expression for Z_{0s} and wavelength, which could be used in the circuit analysis and design. Based on Cohn's analysis, the solution was presented by [117] and is given below.

The characteristic impedance for SL for two ranges of ϵ_r is given by (3.13) and (3.14) where W_s is the width of the slot and h is the height of the substrate.

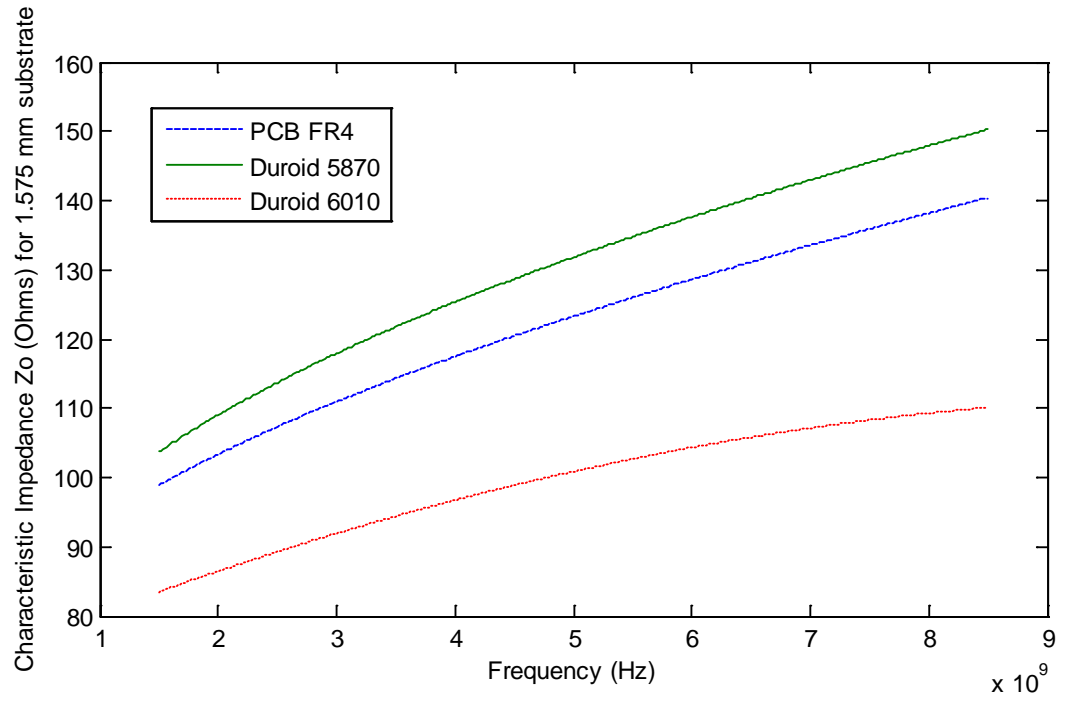
For $0.0015 \leq \frac{W_s}{\lambda_0} \leq 0.075$ and $2.22 \leq \epsilon_r \leq 3.8$,

$$\begin{aligned}
 Z_{0s} = & 60 + 3.69 \sin \left[\frac{(\epsilon_r - 2.22)\pi}{2.36} \right] + 133.5 \ln(10\epsilon_r) \sqrt{\frac{W_s}{\lambda_0}} \\
 & + 2.81[1 - 0.011\epsilon_r(4.48 + \ln(\epsilon_r))] \left(\frac{W_s}{h} \right) \ln \left(\frac{100h}{\lambda_0} \right) \\
 & + 131.1(1.028 - L_s(\epsilon_r)) \sqrt{\frac{h}{\lambda_0}} \\
 & + 12.48(1 + 0.18 \ln(\epsilon_r)) \frac{W_s}{h \sqrt{\epsilon_r - 2.06 + 0.85 \left(\frac{W_s}{h} \right)^2}}. \tag{3.13}
 \end{aligned}$$

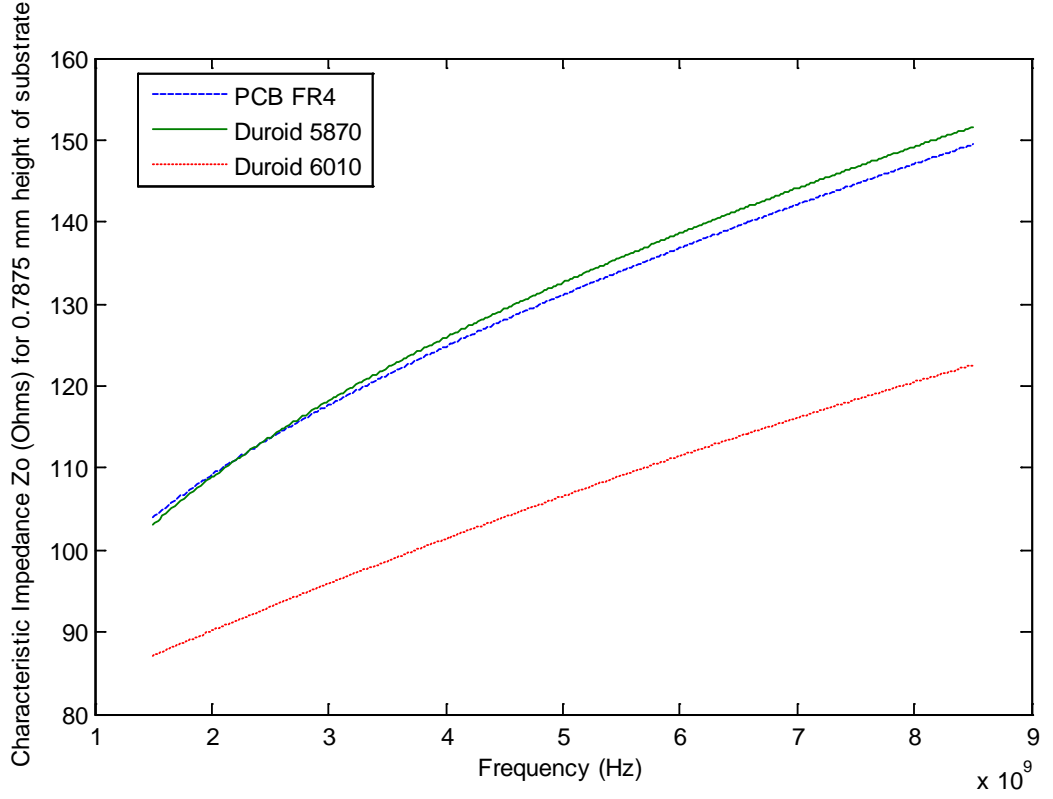
For $0.0015 \leq \frac{W_s}{\lambda_0} \leq 0.075$ and $3.8 \leq \epsilon_r \leq 9.8$,

$$\begin{aligned}
Z_{0s} = & 73.6 - 2.15\varepsilon_r + (638.9 - 31.37\varepsilon_r) \left(\frac{W_s}{\lambda_0} \right)^{0.6} \\
& + \left(36.23\sqrt{\varepsilon_r^2 + 41} - 225 \right) \frac{\frac{W_s}{h}}{\frac{W_s}{h} + 0.876\varepsilon_r} \\
& + 0.51(\varepsilon_r + 2.12) \left(\frac{W_s}{h} \right) \ln \left(\frac{100h}{\lambda_0} \right) \\
& - 0.753 \frac{\left(\frac{h}{\lambda_0} \right) \varepsilon_r}{\frac{W_s}{\lambda_0}} .
\end{aligned} \tag{3.14}$$

The above equations are used to determine Z_{0s} .



(a)



(b)

Fig. 3.8 Frequency response of characteristic impedance for substrates PCB FR4, Duroid 5870 and Duroid6010 with height: (a) 1.575 mm, and (b) 0.7875 mm.

From the results shown in Fig. 3.8, the characteristic impedances are proportional to the frequency for both heights, and at one fixed frequency point, the characteristic impedance is inversely proportional with the dielectric constant value.

Closed form expressions for the slot wavelength, which is also a function of effective dielectric constant ($\frac{\lambda_s}{\lambda_0} = \frac{1}{\sqrt{\epsilon_{reff}}}$), are given in (3.15) and (3.16) and the frequency response is shown in Fig. 3.9.

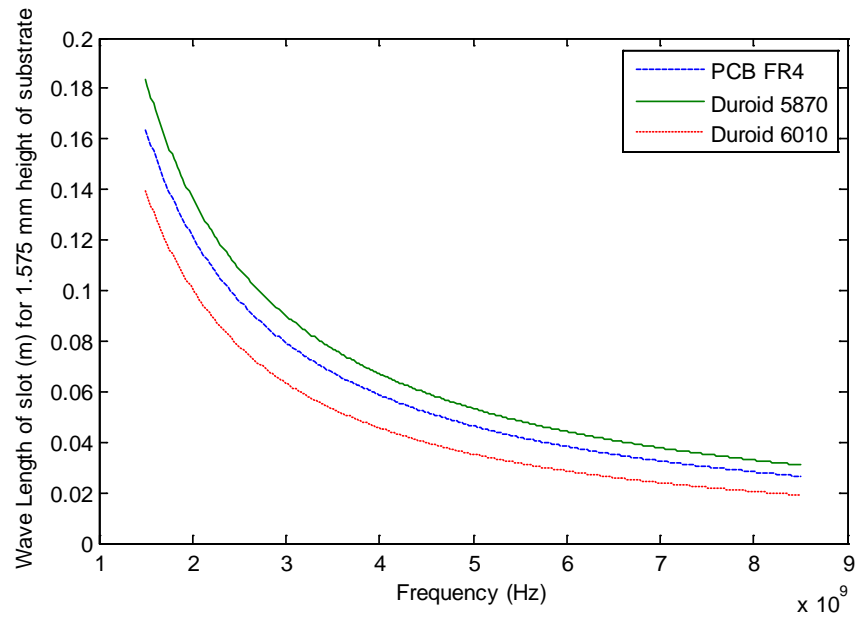
For $0.0015 \leq \frac{W_s}{\lambda_0} \leq 0.075$ and $2.22 \leq \varepsilon_r \leq 3.8$,

$$\begin{aligned} \frac{\lambda_s}{\lambda_0} = & 1.045 - 0.365 \ln(\varepsilon_r) + \frac{6.3 \left(\frac{W_s}{h}\right) \varepsilon_r^{0.945}}{238.64 + \frac{100W_s}{h}} \\ & - \left[0.148 - \frac{8.81(\varepsilon_r + 0.95)}{100\varepsilon_r} L_s \left(\frac{h}{\lambda_0}\right) \right]. \end{aligned} \quad (3.15)$$

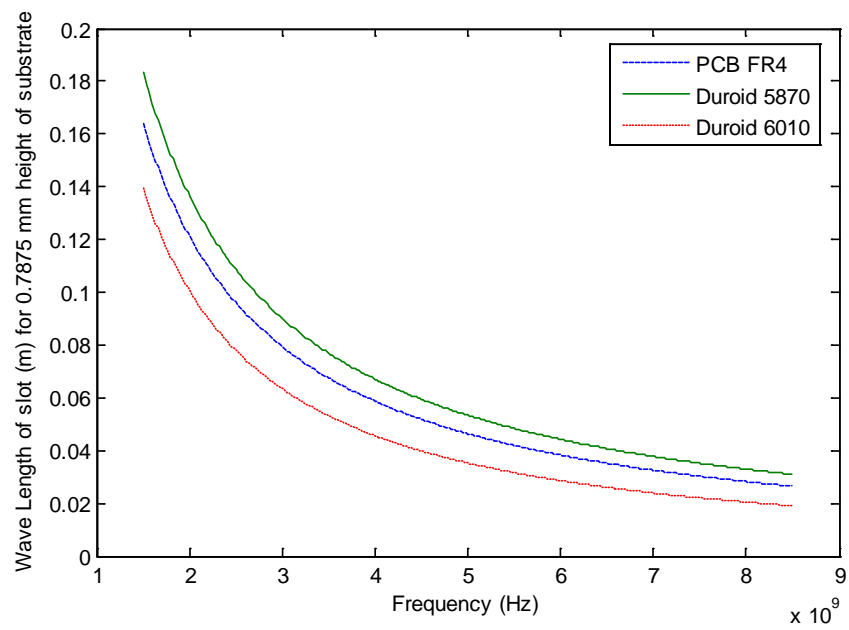
For $0.0015 \leq \frac{W_s}{\lambda_0} \leq 0.075$ and $3.8 \leq \varepsilon_r \leq 9.8$,

$$\begin{aligned} \frac{\lambda_s}{\lambda_0} = & 0.9217 - 0.277 \ln(\varepsilon_r) + 0.0322 \left(\frac{W_s}{h}\right) \left[\frac{\varepsilon_r}{\frac{W_s}{h} + 0.435} \right]^{\frac{1}{2}} \\ & - 0.01 \ln\left(\frac{h}{\lambda_0}\right) \left[4.6 \right. \\ & \left. - \frac{3.65}{\varepsilon_r^2 \sqrt{\frac{W_s}{\lambda_0}} \left(9.06 - 100 \frac{W_s}{\lambda_0}\right)} \right]. \end{aligned} \quad (3.16)$$

This wavelength ratio within specified slot line width and dielectric constant range are decreasing in terms of frequency and also with the dielectric constant of the substrate for a fixed frequency.



(a)



(b)

Fig. 3.9 Frequency response of wave length for PCB FR4, Duroid 5870 and Duroid6010 with different height of substrate: (a) 1.575 mm, and (b) 0.7875 mm.

3.4 Investigation of Microstrip/Slot Structure and Coupling Ratio between Microstrip Feed and Slot n_f

A SL fed by a ML is shown in Fig. 3.10 where the two lines are oriented at right angle to each other to obtain tight coupling. This structure is investigated by different researchers and the most frequent used is Galerkin's method in the spectral domain. From this analysis, two models are used which are quasi microstrip model and quasi slot line model. The electric fields are shown in Fig. 3.11.

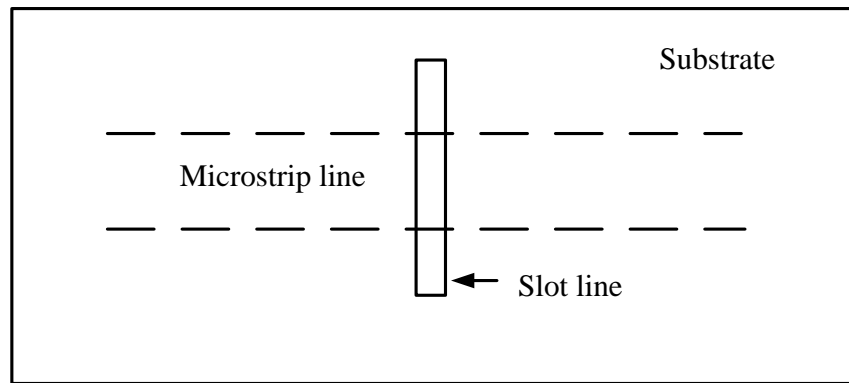
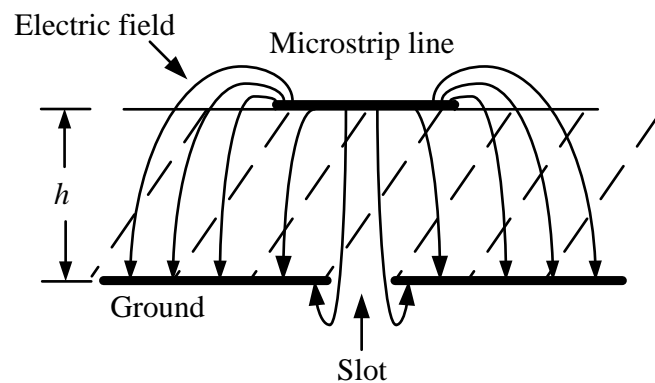


Fig. 3.10 Physical structure of microstrip/slot structure.



(a)

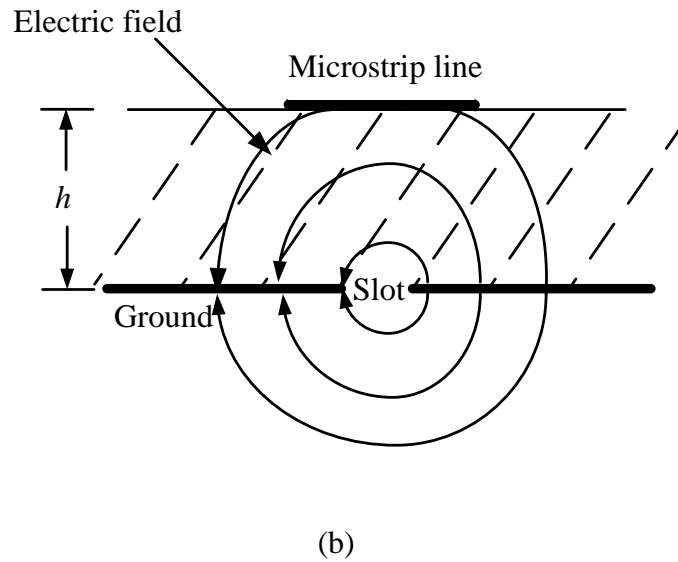


Fig. 3.11 Electric field propagation of microstrip/slot structure: (a) even model, and (b) odd model.

In Fig. 3.11(a) this field propagates like a ML, which has even symmetry and called even model. The model transferred in Fig. 3.11(b) behaves like SL which is called the odd model. The equivalent circuit of a microstrip/slot structure is shown in Fig. 3.12.

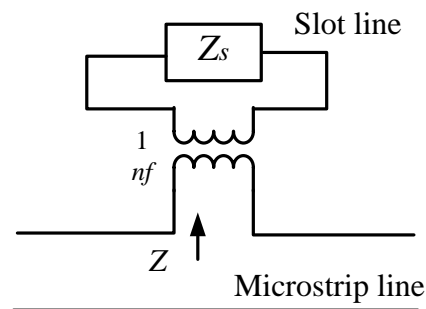


Fig. 3.12 Equivalent circuit of the slot/microstrip structure.

In the equivalent circuit the transformer (with n_f) models the coupling between SL and the microstrip feed line, while Z_s is the SL input impedance and Z is the impedance produced on the microstrip feed line. To investigate n_f , Knorr [119] derived equation (3.17) for n_f by assuming that the SL is infinitely long in one direction and extends a quarter-wave length beyond the strip line in the opposite direction. Also the microstrip feed line is infinitely long in one direction and extends a quarter-wave length beyond the SL in the other direction.

$$n_f = \cos\left(\frac{2\pi hu}{\lambda_0}\right) - \cot(q) \sin\left(\frac{2\pi hu}{\lambda_0}\right), \quad (3.17)$$

where $v = \sqrt{\epsilon_{rs} - 1}$, $u = \sqrt{\epsilon_{rm} - \epsilon_{rs}}$, $q = \frac{2\pi hu}{\lambda_0} + \tan^{-1}\left(\frac{u}{v}\right)$,

ϵ_{rm} is the effective dielectric constant of the microstrip line, and

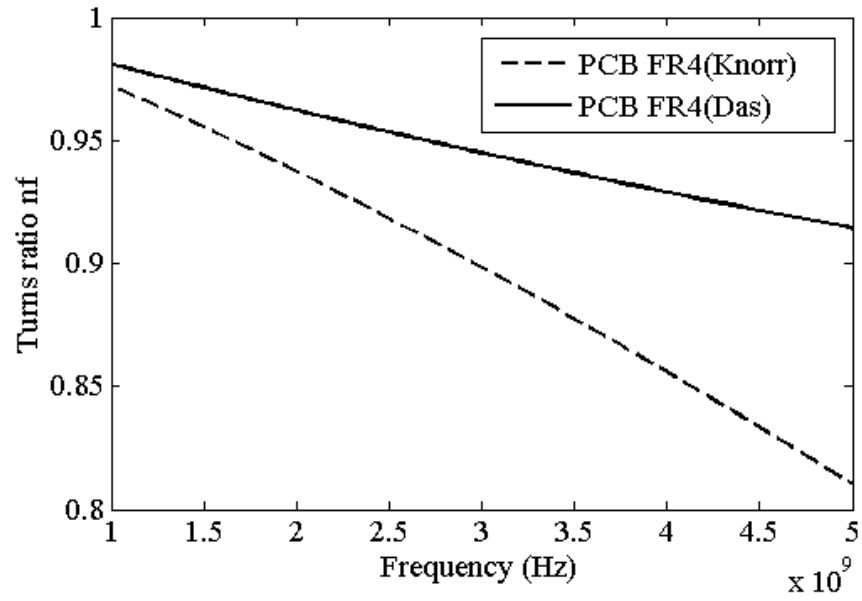
ϵ_{rs} is the effective dielectric constant of slot line.

Das [120] derived the following approximate closed form equation for the turn ratio shown in (3.18), in terms of the microstrip and SL parameters for infinitely long slot and MLs.

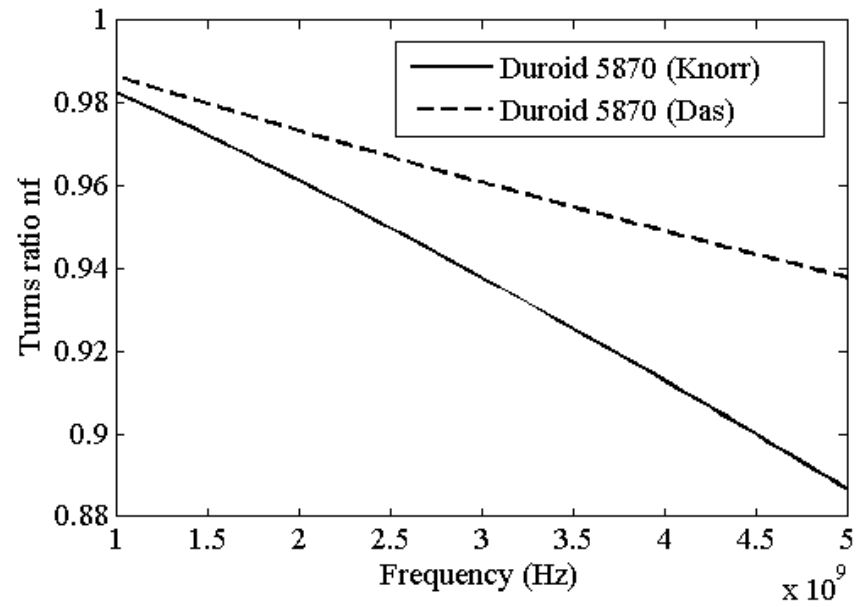
$$n_{fD} = \left(\frac{J_0\left(\frac{\beta_s W_f}{2}\right) J_0\left(\frac{\beta_m W_s}{2}\right)}{\beta_s^2 + \beta_m^2} \right) * \left[\frac{\beta_m^2 k_2 \epsilon_r}{k_2 \epsilon_r \cos(hk_1) - k_1 \sin(hk_1)} + \frac{\beta_m^2 k_1}{k_1 \cos(hk_1) + k_2 \sin(hk_1)} \right], \quad (3.18)$$

where n_{fD} is turns ratio n_f derived by Das. $\beta_s = k_0 \sqrt{\epsilon_{rs}}$, $\beta_m = k_0 \sqrt{\epsilon_{rm}}$, $k_1 = k_0 \sqrt{|\epsilon_r - \epsilon_{rs} - \epsilon_{rm}|}$, $k_2 = k_0 \sqrt{|\epsilon_{rs} + \epsilon_{rm} - 1|}$.

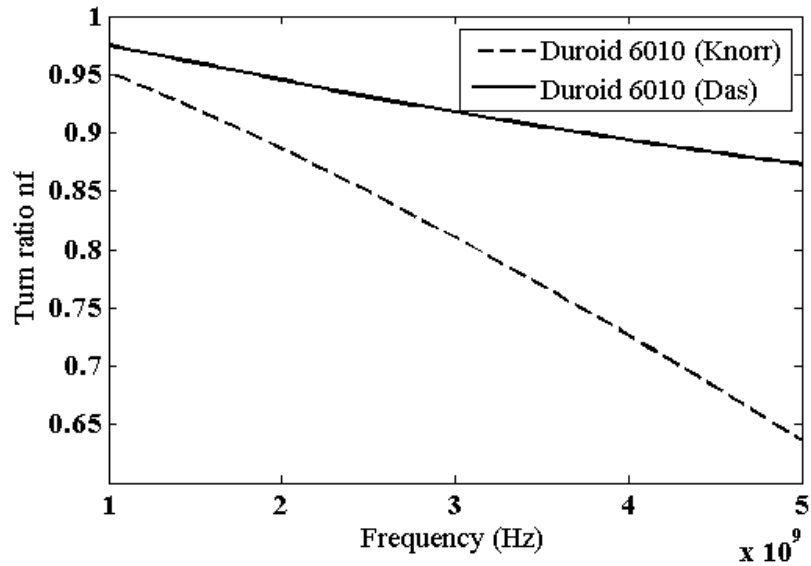
Both equations are plotted in Fig. 3.13 for a range of frequently used substrates in the frequency range 1 to 5 GHz.



(a)



(b)



(c)

Fig. 3.13 Frequency response of n_f using Knorr and Das's equations with different substrate: (a) PCB FR4, (b) Duroid 5870, and (c) Duroid 6010.

The frequency response of n_f predicted by Knorr and Das decreases gradually with frequency and the value of the dielectric constant of the substrate. For the same frequency and substrate conditions, the turn ratio based on Knorr's derivation is lower than that predicted by Das. Himdi[121], and Jaisson[112] derived equations for n_f in terms of substrate and finite slot dimensions. Himdi modelled the slot as a cavity consisting of four magnetic and two electric walls in deriving the formula of the turn ratio shown in (3.19), where k_s ($k_s = \frac{2\pi}{\lambda_s}$) is the propagation parameter in the slot line.

$$n_{fH} = \frac{2(\cos(k_s(\frac{L_s}{2} - \frac{W_f}{2})) - \cos(\frac{k_s L_s}{2}))}{k_s \sin(\frac{k_s L_s}{2}) \sqrt{W_f h}}, \quad (3.19)$$

where n_{fH} is turns ratio n_f derived by Himdi.

Jaisson simplified Pozar's piecewise [108] sinusoidal function for the usual condition that the design frequency is below the resonant frequency of the slot. Then using Taylor's series [122, 123] the derived equation for the turns ratios is given by:

$$n_{fJ} = \frac{2G(w) - G(w+l) - G(w-l)}{2\pi w l}, \quad (3.20)$$

where n_{fJ} is turns ratio n_f derived by Jaisson.

$$G(x) = (1 - x^2) * (\tan^{-1}x) + x * (\ln(1 + x^2)) \text{ and } w = \frac{W_f}{2h} \text{ \& } l = \frac{L_s}{2h}.$$

This coupling ratio in terms of slot length (2 GHz) for PCB FR4, Duroid5870 and Duroid 6010 is plotted in Fig. 3.14.

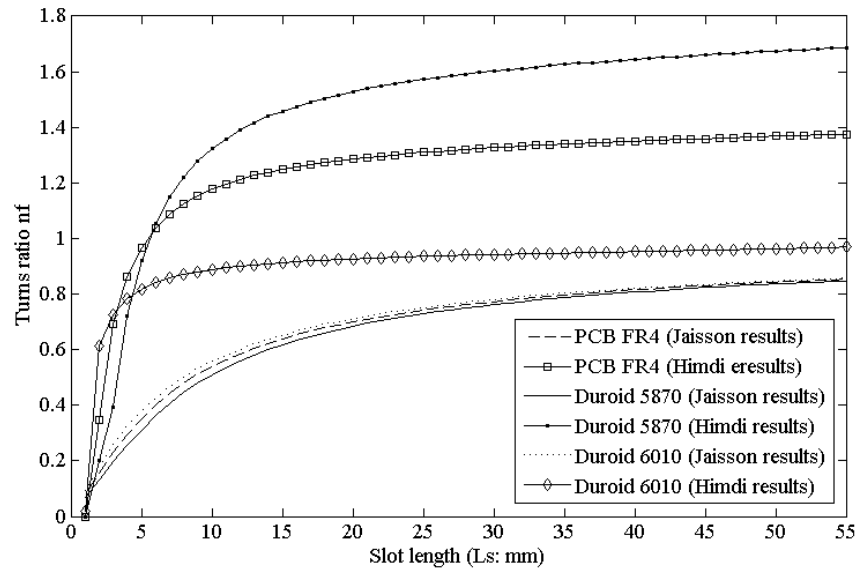


Fig. 3.14 n_f as a function of slot length for Jaisson and Himdi equations using PCB FR4, Duroid 5870 and Duroid 6010.

These results are not in good agreement. Based on Himdi's derivations, n_f is proportional to the slot length and tend to a constant value when the slot length is greater than 10 mm. However, substrates with different dielectric constants will affect n_f . Jaisson' results also tend to a constant when the slot length is greater than 10 mm but the substrate effects are small. As the derived equations do not agree, it is decided to model the above structure using the S_{21} and S_{11} in terms of slot length. Then the predicted results for n_f are compared to measured S parameters as given in the next section.

3.5 A Novel Method to Determine the Coupling Ratio of Feed/Slot and Slot/Patch using the S Parameter

As discussed in the analysis from the last section, Knorr and Das derived equations for n_f for an infinitely long SL showing that $n_f < 1$. Bhattacharyya [124] used the full wave analysis to obtain integral equations to plot n_f as a function of the SL length and height of the substrate. It was shown n_f increases with the SL length and decreases with the substrate thickness, but does not change much with the SL width. Bhattacharyya [110] also used the spectral domain analysis to derive complex equations computed numerically to obtain a matched ACMA. Himdi and Jaisson derived different equations for n_f (and similarly for n_p), however it was found that the equations did not agree with each other and the value of $n_f > 1$ as the SL length increased. Hence in this section n_f and n_p are investigated by simulation and practical measurements.

3.5.1 Determine Turns Ratio n_f using S_{21} Parameter

To obtain n_f it is first necessary to determine Z from the S_{21} parameter as shown in Fig. 3.15. In Fig. 3.16(a), the SL is fed by a 50 Ω microstrip feed line of length $L_1 + L_2$ and to calibrate for measurement errors produced by the length $L_1 + L_2$ a 50 Ω calibration line of the same length is used as in Fig. 3.16(b).

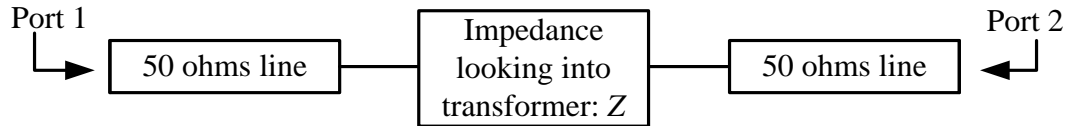


Fig. 3.15 Equivalent impedance of slot after coupling into microstrip feed line.

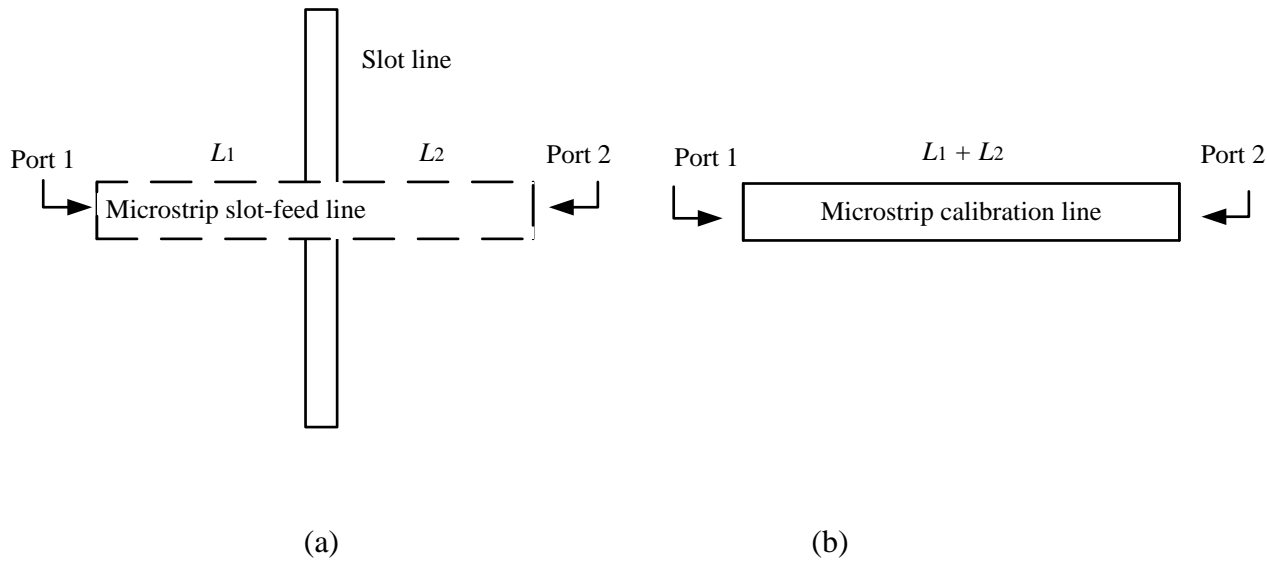


Fig. 3.16 Geometries of: (a) feed and slot lines, and (b) calibration line.

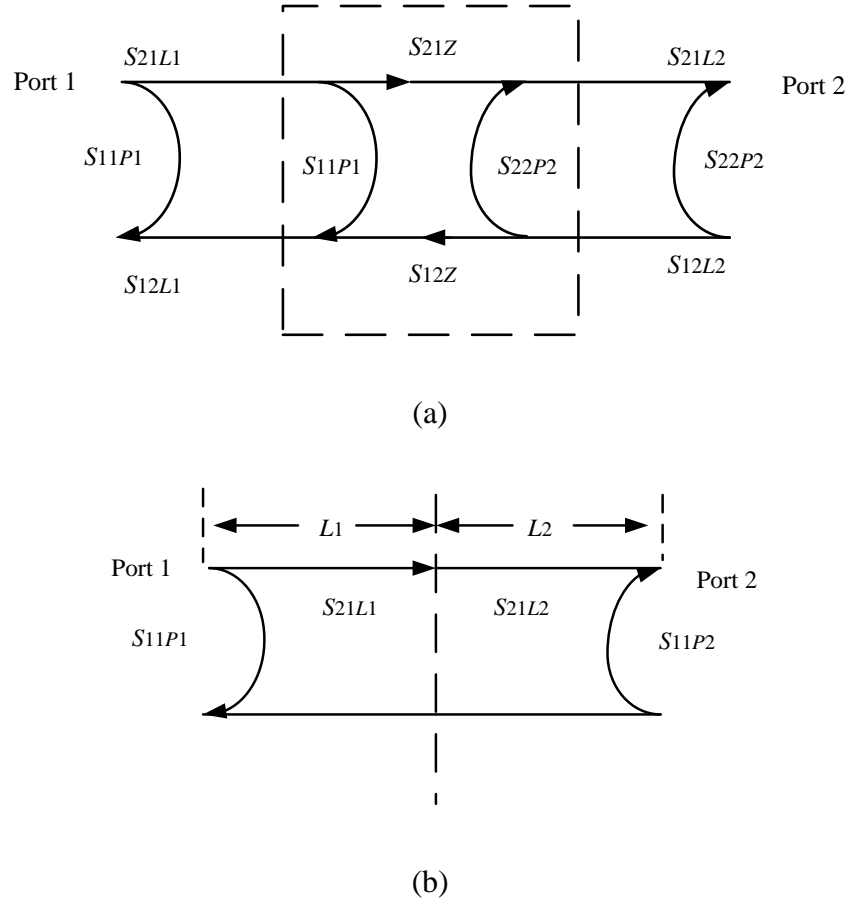


Fig. 3.17 Signal flow graphs: (a) the feed line with coupling slot effects, and (b) the calibration line.

The impedance of the ports is 50Ω and the signal flow graphs of the two structures in terms of S parameters are shown in Fig. 3.17. In Fig. 3.17(a), S_{21L1} , S_{21L2} are the transmission parameters for L_1 and L_2 of the microstrip feed line, respectively. Z is modelled by a two port network defined by S_{11Z} , S_{22Z} , S_{21Z} , and S_{12Z} . In Fig. 3.17(b) S_{21L1} and S_{21L2} are the transmission parameters of the microstrip calibration line. Equations (3.21) and (3.22) are obtained from the two signal flow graphs where S_{21T} is the transmission parameter between ports 1 and 2 as in Fig. 3.17(a) and S_{21C} between ports 1 and 2 as in Fig. 3.17(b).

$$S_{21T} = S_{21L1} * S_{21Z} * S_{21L2}. \quad (3.21)$$

$$S_{21C} = S_{21L1} * S_{21L2}. \quad (3.22)$$

(3.23) and (3.24) are used to determine S_{21Z} and Z by means of practical measurements and simulation.

$$S_{21z} = \frac{S_{21T}}{S_{21C}}. \quad (3.23)$$

$$Z = \frac{2Z_0 - 2Z_0 S_{21z}}{S_{21z}}. \quad (3.24)$$

To investigate how n_f depends on the relative permittivity of the substrate, substrate PCB FR4, Duroid 5870 and Duroid 6010 are used with the slot length up to 50 mm. The simulated results are shown in Fig. 3.18.

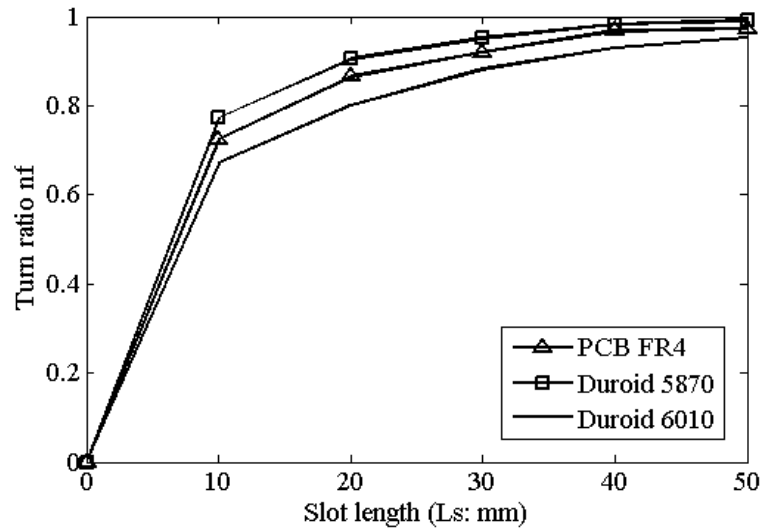


Fig. 3.18 n_f as a function of slot length with PCB FR4, Duroid 5870 and 6010 substrate.

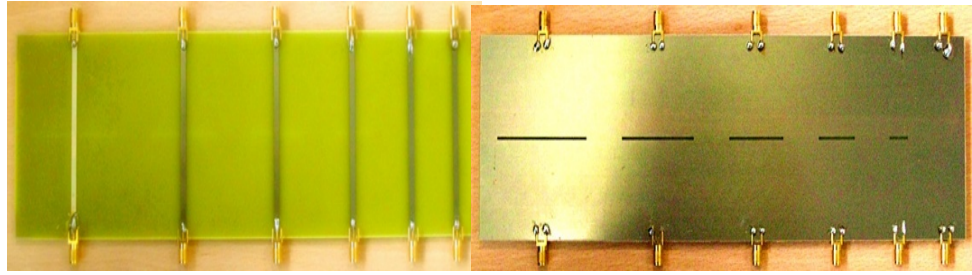


Fig. 3.19 Microstrip feed lines on one side, and five slot lines on the other, of a fabricated PCB board.

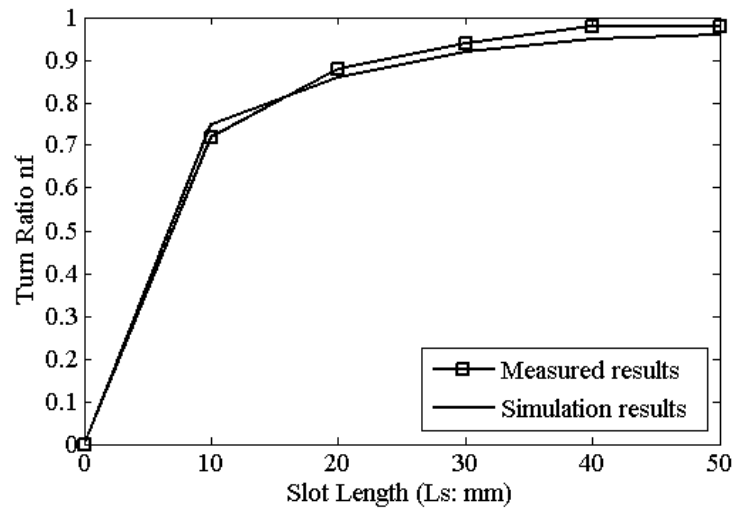


Fig. 3.20 Measured and simulation results for n_f as a function of slot length.

The PCB FR4 board shown in Fig. 3.19 was used for practical measurements: one side of the board shows 5 SLs of lengths 10, 20, 30 40 and 50 mm and the other side shows the five 50 Ω feed MLs, as well as a 50 Ω microstrip calibration line. The width of the SL was 1 mm and the equations derived in [117] were used to determine the SL input impedance Z_S . n_f was obtained from the S_{21} parameter determined by both practical measurement and simulation. Fig. 3.20 shows excellent agreement between these two approaches for determining n_f . It is important to note that this turns ratio has a limited range of 0.9 to 0.98

for a slot line length over 25 mm that is typical in the design of an antenna at around 2 GHz.

The effect of three different substrate thicknesses (0.7875, 1.575 and 2.5 mm) on n_f was also investigated by simulation as described above and (3.25) was obtained by means of curve fitting of Fig. 3.20.

$$n_f = 1 - e^{\frac{-L_s}{4h}}. \quad (3.25)$$

For three substrates of different permittivity, with a fixed SL of length 30mm, the above method was used to obtain the frequency response of Z for the physical structure and the equivalent circuit. It was found that the obtained frequency response of the physical structure, even over an extended range of 1 GHz to 5 GHz, agreed very closely with the frequency response obtained from the equivalent circuit. As n_f has a constant value in the equivalent circuit it can be concluded that n_f is effectively independent of both frequency and the relative permittivity of the substrate across the parameter ranges investigated.

3.5.2 Determine Turns Ratio n_f using S_{11} Parameter

To obtain n_f it is first necessary to determine Z from the S_{11} parameter. SL is fed by a 50 Ω microstrip feed line of length L_1+L_2 as in Fig. 3.21(a) and to calibrate out the measurements errors produced by L_1 a 50 Ω calibration open circuit microstrip shown in Fig. 3.21(b) is used.

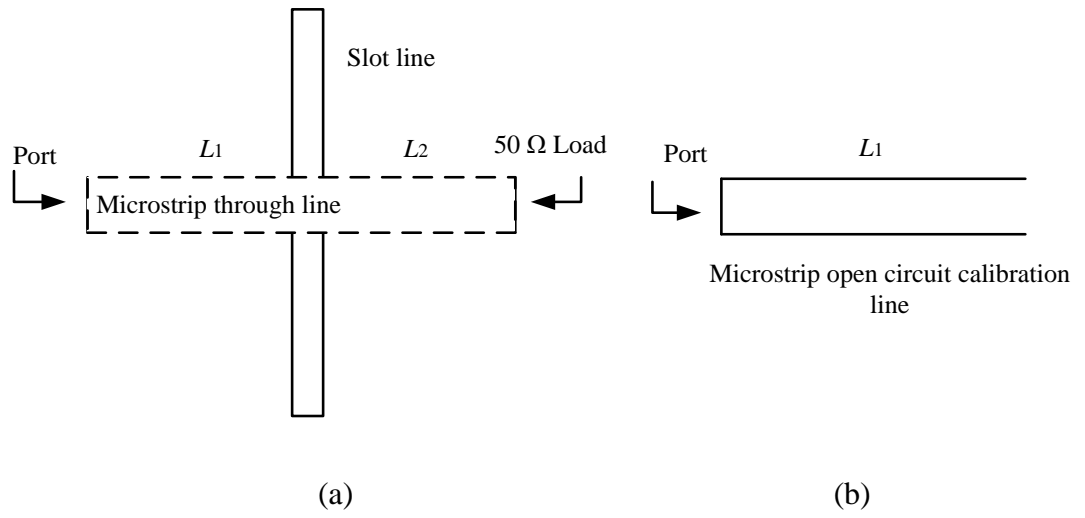
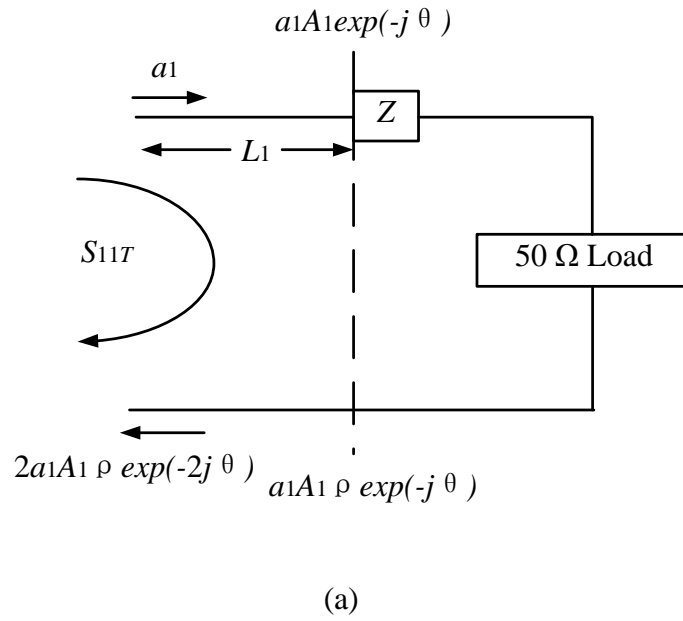
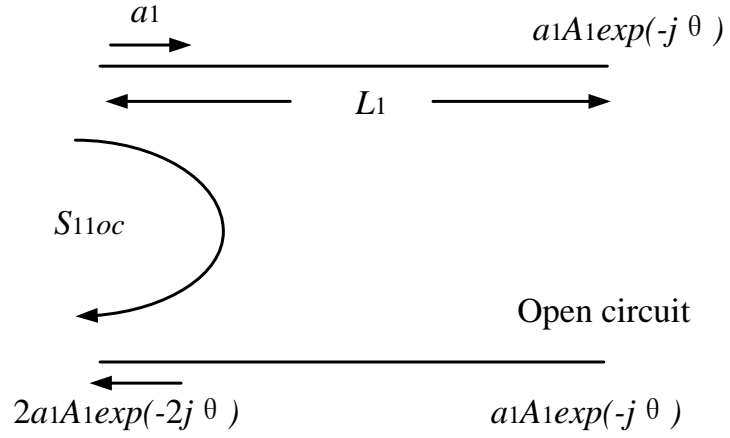


Fig. 3.21 Structure of model established for S_{11} test: (a) ML with slot, and (b) open circuit microstrip calibration line.





(b)

Fig. 3.22 Signal flow graphs: (a) ML with coupling slot impedance Z , and (b) microstrip open circuit calibration line.

The signal flows of models in Fig. 3.21 are given in Fig. 3.22. In Fig. 3.22(a), the incident signal is a_1 while the reflected signal at the input is $2a_1A_1\rho\exp(-2j\theta)$, where A_1 is the attenuation, ρ is the reflection coefficient and θ is the phase delay. For the open circuit the reflection coefficient is one so the reflected signal is $2a_1A_1\exp(-2j\theta)$. At the source part, the reflected signal S_{11T} and S_{11oc} are given by (3.26) and (3.27):

$$S_{11T} = \frac{2a_1A_1\rho e^{-2j\theta}}{a_1} = 2A_1\rho e^{-2j\theta}, \quad (3.26)$$

$$S_{11oc} = \frac{2a_1A_1 e^{-2j\theta}}{a_1} = 2A_1 e^{-2j\theta}. \quad (3.27)$$

The reflection coefficient ρ and then the series impedance Z can now be obtained using (3.28) and (3.29):

$$\frac{S_{11T}}{S_{11oc}} = \frac{2A_1\rho e^{-2j\theta}}{2A_1e^{-2j\theta}} = \rho, \quad (3.28)$$

$$Z = \frac{2\rho Z_0}{1-\rho}. \quad (3.29)$$

Note $Z_s = \frac{1}{2}jZ_{0s}\tan(\theta_s/2)$. Z_{0s} and θ_s of SLs can be obtained from [117]. The final n_f can be calculated by (3.30):

$$n_f = \sqrt{\frac{Z}{Z_s}}. \quad (3.30)$$

Simulations have been carried out by using substrates PCB FR4, Duroid 5870 and Duroid 6010 which agree with the results shown in Fig. 3.18 obtained using the S_{21} method. It is obvious that n_f increases rapidly with SLs. For the $SL > 20$ mm, n_f is almost constant (closer to 1) and the results from these three substrates are in good agreement. Hence, n_f is only marginally affected by the dielectric constant of the substrate. These results could be used in future designs where the numbers of design parameters of ACMA can be reduced.

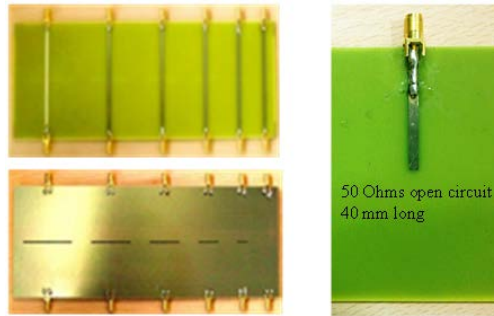


Fig. 3.23 Microstrip feed lines with slot lines (0 – 50 mm) and open circuit microstrip calibration line.

The fabricated boards using PCB FR4 substrate as shown in Fig. 3.23 are used to obtain S_{11T} , S_{11OC} , the reflection coefficient ρ and hence the series impedance Z . The simulation and measured results are in good agreement as shown in Fig. 3.24. By using curve fitting the equation obtained is the same as (3.25).

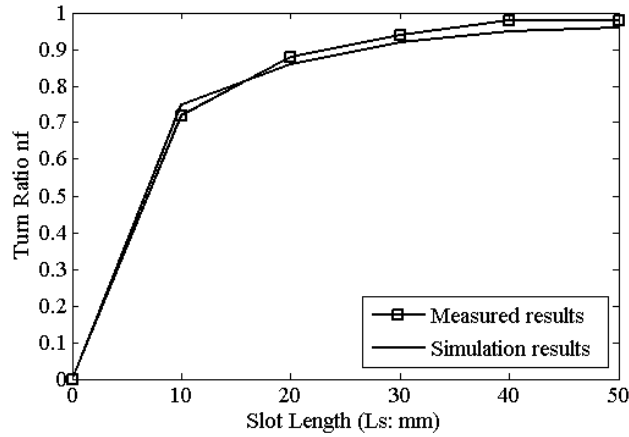


Fig. 3.24 Measured and simulation results for the turn ratio n_f as a function slot line lengths.

In order to validate the results obtained, a practical PCB board was fabricated with 40 mm open circuit ML, 80 mm microstrip through line with 30 mm slot length as shown in Fig. 3.25. By using the turn ratio obtained from (3.30), circuit simulation results and practical measurement carried out for Z to validate this method are compared in Fig. 3.26, which are in good agreement.

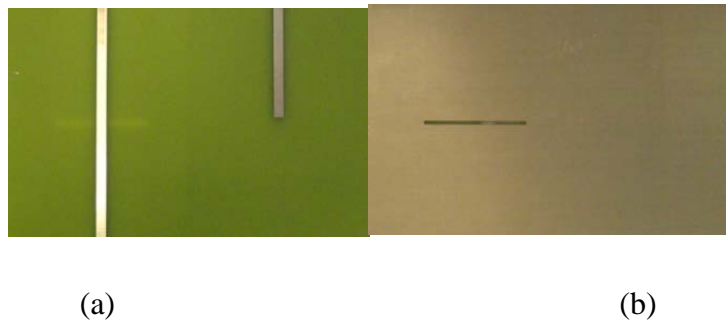


Fig. 3.25 Fabricated boards with (a) feed and open circuit side, and (b) slot line side.

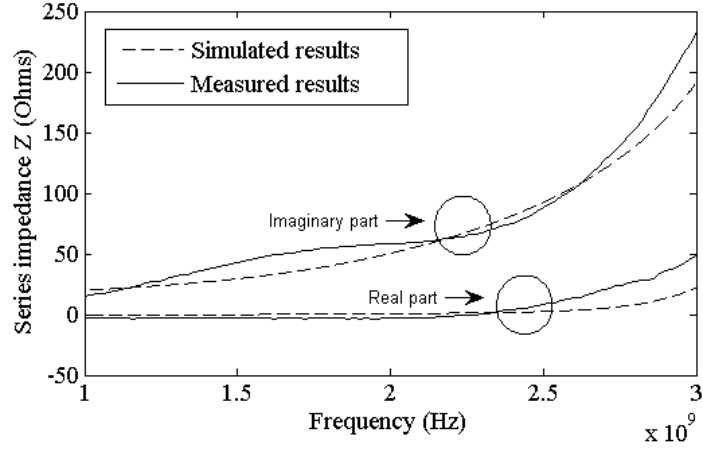


Fig. 3.26 Frequency response of the series impedance Z .

3.6 Investigation of the End Effects of the Slot

The two types of discontinuities of slot are investigated, which are short-end and open-end. The open end structure is not commonly used due to the impractical implementation and lots of radiation loss. A short end is created by just ending the slot with a conducting surface. Due to the current flows in the conductor plane at both ends of the SL there is stored magnetic energy which gives an inductive reactance that behaves as an electrical extension ΔL_s to physical length of the slot. Full wave analysis was presented by [125, 126] and also practical measurements were carried out in [127] showing the normalized reactance in terms of the thickness to wavelength ratio, which is in a good agreement. Losses of the short end also exist due to the power propagation in surface waves and radiation, which could be modelled as R_s . Yang and Alexopoulos [126] presented the investigation of the normalized resistance in terms of thickness to wavelength ratio of the substrate.

In this section, a simplified method to investigate ΔL by comparing the resonant frequency of the slot with tuned circuit results and measured results is given. Based on the application of the proposed antenna design, the width of slot is fixed to 1 mm and working frequency is 2 GHz. To determine ΔL_s , S_{21} could be used to determine the resonant frequency as the value drops to minimum at that point. A two port network shown in Fig. 3.27(a) is used to measure S_{21} physically and compare it with the tuned circuit results based on Fig. 3.27(b) in terms of physical slot length. Results given in Fig. 3.28 show that ΔL is proportional to the physical length and inversely proportional to the dielectric constants for a fixed substrate height of 1.575 mm.

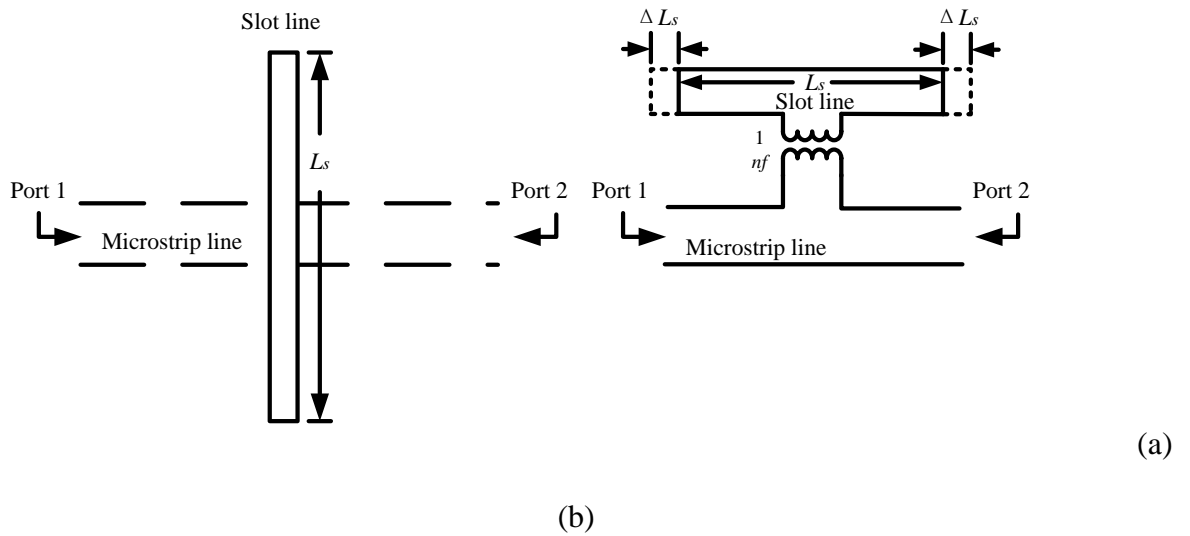


Fig. 3.27 Two port network of feed slot structure used for S_{21} test: (a) physical structure, and (b) circuit structure.

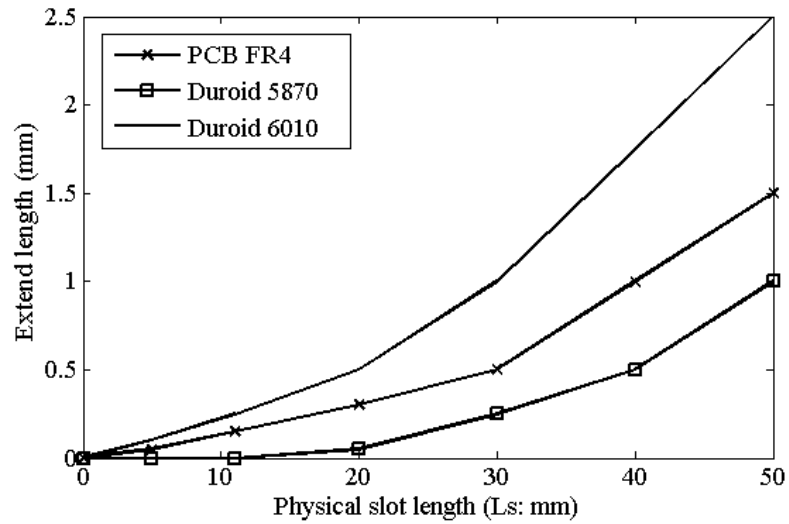


Fig. 3.28 Extended end effect slot length in terms of physical slot length using substrate PCB FR4, Duroid 5870 and Duroid 6010.

Using the same methodology for determining ΔL_s , the equivalent end resistance R_s could be measured and obtained by S_{21} parameters using (3.21) - (3.24) at the resonant frequency. Increase the physical length of slot (0 – 50 mm) by comparing the measured results with tuned circuit results based on Fig. 3.27. Results are given in Fig. 3.29, which indicates that R_s is slightly reduced from 0 to 20 mm and levelling off at 7, 11, and 2 Ω for PCB FR4, Duroid 5870 and Duroid 6010, respectively between the range of 20 to 50 mm of slot length. Also shown is that R_s is inversely proportional to dielectric constants for a fixed substrate height of 1.575 mm.

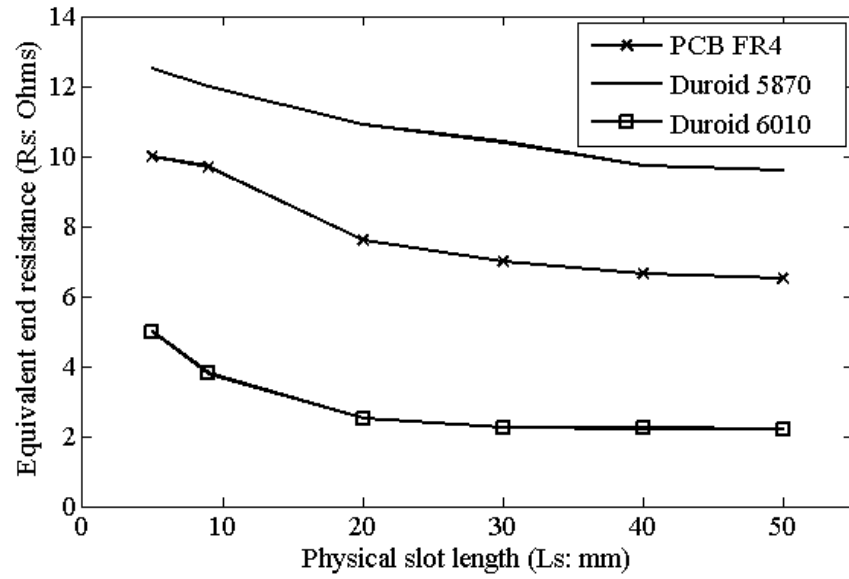


Fig. 3.29 R_s varies in terms of the physical slot length with the effects of substrate PCB FR4, Duroid 5870 and Duroid 6010.

3.7 Investigation of the Coupling Ratio between the Slot and the Patch

Coupling between the slot and patch is modelled by n_p , and the equivalent circuit of the slot/patch physical structure with transformer is shown in Fig. 3.30.

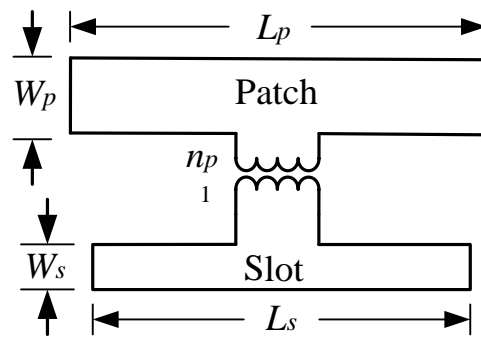


Fig. 3.30 Equivalent circuit of slot/patch structure.

From the literature review, Himdi [121] suggested that n_p is a function of the SL and patch width as given by:

$$n_{pH} = \frac{L_s}{W_p}, \quad (3.31)$$

where n_{pH} is n_p defined by Himdi.

However, Jaisson [112] proposed different suggestions based on the theorem of reciprocity and computed with a table of integrals in hand that the coupling ratio is affected by the effective width of patch W_p' and length of slot, which is given by:

$$n_{pJ} = \frac{L_s}{2W_p'}, \quad (3.32)$$

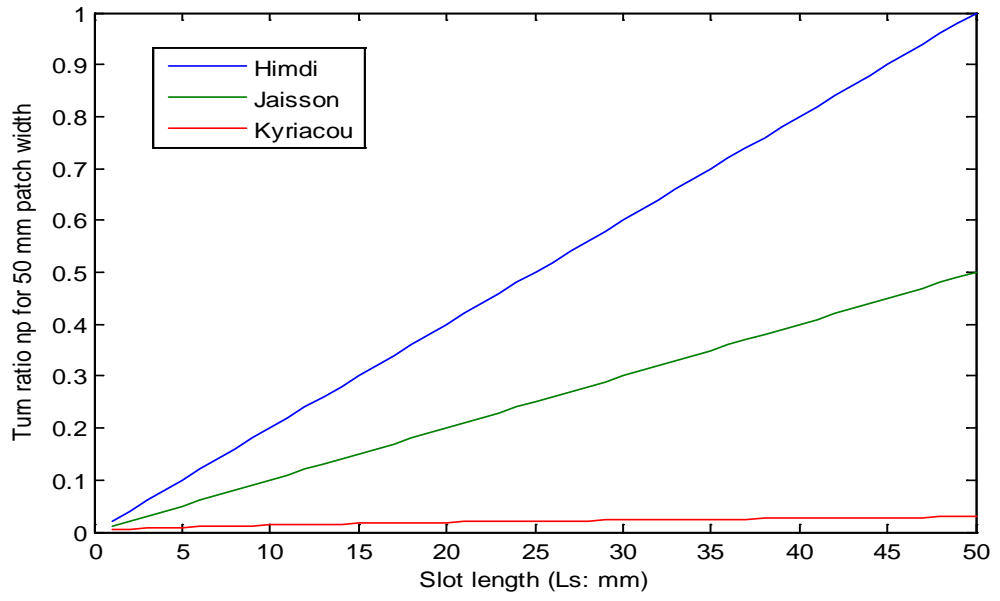
where n_{pJ} is n_p defined by Jaisson.

Kyriacou [128] considered the patch as a short but wide ML and using the curve fitting derived the following:

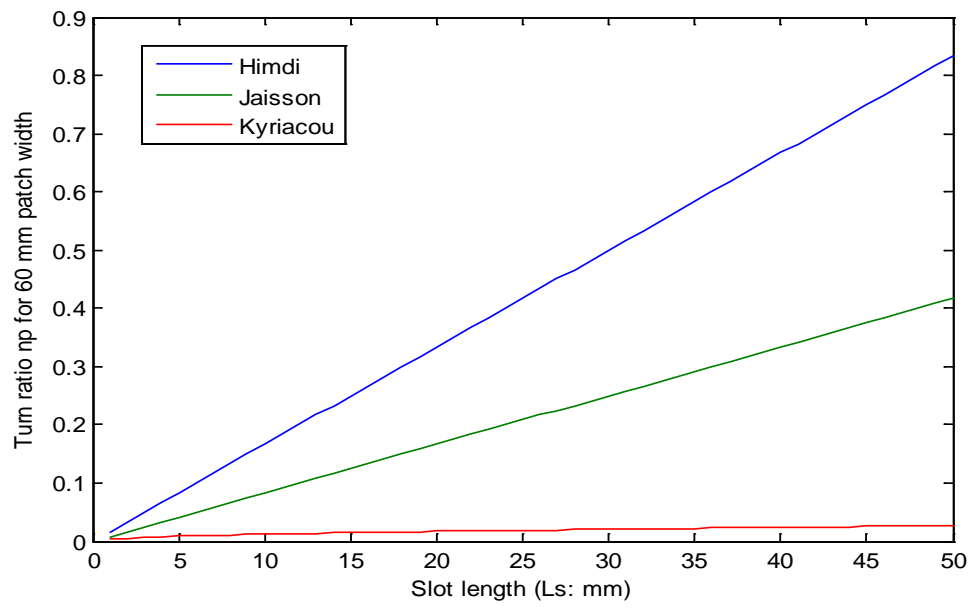
$$n_{pK} = \sqrt{2.42 \frac{W_p^2}{L_s W_s \sqrt{\epsilon_r}}}, \quad (3.33)$$

where n_{pK} is n_p defined by Kyriacou.

Equations (3.31-3.33) are plotted in Fig. 3.31 with SLs up to 50 mm for the patch width of 50 and 60 mm, showing large differences for the turns ratio.



(a)



(b)

Fig. 3.31 n_p as a function of slot length and the patch width of: (a) 50 mm, and (b) 60 mm.

To address this problem, the following analysis is carried out. First, the feed/slot dimensions were kept constant to ensure that n_f had a fixed value and the patch width was varied from 50 mm to 70 mm. Then the SL length was varied up to 50 mm and for each SL, n_p was tuned using the AWR software until the input impedance of the equivalent circuit and that of the physical structure using CST simulation were in good agreement. The determined turns ratio agreed very closely with (3.32) derived by Jaisson, see Fig. 3.32.

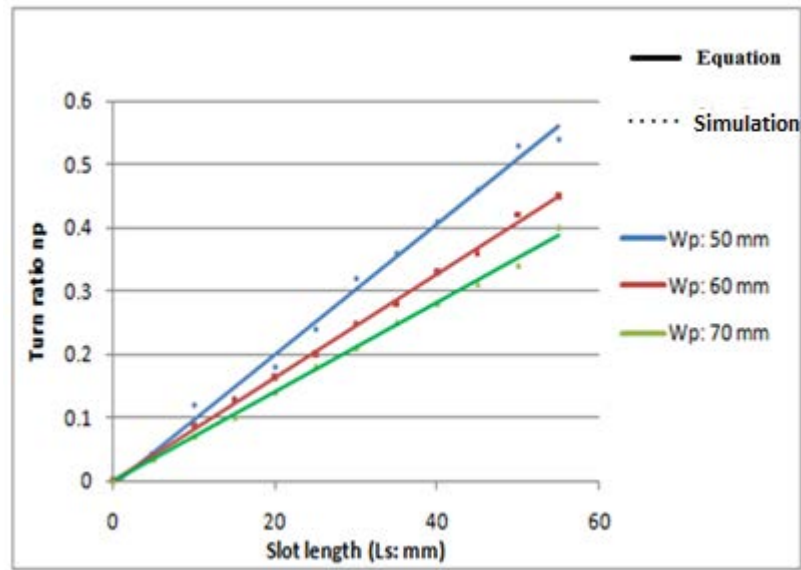


Fig. 3.32 n_p as a function of L_s and W_p with the comparison of simulation and Jaisson's results.

3.8 Design Procedure of an ACMA

Based on the analysis carried out in this chapter, a simplified design procedure for a typical ACMA could be obtained. The patch and SLs are connected in parallel, see Fig 3.33, and the input admittance looking up from slot is given by Fig. 3.34. Because of the parallel structure, the admittance instead of impedance is adopted in the analysis.

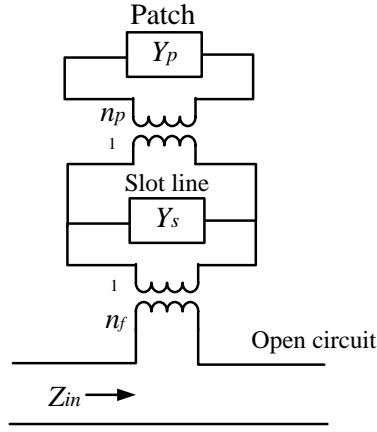


Fig. 3.33 Equivalent structure of the parallel patch and slot.

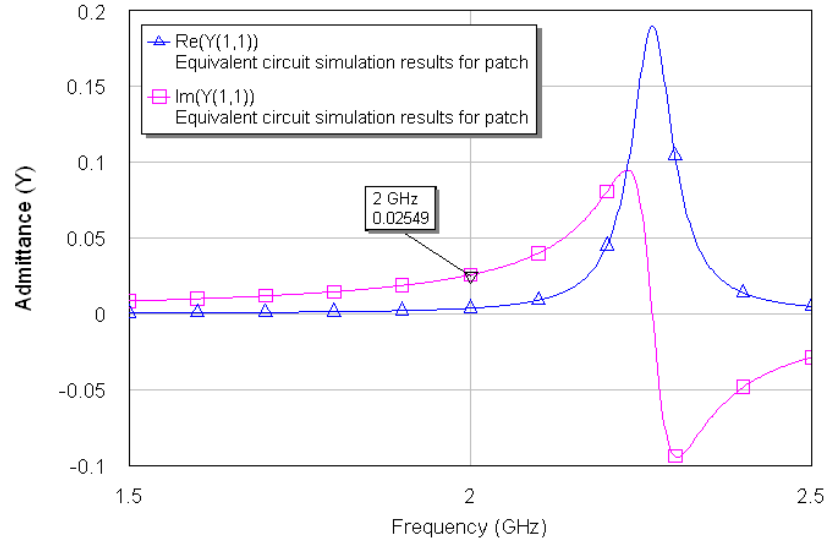


Fig. 3.34 Input admittance of the patch.

Due to the slot coupling technique, the patch behaves as a series tuned circuit and the resonant frequency of the patch is slightly larger than the design frequency. Hence the length L_p is slightly less than the half-wavelength at the design frequency ($\sim 0.9\lambda_p/2$), where λ_p is the patch wavelength. The imaginary part of the admittance has a capacitive value,

which is used to calibrate the inductive value produced by the slot. The frequency response of the input admittance of the SL is shown in Fig. 3.35

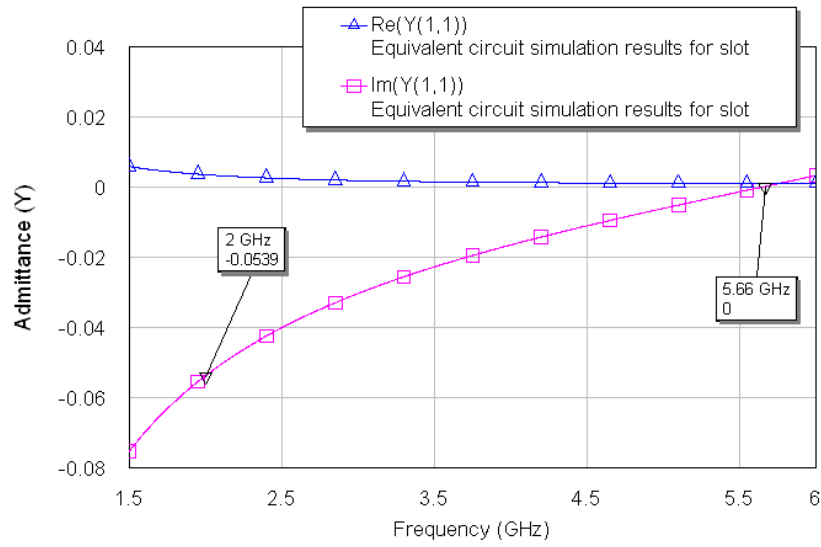


Fig. 3.35 Input admittance of SL.

The resonant frequency of the slot is again higher than the design frequency however the inductive value of the imaginary admittance could be used to cancel out the value produced by the patch. The slot length should be $\sim 0.7\lambda_s/2$. Based on the above results and the investigations carried out previously, the design process and the approximate starting values of the components in the equivalent circuit are suggested below.

- 1) In the investigation of this antenna it has been found that the resonant frequency of the series impedance of the patch is above the design frequency. Hence $L_p < \sim 0.9\lambda_p/2$.
- 2) W_p could be determined by (3.3).
- 3) To reduce spurious radiation, W_s is specified as 1 mm. So Z_{0s} , which is mainly based on W_s [9], is $\sim 100 \Omega$.

- 4) The parallel resonant frequency of the slot is also higher than the design frequency and $L_s = \sim 0.7\lambda_s/2$, and $n_p = L_s/2W_p$.
- 5) n_f is largely independent of relative permittivity of the substrate. Above a slot length of ~ 20 mm it has a constant value of 0.9.
- 6) All the parameters of the physical and equivalent circuit of the antenna are now approximately known but are required to be fine-tuned so that the input impedance at the microstrip feed position is in the form $50 + jX \Omega$. The open circuit length beyond the above feed position of the microstrip line can be obtained so that the antenna is matched.

Following the design procedure, a narrow bandwidth ACMA is designed. The dimensions are shown in table 3.1 and the return as a function of the frequency loss for S_{11} for the equivalent circuit simulation and full wave simulation is depicted in Fig. 3.36, showing good agreement. The bandwidth is about 50 MHz. The height of substrate between patch/slot, and the slot feed line are both 1.575 mm and n_f and n_p are 0.89 and 0.22, respectively.

Parameter	Unit: mm
W_p	55
L_p	30.9
W_s	1
L_s	19.1
W_{st}	3
L_{st}	8

Table 3.1 Dimension of an ACMA.

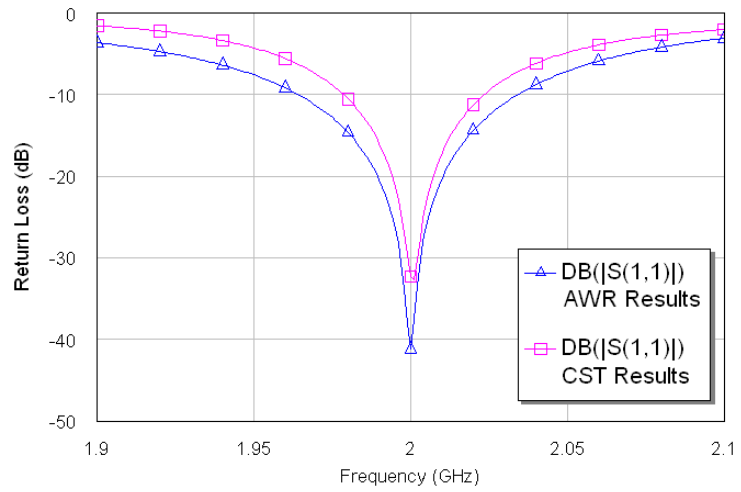
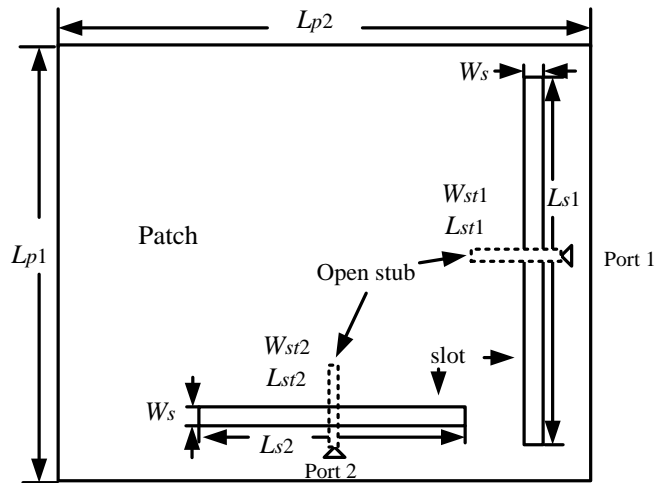


Fig. 3.36 Frequency response of the return loss.

3.9 Design of Broadband Dual Frequency ACMA

To obtain a dual frequency antenna, modes at 1.9 GHz and 2.4 GHz are excited by the two SLs near the edges of the patch as shown in Fig. 3.37(a).



(a)

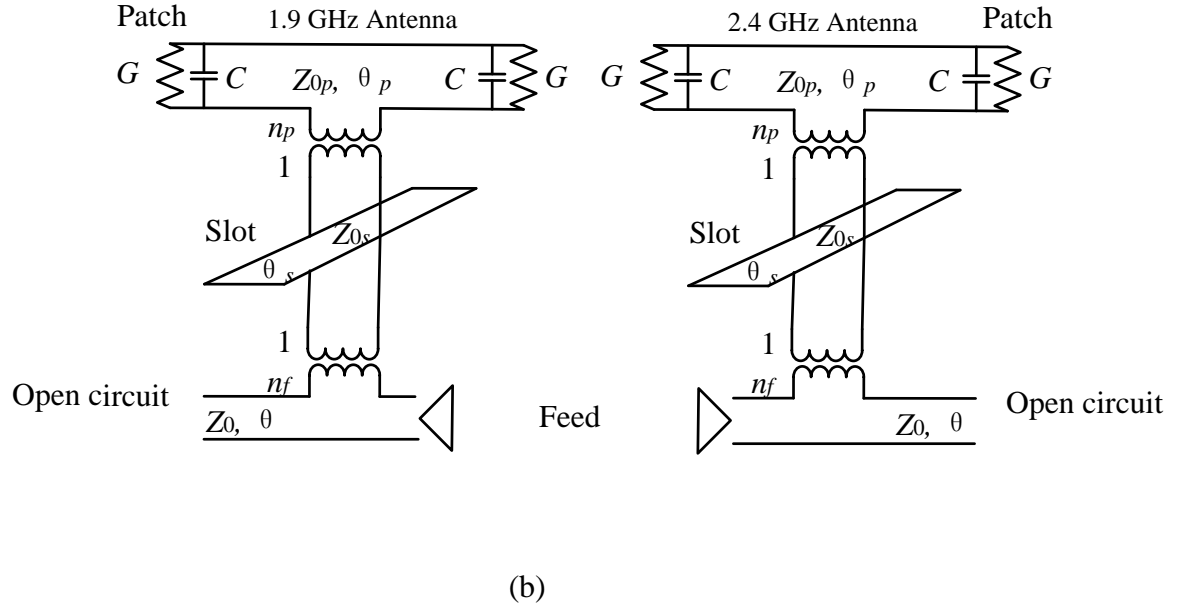


Fig. 3.37 (a) Physical structure of the antenna, and (b) equivalent circuits of the antenna at the two frequencies.

In this figure L_{p1} and L_{p2} are the physical dimensions of the patch while L_{s1} and L_{s2} are the lengths of the two slots. The height of the air substrate above the ground plane was designed as to be 8 mm (it is easy to achieve practically) and the substrate below the ground plane was PCB FR4. The equivalent circuits of the two modes are shown in Fig. 3.37(b) where G models the radiated power from the patch's radiating slots and C models the fringing fields at the physical edges of the patch [9].

A wide matching bandwidth and a high gain can be obtained by the antenna if a thick air substrate is used below the patch [45]. However, a thick substrate will change the surface wave efficiency and equation (3.1) will not fit for this case. In Fig. 3.38, results obtained from (3.1) are compared with the simulation data for ΔL of the fringing field as function of the height of the air substrate for patch widths of 43 mm and 57 mm that will be used in the

dual frequency aperture coupled antenna design. The obtained ΔL of the air substrate of both patch widths is greater than predicted from (3.1).

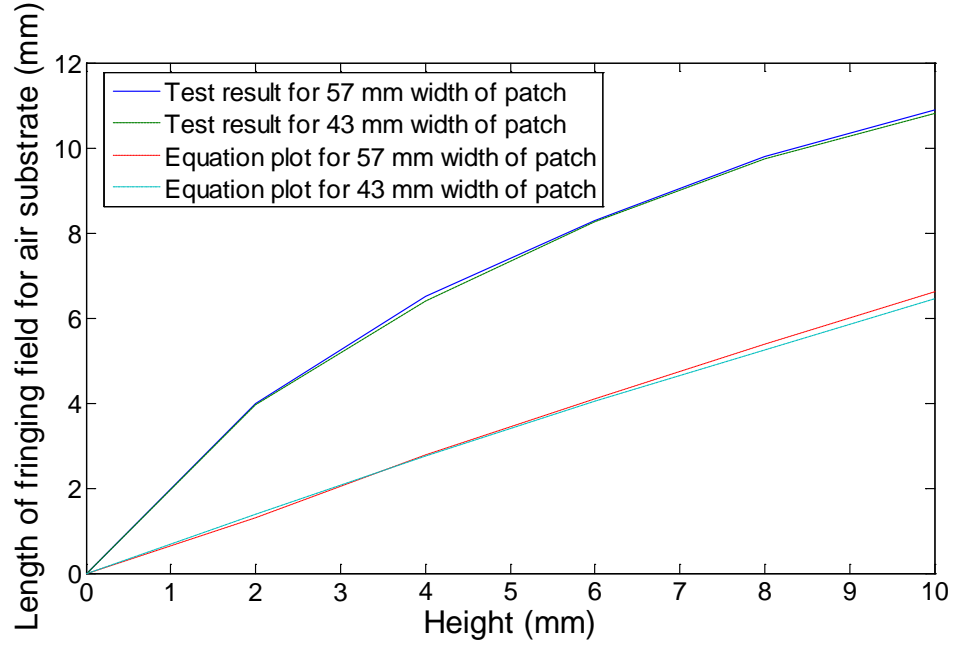


Fig. 3.38 Length of the fringing field ΔL as a function of the height of air substrate obtained from simulation and equation (3.1).

Equation (3.34) was derived for the length of the fringing field as a function of the height H (mm) of the air substrate using a curve fitting approach.

$$\Delta L = 12(1 - e^{\frac{-H}{5}}). \quad (3.34)$$

The resonant frequency of the series input impedance of the patch at the position of SL is normally above the design frequency. Hence the effective length of the patch should be slightly less than half-wavelength ($\sim 0.9\lambda_p/2$) where λ_p is the patch wavelength at the design frequency. The approximate effective dimensions of the patch are 76 mm at 1.9 GHz and 61 mm at 2.4 GHz. The corresponding physical dimensions of the patch are 57 mm at 1.9

GHz and 43 mm at 2.4 GHz. The resonant frequency of the SL is normally higher than the design frequency so that $L_s \sim 0.7\lambda_s/2$. Consequently the assumed initial physical lengths of SLs obtained are 33 mm at 2.4 GHz and 42 mm at 1.9 GHz. These lengths were then used in (3.25) and the initial approximate value of n_f was 0.96 at 1.9 GHz and 0.95 at 2.4 GHz. By substituting the above SL lengths and the physical widths of the patch into (3.32) the approximate values for n_p are 0.217 and 0.33 at 2.4 GHz and 1.9 GHz, respectively. For the two frequencies the initial and final tuned values for the two equivalent circuits and physical dimensions of the two antennas are close to each other as shown in table 3.2.

Dimension of dual frequency ACMA		
1.9 GHz		
Parameter	Initial value	Final tuned value
$L_p 1$	38 mm	43 mm
$L_p 2$	53 mm	57 mm
W_s	1 mm	1 mm
$L_s 1$	42 mm	41 mm
$\Delta L_p 1$	9.5 mm	9.3 mm
Turn ratio n_f	0.965	0.972
Turn ratio n_p	0.327	0.326
R	646 Ω	646 Ω
2.4GHz		
Parameter	Initial value	Final tuned value
$L_p 1$	38 mm	43 mm
$L_p 2$	53 mm	57 mm
W_s	1 mm	1 mm
$L_s 1$	33 mm	35 mm
$\Delta L_p 1$	9.5 mm	9.3 mm
Turn ratio n_f	0.952	0.94
Turn ratio n_p	0.217	0.228
R	368 Ω	368 Ω

Table 3.2 Dimension of a broadband dual frequency ACMA.

The obtained frequency responses of the return loss of the equivalent circuit and the physical antenna at ports 1 and 2 are shown in Fig. 3.39.

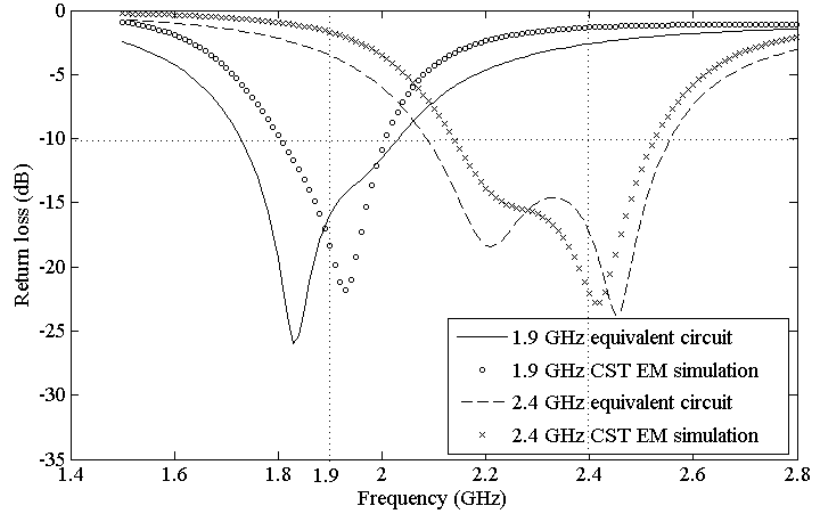


Fig. 3.39 Frequency response of the return loss of the two matched antenna.

The -10 dB matching bandwidth at 1.9 GHz is 260 MHz and at 2.4 GHz it is 430 MHz. Also there is a good agreement for the return loss obtained from the circuit simulation carried out by AWR and the full wave simulation by CST.

Finally the two feed ports shown in Fig. 3.37(b) are joined together by two arms ($50\ \Omega$ MLs) of lengths L_{f1} and L_{f2} , see Fig. 3.40. The input impedance of Z_1 at 1.9 GHz and 2.4 GHz are $50\ \Omega$ and $101.6 + j221\ \Omega$, respectively. Matching the impedance that for L_{f1} of 71.4 mm the input impedance Z_f at the feed port increases to $689\ \Omega$ at 2.4 GHz but of course the antenna is still matched at 1.9 GHz. Similarly at 2.4 GHz, Z_2 is $50\ \Omega$ and, Z_2 is $7.63 - j41.14\ \Omega$ at 1.9 GHz. For L_{f2} of 35.4 mm the input impedance Z_f at the feed port increases to $984\ \Omega$ at 1.9 GHz but at 2.4 GHz the antenna is still matched.

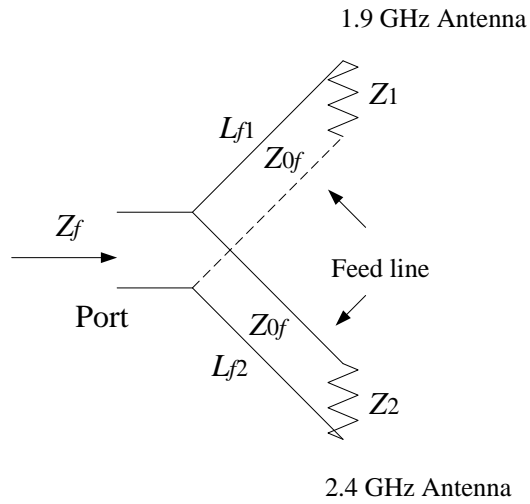


Fig. 3.40 Circuit diagram of 1.9 GHz and 2.4 GHz antennas connected by feed arms.

The fabricated board of the designed antenna is shown in Fig. 3.41 and simulated and practical frequency responses of the return loss and measured gain are shown in Fig. 3.42.

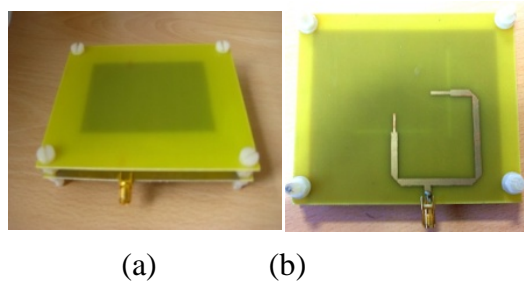
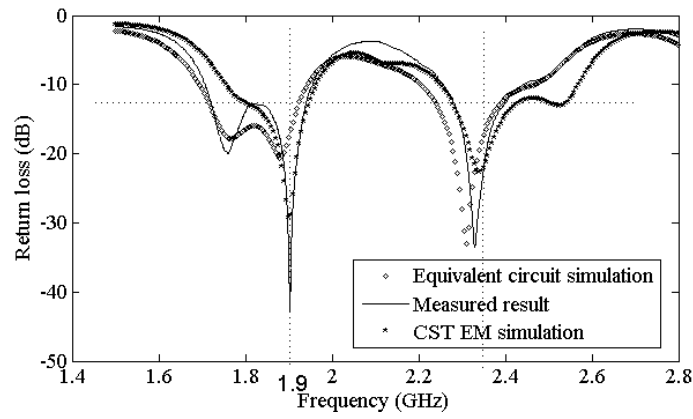
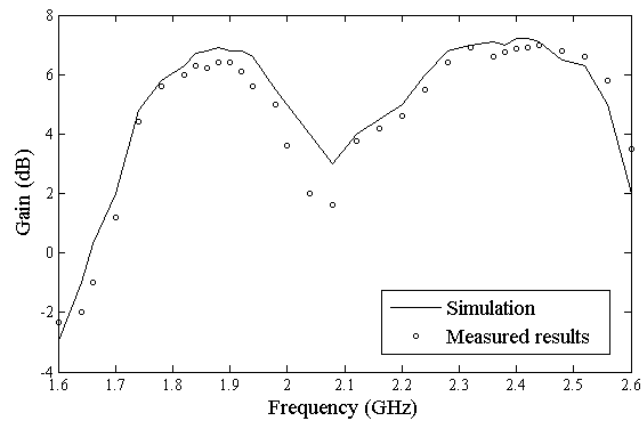


Fig. 3.41 Photograph of the fabricated antenna (a) radiation element, and (b) feed line.



(a)



(b)

Fig. 3.42 Simulated and practical frequency responses: (a) reflection coefficient, and (b) gain of the antenna.

A very good agreement has been obtained between the simulated and measured frequency responses for the reflection coefficient and for the gain of the antenna. Simulation results showed that gain of 6.3dB and 7dB at 1.9 GHz and at 2.4 GHz, respectively with corresponding practical measurements of 6.6 dB at 1.9 GHz and 7.2 dB at 2.4GHz.

3.10 Summary

This chapter analysed the equivalent circuit of an ACMA, which consisted of radiating patch, slot line and microstrip feed line. The patch was reviewed using TL model. Numerical methods were given to calculate the physical width and length of the patch. The coupling ratio between feed and slot was defined as n_f ; and the coupling ratio between the slot and patch was defined as n_p . In this chapter a novel method using the S parameter to investigate n_f was proposed and validated by practical measurement, thus showing that n_f mainly varied with the slot length and height of substrate. n_p also was investigated by fix feed/slot dimension, tuning width of path until the frequency response of impedance agreed with full wave simulation results. A simplified design procedure was proposed for an ACMA by reducing the number of design parameter and obtaining a matched antenna logically. Finally, a dual polarized dual frequency wide bandwidth ACMA was designed by using the design procedure. Practical results showed a good agreement with the circuit simulation results.

Chapter 4 Review and Theoretical Analysis of Power Amplifier using Linear Model

4.1 Introduction

A PA is one of the most commonly used electrical elements for converting the input DC power into the microwave output signal. It can be utilized in wireless communication systems, radar and medical applications, as well as in RF heating systems where high efficient PAs are used [129-131]. The main objective in the design of these amplifiers is to produce high efficiency conversion from DC to AC that is used in the transmitter. If the high efficiency is to be achieved then considerable reduction in dissipated power becomes increasingly an important issue [132-135]. This chapter introduces design parameters of typical PAs. Gain and efficiency are the key parameters to measure the ability of signal amplification and DC to AC power conversion respectively. PAs are defined as classical type (class A to class C PAs) and high efficiency type (class D to inverse class F PAs) which depend on the quiescent bias point Q to the conduction angel θ . The class F and inverse class F PAs are picked out for the further investigation due to their high gain and high efficiency performance. The active device is modelled by an ideal switch connected with a resistor which models the power loss. Harmonic load matching networks are designed with infinity harmonics and up to third harmonic frequency to shape the voltage and current waveforms over the active device. Effects of internal resistance of transistor and harmonics of frequencies on the power convert efficiency are presented.

4.2 Reviews of PAs

Historically RF power was generated by spark, arc, and alternator techniques for wireless communications between 1890 and 1920s. In 1907, the RF signal was generated and controlled by the thermoionic vacuum tubes, and the vacuum tube based PAs were widely used from 1920s to 1970s [136]. In 1948, Bardeen, Brattain, and Shockley [137, 138] invented the first bipolar transistor, which lead to a telecommunication revolution, but with poor gain and noise figures. In 1965, a Germanium (Ge) based transistor was fabricated that was limited by the low band gap thus leading to a high leakage current and poor thermal performance. In 1990s a number of novel solid state devices [139, 140] based on the high electron mobility transistor (HEMT), pseudomorphicHEMT (pHEMT), heterojunction field effect transistor (HFET), and heterojunction bipolar transistor (HBT) using new materials such as indium phosphide (InP), aluminium gallium arsenide (AlGaAs), indium gallium arsenide (InGaAs), silicon carbide (SiC), and gallium nitride (GaN) offered additional improvement in performance. The efficiency and linearity of the combination of digital signal processing [141, 142] and microprocessor control could be further enhanced by using feedback and pre-distortion technologies. In today's world, the applications of PAs are diverse. E.g. communications, navigation and broadcasting applications across a wide frequency range from very low frequency (VLF) to extremely high frequency with power levels from 10 mW to 1 MW [1, 143, 144]. Also in radar, RF heating, plasma generation, laser drivers, magnetic resonance, and miniature DC/DC converters, PAs and transmitters are widely used.

4.3 Design Parameters of PAs

The block diagram of a PA is shown in Fig. 4.1 where P_{DC} is the DC power supply, P_{AC} is the AC input power, P_{diss} is the total power dissipation and P_{out} is the output power. The circuit model of a PA is given by Fig. 4.2. V_{DD} and I_{dc} are the DC voltage and current from the DC power supply, respectively. V_{ds} and I_{ds} are the voltage and current that flow through the active device, respectively, and R_L is the load resistance of the active device.

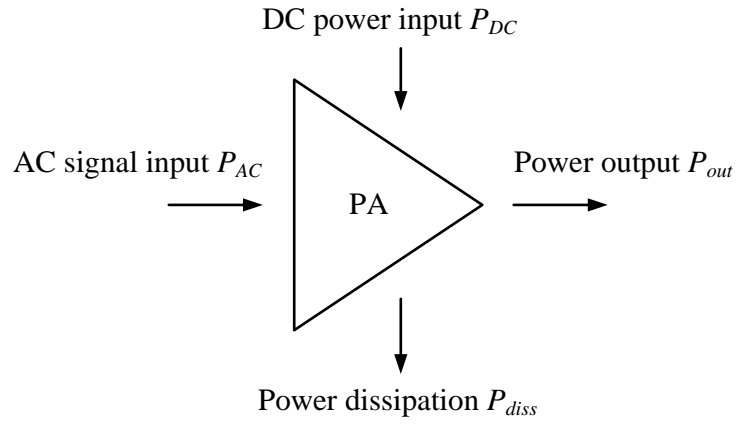


Fig. 4.1 Block diagram of PA.

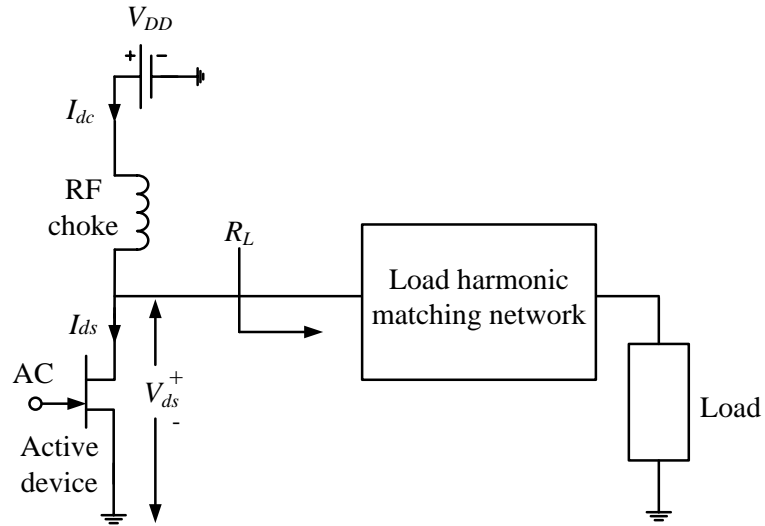


Fig. 4.2 Circuit model of PA.

The total input power must equal to the output power as defined by (4.1):

$$P_{DC} + P_{AC} = P_{out} + P_{diss} . \quad (4.1)$$

Efficiency is a critical factor in PA design, which is normally described as the drain efficiency and PAE. Also the instantaneous efficiency (i.e. the efficiency at one specific output level) is the highest at the peak output power (PEP) for most PAs.

The drain efficiency is defined as the ratio of output power to the DC power input which is defined by:

$$\eta = \frac{P_{out}}{P_{DC}} . \quad (4.2)$$

For time varying amplitude measurement, the average efficiency is defined by:

$$\eta_A = \frac{P_{outA}}{P_{DCA}} , \quad (4.3)$$

where P_{outA} and P_{DCA} is the average output power and average DC power, respectively.

PAE indicates the AC power by subtracting it from the output power, which gives a reasonable indication of PA performance, as defined by:

$$PAE = \frac{P_{out} - P_{AC}}{P_{DC}} . \quad (4.4)$$

The power gain G_p could be defined by:

$$G_p = \frac{P_{out}}{P_{AC}} . \quad (4.5)$$

4.4 Types of PAs

PAs are normally classified as class A to F [145] which operate in different efficiency and output power capabilities. The power capability is the output power per transistor normalized to the peak drain voltage and current of 1 V and 1 A, respectively [131]. The single end topology is used to analyse a typical PA shown in Fig. 4.2, which includes the active device, DC power supply, and an output harmonic matching network.

4.4.1 Classical PAs

The type of the amplification determines the kind of bias applied to a RF power transistor. The classical PAs (classes A, AB, B, and C) operate in the linear region and the output current is in the saturation area, which is controlled by the input voltage V_{gs} . For these classes of PAs it is convenient to relate to Q and θ [146, 147].

A class A PA is defined by the output current flowing for a full-cycle (360 degrees) of the input signal. The drive level is kept small enough to avoid driving the transistor into the cut-off mode (i.e. the transistor remains forward biased throughout the input cycle). In class A PA, the transistor is active at all times acting as a current source controlled by the gate voltage. The drain voltage and current are both sinusoids, see Fig. 4.3 [148] where V_p is the pinch off voltage and i_{max} is the peak current of active device. This PA is typically used for its low power requirement, high linearity, high gain, low distortion and broadband operation [14, 149,150].

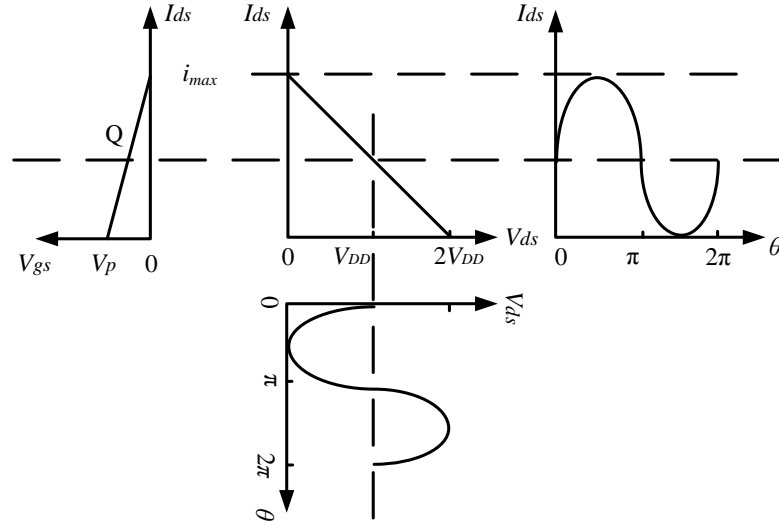


Fig. 4.3 Load line, voltage and current waveform of class A PA.

However, class A PA is not very efficient in that the instantaneous efficiency is proportional to the output power offering theoretically a maximum of 50%. In addition such amplifiers are large, heavy, and operating at high temperature and full power [151].

For class B PA, the Q point is set such that only half of the input wave cycle is amplified. Thus leading to generation of a large amount of distortion, but with greatly improved efficiency (up to 78.5%) compared to class A PAs [132]. The θ of class B PA is approximately 180° [152]. The load line, voltage and current waveforms are shown in Fig. 4.4 [152, 153].

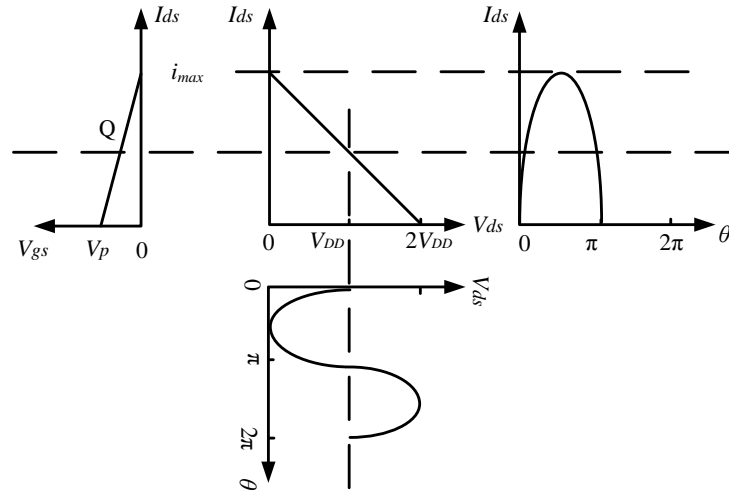


Fig. 4.4 Load line, voltage and current waveform of class B PA.

Class AB PA is a compromise between class A and class B in terms of the efficiency and linearity. As shown in Fig. 4.5 [154, 155], the Q point is set between the cut off region and class A point. So the transistor will be on more than a half cycle but less than a full circle. θ is between 180° and 360° and the efficiency is between 50 % and 78.5 % [2, 156].

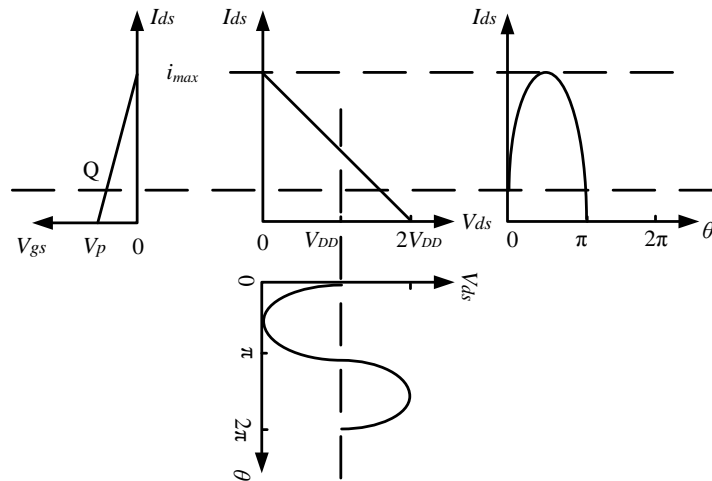


Fig. 4.5 Load line, voltage and current waveform of class AB PA.

Class C PA is biased below V_p and θ is less than 180° , see Fig. 4.6 [154, 155]. This PA is biased under the steady state conditions and there is no flow of the collector current. It has the poorest linearity of these PAs with the efficiency reaching more than 80 % but large amount of signal distortion. [147, 157].

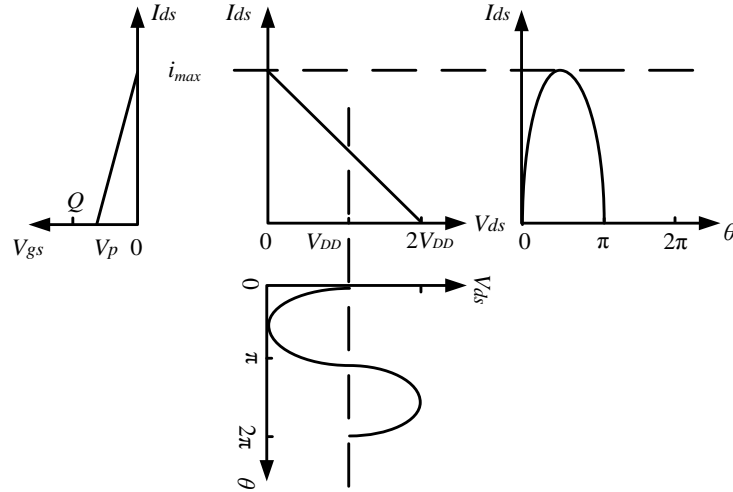


Fig. 4.6 Load line, voltage and current waveform of class C PA.

4.4.2 High Efficiency PAs

Due to the overlapping of the voltage and current waveforms of classical PAs, the power dissipation is considerable, which can lead to degradation of the efficiency. In order to minimise the power dissipation from the active device, higher efficiency PAs [152, 158-161] are introduced and the most popular and typical types are class D, E, F and inverse F. For the class D PA, where the circuit shown in Fig. 4.7 [154, 155], two active devices behave as switches, which are alternatively switched on and off by the drive signal to generate the square drain voltage waveform, see Fig. 4.8 [152, 162, 163]. The load resonant circuit is used to ensure that PA is only working at the fundamental frequency. However, it is difficult to realize this particularly at higher frequencies. The available

active devices for the upper switch are limited and losses are due to the saturation, switching speed and drain capacitance.

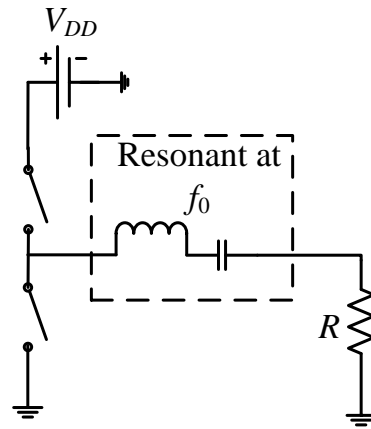


Fig. 4.7 Class D PA.

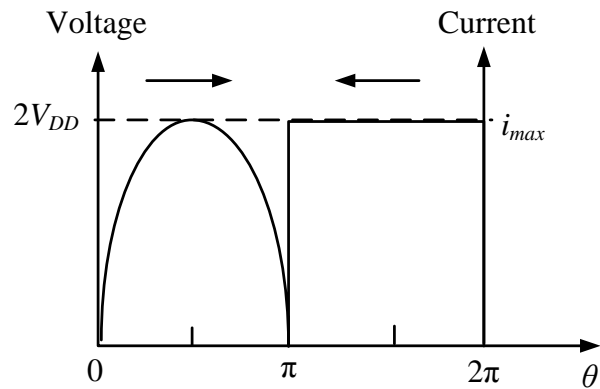


Fig. 4.8 Voltage and current waveform of class D PA.

The class E PA is a switching type device, which has a single active device acting as an ideal switch [158, 164-166]. It can achieve 100% efficiency theoretically but the internal resistance of the transistor and the non-ideal filter at the output stage will degrade the efficiency. As shown in Fig. 4.9, the load tuned circuit is used to ensure that only the fundamental current can flow through the load. The voltage and current waveforms

through the active device are shown in Fig. 4.10. It is the result of summation of DC and RF currents charging the capacitance C_p which is in parallel with the transistor.

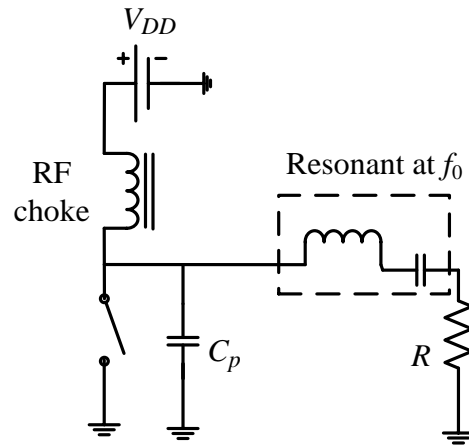


Fig. 4.9 Class E power amplifier.

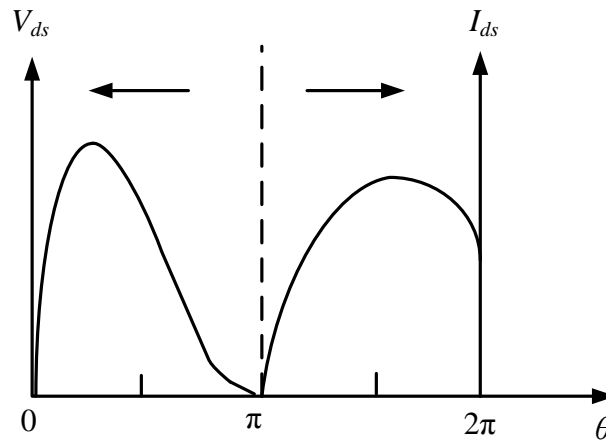


Fig. 4.10 Voltage and current waveform of class E PA.

The class F and inverse class F PAs are both highly efficient with the drain waveforms mainly shaped by controlling the output harmonic resonators. The theoretical analysis and modelling of the class F and inverse class F PAs are presented in the next section.

4.5 Theoretical Analysis and Comparison of Class F and Inverse Class F PAs

The active device of class F PA and inverse class F PA could be modelled as an ideal switch connected with an internal resistance R_{on} which indicate the power dissipation in the transistor, see Fig. 4.11. The voltage and current flow over the drain are controlled by harmonic load resonators in the output network. To obtain maximum DC to AC power convert efficiency, the voltage waveform is square while the current waveform is half sinusoid for a class F PA. Alternately, half sine voltage wave and square current wave are applied for inverse class F PA, see Fig. 4.12.

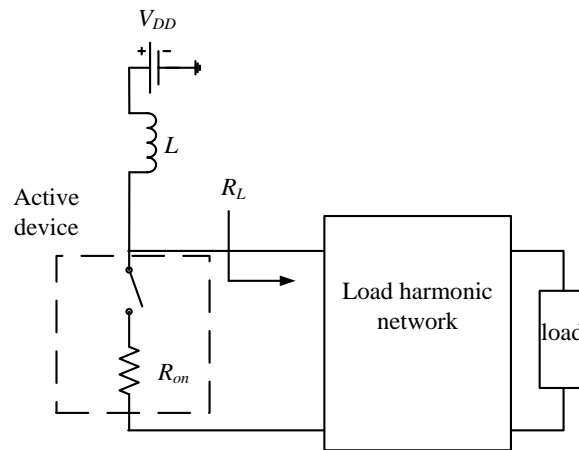


Fig. 4.11 Circuit model for class F and inverse class F PA.

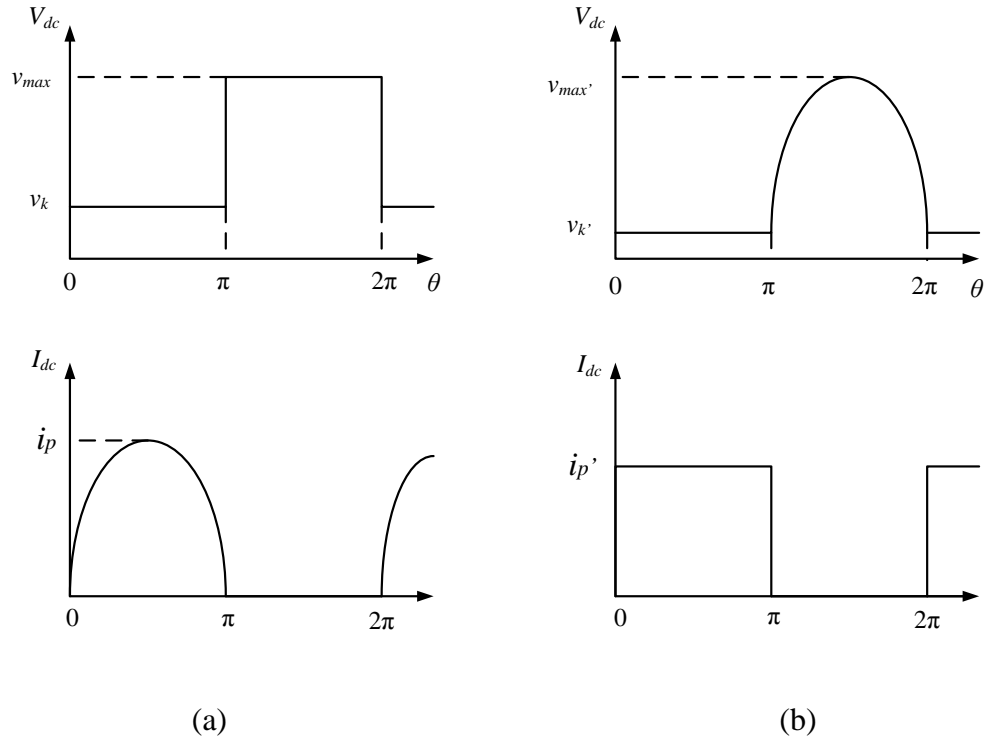


Fig. 4.12 Voltage and current waveform: (a) class F PA, and (b) inverse class F PA.

v_{max} (v_{max}') and i_p (i_p') are the peak voltage and current flowing through the active device, respectively of class F PA (inverse class F PA). v_k (v_k') is the knee voltage, which is due to the effects of R_{on} of class F PA (inverse class F PA).

The required impedance of the load harmonic network for the class F and inverse class F PAs to obtain ideally 100% efficiency is defined by:

$$Z_{Fun} = R_L , \quad (4.6a)$$

$$Z_{2n} = 0 , \quad (4.6b)$$

$$Z_{2n+1} = \infty , \quad (4.6c)$$

where Z_{Fun} is the load impedance of the active device at the fundamental frequency, Z_{2n} is the impedance at even harmonics, Z_{2n+1} is the impedance at odd harmonics, and $n = 1, 2, 3 \dots$.

Similarly, for the inverse class F PA:

$$Z_{Fun} = R_L, \quad (4.7a)$$

$$Z_{2n} = \infty, \quad (4.7b)$$

$$Z_{2n+1} = 0. \quad (n = 1, 2, 3 \dots) \quad (4.7c)$$

The ideal current and voltage waveforms are expanded by the Fourier series [9] for the class F PA and are given by:

$$V_{ds}(\theta) = V_{DD} - \frac{4(V_{DD} - v_k)}{\pi} \sum_{n=1,3,5\dots} \sin(n\theta), \quad (4.8a)$$

$$I_{ds}(\theta) = i_p \left[\frac{1}{\pi} + \frac{1}{2} \sin(\theta) - \frac{2}{\pi} \sum_{n=2,4,6\dots} \frac{\cos(n\theta)}{n^2 - 1} \right]. \quad (4.8b)$$

From (4.6) and (4.7), I_{dc} , P_{DC} , fundamental voltage V_{Fun} , fundamental current I_{Fun} , fundamental power output P_{Fun} , R_L , and η could be derived by:

$$I_{dc} = \frac{i_p}{\pi}, \quad (4.9a)$$

$$V_{Fun} = \frac{4(V_{DD} v_k)}{\pi}, \quad (4.9b)$$

$$I_{Fun} = \frac{i_p}{2}, \quad (4.9c)$$

$$P_{DC} = \frac{V_{DD} i_p}{\pi}, \quad (4.9d)$$

$$P_{Fun} = \frac{(V_{DD} - v_k) i_p}{\pi}, \quad (4.9e)$$

$$R_L = \frac{V_{Fun}}{I_{Fun}} = \frac{8(V_{DD} - v_k)}{\pi i_p}, \quad (4.9f)$$

$$\eta = \frac{V_{DD} - v_k}{V_{DD}}. \quad (4.9g)$$

The voltage and current waveforms are expanded by the Fourier series for the inverse class F PA and defined by:

$$V_{ds}'(\theta) = v_k' + (v_{max}' - v_k') \left(\frac{1}{\pi} - \frac{1}{2} \sin(\theta) + \frac{2}{\pi} \sum_{n=2,4,6...} \frac{\cos(n\theta)}{n^2 - 1} \right), \quad (4.10a)$$

$$I_{ds}'(\theta) = \frac{i_p'}{2} \left(1 + \frac{4}{\pi} \sum_{n=1,3,5...} \frac{\sin(n\theta)}{n} \right). \quad (4.10b)$$

The corresponding equations for the inverse class F PA are defined by:

$$I_{dc}' = \frac{i_p'}{2}, \quad (4.11a)$$

$$V_{Fun}' = \frac{\pi(V_{DD} - v_k) \sin(\theta)}{2}, \quad (4.11b)$$

$$I_{Fun}' = \frac{2i_p' \sin(\theta)}{\pi}, \quad (4.11c)$$

$$P_{DC}' = \frac{V_{DD} i_p'}{2}, \quad (4.11d)$$

$$P_{Fun}' = \frac{\pi(V_{DD} - v_k') i_p'}{2}, \quad (4.11e)$$

$$R_L' = \frac{V_{Fun}}{I_{Fun}} = \frac{\pi^2(V_{DD} - v_k')}{4i_p'}, \quad (4.11f)$$

$$\eta' = \frac{V_{DD} - v_k'}{V_{DD}}. \quad (4.11g)$$

The performance of the two amplifiers can be compared by deriving equations for the inverse class F amplifier in terms of the design parameters of the class F amplifier. This is obtained by ensuring that the DC input power for both amplifiers is the same so that i_p' can be expressed in terms of i_p :

$$i_p' = \frac{2i_p}{\pi}. \quad (4.12a)$$

v_k' is obtained in terms of i_p and R_{on} .

$$v_k' = i_p' R_{on} = \frac{2i_p}{\pi} R_{on}. \quad (4.12b)$$

Similarly R_L' is defined by:

$$R_L' = \frac{\pi^3(V_{DD} - \frac{2i_p}{\pi} R_{on})}{8i_p}. \quad (4.12c)$$

From the derived equations, the output characteristics of an active device are shown in Fig. 4.13.

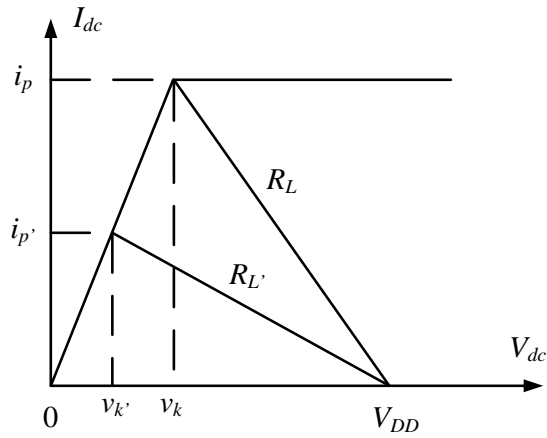


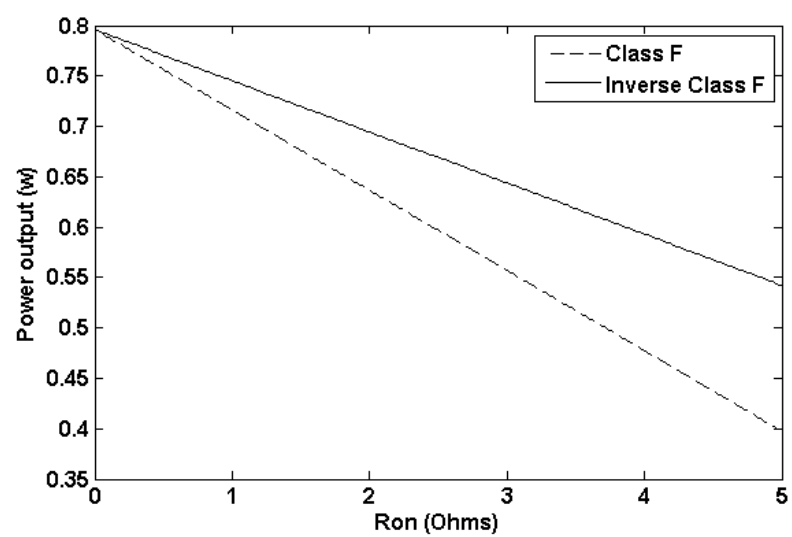
Fig. 4.13 Output characteristic of the active device.

To compare the efficiencies of the two amplifiers the following modified equations for the inverse class F amplifier can be obtained by using the following equations:

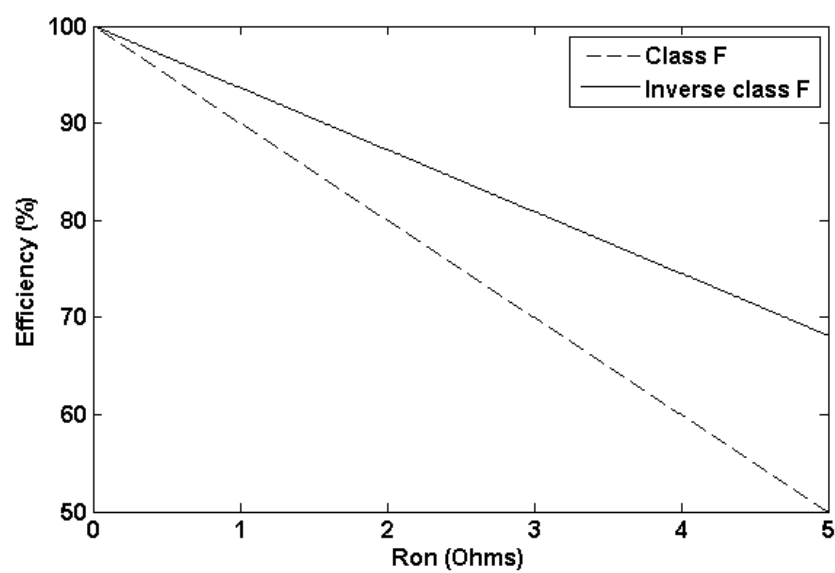
$$P_{Fun}' = \frac{(V_{DD} - \frac{2i_p}{\pi}R_{on})i_p}{\pi}, \quad (4.12d)$$

$$\eta' = \frac{V_{DD} - \frac{2i_p}{\pi}R_{on}}{V_{DD}}. \quad (4.12e)$$

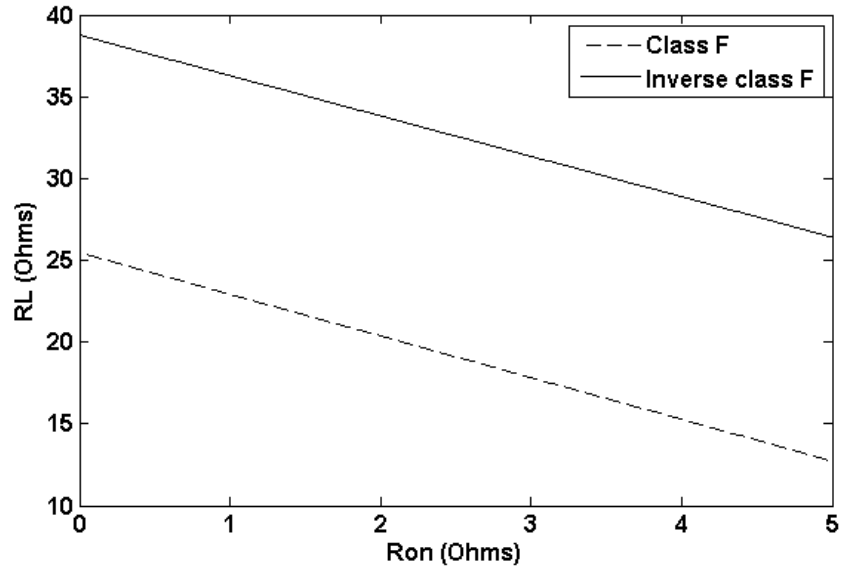
Assuming the condition that for $V_{DD} = 5$ V and $i_p = 0.5$ A, the input DC power is 0.796 W. The output power, efficiency and the load resistance in terms of R_{on} (0 to 5 ohms) for the two amplifiers are shown in Fig. 4.14.



(a)



(b)



(c)

Fig. 4.14 Effects of R_{on} on: (a) power output, (b) DC to AC power conversion efficiency, and (c) load resistance.

Fig. 4.14 indicates that the efficiency reduces as a function of R_{on} but this reduction is greater for the class F amplifier than it is for the inverse class F. For $R_{on} = 2 \Omega$ the power conversion efficiencies are 87.3% and 80% for the inverse class F and the class F amplifiers, respectively. The calculated load resistances will be used to design the load harmonic networks for the two amplifiers as discussed in the next section.

4.6 Linear Switch Model Analysis of Class F and Inverse Class F PAs

As discussed in the last section, efficiency degrades with increasing R_{on} . The efficiency is also affected by the load impedance of active device not only at the fundamental frequency but also at all the other harmonics [160, 167]. Tyler [168] has produced a class F PA

design using multiple resonators for amplitude modulation (AM) broadcast transmitters at low frequency (LF) to high frequency (HF) ranges. He also proposed a TLM to overcome the difficulty in using it in the very high frequency (VHF) range. Also other researchers have proposed different methods to control the second, third, and even fifth and seventh harmonics [169-174] in order to minimise the overlap of voltage and current waveforms. However, these topologies were complicated and created higher power losses with increased frequency. Hence, in the following sections, simplified and novel designs of the harmonic load matching networks are given to produce impedance conditions at infinity harmonics and up to third harmonic using lump elements model and TLM for the Ultra high frequency (UHF) applications. Also the effects on efficiency and the waveforms of voltage and current flowing through the active device are discussed.

4.6.1 Linear Switch Model Analysis with Infinite Harmonics Conditions

Theoretical investigation of the harmonics effects for the class F was well reviewed in [160, 167] outlining that the efficiency drops with decreasing numbers of harmonics. However, this theory has only been introduced roughly without rigorous investigation. In this section the transistor is modelled by using an ideal switch with an internal resistance R_{on} , and details of design investigation for an infinity harmonic load, and harmonic load up to third harmonics using the lump elements and TLs are given. Since ideal voltage and current waveforms are the requirement with the harmonic load matching network to make the even harmonic impedance equal to 0 and the odd harmonic equal to infinity for the class F PA, the structure of linear switch model with infinity harmonic load matching network is show in Fig. 4.15.

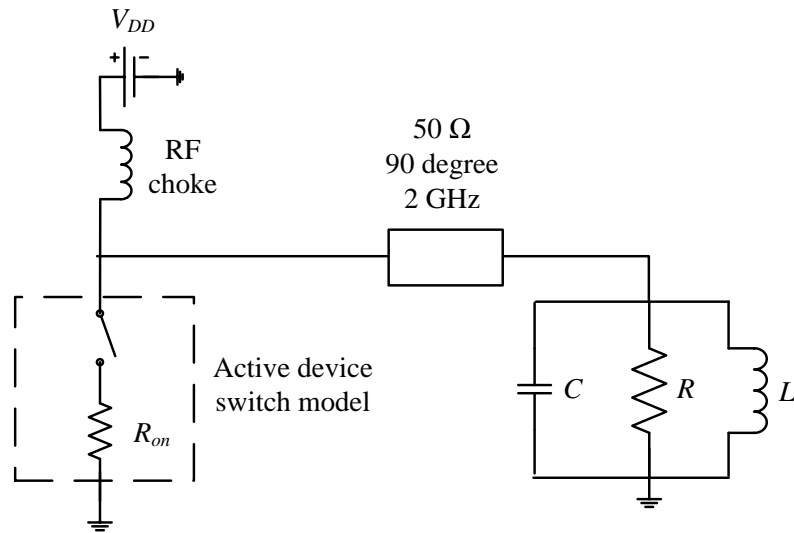


Fig. 4.15 Ideal linear switch model of class F PA.

An infinite harmonics load matching network consists of a TL ($50\ \Omega$, 90° , and $2\ \text{GHz}$) which series connect with an RLC parallel tuning circuit. The RLC circuit resonant at $2\ \text{GHz}$, and the TL makes even and odd harmonics to be 0 and ∞ , respectively. The drain voltage and current waveforms are produced by ADS software which is shown in Fig. 4.16.

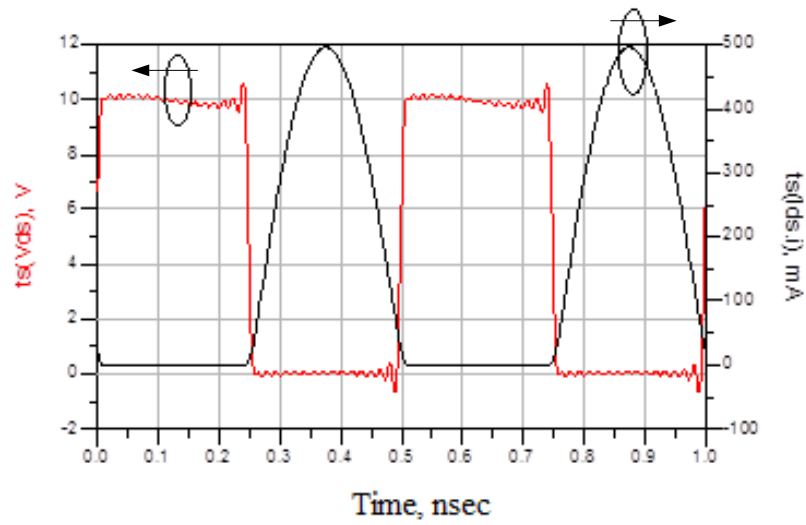


Fig. 4.16 Voltage and current drain waveforms of ideal linear switch model of class F PA.

Square voltage and half sine current wave forms are obtained as predicted in Fig. 4.12. For the inverse class F PA, the structure of the circuit and waveforms are shown in Fig. 4.17, and Fig. 4.18.

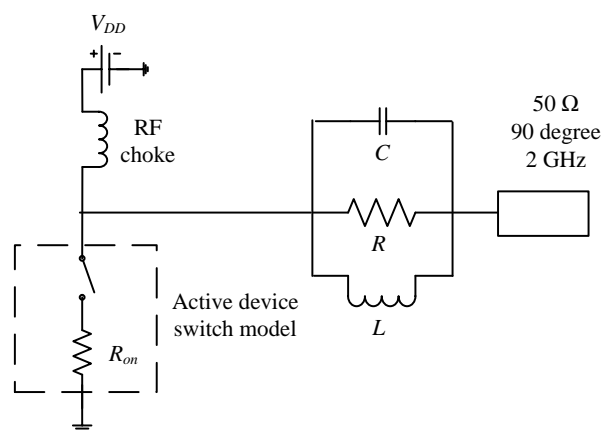


Fig. 4.17 Ideal linear switch model of inverse class F PA.

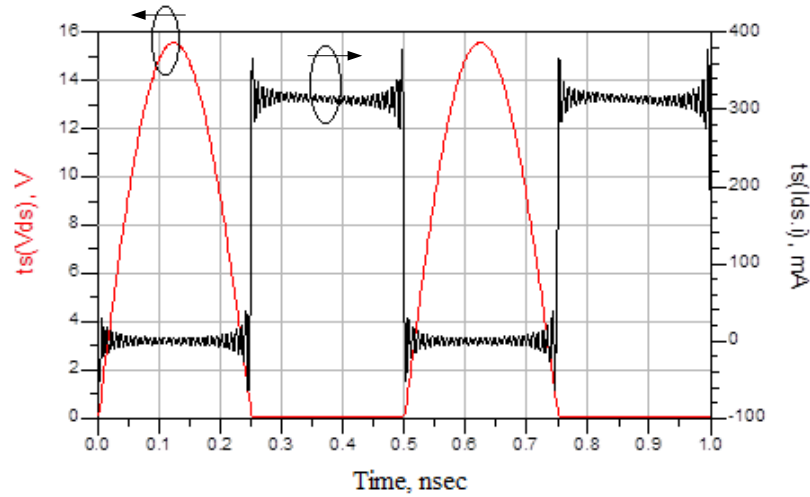


Fig. 4.18 Voltage and current drain waveforms of ideal linear switch model of inverse class F PA.

The simulation waveforms shown in Fig. 4.18 are in good agreement with predicted results outlined in Fig. 4.12.

4.6.2 Linear Switch Model Analysis with up to Third Harmonics Conditions using Lump Element

It is impossible to obtain load matching with an infinite number of harmonics. It is also not necessary to do this because of the power dissipation produced by the network elements. Up to third harmonics matching networks has been widely reported in [131, 160,175]. Designs carried out in [176, 177] have shown that intelligent based approach in tuning the separate harmonic matching load has been adopted to obtain the predicted voltage and current waveforms through the active device. A simplified novel design method is presented in this section, which does require no tuning but with logical and accurate

calculation of the harmonic load matching networks for both class F and inverse class F PAs. The schematic shown in Fig. 4.19 is a lumped element design for the class F PA.

Fig. 4.19 Lumped elements harmonic load design for class F PA.

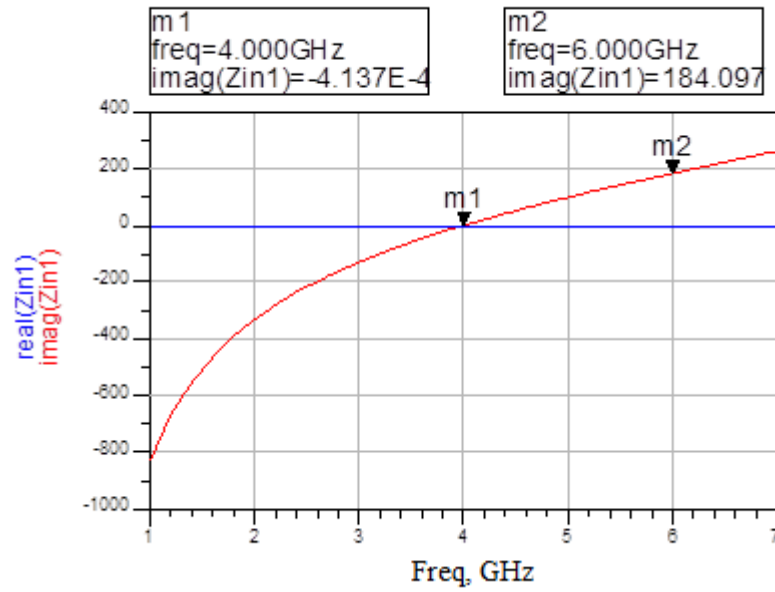


Fig. 4.20 Frequency response of impedance produced by LC circuit.

Block S_3 is used to obtain infinite impedance at the third harmonic. The series LC resonant circuit L_3 and C_3 are used to obtain a short circuit at point A for the third harmonic, which aims to eliminate the fundamental matching effects. The capacitance C_4 is used to add the negative reactance to obtain an opposite sign but the same value created by the block S_2 . Due to the shunt connection, the infinite impedance could be obtained from this parallel network by looking from the load of active device model. The fundamental matching circuit could be easily obtained by using the LC impedance matching method [14] and calculating R_L from the last section. The voltage and current waveforms are shown in Fig. 4.21, which indicates the waveform overlap due to the reduced number of harmonics.

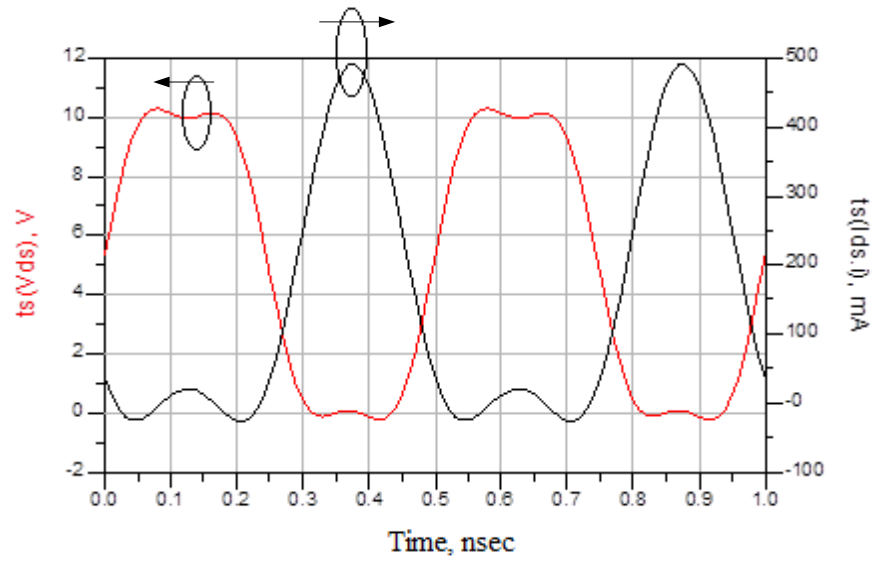


Fig. 4.21 Voltage and current drain waveforms of class F PA with up to third harmonics condition.

The design of lumped element harmonic load matching network for the inverse class F PA uses a similar principle as the class F PA. The design schematic is shown in Fig. 4.22.

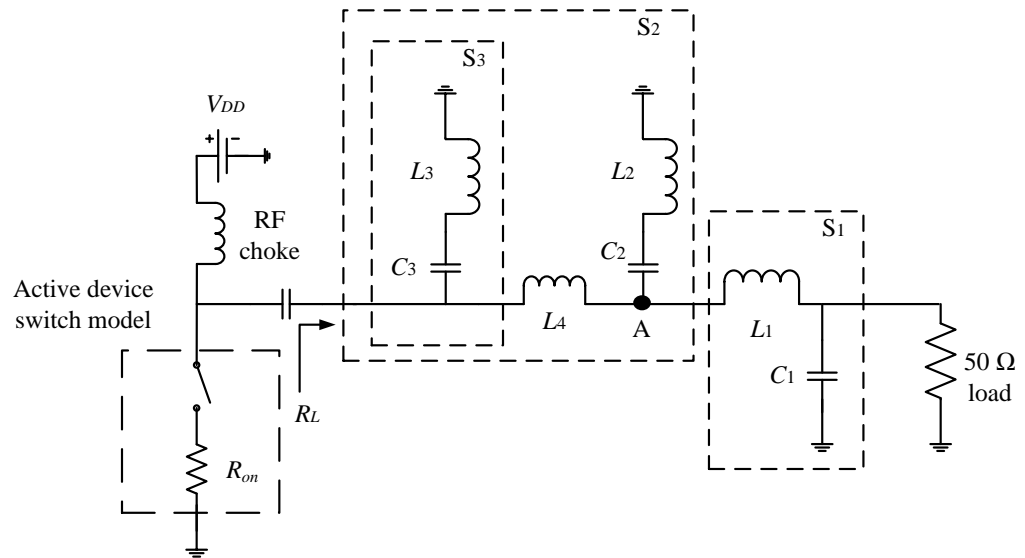


Fig. 4.22 Lump elements harmonic load design for inverse class F PA.

The inverse class F PA requires half sine voltage and square current waveforms through the active device, so block S_3 is used to produce a short circuit for the third harmonic and negative reactance at the second harmonic. C_2 and L_2 create a short circuit at point A for the second harmonic and L_4 is used to add a positive reactance in parallel connected with S_3 circuit to obtain the predicted infinite impedance. The voltage and current waveforms through drain are shown in Fig. 4.23.

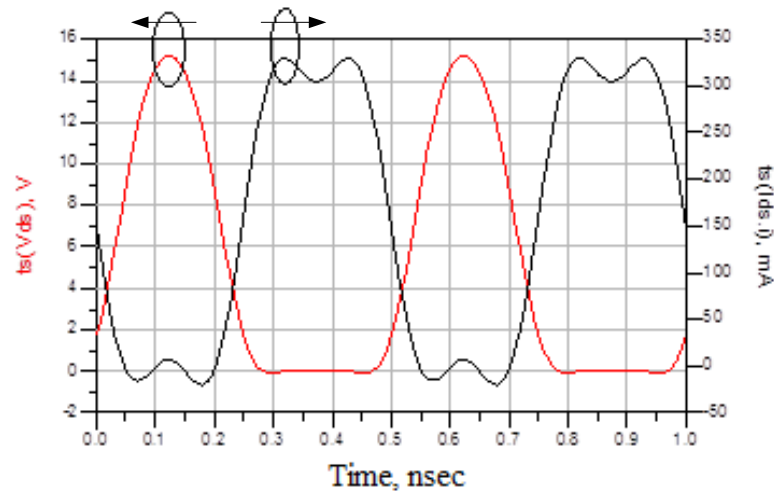


Fig. 4.23 Voltage and current drain waveforms of inverse class F PA with up to third harmonics.

Based on the model established above, simulations were carried out using ADS by varying R_{on} and using different load harmonic matching networks to obtain the effects on the efficiency. The results are given in Table 4.1.

Efficiency	Class F				Inverse class F			
$R_{on} (\Omega)$	0	1	2	4	0	1	2	4
Predicted results	100%	90%	80%	60%	100%	93.60%	87.30%	74.50%
Simulated with infinity harmonics	99.60%	90.20%	80.00%	59.40%	99.80%	93.57%	87.00%	74.00%
Simulated up to third harmonic	92.00%	84.00%	76.90%	56.90%	94.00%	88.51%	83.40%	72.50%
Efficiency reduction	7.60%	5.80%	3.10%	2.50%	5.80%	5%	3.60%	1.50%

Table 4.1 Efficiency comparison of class F and inverse class F PAs with R_{on} and harmonics effects

Table 4.1 indicates that the efficiency is reduced with increasing R_{on} as expected. The harmonics also affect the efficiency for both PAs and the effects are reduced with increasing R_{on} . For the same R_{on} and harmonics conditions, the efficiency of the inverse class F PA enhances by ~2% to 15% (depending on the value of R_{on}) compared to the class F PA.

4.6.3 Novel Methods of Harmonic Load Matching Network Design using TL

Instead of lumped elements, which cannot be used for UHF applications, TLM is normally used in PAs design. By using the same principle as in section 4.6.2, the schematic diagram of the class F PA harmonic matching network is shown in Fig. 4.24.

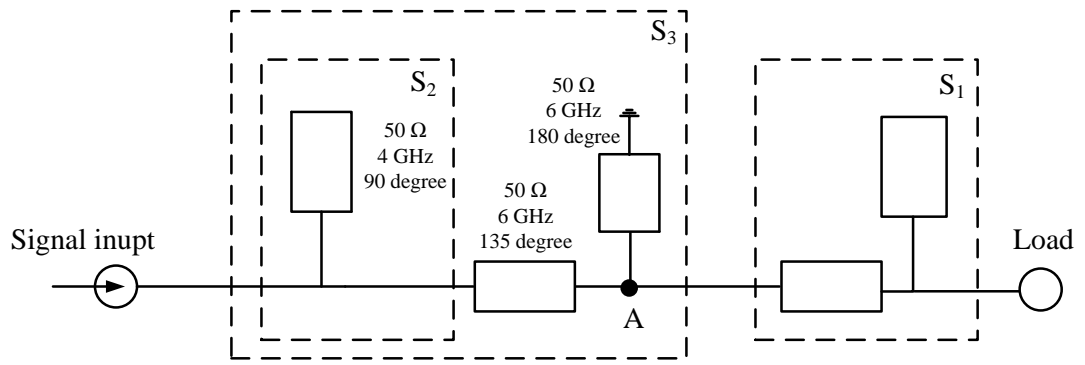


Fig. 4.24 Harmonic load matching network of class F PA using TLM.

Block S_2 indicates a short circuit produced by a 90 degree 50 Ω TL at the second harmonic, which also make a negative susceptance at the third harmonic. To obtain infinite impedance at the third harmonic, short circuit is produced at joint point A by a 90 degree 50 Ω TL working at 6 GHz in block S_3 . A 135 degree 50 Ω TL working at 6 GHz is connected with the short circuit produced by the joint point A. The infinity impedance is obtained with eliminating the susceptance produced by block S_2 using that from S_3 . Using the same topology on the inverse class F PA, the schematic is shown in Fig. 4.25.

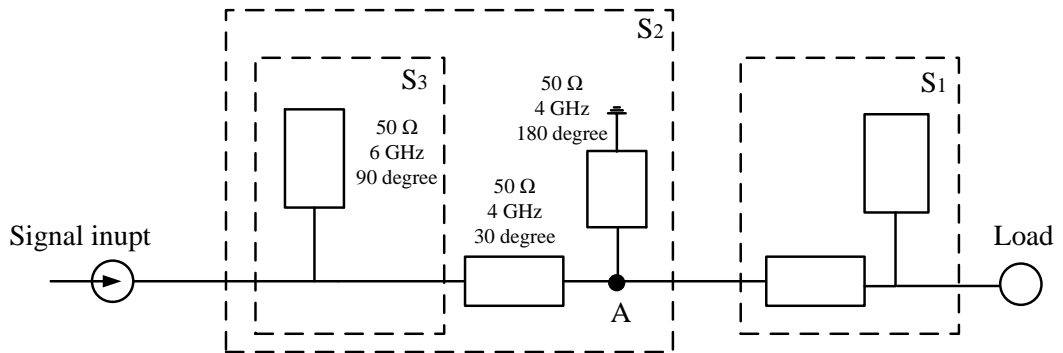


Fig. 4.25 Harmonic load matching network of inverse class F PA using TLM.

A 90 degree, 6 GHz, and 50 Ω open circuit TL in block S_3 is adapted to produce a short circuit at third harmonic. A 180 degree, 4 GHz, and 50 Ω short circuit TL is utilized to

make a short circuit at the joint point A. Another TL in S_2 is used in connection with the open circuit TL in S_3 to produce an infinite impedance effect at the second harmonic. The value obtained is 50 Ω , 30 degree operating at 4 GHz.

4.7 Summary

This chapter reviewed PAs and the output stages were classified as A to F based on the different Q points and θ . The active device of classical A, B, AB, and C PAs work in the linear region and the output current is linearly controlled by the input voltage, but practically the efficiency of these PAs is low or a low output power is produced, which is the trade off. Classes D, E, F and inverse F PAs have high efficiency as the active device behaves as a switch. The objectives of the design were to minimize the voltage and current overlap through the active device and power dissipation. A switch model of active device, which consists of an ideal switch connected with an internal resistance R_{on} was proposed. R_{on} effects on the efficiency were analysed and it was theoretically shown that the efficiency linearly reduced with increasing R_{on} . The comparison results showed that the inverse F PA had improved performance over the class F PA with the same R_{on} and harmonic load conditions. The reduction of load harmonics also degraded the efficiency. Simplified and novel methods of the harmonic load matching network with infinite and up to the third harmonic were designed using the lumped elements. Simulation results showed less than 10% efficiency reduction due to using a load matching network with fewer harmonics. Also with higher value of R_{on} , the power of harmonics effects became weaker. Finally, the TLM harmonic matching networks were designed for UHF application using the same principle as the lump elements design.

Chapter 5 Investigation and Design of Non-linear Class F and Inverse Class F Power Amplifiers

5.1 Introduction

The linear model of class F and inverse class F PAs were investigated in Chapter 4. The power loss from the internal resistance of a transistor was modelled by a resistor R_{on} and also it was shown that a limited number of load harmonics affected the efficiency [178-183]. In this chapter, the investigation of the power dissipation from the load matching TL is carried out using S parameters. The nonlinear model of active device ATF 33143 is presented using Statz model by the harmonic balance (HB) method [184-186]. In order to obtain predicted voltage and current waveforms through the active device and the determination of the maximum PAE and gain, a novel simplified simulated load/source pull method is proposed. Based on these analysis and results, novel methods for the class F and inverse class F PAs designs are presented.

5.2 Loss Investigation of Harmonic Matching Network using S Parameter

The load harmonic matching network of transmission line model consists of series and shunt connected elements. These power losses in series TLs have been extensively investigated showing that it is proportional to the line length [187]. The shunt stub loss is investigated by Helaoui[188], who presented a good solution by using a microstrip open stub based network and gave a numerical method to calculate the power loss. In this

section, a novel method to investigate and model the power dissipation of the shunt element caused by impedance using mathematically modelling and S parameter measurement is proposed. In order to simplify the design, PCB FR4 has been chosen as substrate of 50 Ω TLs where the height is 1.575 mm.

5.2.1 Loss Investigation of Impedance Effects of Shunt Stub using S_{21} Parameter

To investigate the impedance effects of the loss for the harmonic load network, a shunt microstrip stub parallel with a load R_{o2} and its equivalent circuit are proposed in Fig. 5.1.

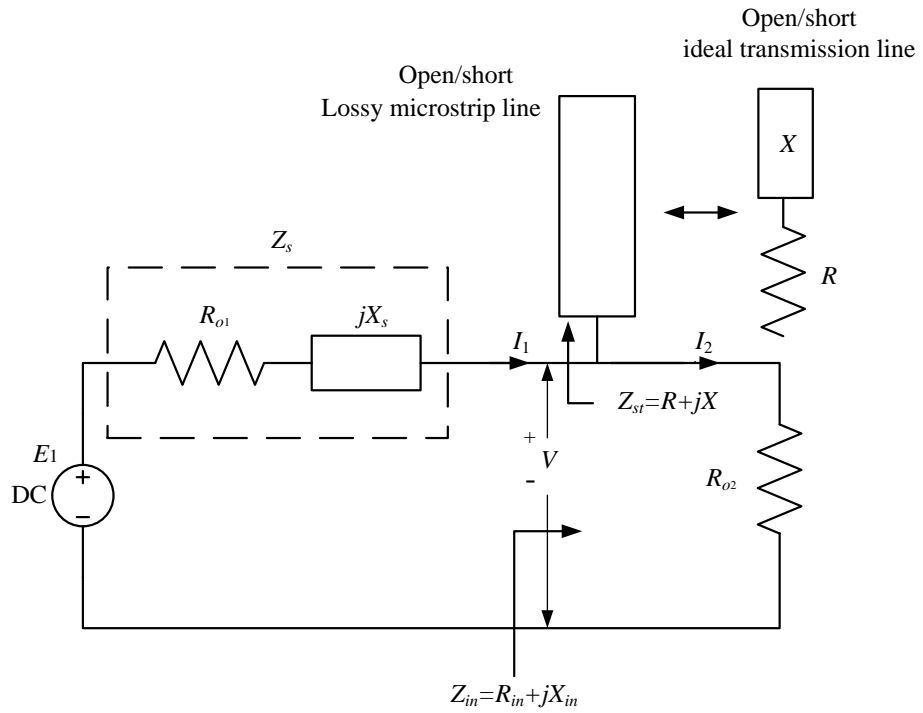


Fig. 5.1 Microstrip open/short shunt stub network and equivalent model.

The resistance R and an ideal lossless TL are used to model the shunt stub where Z_{st} is the input impedance looking into the stub. To ensure that the circuit is matched with no power being reflected back to the source R_{o1} and X_s are added to the circuit with the impedance $Z_s = Z_{in}^*$ where $Z_{in} = R_{in} + jX_{in}$. The power obtained by the load P_L and the power available from the source P_a can be defined as:

$$P_L = \frac{1}{2} \text{Re}\{V * I_2^*\} = \frac{|V|^2}{2} * \frac{1}{R_{o2}}, \quad (5.1)$$

$$P_a = \frac{1}{2} \text{Re}\left\{\frac{|V|^2}{Z_{in}}\right\} = \frac{|V|^2}{2} * \frac{R_{in}}{|Z_{in}|^2}. \quad (5.2)$$

The power dissipated by the impedance effect from the shunt microstrip stub over the total power input can be expressed by:

$$\frac{P_{diss}}{P_a} = 1 - \frac{P_L}{P_a} = 1 - \frac{|Z_{in}|^2}{R_{in} R_{o2}}. \quad (5.3)$$

Considering a two port network by replacing the source and load by two ports, the transmission parameter S_{21} could be derived from (2.27) which is given by:

$$S_{21} = \frac{2I_2 \sqrt{R_{o1} R_{o2}}}{E_1}.$$

Since $R_{in} = R_{o1}$, and $R_{o2} = 50 \Omega$, then (2.27) could be written as:

$$S_{21} = \frac{2I_2 \sqrt{50 R_{in}}}{E_1}. \quad (5.4)$$

Also, $Z_{in} I_1 = R_{o2} I_2$, $I_1 = \frac{E}{2R_{in}}$.

So,

$$Z_{in} E_1 = 2R_{o2} R_{in} I_2, \quad (5.5)$$

$$\frac{2I_2}{E} = \frac{Z_{in}}{R_{o2} R_{in}}. \quad (5.6)$$

Hence (2.27) could be deduced as:

$$S_{21} = \frac{Z_{in} \sqrt{R_{o2} R_{in}}}{R_{o2} R_{in}}. \quad (5.7)$$

From (5.7) and the circuit in Fig. 5.1, it is not too difficult to derive the equation for the power through $|S_{21}|^2$, which is given by:

$$|S_{21}|^2 = \frac{|Z_{in}|^2}{R_{in} R_{o2}}. \quad (5.8)$$

Equation (5.8) equals to $\frac{P_L}{P_a}$. Hence, by combining (5.3) and (5.8), $\frac{P_{diss}}{P_a}$ can be presented as:

$$\frac{P_{diss}}{P_a} = 1 - \frac{|Z_{in}|^2}{R_{in} R_{o2}} = 1 - |S_{21}|^2. \quad (5.9)$$

Using this method, $\frac{P_{diss}}{P_a}$ could be calculated and measured by S_{21} . The comparative results

are shown in Fig. 5.2.

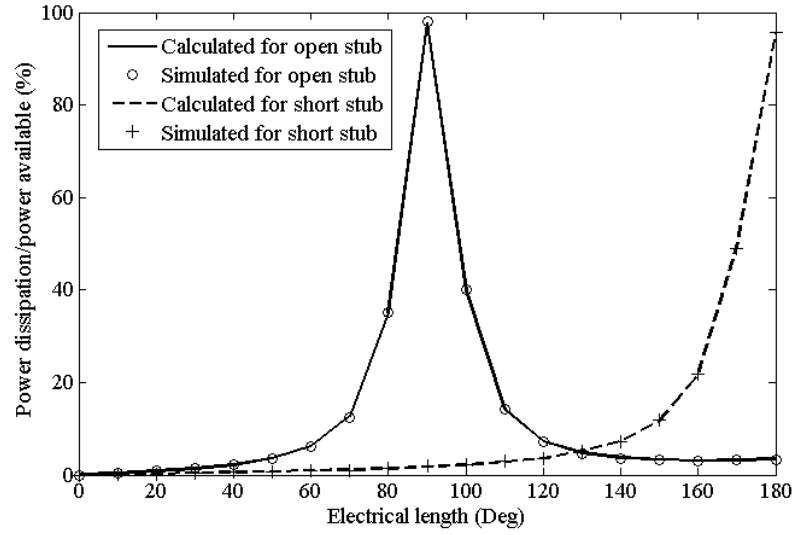


Fig. 5.2 Ratio of power dissipated over power available $\frac{P_{diss}}{P_a}$ in terms of electrical length.

The calculated and simulated results are in good agreement for both open and short circuit shunt stub conditions. Due to the short circuit effect brought by the impedance provided by the stubs, most of the power dissipation are at 90 degree and 180 degree for open and short circuits, respectively.

To investigate how R varies with the length of the stub, it is assumed that the input impedance of the shunt stub $Z_{st} = R + jX$. $X = Z_0 / \tan\theta$ and $X = Z_0 \tan\theta$ are the calculations for the open circuit and short circuit shunt stubs, respectively. R could be determined in terms of the stub length θ as plotted in Fig. 5.3.

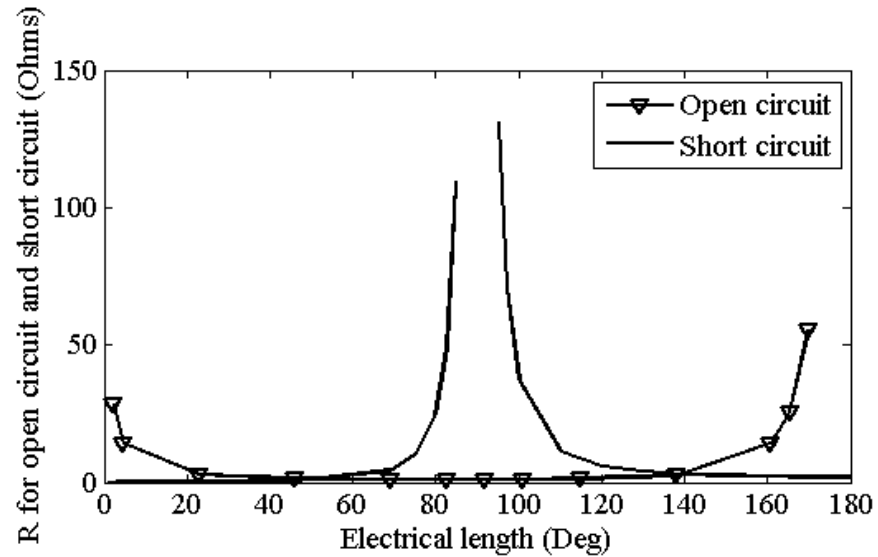


Fig. 5.3 Resistance R varies with shunt stub length.

R is almost independent of the length of the shunt stub. However it increases rapidly when the open circuit stub approaches 0 and 180 degrees and the short circuit stub approaches 90 degrees. At these lengths, the reactance X approaches a maximum value (at these points, X will be infinity and value of R could be ignored).

5.2.2 Practical Measurement for Shunt and Series Connected Lines

In order to verify the loss investigation results obtained by section 5.2.1, the circuit shown in Fig. 5.4 is used to measure the shunt stub loss and also a series line loss using the S parameter.

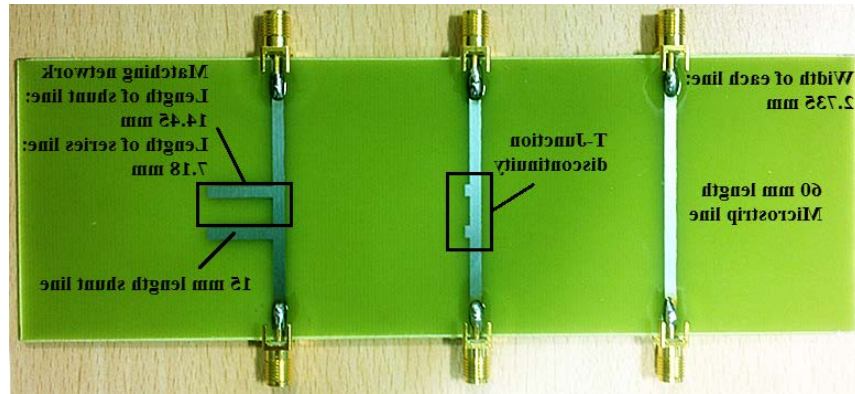
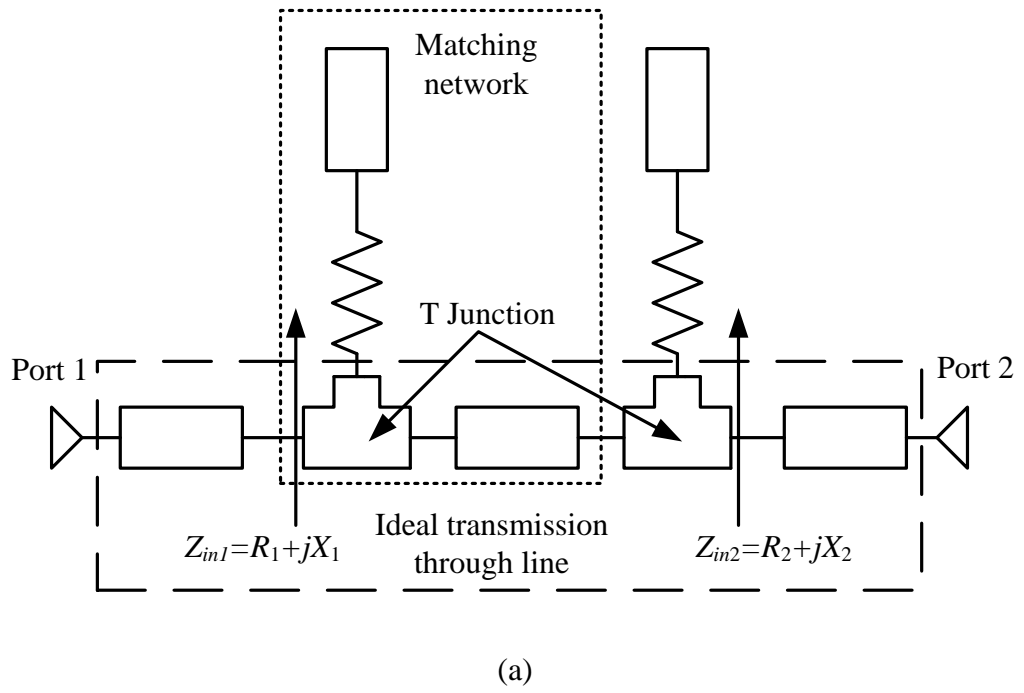
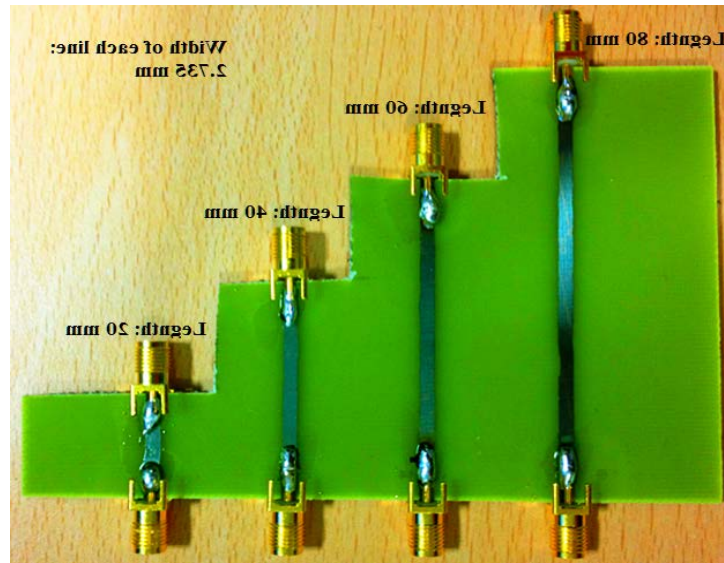


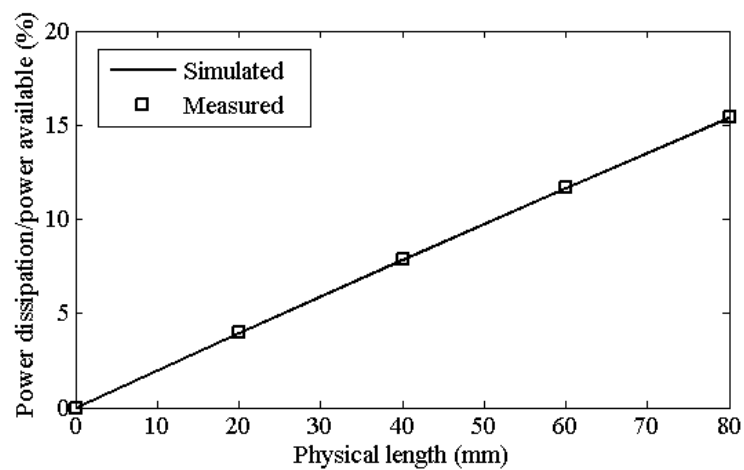
Fig. 5.4 (a) Theoretical circuit model used to calculate shunt connected loss of ML, and
(b) a practical board.

Fig. 5.4(a) shows an ideal transmission through line connected with two parallel shunt circuits, which are modelling the shunt lines in Fig. 5.4(b). The matching network is used to match the total circuit to 50Ω for measurement. The discontinuity line in Fig. 5.4(b) is used to test the T-junction effects for the total circuit. The series loss is tested by a group of

series $50\ \Omega$ MLs (0-80mm) and the measured power loss compared to the theoretical results are shown in Fig. 5.5(b), which are also in good agreement.



(a)



(b)

Fig. 5.5 (a) Practical design of 0 – 80 mm ML, and (b) power dissipation ratio vs. the physical length.

The total comparison results shown in table 5.1 indicate that the discontinuity of T-junction has little effect. The predicted and measured total power dissipation applied to the series and shunt lines are 33.6% and 31.7%, respectively which are in good agreement.

	Theoretical	Practical
Shunt	22.00%	20.00%
Series with T	11.74%	11.8%
Series without T	11.60%	11.70%
Total	33.60%	31.70%

Table 5.1 Comparison data of theoretical and practical results.

5.3 Characteristics of Nonlinear Device Model

The nonlinear modelling is essential for the PA design using the computer design method, which provides accurate and valuable design parameters for the final practical fabrication. The nonlinear device used for the design in this thesis is ATF 33143 and its large signal modelling is given in Fig. 5.6.

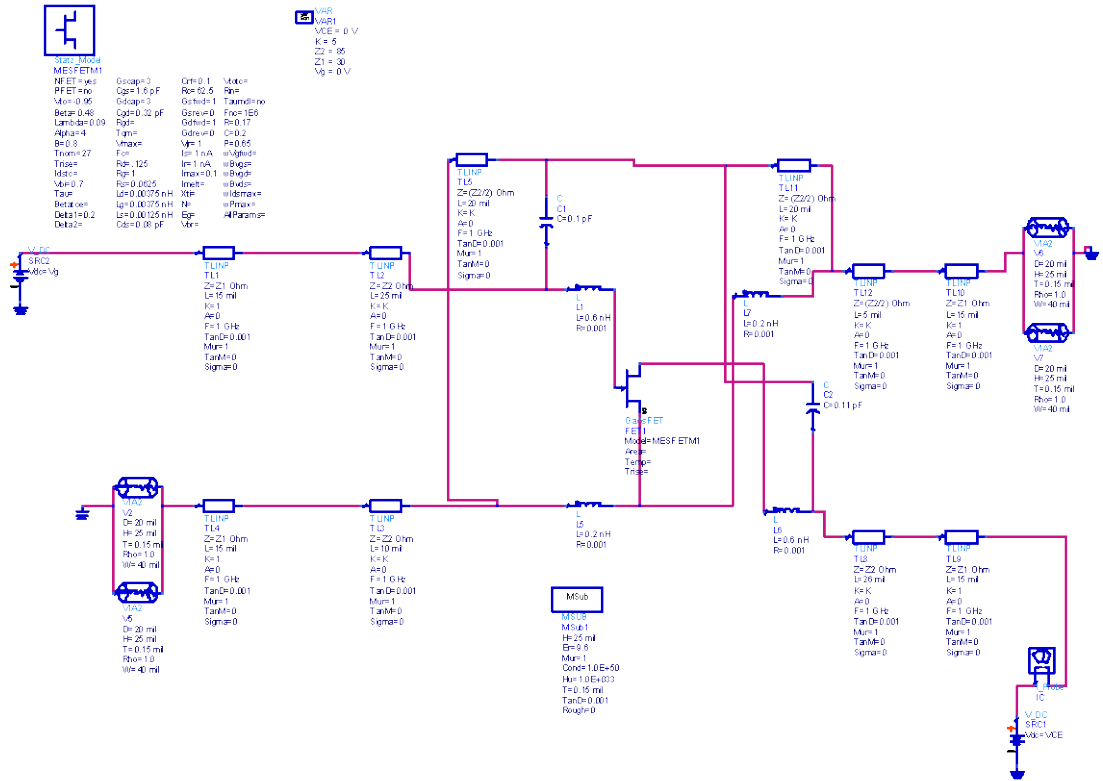


Fig. 5.6 Nonlinear model of low noise pHEMT ATF 33143 (Large figure is shown in appendix).

The manufacturing parameters of ATF 33143 are used in the Statz model and this nonlinear model is simulated by ADS, with characteristics of $I_{ds} - V_g$, and $I_{ds} - V_{ds}$ curves shown in Fig. 5.7 and Fig. 5.8.

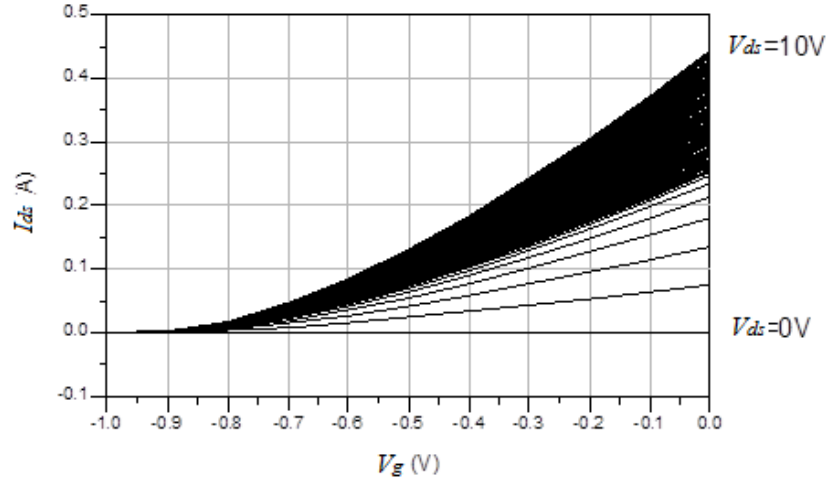


Fig. 5.7 $I_{ds} - V_g$ characteristics of ATF33143.

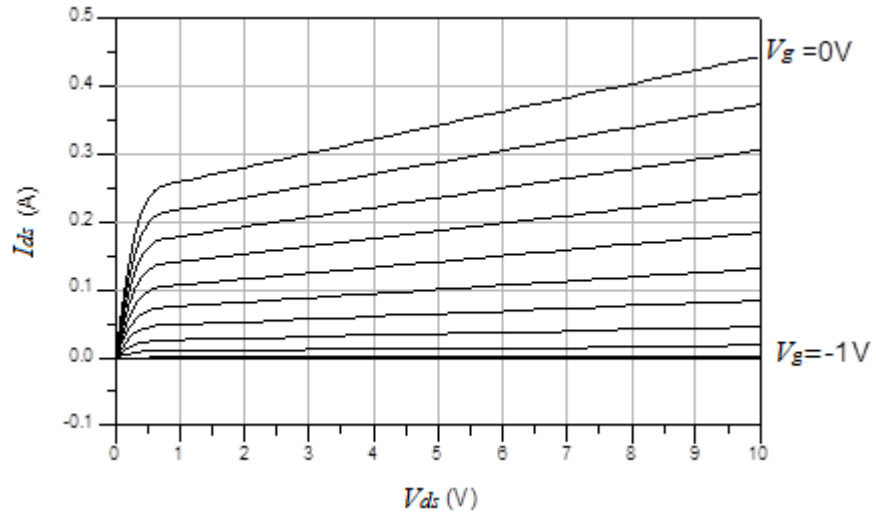


Fig. 5.8 $I_{ds} - V_{ds}$ characteristic of ATF 33143.

Fig. 5.7 indicates that the pinch off voltage V_p is -0.9 V with V_{ds} varied from 0 to 10 V. v_k is ~ 0.5 V with V_g varies from -1 to 0 V. The $I_{ds} - V_{ds}$ characteristic of ATF 33143 indicates that the internal resistance is equal to 2 Ω , and the optimum load impedance R_L calculated using (4.9f) and (4.11f) are 20.372 Ω and 33.823 Ω for the class F and inverse class F PAs, respectively.

5.4 Classical Load Pull Method

In order to obtain maximum PAE, the load pull method [189-193] is normally used to obtain the optimum load and the source impedance. The classical block diagram is shown in Fig. 5.9.

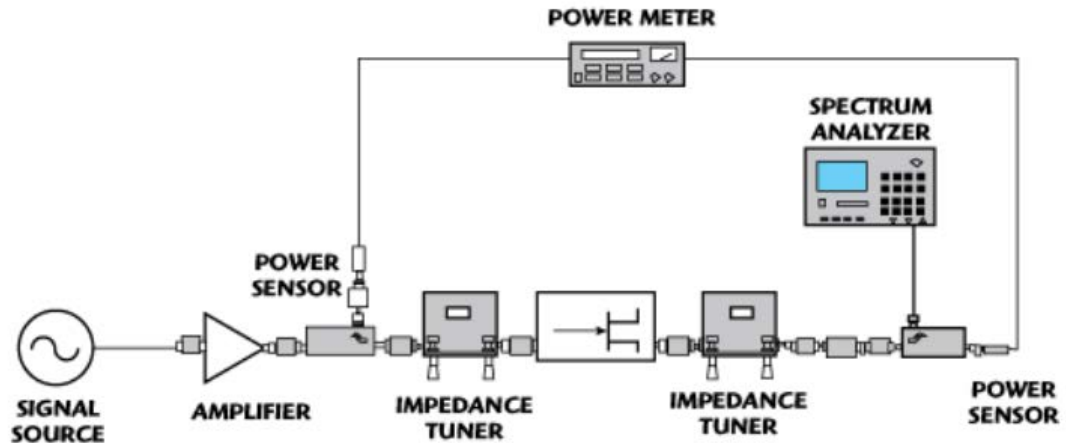


Fig. 5.9 Classical block diagram of load/source pull setup [194].

The traditional load pull system comprises the signal source, source/load impedance tuners and scalar measurements as the power meter. The source and load tuners are used to adjust the source and load impedances, respectively to obtain the minimum reflected power and the maximum output efficiency. Calibration needs to be carried out to the required accuracy. Should multi – harmonics be required then concatenated tuners could be used, however one option would be handled to use a single passive tuner [195-197]. However, power meters are wideband in nature, which measures both the fundamental and harmonic output power levels. Hence it is difficult to obtain the percentage of power allocated at each frequency. To overcome this problem, a spectrum analyser can be used.

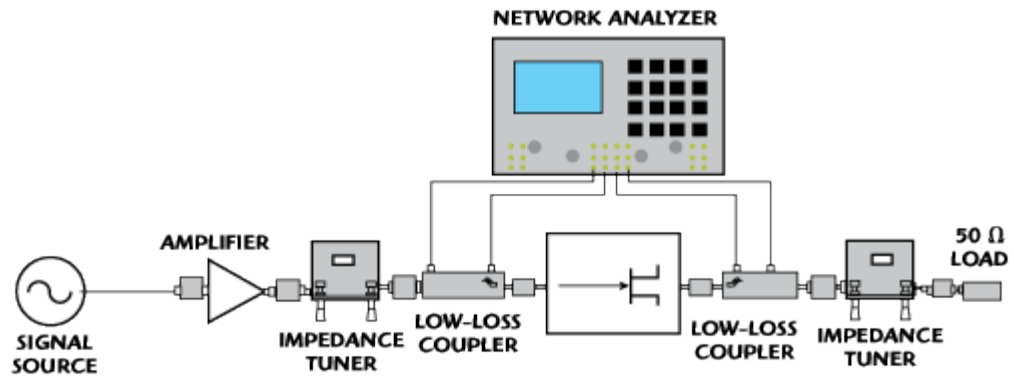


Fig. 5.10 Vector-receiver load pull block diagram [194].

Another method introduced in [194] is shown in Fig. 5.10, which includes a signal source, and impedance tuners with a network analyzer. The network analyzer measures the input and output signals and determines the measurement parameters based on each frequency. So the fundamental and higher harmonics power can be easily separated and measured independently. Also a network analyzer is more accurate than the simple power meter or the spectrum analyzer for practical measurement.

5.5 A Simplified Design Method of Class F PA

The linear model of class F and inverse class F PAs were theoretically investigated with the predicted optimum load impedance to obtain the ideal voltage and current waveforms through the drain. For the nonlinear device, both the source and load harmonic impedances affect the efficiency [198] and the optimum load impedance at the fundamental frequency will change with the modified supply voltage. It is difficult to optimise these impedances at different harmonics to obtain both the maximum efficiency and the wide bandwidth. However, this problem can be solved by using simulation methods based on the nonlinear

Statz modelling of an active device using the HB method. The load and source pull method could be used to obtain the maximum efficiency and to minimize the overlap of voltage and current waveforms of the drain. The basic schematic is shown in Fig. 5.11.

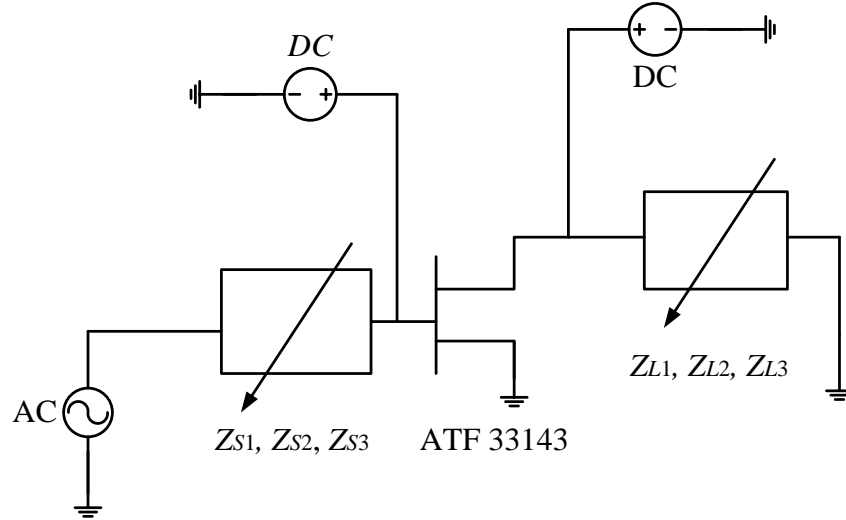


Fig. 5.11 Schematic of load and source pull method based on nonlinear simulation.

Z_{s1}, Z_{s2}, Z_{s3} are the source impedances and Z_{L1}, Z_{L2}, Z_{L3} are the load impedances at the fundamental frequency, the second, and the third harmonics, respectively. For a class F PA design, the drain voltage and current waveforms are shaped by short circuits for even harmonics, open circuits for odd harmonics and the optimum impedance at fundamental frequency. Also the source harmonic impedances are used to optimise efficiency and gain. The input harmonic control of high efficiency design was proposed in [199-205] indicating that the second harmonic input termination had significant influence on the efficiency and linearity. The rest of this chapter compares the effects of two different harmonic load matching networks on PAE, gain with second and third source harmonic controls. Using the nonlinear TL model, the schematic of the class F PA is depicted in Fig. 5.12.

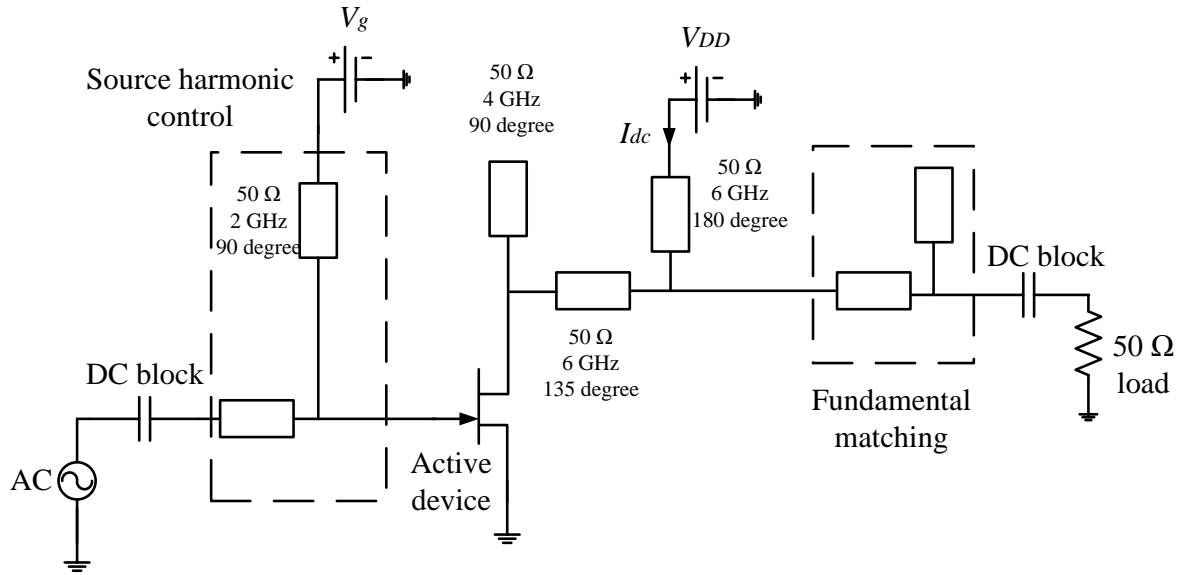
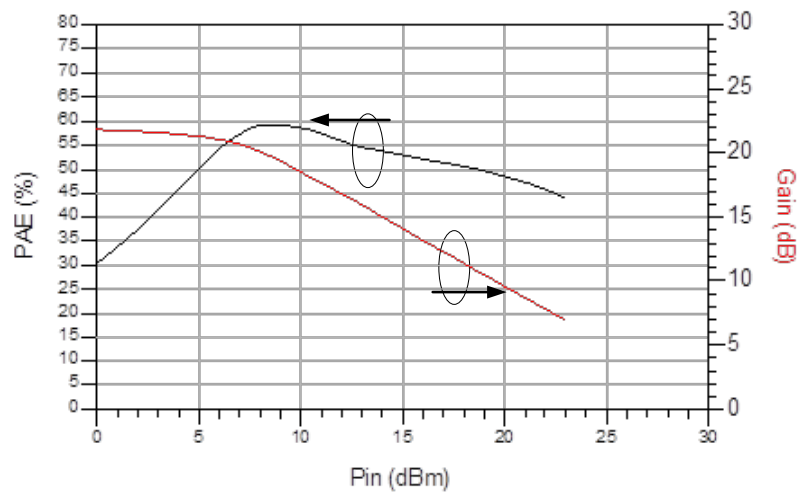
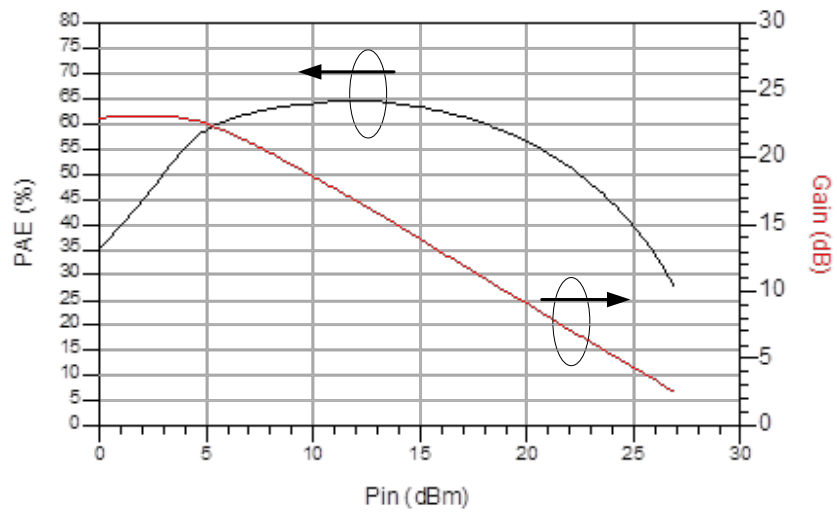


Fig. 5.12 Schematic of nonlinear model class F PA with up to third harmonic load control.

The harmonic load matching network was proposed in Chapter 4. It has been suggested that the optimum second harmonic of the input impedance of the source for class F PA is close to the short circuit [202, 203]. Hence, a 50 Ω TL is used to make the second harmonic short at the input termination with the simulation results shown in Fig. 5.13 and Fig. 5.14. These figures show the comparison results with and without the second harmonic control at the source termination.

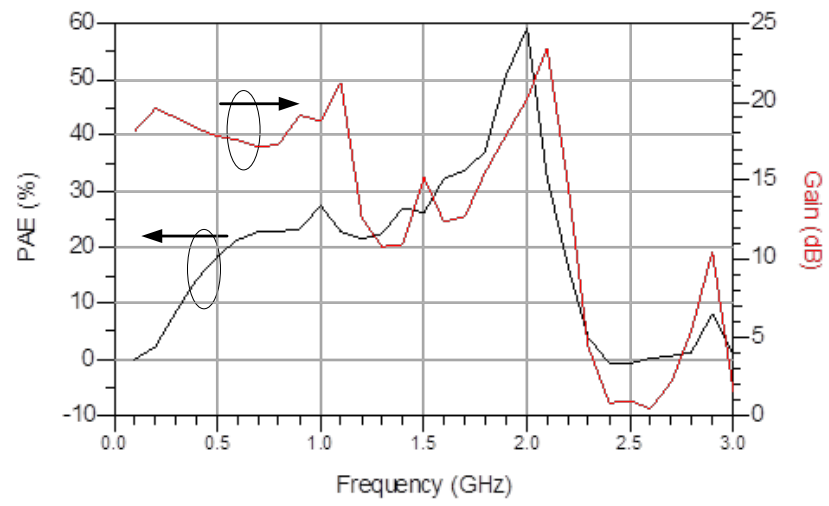


(a)

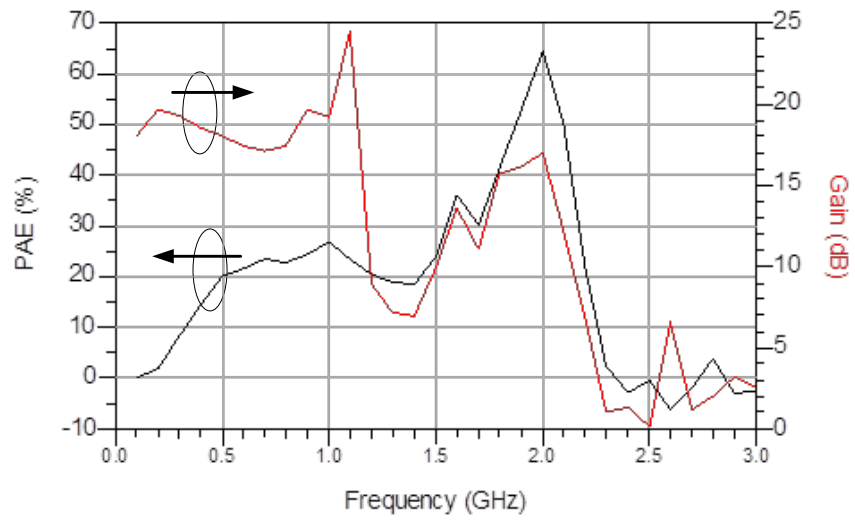


(b)

Fig. 5.13 PAE and gain in terms of input power: (a) no input harmonic control, (b) with second harmonic control at input termination.



(a)



(b)

Fig. 5.14 PAE and gain in terms of frequency: (a) no input harmonic control, (b) with second harmonic control at input termination.

With the second harmonic control the peak PAE is 65%, which is 5% higher than the model without control. For the input power range of 0 to 20 dBm the gain achieved is 10 dB for both models. The bandwidth above 50 % PAE level is ~200 – 300 MHz for both models. Another novel class F PA design with the even harmonic short circuit of the load matching network is illustrated in Fig. 5.15.

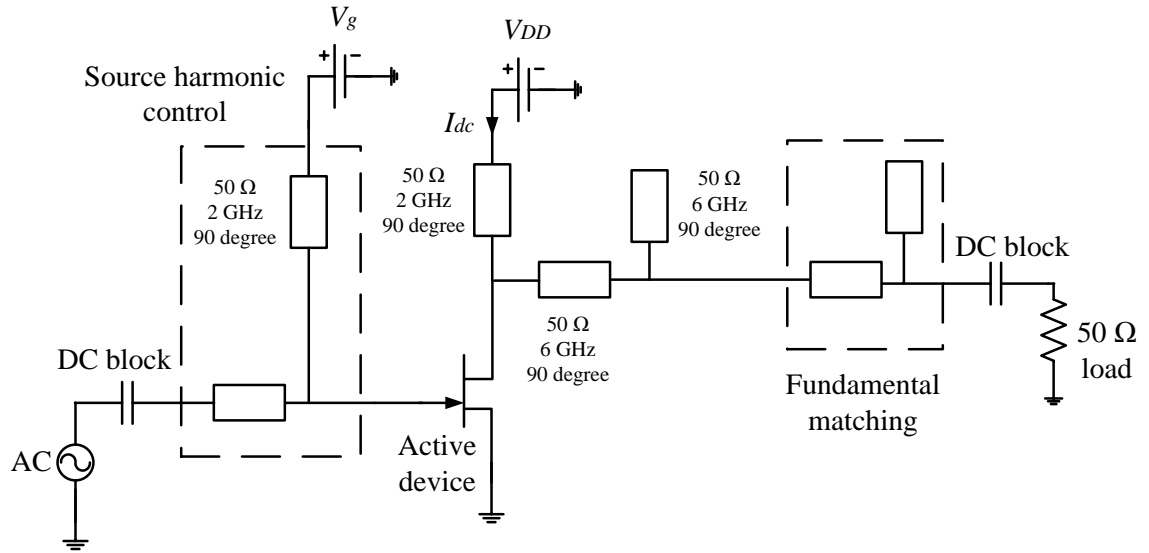
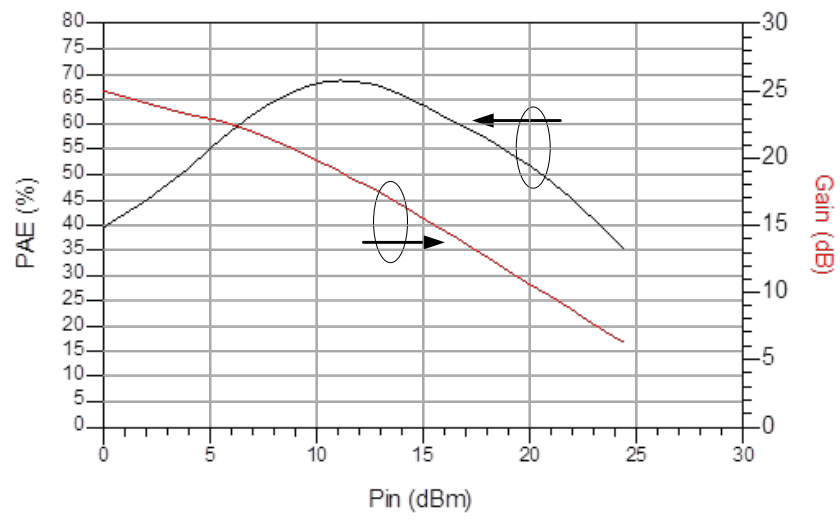
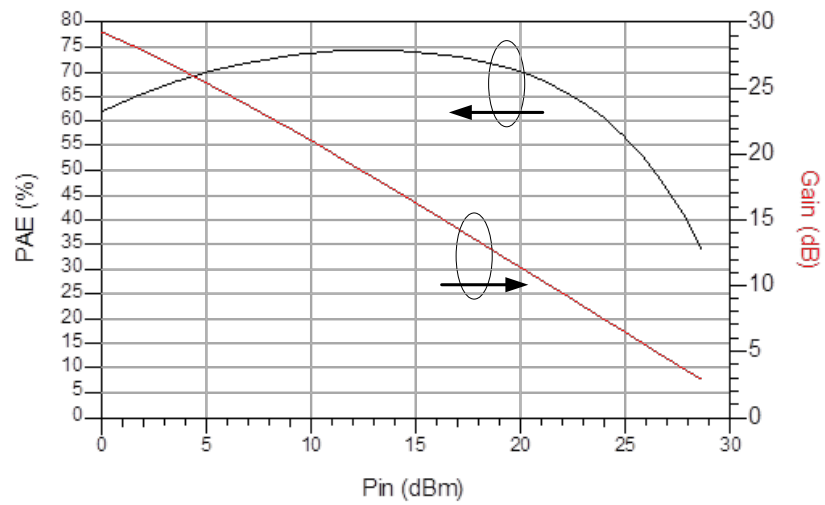


Fig. 5.15 Schematic of class F PA with even harmonic short circuit of load matching network.

The ML element connected with the power source V_{DD} produces even harmonics at the short circuit. Two 50 Ω , 90 degree TLs operating at 6 GHz produce an open circuit at the third harmonic. The simulated PAE and gain in terms of the input power and frequency with and without the input harmonic control are shown in Fig. 5.16 and Fig. 5.17.

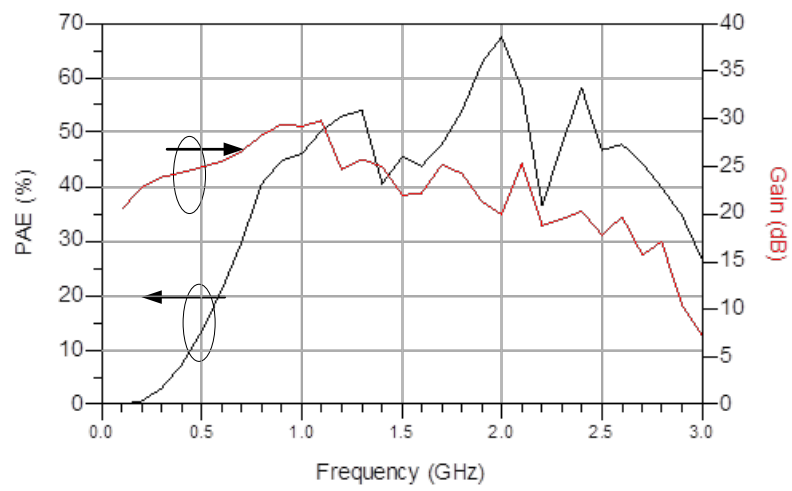


(a)

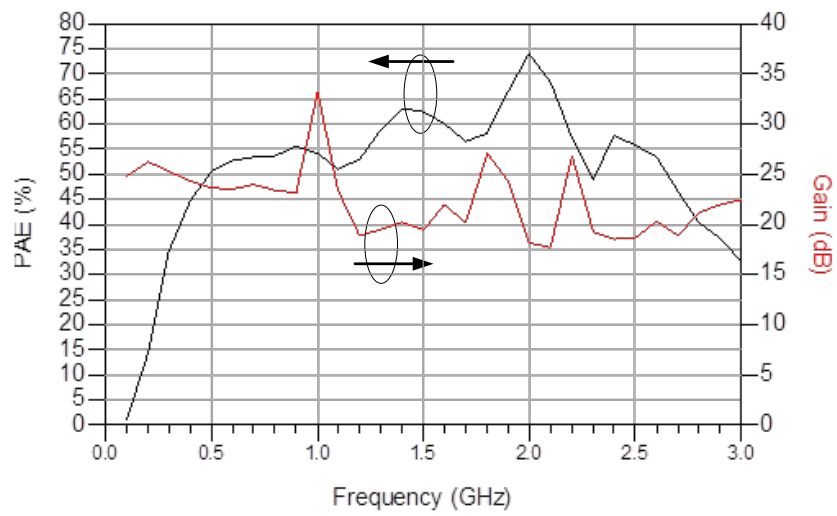


(b)

Fig. 5.16 PAE and gain in terms of input power: (a) no input harmonic control, (b) with second harmonic control at input termination.



(a)



(b)

Fig. 5.17 PAE and gain in terms of frequency: (a) no input harmonic control, (b) with second harmonic control at input termination.

The peak PAE is improved from 69% to 75% by the control of the second harmonic at the input termination. The bandwidth of PAE and gain are also improved considerably. For the non source harmonic control model where the bandwidth of more than 50% PAE is ~500 MHz and the bandwidth of more than 40% PAE is ~2 GHz. With the source impedance at second harmonic short, the bandwidth of PAE over 50% is improved to 2.2 GHz. The gains of both models are over 10 dB and 15 dB for the input power range of 0 – 20 dBm and 1- 3 GHz, respectively.

Consequently, the second harmonic of input termination improves both models. The even harmonics short circuit of the load network has improved performance, which yields about 10% peak PAE improvement.

5.6 A Simplified Design of Inverse Class F PA

For the inverse class F PA design, the harmonic load matching network was proposed in Chapter 4. Using the nonlinear model, the schematic of the design is depicted in Fig. 5.18.

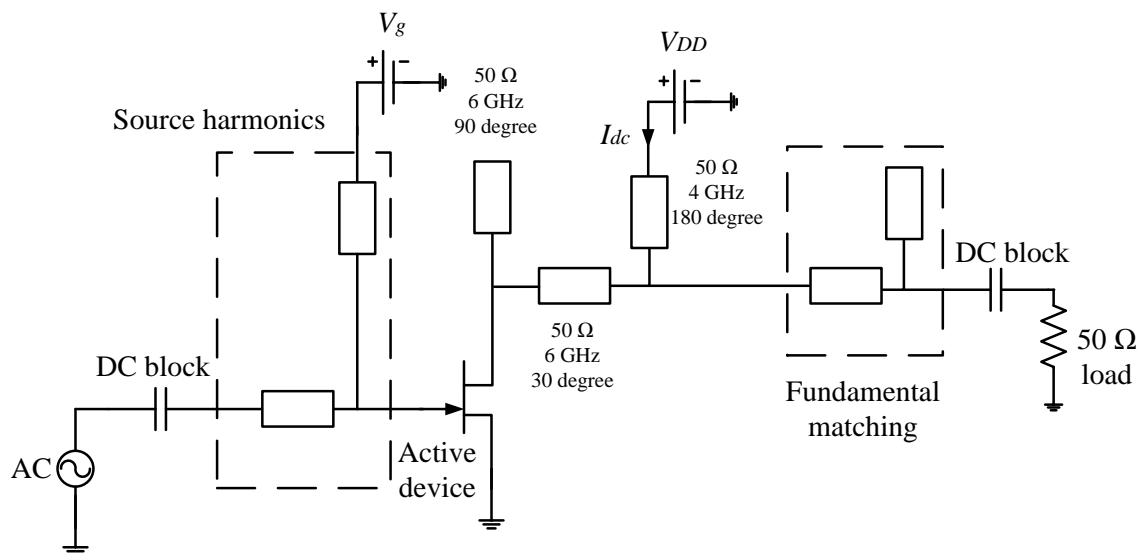
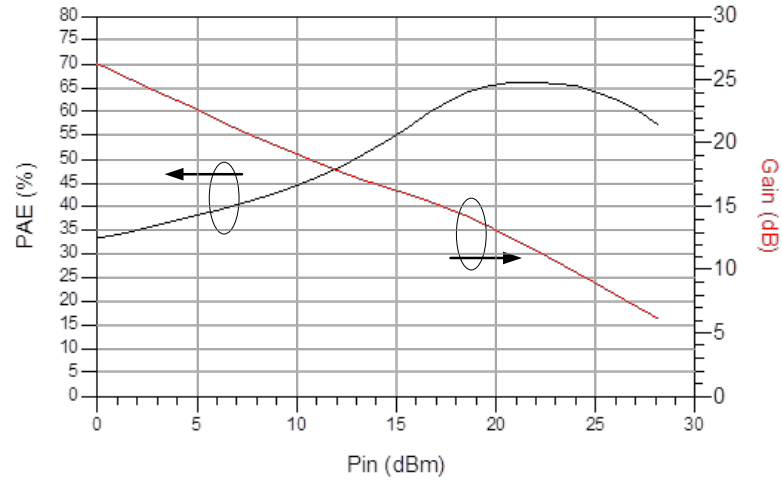


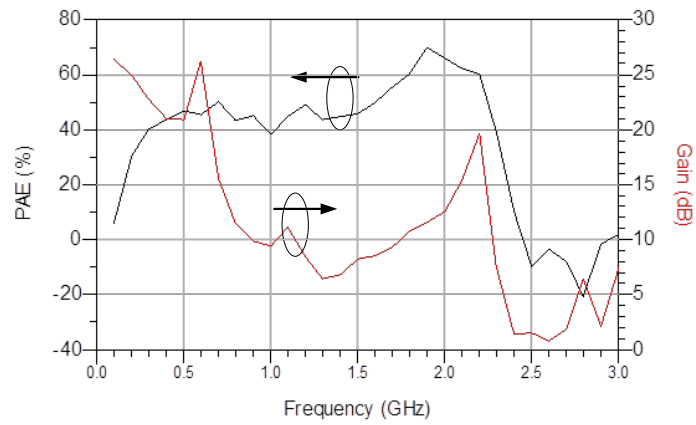
Fig. 5.18 Nonlinear model of inverse class F PA.

Without the source harmonics control, the optimum PAE and the gain are illustrated in Fig.

5.19.



(a)



(b)

Fig. 5.19 Simulated PAE and gain of the inverse class F PA design without source harmonic control in terms of: (a) input power, and (b) frequency.

From this structure, the maximum PAE obtained is 67% with a 21 dBm input power. The bandwidth of more than 50% PAE is ~600 MHz (from 1.6 GHz to 2.2 GHz) and more than 40% PAE is ~2 GHz (from 0.3 GHz to 2.3 GHz). The gain decreases linearly with the increasing input power with >10 dB gain is obtained between 1.75 GHz and 2.3 GHz frequency range. The short circuit of the second harmonic at the input termination increases the PAE of class F PA, which was well reviewed in [200] and shown experimentally in section 5.5. The inverse class F PA is similar to the class F with the second harmonic behaving as an open circuit (see Fig. 5.20).

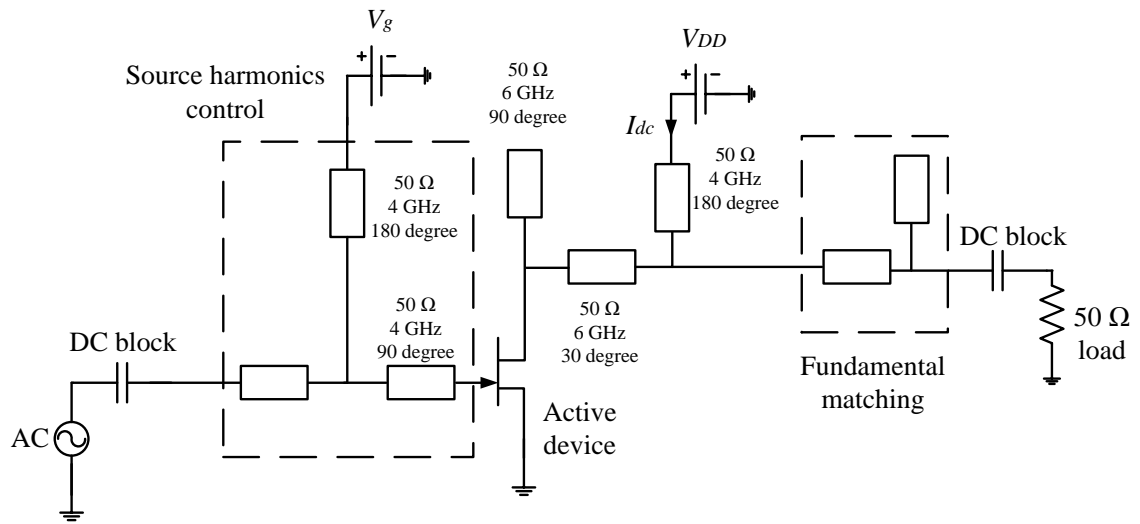
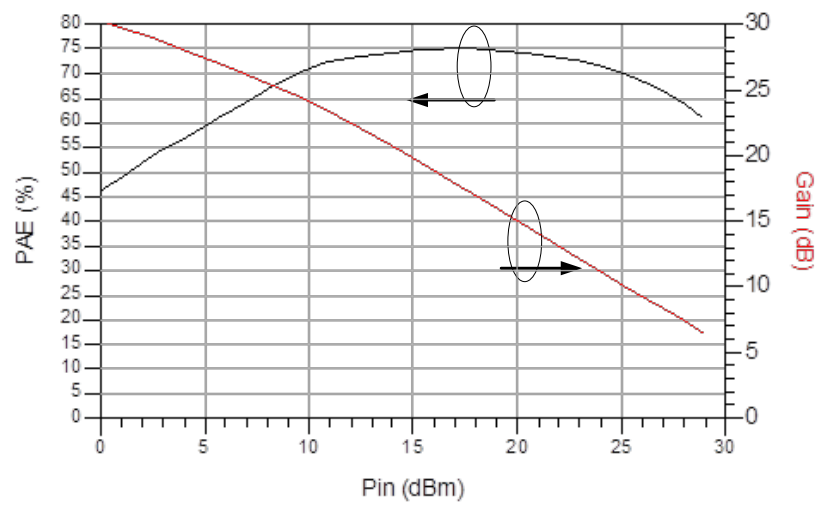
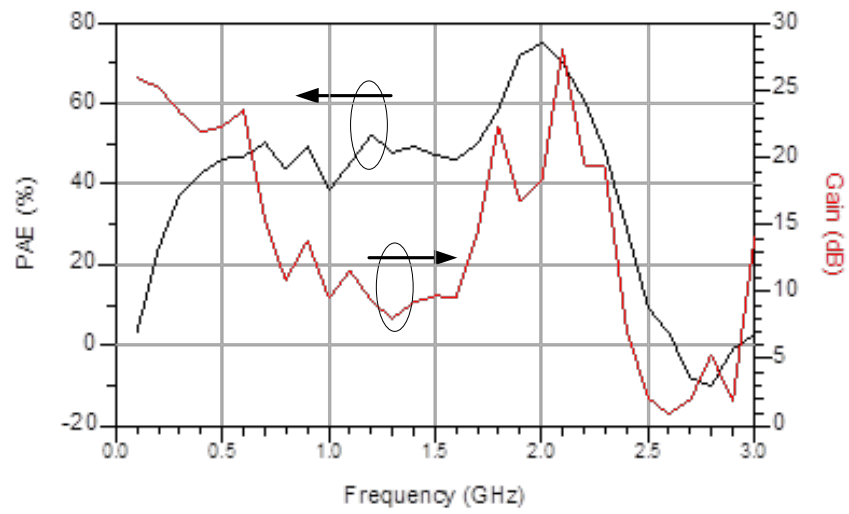


Fig. 5.20 Nonlinear model of inverse class F PA with source harmonics control.

With the condition of open circuit of the second harmonic at the source, the obtained PAE and the gain are shown in Fig. 5.21:



(a)



(b)

Fig. 5.21 Simulated PAE and gain of the inverse class F PA design with source impedance second harmonic control in terms of: (a) input power, and (b) frequency.

With the control of second harmonic of the source impedance, the peak PAE increases to 75% using 17 dBm input power which is ~7% increase compared with the result carried out by the model without source control. The bandwidth for the 10 dB gain level also increases to 750 MHz. By controlling both the second and third harmonics of the source impedance, the schematic of matching network is illustrated in Fig. 5.22.

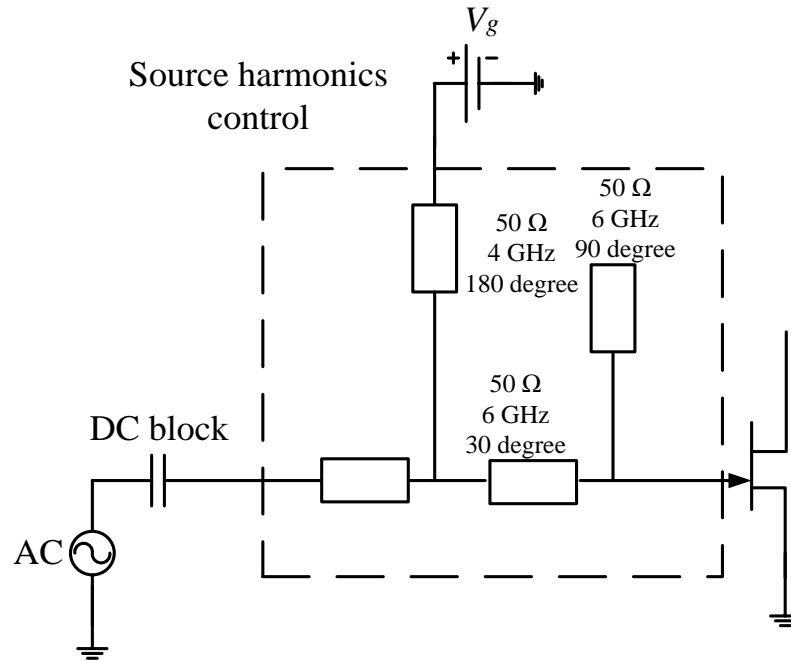
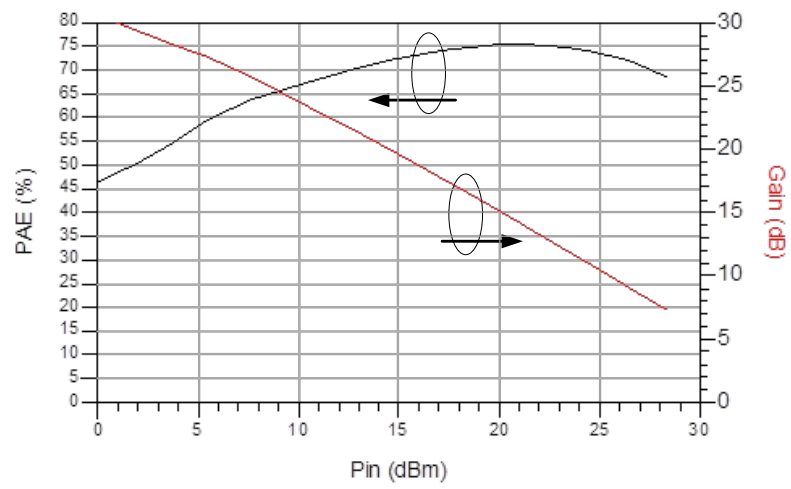
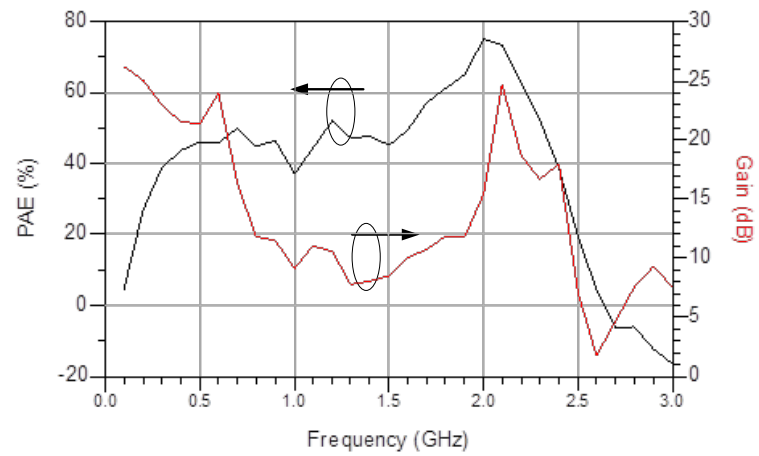


Fig. 5.22 Source matching network of nonlinear model of the inverse class F PA with source control up to third harmonics.

The plots of PAE and the gain in terms of the input power and frequency are depicted in Fig. 5.23.



(a)



(b)

Fig. 5.23 Simulated PAE and gain of the inverse class F PA design with source impedance second and third harmonic control in terms of: (a) input power, (b) frequency.

By comparing with the model with the second harmonic source control, the results of the model with up to the third harmonic source control show no further improvement. However the difference is in the peak PAE when the input power is around 20 dBm, which is 16 dBm of the second harmonic control model. To conclude, for both the class F and inverse class F PAs designs, the harmonic load matching network design is the key factor, which affects the voltage and current flow through the active device. PAE is improved with more harmonics controlled by the load matching network but the increased components of matching network will lead to power dissipation from the ML (low pass filtering) [131, 160, 161]. The second harmonic of input termination also improves the PAE and the gain for the class F PA. For the inverse class F design, without source harmonic control circuit, with second harmonic control, and up to the third harmonic control of the source termination circuits are compared and results shown in Fig. 5.19, Fig. 5.21, and Fig. 5.23 indicate that with an open circuit at the second harmonic of the source improve the PAE by up to 75 %. This is close to the results of the class F PA with the even harmonics short circuits model.

5.7 Practical Design and Test of Class F PA

In practical designs for the class F PA, ideal TLs are replaced by the MLs and the substrate PCB FR4 is used due to low cost. A T-junction is used to connect MLs for practical design and the load matching network of even harmonics short circuit is utilized to shape the voltage and current waveform flowing through the active device. An 18 Ω resistor is located before the active device for the stability requirement [206-210]. The schematic of ML model is shown in Fig. 5.24.

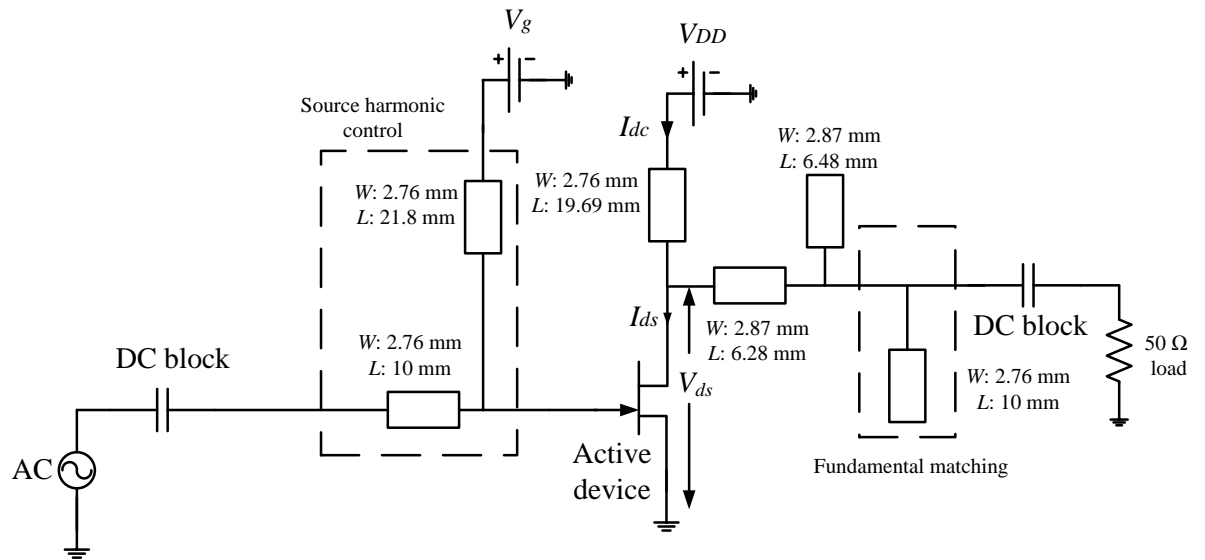
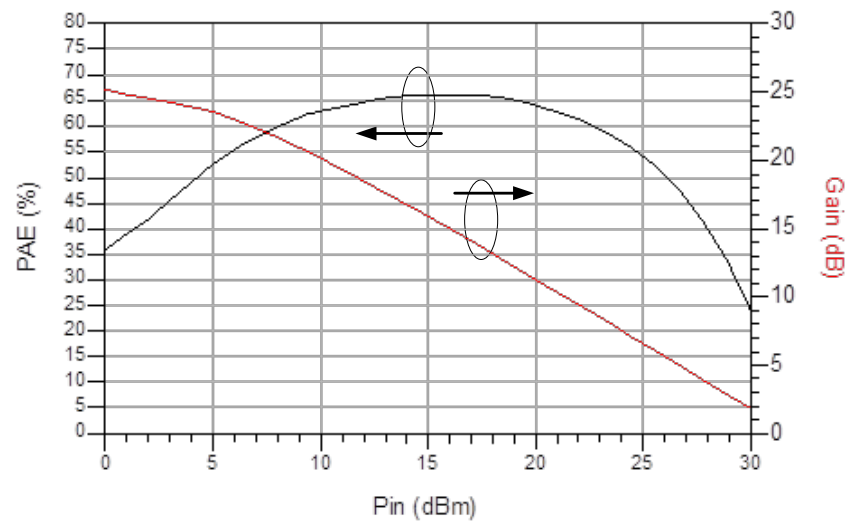


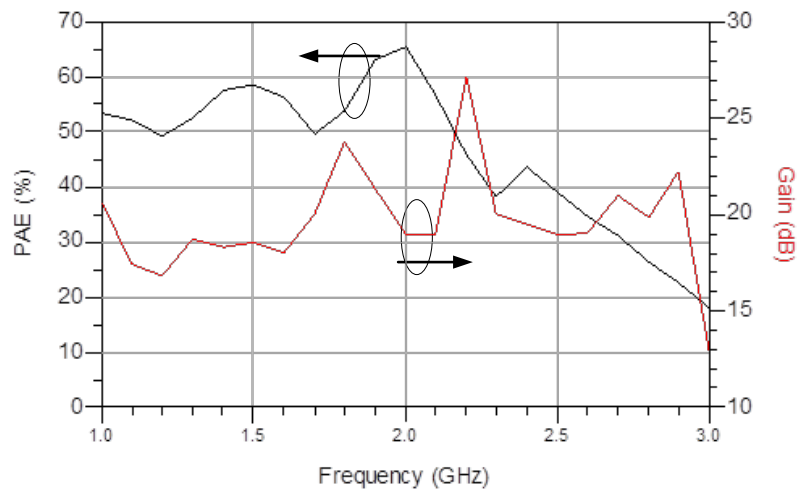
Fig. 5.24 ML model of class F PA design.

The PAE and the gain in terms of the input power and frequency are shown in Fig. 5.25.

V_{ds} and I_{ds} waveforms through transistor ATF 33143 (see Fig. 5.24) is shown in Fig. 5.26.



(a)



(b)

Fig. 5.25 PAE and gain of the class F PA design with the ML model in terms of: (a) input power, and (b) frequency.

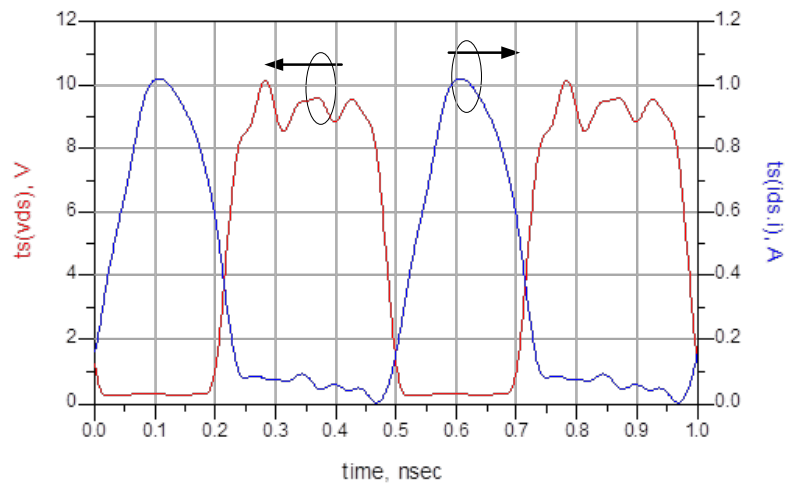


Fig. 5.26 The V_{ds} and I_{ds} waveform over active device.

By replacing the ideal TL with the lossy ML, the maximum PAE value drops from 75% to 67% due to the power dissipates at the MLs. Square voltage and half sine current waveforms are obtained with little overlaps which are very similar to the predicted results in Chapter 4. The load impedance at fundamental, second and third harmonics are $11.394 + j2.721 \Omega$, $1.751 + j0.744 \Omega$, and $542.75 - j31.504 \Omega$, respectively. The schematic diagram for the class F PA with a T-junction is outlined in Fig. 5.27.

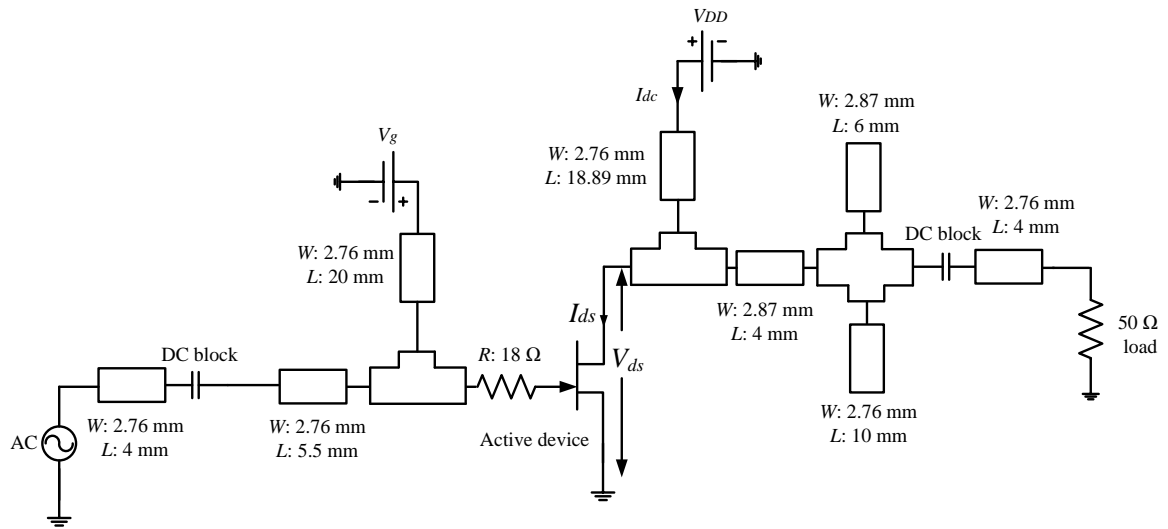


Fig. 5.27 Schematic of the ML model for the class F PA with T-junction.

The simulated V_{ds} and I_{ds} waveform through transistor ATF 33143 (see Fig. 5.27) is depicted in Fig. 5.28.

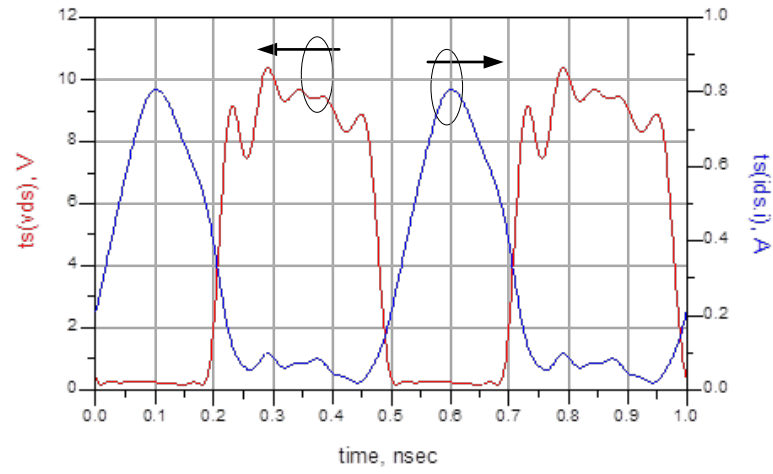


Fig. 5.28 The V_{ds} and I_{ds} waveform over active device.

The printed circuit layouts of the class F PA and the fabricated version are shown in Figs. 5.29(a) and (b), respectively. The dimension of practical board of class F PA is shown in table 5.2.

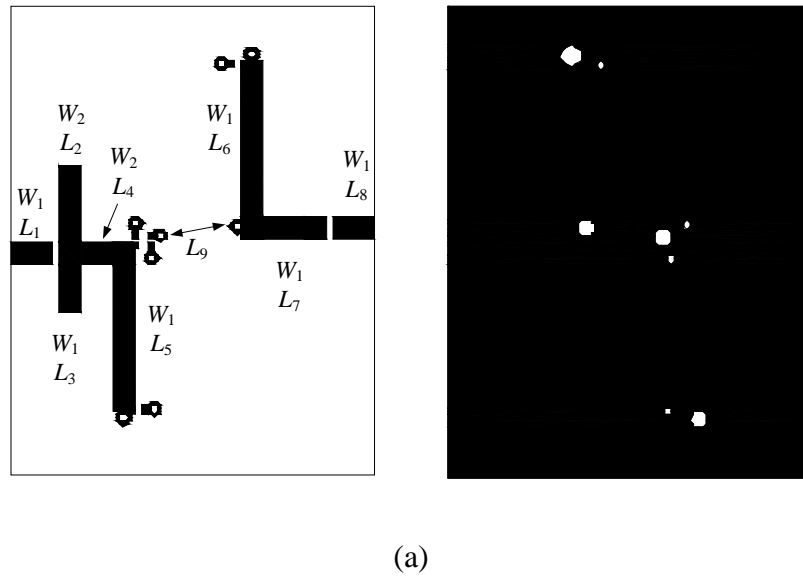
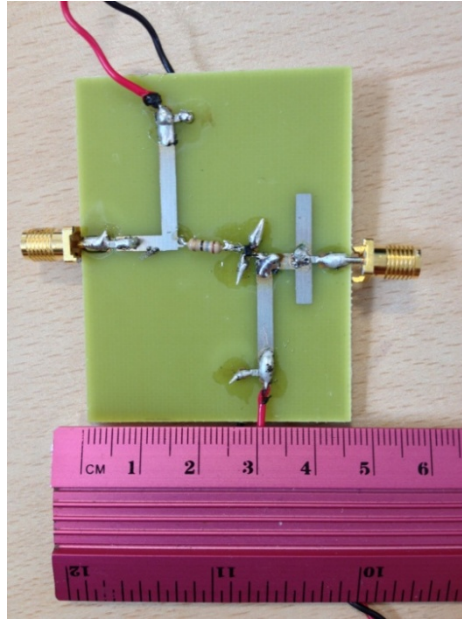


Fig. 5.29 Footprint mirror layout of class F PA.



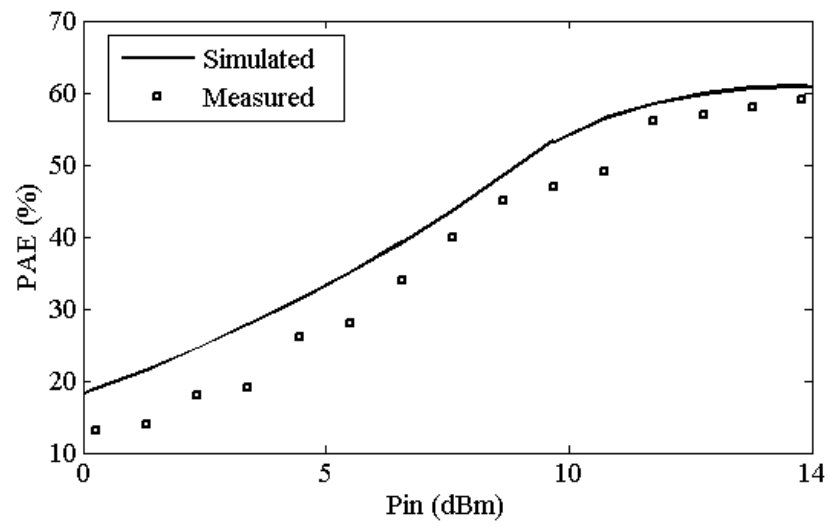
(b)

Fig. 5.30 Fabricated board of the class F PA.

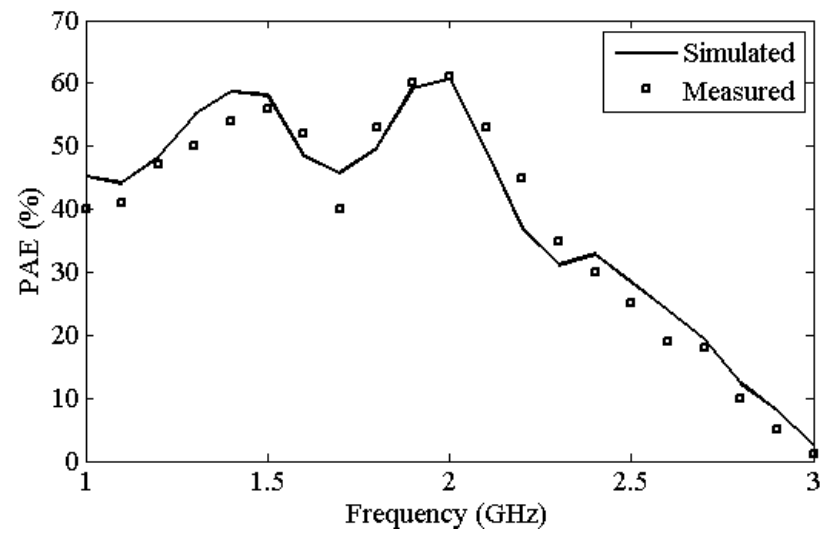
Unit:	W_1	W_2	L_1	L_2	L_3	L_4	L_5	L_6	L_7	L_8	L_9
mm	2.76	2.87	4	6	10	5	18.89	20	5.5	4	10

Table 5.2 Dimension of fabricated board of class F PA.

The measured and simulated PAE using 2 V V_{DD} (because of the limitation of the transistor, see data sheet of ATF 33143 and also output power of signal generator) are compared in Fig. 5.31 and Fig. 5.32.

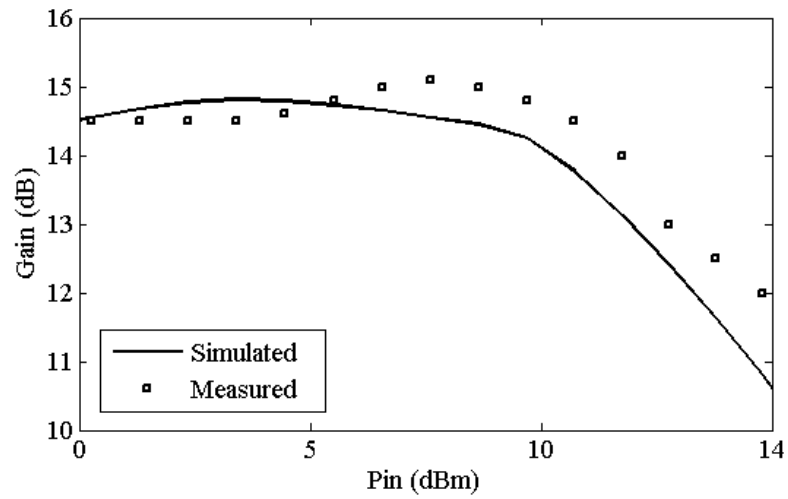


(a)

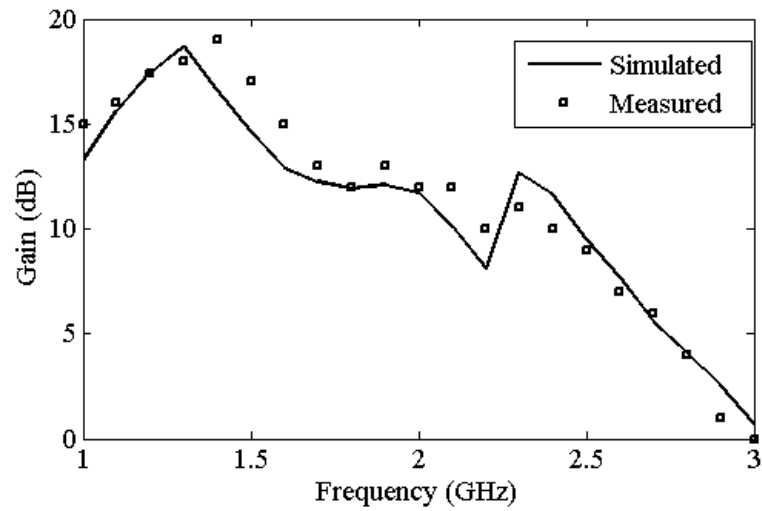


(b)

Fig. 5.31 Measured and simulated PAE for the class F PA in terms of: (a) input power, and (b) frequency.



(a)



(b)

Fig. 5.32 Measured and simulated gain for the class F PA in terms of: (a) input power, and (b) frequency.

The peak PAE obtained is ~61% which is 6% less than the results of ML model (with respect to Fig. 5.26) due to the T-junction connection and the loss across the resistor [208]. The square voltage and half sine current waveforms are obtained (see Fig. 5.28) and

overlap is small which is very close to the predicted results given in Chapter 4. The load impedance at the fundamental, second and third harmonics are $15.271 + j3.705 \Omega$, $2.44 + j0.331 \Omega$, and $323.284 + j175.864 \Omega$, respectively which are close to the predicted conditions analysed in Chapter 4. The simulation results are in good agreement with the measured results.

5.8 Practical Design and Test of Inverse Class F PA

Using a lossy ML model instead of the lossless TLM, the schematic of the inverse class F PA is given in Fig. 5.33.

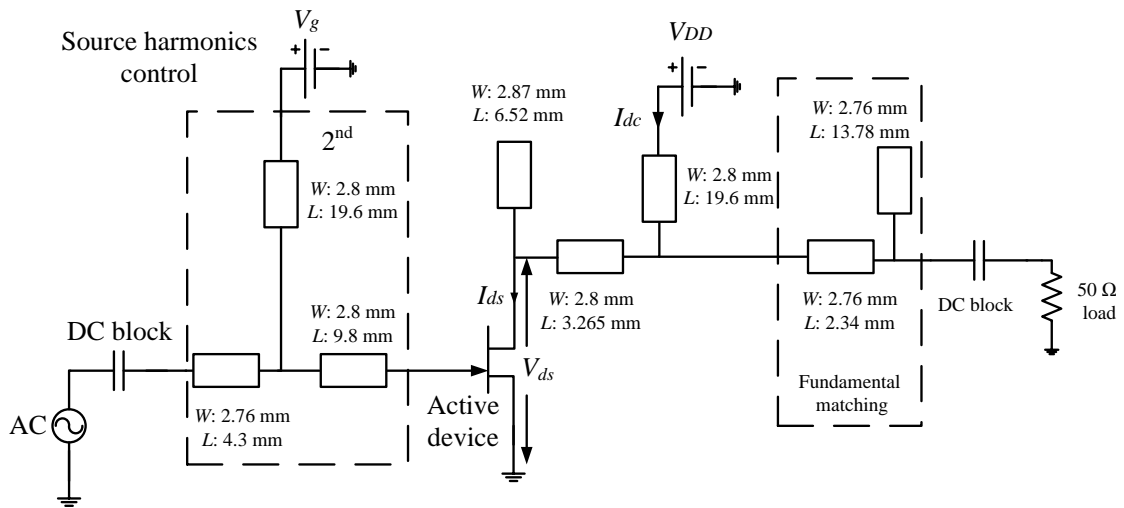
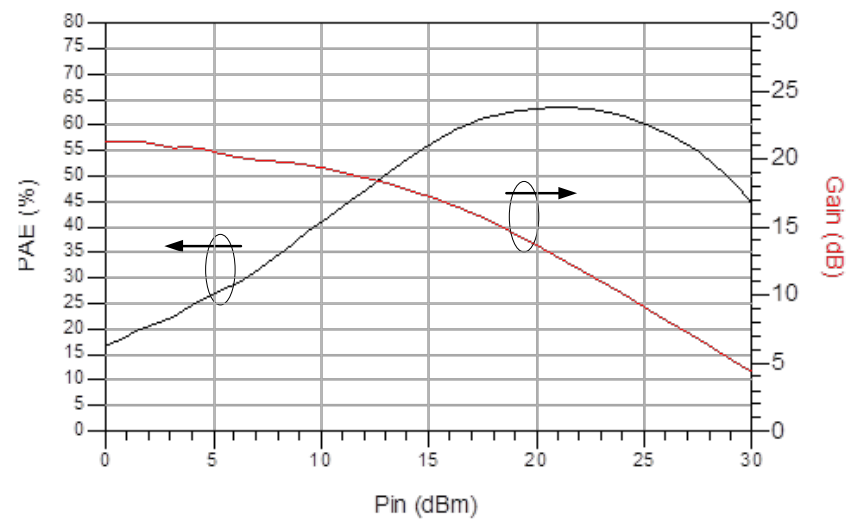
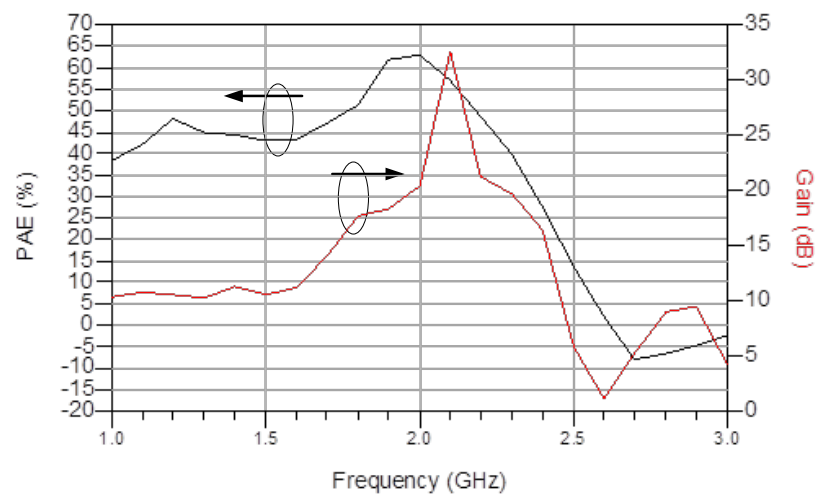


Fig. 5.33 Schematic of ML model of inverse class F PA.

The simulated PAE, the gain in terms of the input power and frequency are shown in Fig. 5.34.



(a)



(b)

Fig. 5.34 PAE and gain of the inverse class F PA design with the ML model in terms of:

(a) input power, and (b) frequency.

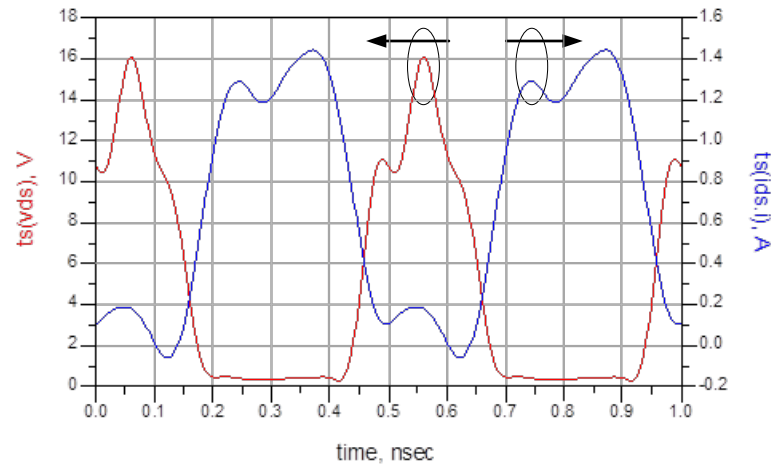


Fig. 5.35 The V_{ds} and I_{ds} waveforms over active device.

The peak PAE of the ML model for the inverse class F PA is 64% which is 11% lower than the lossless TL model. Over 40% PAE obtained from 1.1 GHz to 2.1 GHz. The gain drop smoothly with the increasing input power, see Fig. 5.34(a). At the frequency domain, the gain drop below 10 dB when the frequency is above 2.45 GHz. Improvement in control of the harmonic load matching network shapes V_{ds} and I_{ds} waveforms (see Fig. 5.33 and Fig. 5.35) with half sine voltage and square current with very little overlaps as theoretical predicted in Chapter 4. For the practical fabrication purpose, The ML model with the T-junction schematic is shown in Fig. 5.36, whereas simulated V_{ds} and I_{ds} waveforms at the transistor is depicted Fig. 5.37.

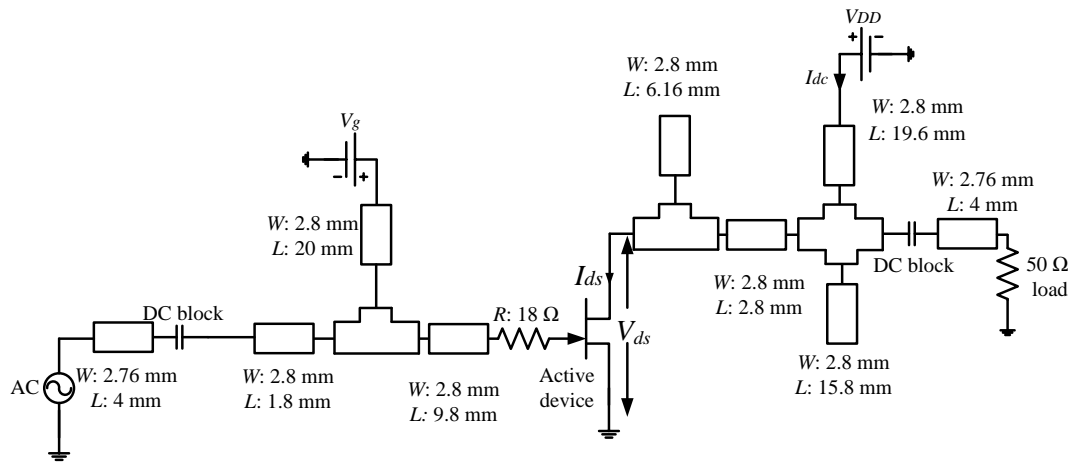


Fig. 5.36 Schematic of ML model inverse class F PA with T-junction.

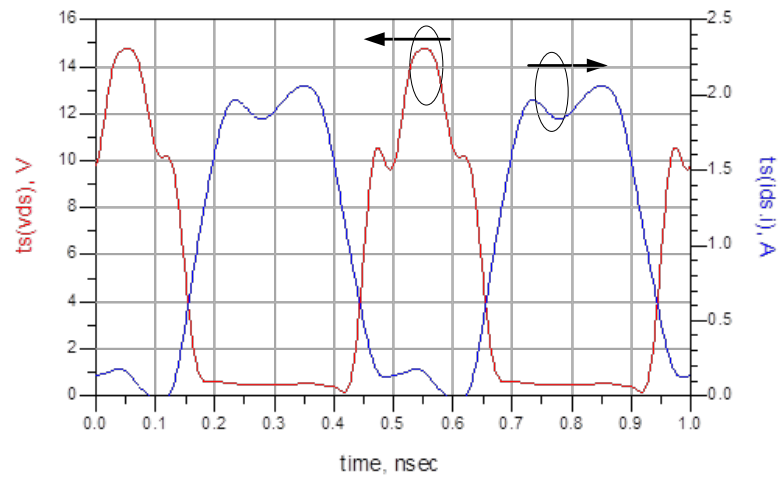


Fig. 5.37 The V_{ds} and I_{ds} waveforms over active device.

The printed circuit layouts and the fabricated board version of the inverse class F PA are shown in Fig. 5.38, and Fig. 5.39, respectively. The dimensions of the practical board are given in table 5.3.

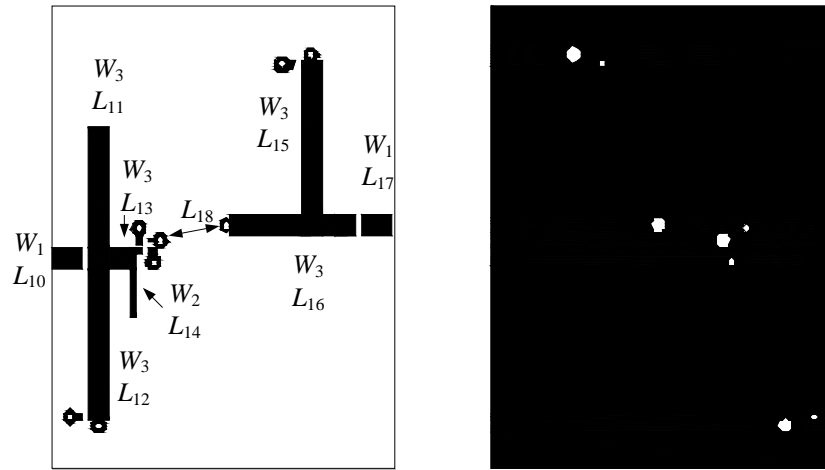


Fig. 5.38 Printed circuit layouts of the inverse class F PA.

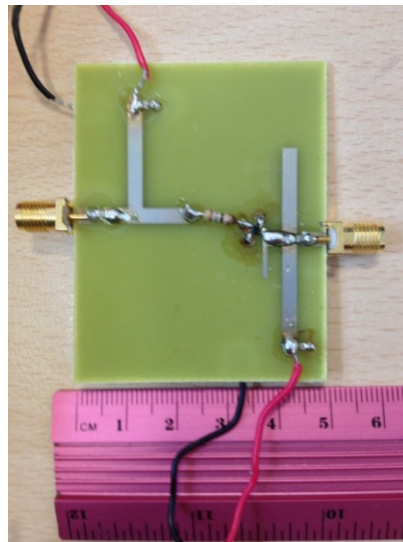
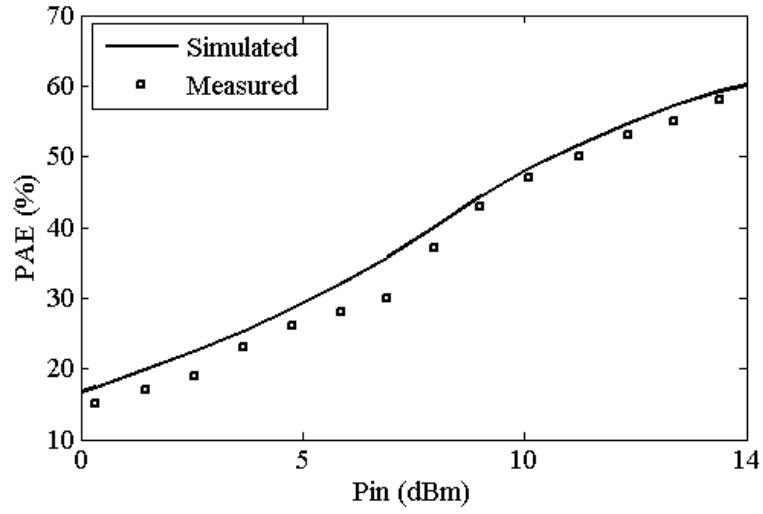


Fig. 5.39 Fabricated board of the inverse class F PA.

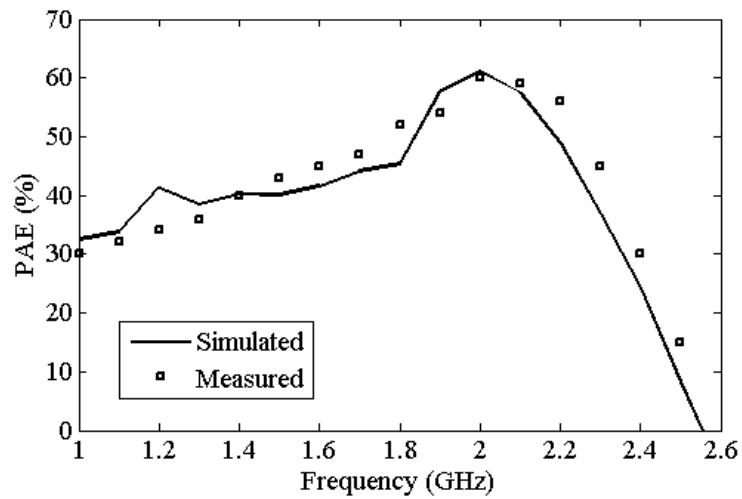
Unit:	W_1	W_3	L_{10}	L_{11}	L_{12}	L_{13}	L_{14}	L_{15}	L_{16}	L_{17}	L_{18}
mm	2.76	2.8	4	19	15	3	6	20	13	4	10

Table 5.3 Dimensions of fabricated board of inverse class F PA.

The measured and simulated results for PAE and the gain in terms of the input power and frequency are illustrated in Fig. 5.40, and Fig. 5.41, respectively.

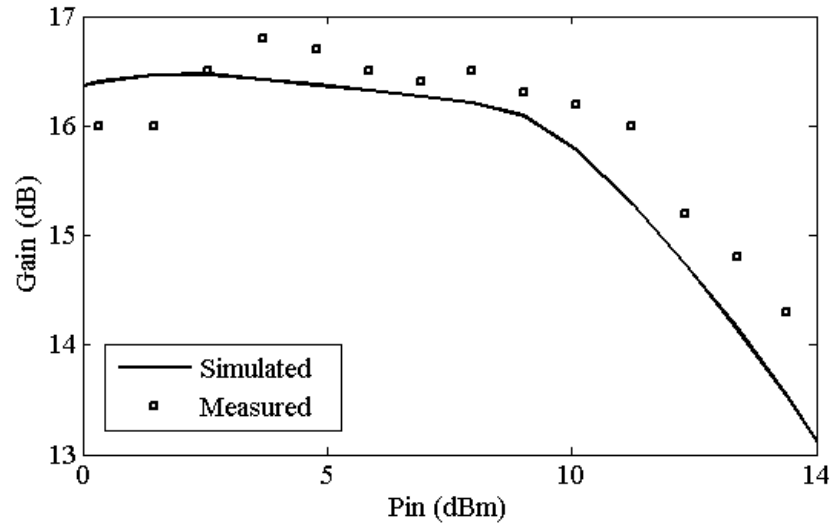


(a)

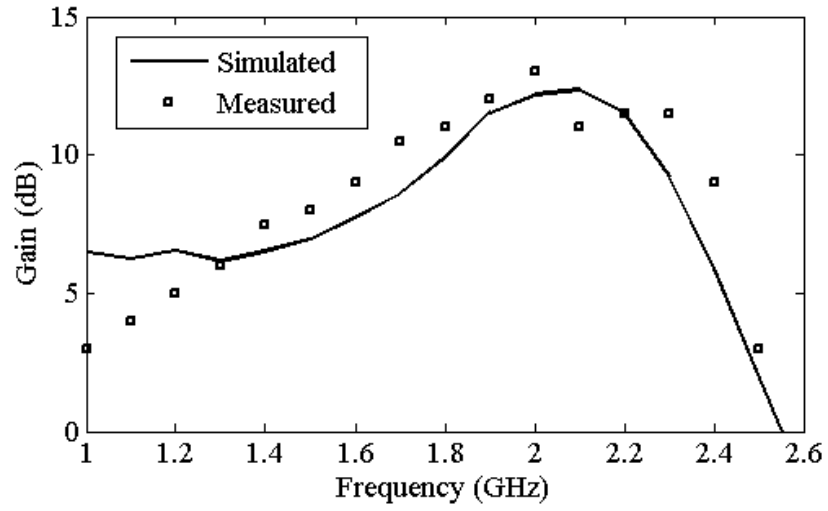


(b)

Fig. 5.40 Measured and simulated PAE for the inverse class F PA in terms of: (a) input power, and (b) frequency.



(a)



(b)

Fig. 5.41 Measured and simulated gain for the inverse class F PA in terms of: (a) input power, and (b) frequency.

With the T-junction and the resistor loss, 60% peak PAE is obtained at 14 dBm input power, showing a 4% drop compared to the non T-junction and the resistor model. The peak gain is ~12 dB obtained with 14 dBm input power at 2.1 GHz. The V_{ds} and I_{ds}

waveforms (see Fig. 5.36 and Fig. 5.37) is shaped and the overlap is minimized because of the effects of load matching network design. The simulated and measured PAE plots are in good agreement, see Fig. 5.41.

5.9 Summary

This chapter investigated the power loss of harmonic matching network. The power dissipation was not only from the internal resistance and non-covered harmonics conditions, but also from the lossy MLs of the harmonic matching network. The MLs of the harmonics matching network were series connected and shunt connected. The series resistance losses of MLs were well reviewed by [187], which was almost linearly increased with increasing length. Also the shunt line was analysed by [188] rigorously. A different model was proposed to analyse the open and short circuit shunt lines with equations derived showing that the S_{21} parameter could be used to measure the power dissipation. The measured results for the short circuit due to the impedance showed that almost all the power was dissipated. Based on the investigation of linear modelling from Chapter 4, the nonlinear model using the transistor ATF 33143 was analysed by the lossless TL and the lossy ML models for UHF applications at around 2 GHz. An even harmonic short circuit load matching network was designed for the class F PA, which had a 6% PAE improvement than the 2nd and 3rd harmonic control models. The harmonic matching network from source termination also improved the performance of PAE for both class F and inverse class F PAs by 5% - 7%. Practical design and measurement were carried out for both class F and inverse class F. ~60% PAE and ~10 dB gain were obtained for both PAs, which were in agreement with ADS simulation results.

Chapter 6 Review and Design of Active Integrated Antenna

6.1 Introduction

In active antennas the radiation element and the active device could be integrated without the need for a matching circuit or connecting cables, which reduces the size and increases the frequency bandwidth. In recent years, the AIA has been rapidly developed using microwave integrated circuit technology and the output or input port of microwave circuit could be free space instead of a traditional $50\ \Omega$ interface. In this case, the AIA can integrate certain circuit functions and also build in signal and wave processing capabilities such as: resonators, filters, mixers, and power amplifiers. A typical AIA contains an active device, such as FET or a Gunn diode, and with the radiation element such as dipoles, microstrip patch antennas, bowties, or aperture coupled microstrip antennas. This chapter introduces the history and modelling of AIA. A circular polarized aperture coupled microstrip antenna is modelled and designed as the load of class F and inverse class F PA. Simulations are carried out using ADS software and practical measurements for the circular polarized antenna and AIA are carried out in the anechoic chamber.

6.2 Literature Review of AIA

The active antenna, which consists of a small antenna and an electron tube, was first proposed for the application of radio broadcast receivers at around 1 MHz frequency band [211]. Due to the invention of high frequency transistors, much more attention was

attracted in 1960s and 1970s and some pioneering works were reported in [212-218]. The advantages of implementing the active devices using passive radiating elements helped to improve the performance; such as increasing the efficiency and bandwidth, reducing the size and mutual coupling between the array elements and also improving the noise factors [219]. In the 1980s and 1990s, the AIA was developed by a quasi optical technique [2, 7] which was used to combine the output power from arrays of solid state devices to overcome the combiner loss limitations for millimetre wave frequency use [5, 6]. The innovative designs like practical implementation of microwave and millimetre wave have been developed because it could provide effective solutions for TL power dissipation, limited source power, low antenna efficiency and also low performance phase shifters [1]. Recently, we have seen research in the areas of power combining, beam steering and switching, retro-directive arrays, and high efficiency PA designs. Research of AIA has recently been focussed on integrated antenna oscillators, coupled oscillators and phase control, high efficiency RF front ends, retro-directive arrays and AIA systems. This chapter will focus on the RF front end technologies.

Radisic has proposed three novel methods for AIA designs. A 55% PAE was obtained by using a class B PA working at 2.48 GHz and integrated with a patch antenna with the probe feed method to suppress the second harmonic [220]. The second design used a class F PA integrated with a circular sector patch antenna to obtain a PAE of 63%, which is based on the roots of Bessel function to optimise the power loss for the second and third harmonics [221]. The third method aimed to obtain a broadband response, which used a wide bandwidth slot antenna yielding a peak PAE of 61% and 8% bandwidth over 50% PAE [222]. Also in [223, 224] AIAs were designed using a breakdown voltage active device and circular sector patch antennas. Such AIA designs were used as an output

matching network to obtain the optimum efficiency at the operating frequency. Kim [225] proposed a direct integration method, which obtained a PAE of 67.5% by combining a class F PA with an antenna that provided an optimum impedance at the fundamental frequency, a short circuit at the second harmonic and an open circuit at the third harmonic. A similar method was used by [226] to produce a two layer planar inverted F antenna and the PAE obtained at 1.05 GHz, 1.55 GHz, and 1.8 GHz were 58%, 52%, and 50%, respectively. By using a class E PA, Weiss [227] eliminated the output matching network by using a slot antenna as the harmonic load of PA to achieve 62% of PAE. All these three designs were investigated based on the lossless switch model of an active device. Colantonio [205, 228,229] investigated the effects of an active device and obtained the optimum load impedance of the fundamental frequency, second and third harmonics. By using an output matching network to transform the second and third harmonics of the patch a maximum PAE of 60% at 5 GHz was achieved.

6.3 Design of AIA

6.3.1 Introduction

The AIA [86, 230-236] is used as the front-end of a transmitter, which normally consists of a PA unit and an antenna unit. High efficiency PA includes the input matching block, active device, harmonic load matching, and fundamental frequency matching blocks that saves power and increase the life of battery. The load of PA can be replaced by antennas. Also space is saved by eliminating the load harmonic matching network of the PA using an antenna that also behaves as the impedance matching function. The basic block diagram of an AIA is shown in Fig. 6.1:

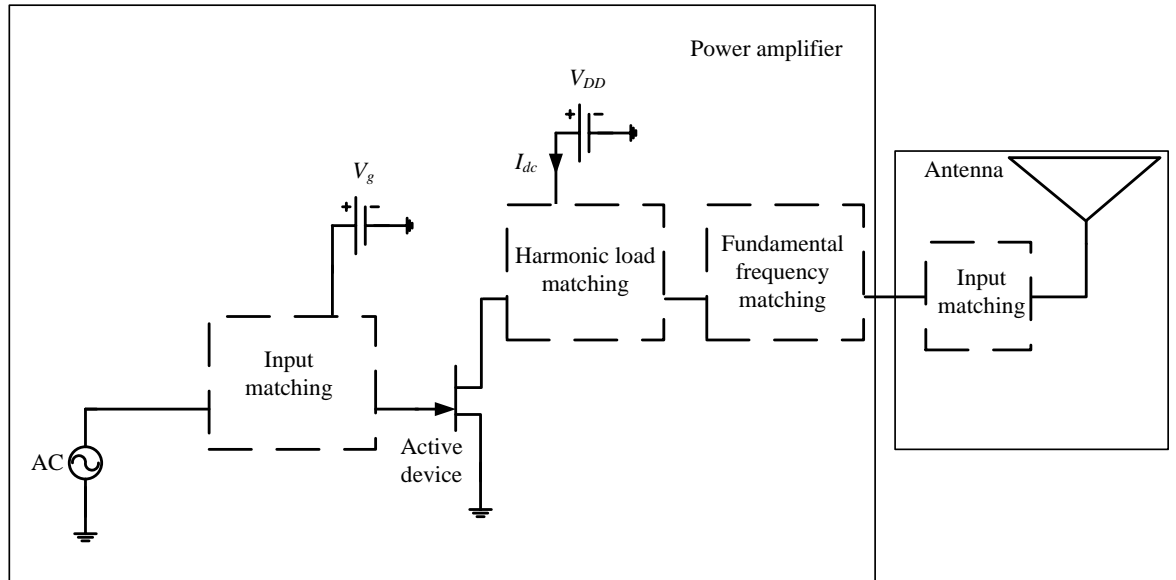


Fig. 6.1 Block diagram of AIA.

In the following section, the design of a broad band circular polarized ACMA is discussed that was outlined in chapter 5.

6.3.2 Design of a Circular Polarized ACMA for AIA Design

The structure and dimension of a broad band circular polarized ACMA is depicted in Fig. 6.2.

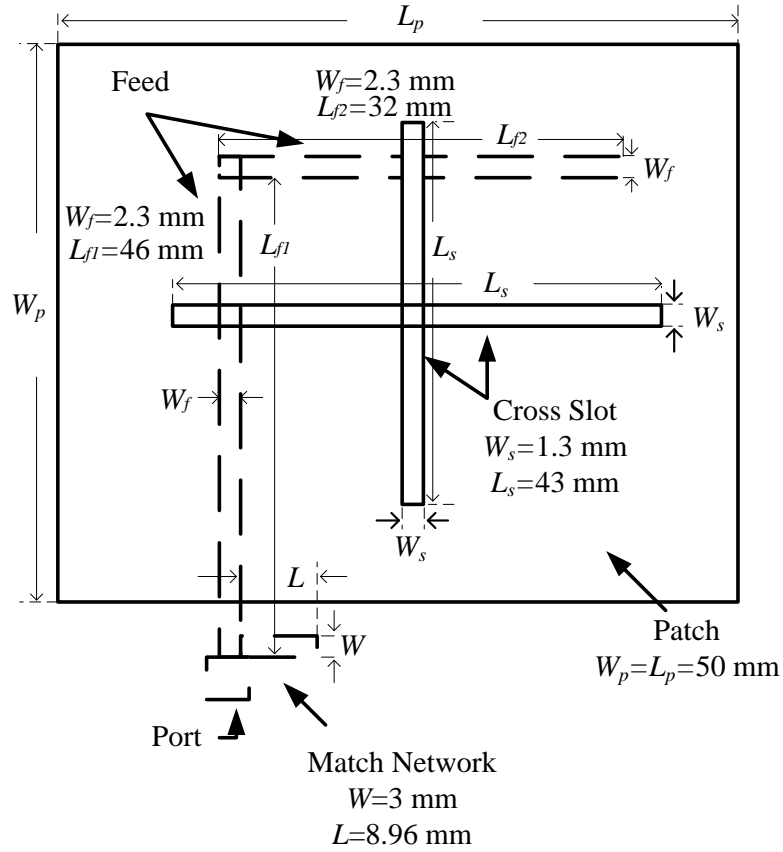


Fig. 6.2 Schematic of broad band circular polarized ACMA.

To obtain circular polarization, two modes are excited in the square patch by the cross slot in the ground plane, which is fed by a single TL with a 90 degree phase shift. A wide bandwidth of return loss is obtained by supporting the square patch by non metallic screws such that the substrate below the patch is air which has low relative permittivity. Following the design procedure outlined in Chapter 3, the resonant frequency of the patch is slightly higher than the working frequency (2 GHz) so the ‘flat’ imaginary impedance could be obtained. The resonant frequency of the slot is still higher than the working frequency to obtain an almost pure inductance of the impedance to eliminate the capacitance response produced by the patch. The equivalent circuit of this antenna is shown in Fig. 6.3.

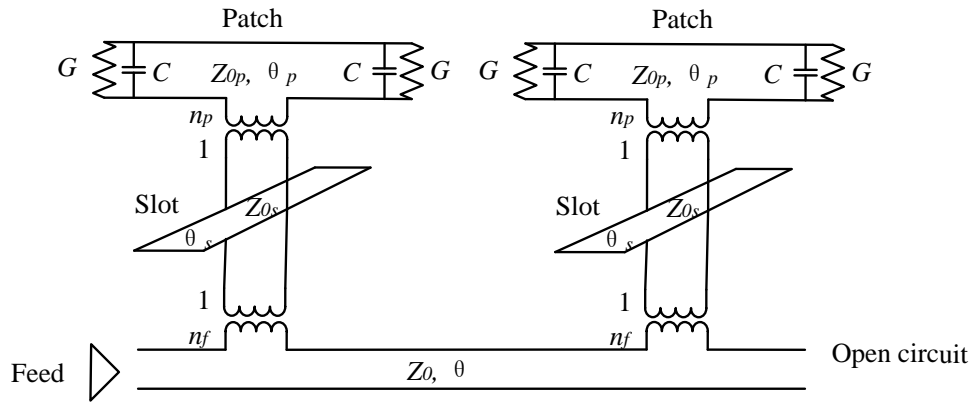


Fig. 6.3 Equivalent circuit of broad band circular polarized ACMA.

Since the two equivalent antennas are connected in series, the open circuit could be used to eliminate the imaginary part of the impedance and the whole antenna would behave as a 50Ω load. Hence, a matching network is required between the antenna and feed in order to obtain the optimum impedance matching. The fabricated boards are shown in Fig. 6.4:

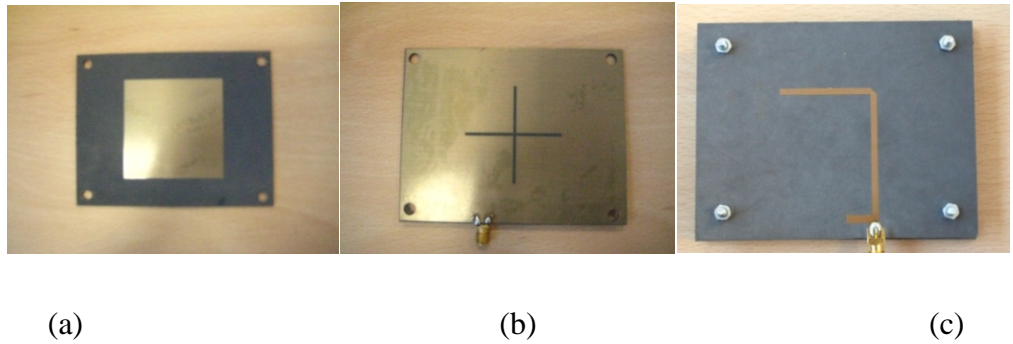


Fig. 6.4 Practical fabricated boards of the broadband circular polarized ACMA: (a) radiation element, (b) slot, and (c) feed and matching stub.

Using the substrate Duroid 5870 with an 8 mm gap between patch and slot, the simulation and measured results using Agilent Network Analyser N5230A (see Fig. 6.5) are shown in Fig. 6.6:

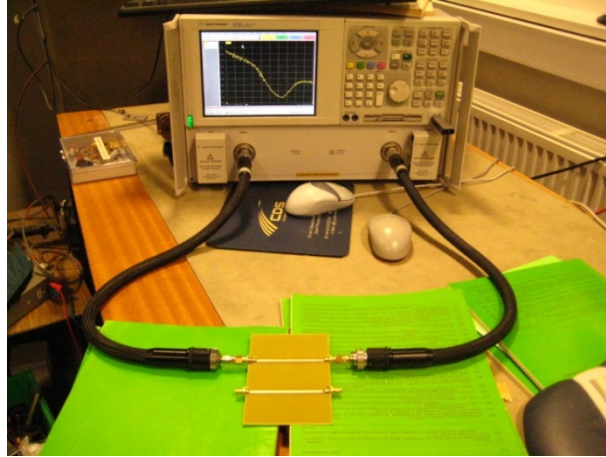


Fig. 6.5 Agilent Network Analyser N5230A.

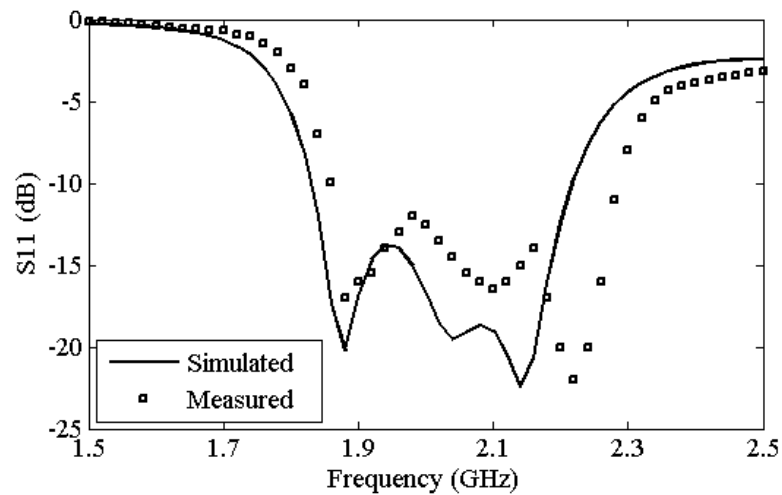


Fig. 6.6 Simulated and measured results for S_{11} .

The bandwidth of S_{11} under -10 dB level is about 350 MHz (1.85 GHz – 2.2 GHz). The simulated results are agreed with measured results.

In order to measure the passive antenna output power and also of AIA, based on the Friis transmission equation (6.1), a conical log spiral antenna (model 3102 from ESCO technologies), see Fig. 6.7 is chosen as the reference antenna with working frequency range of 1 to 10 GHz and a 3-dB gain at 2 GHz.

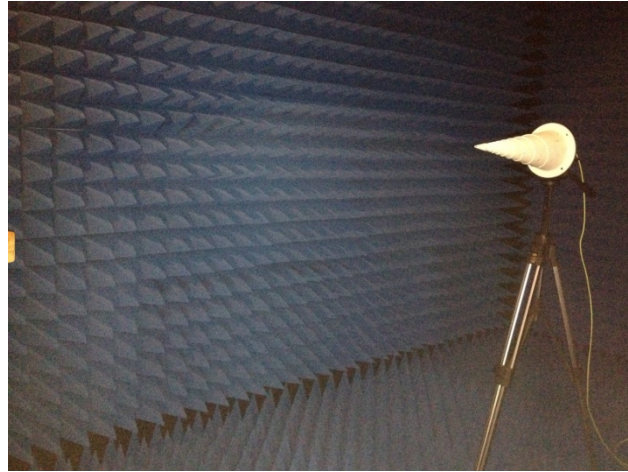


Fig. 6.7 Conical log spiral antenna model 3102.

$$\frac{P_r}{P_t} = G_t G_r \left(\frac{\lambda}{4\pi R} \right)^2 \quad (6.1)$$

This antenna is left hand circular polarized, which is 38.1 cm long with a diameter of 12.7 cm. Signal generator and power meter are setup to generate RF signal and receive power outside the anechoic chamber separately. The range length r is designed to meet the Far-Field criterion $r > \frac{2D^2}{\lambda}$, in which D is the largest dimension of the source. Axial ratio is the ratio of the major axis to the minor axis of the polarization ellipse which is defined as

$$\frac{\text{Major axis } (E_{\max})}{\text{Minor axis } (E_{\min})}.$$



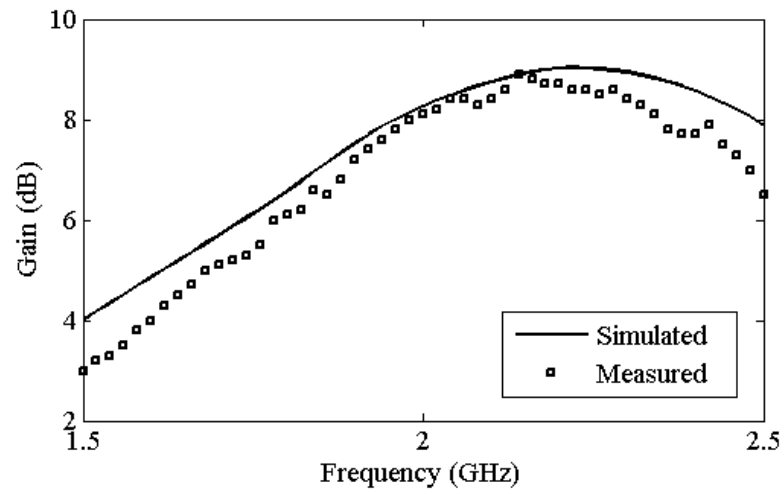
(a)



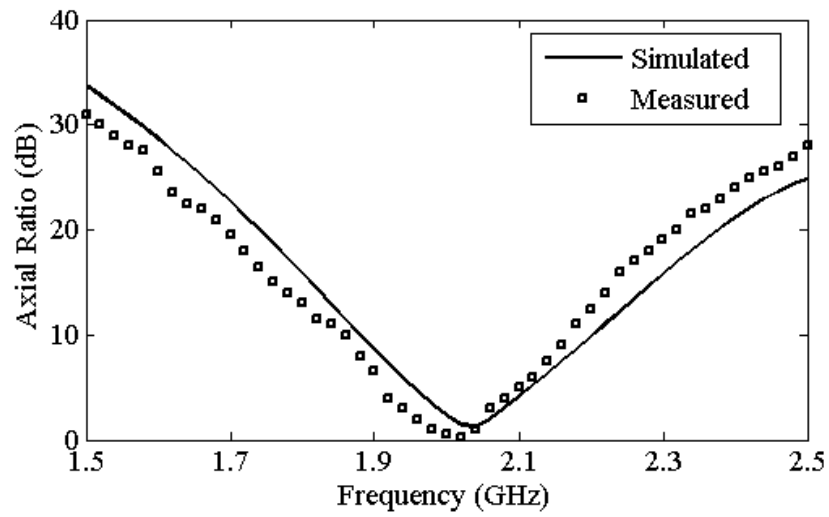
(b)

Fig. 6.8 Equipments setup for antenna testing (a) antennas under test in anechoic chamber (b) signal generator and power meter.

Good agreements have been obtained between simulation and measurement results. The accepted gain and the axial ratio (AR) results are also shown in Fig. 6.9 within ~ 1 dB difference at all frequencies.



(a)



(b)

Fig. 6.9 Simulated and measured results for: (a) gain, and (b) AR.

The maximum gain at 2.2 GHz is 9 dB and the gain in the frequency range from 1.95 GHz to 2.5 GHz is 8 dB. At the design frequency of 2 GHz the AR is close to 0 dB and the bandwidth below the 3 dB axial ratio is ~100 MHz.

6.3.3 Simulation and Practical Design of AIA using Class F PA

The circuit model of AIA is given in Fig. 6.10 where the high efficiency class F and inverse F PA is investigated in Chapter 5. The load of class F PA is replaced by the circular polarized antenna designed in section 6.3.1, which is an AIA. The S parameter data file of the circular polarized antenna is created by CST software and is used in ADS software for simulation.

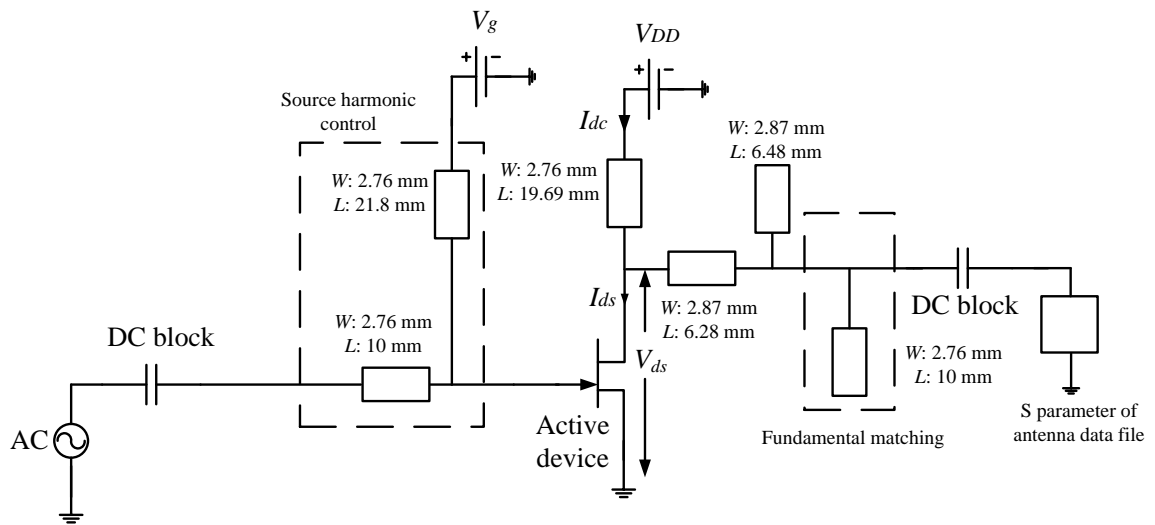


Fig. 6.10 Schematic of AIA by using class F PA.

By replacing the load block by an antenna, the circuit is slightly tuned to make a better match. The bias voltage is -0.9 V and the DC power supply is 2 V. V_{ds} and I_{ds} (see Fig. 6.10) waveforms are shown in Fig. 6.11, illustrating a small amount of overlap between voltage and current.

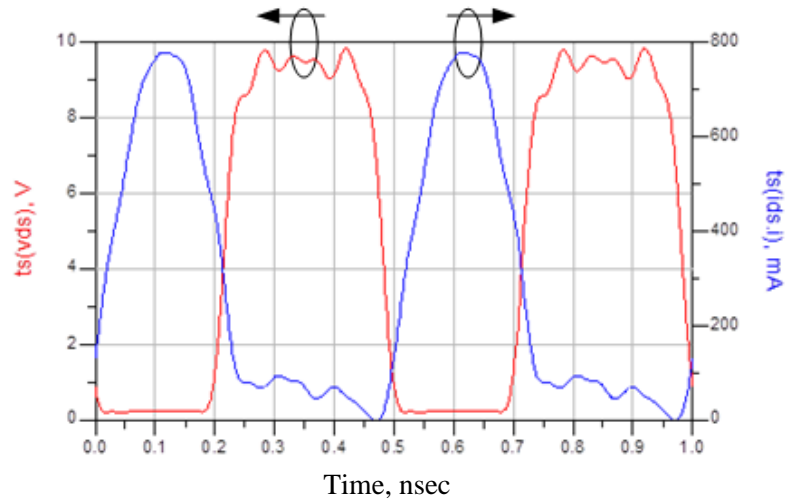


Fig. 6.11 V_{ds} and I_{ds} waveforms for Fig. 6.10.

The optimum input impedances from the load and source simulated by ADS software are given in table 6.1.

Z_{S2}	$1.889+j2.963$
Z_{S3}	$18.398-j25.719$
Z_{L1}	$15.262+j4.244$
Z_{L2}	$1.763+j0.76$
Z_{L3}	$541.413-j37.506$

Table 6.1 Load and source impedances (Unit: Ω).

The printed circuits for the class F PA connected to the slot antenna by SMA connector are shown in Fig. 6.12. The comparison of the simulated and measured results of the PAE and the gain of AIA amplifier module are illustrated in Fig. 6.13.

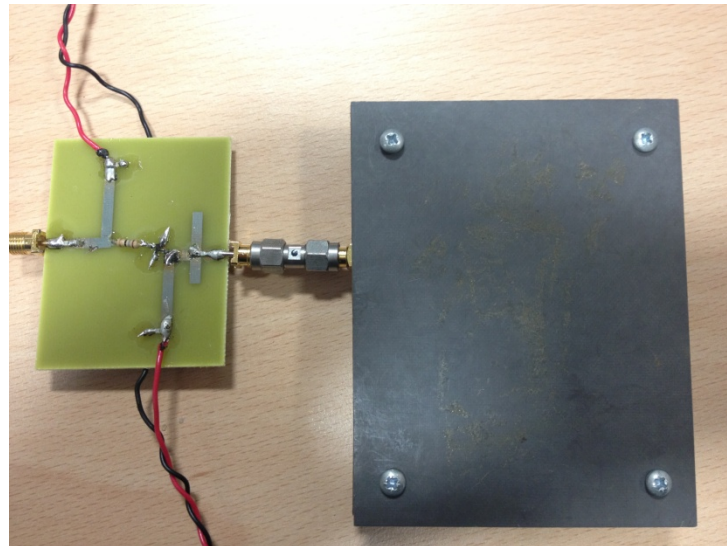
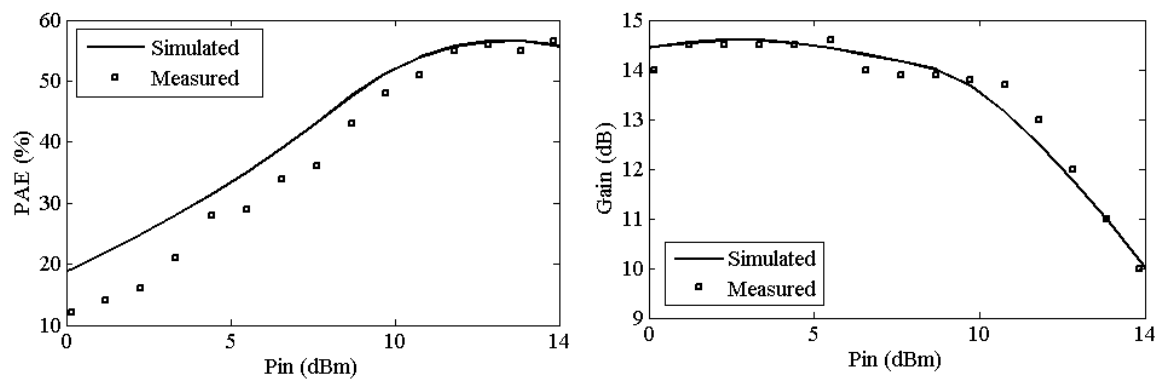


Fig. 6.12 Printed circuits for AIA.



(a)

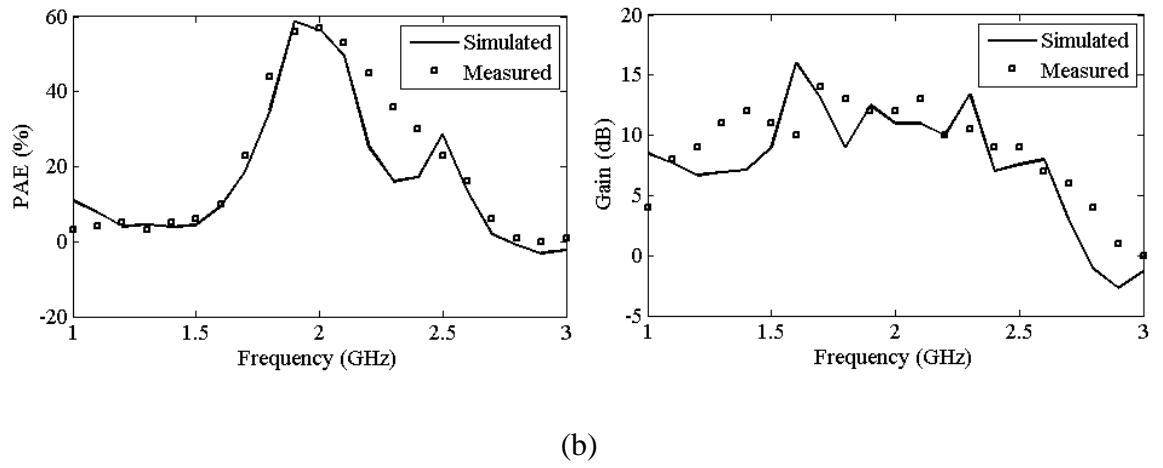


Fig. 6.13 Simulation and measured results for PAE and the gain in terms of: (a) the input power, and (b) the frequency.

Due to the losses associated with connectors, and cables, as well as measured errors, the measured peak PAE and the peak gain are ~56% and 12.5 dBm, respectively at the input power of 13 dB. For PAE of 50% the bandwidth is ~ 400 MHz and for the gain of 10 dB the frequency band is from 1.1 GHz to 2.5 GHz.

6.3.4 Simulation and Practical Design of AIA using Inverse Class F PA

The schematic circuit diagram of an AIA using the inverse class F PA is shown in Fig. 6.14.

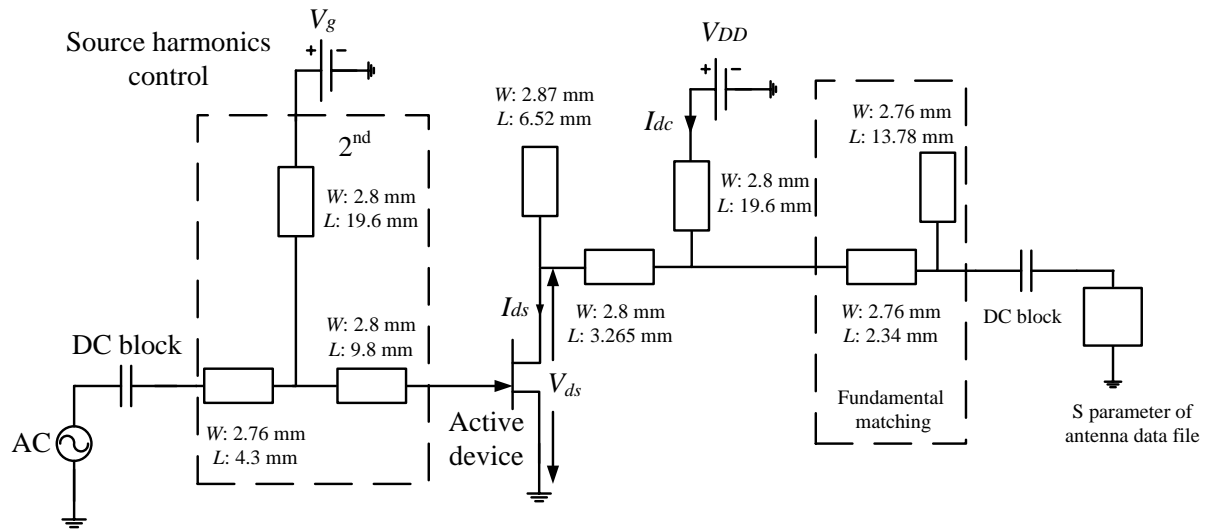


Fig. 6.14 Schematic circuit diagram of AIA using the inverse class F PA.

The load of inverse class F PA was replaced by the S parameter data file for simulation. V_{ds} and I_{ds} waveforms are given in Fig. 6.15:

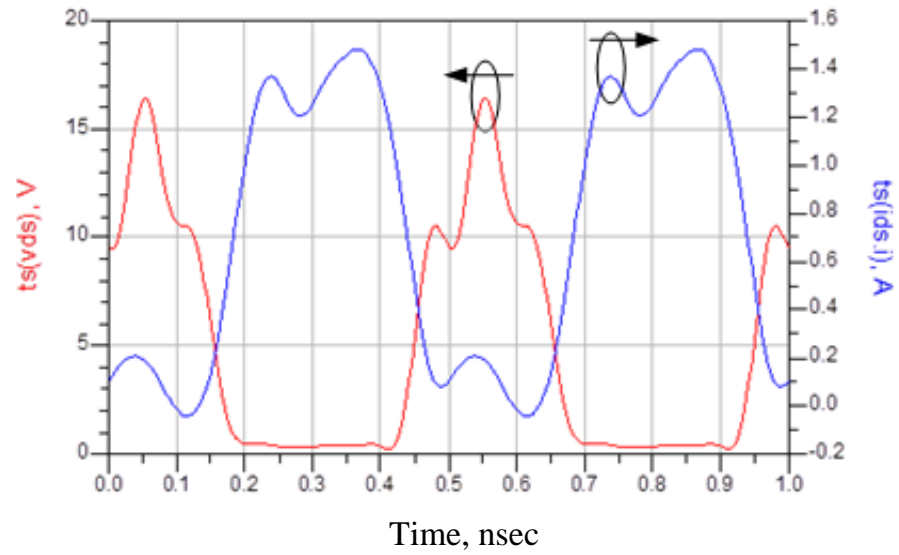


Fig. 6.15 V_{ds} and I_{ds} waveforms for Fig. 6.14.

The optimum input impedances from the load and source simulated by ADS software are given in table 6.2.

Z_{S2}	404.159-j429.469
Z_{S3}	16.847-j3.566
Z_{L1}	8.975+j1.491
Z_{L2}	220.446-j49.942
Z_{L3}	0.96+j0.519

Table 6.2 Load and source impedances (Unit: Ω).

These results are close to the predicted impedance condition for the inverse class F PA as given in Chapter 4. By using the circular polarized antenna as the load of PA, the printed circuits, simulated and measured results of PA section are depicted in Figs. 6.16 and 6.17.

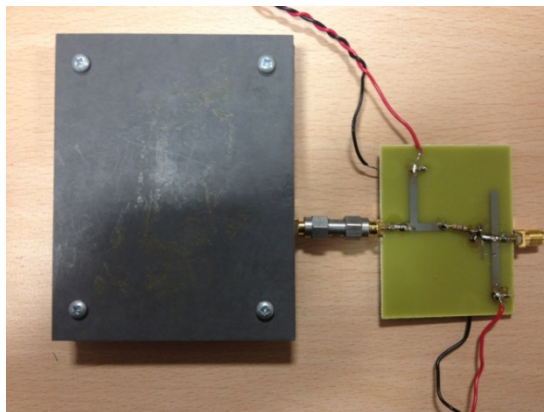


Fig. 6.16 Printed circuit for AIA.

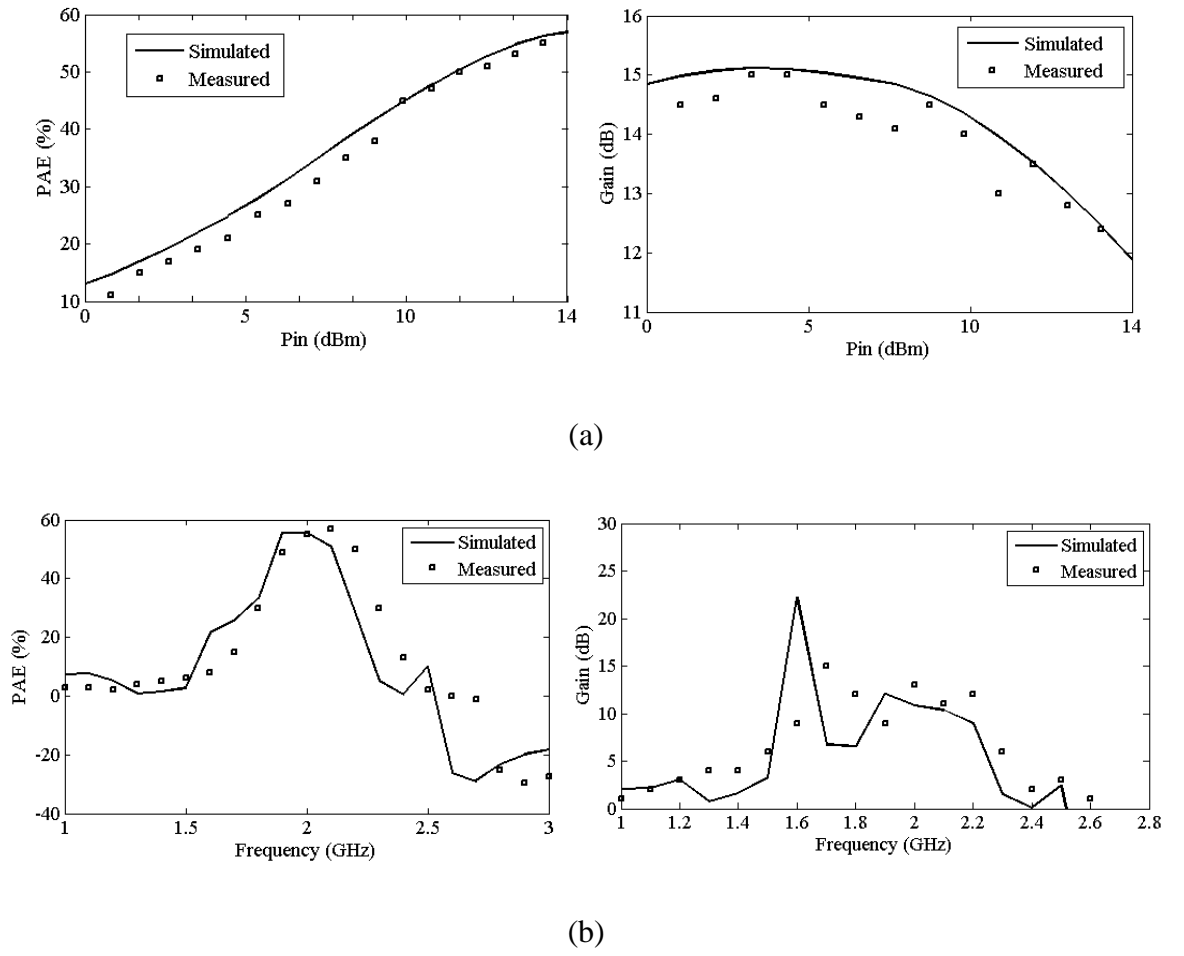


Fig. 6.17 Simulation and measured PAE and gain plots in terms of: (a) the input power, and (b) the frequency.

The peak PAE and the peak gain are 57% and ~12 dB, respectively at the input power of 14 dBm. The frequency band of over 50% PAE is about 300 MHz and over 10 dB gain obtained from 1.6 GHz to 2.3 GHz.

6.4 Summary

This chapter introduced the concept and design of AIA using the microwave integrated circuit technology. The traditional output and input interface were replaced by radiating elements. In addition a number of devices such as resonators, filters, mixers, power amplifiers etc were integrated. A broadband circular polarized aperture coupled microstrip antenna as a front end of AIA and both class F and inverse class F PAs based on the designs given in Chapter 5 were fabricated and tested. For the passive antenna 350 MHz of bandwidth for S_{11} and ~100 MHz for AR were measured. The simulation data for the antenna was used as the optimum load of PAs. About 58 % PAE was achieved for both AIA for different input power values of 13 dBm and 14 dBm for the class F and inverse F designs, respectively. For both designs, the measured gains were in the range of 10 – 12 dB.

Chapter 7 Conclusions and Future Work

7.1 Conclusions

To obtain optimum performance of an AIA, it is essential to fully analyse PA and antenna parts. This thesis investigated an ACMA based on the circuit and TLMs. Research was focused on the turn ratios analysis between feed/slot, and slot/patch. A design procedure was proposed for the ACMA design. Based on these results, a broadband dual frequency ACMA was designed. In order to obtain the optimum performance and minimize the power dissipation of PAs, different types of PAs were reviewed. Switch model class F and inverse class F PAs were analysed using both the linear and non-linear models. Finally, AIAs were designed using the proposed class F and inverse class F PAs by integrating it with a broadband circular polarized ACMA.

In Chapter 1, an introduction and basic review of traditional front-end transmitter and receiver of wireless communication systems were presented and also the limitations were outlined. An AIA was introduced with the advantages of low cost, smaller size, high efficiency, more compact, and easy to integrate with circuit functions as filters, mixer, power amplifier, etc. The motivations, objectives, and contributions of research were proposed.

Chapter 2 reviewed the theories of TLs in terms of primary and secondary parameters. The characteristics of MLs of characteristic impedance, effective relative permittivity, and also the loss factors were analysed in terms of physical structure. The S parameters were reviewed and equations of S_{21} and S_{11} were derived based on unequal source and load impedance. The characteristics of microstrip patch antennas were proposed by different

patch shapes and feed methods. The ACMA was selected to be further analysed due to its independent structure of feed and radiation elements, which was easy to integrate with circuit and array designs for satellite communication application.

Chapter 3 presented the TLM and the design procedure of an ACMA. The radiation element was represented by an array of two radiating slots separated by a TL. The amount of radiation was modelled as a fringing field, which varied in terms of the width of patch, height and effective dielectric constant of substrate. The characteristic impedance and the wavelength of the slot line were reviewed based on Cohn's analysis. In, this work a simplified and novel method was introduced in order to obtain the turns ratio using S parameters, which is based on numerical calculations and simulations. Practical measurement was carried out to verify the predicted results, which showed good agreement. Investigation was also carried out by tuning n_p in the circuit model to agree with the full wave EM simulation results in terms of the slot lengths and the height of substrate. The results for n_p agreed well with data published by Jaisson. Finally, a broadband dual frequency dual polarized ACMA was designed with 250 MHz bandwidth, 6.6 dB gain at 1.9 GHz, and 200 MHz bandwidth, 7.2 dB gain at 2.4 GHz.

Chapter 4 introduced a brief review of PAs by classifying them as classical and high efficiency devices. The design equations for Class F and inverse class F PAs were presented for determining the output power, power convert efficiency, and also the optimum load impedance. The effects of internal resistance of the transistor were investigated for the efficiency and the optimum load impedance for both class F and inverse class F PAs. To minimize the voltage and current overlap, harmonic load matching networks were designed using the lumped element and TLMs. The performance of the

linear model of class F and inverse class F PAs were compared in terms of the internal resistance and load harmonics with the inverse class F PA.

Chapter 5 investigated the power loss of the shunt element of ML, which indicated at 90 and 180 degrees of open and short circuit ML, nearly all the power dissipated were due to the short circuit effects. The non linear model of the active device of class F and inverse class F PAs were modelled, and a novel harmonic load matching network for all the even harmonics short circuit for class F PA was used to compare with the inverse class F PA. Similar performance was obtained for the peak PAE and gain which were around 58% and 10 dB.

Chapter 6 presented AIAs design based on the class F and inverse class F PAs investigated in Chapter 5. A broadband circular polarized ACMA design was proposed as the radiating element of the load of PAs. 350 MHz S_{11} , 100 MHz AR, and 8.5 dB gain were obtained at 2 GHz centre frequency. The performances for both AIAs were similar which were about 58% PAE and 12 dB gain.

7.2 Future Work

The future works of research focus on two parts. First, further improve the gain, efficiency and bandwidth of AIA by eliminating the load matching network of active device. An ACMA can be used as the optimum harmonic load of active device with the function of minimise the power loss of AIA and also enhance the efficiency of radiation. The second suggestion would be further simplification of the circuit model and optimization process of the ACMA using computer aided methods as GA.

7.2.1 Investigation of an AIA without Harmonic Load Matching Networks

The schematic of the proposed design is given in Fig. 7.1.

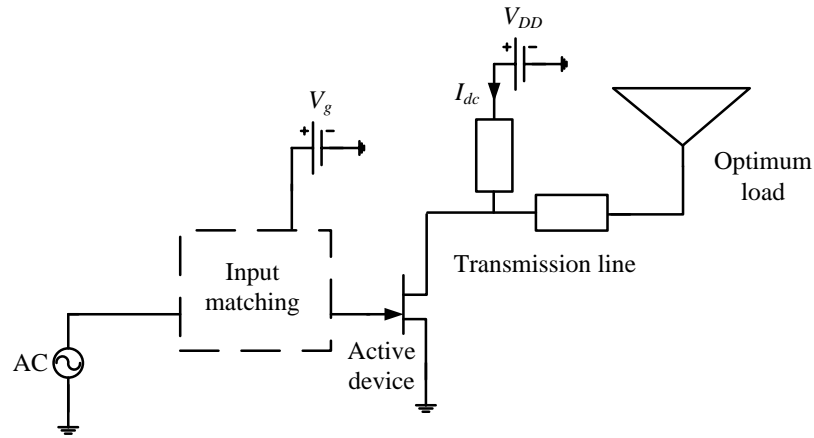


Fig. 7.1 Schematic of an AIA without harmonic load matching network.

For the microwave, millimetre wave and also photonic applications, the reduction in size of the transmitter or receiver could reduce the power dissipation and also save space for other functional devices [237, 238]. For the class F and inverse class F PAs, the antenna could be directly connected to the power source. However, the antenna has to be designed to include the function of harmonic load matching networks to control the second and third harmonics of the load. To increase the gain of AIA, circular polarized antenna arrays [239-244] can be used for satellite applications. For further reduction in power dissipation, the substrate usage could be more stable, low loss factors such as Duroid 5870, and Duroid 6010, which along with higher cost than PCB FR4.

7.2.2 Optimisation of ACMA using GA

GA is adaptive heuristic search algorithms, which are based on the evolutionary ideas of natural selection and genetics. The pioneer of GA was John Holland in the 1960's [245] and since then it has been widely used to optimise designs in a variety of engineering fields [246-253]. In further research GA will initially be used to optimise the design of a linear polarised and a circular polarised aperture coupled antenna. Then GA will be used in the design of the load harmonic networks for the high efficiency switch model PAs. Finally in the AIA design the load harmonic networks will be eliminated and GA will be used to optimise AIA to obtain the maximum efficiency. The implementation of the GA flow chart diagram is shown in Fig. 7.2 [245].

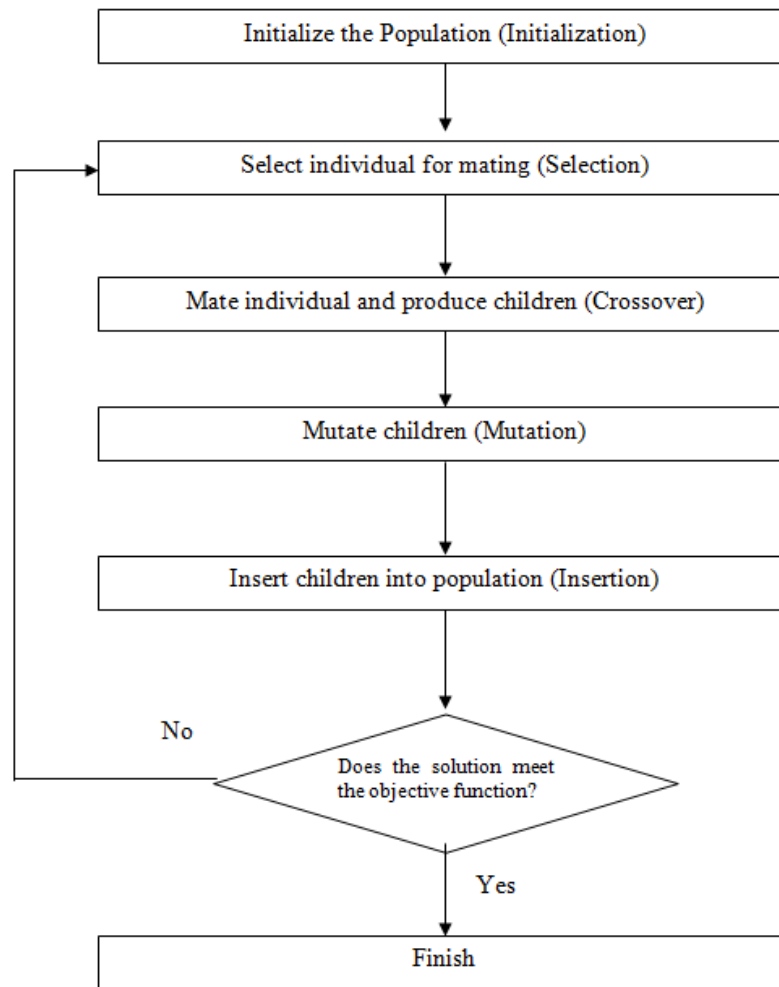


Fig. 7.2 GA implementation flow chart diagram.

The implementation procedure of the GA is defined as:

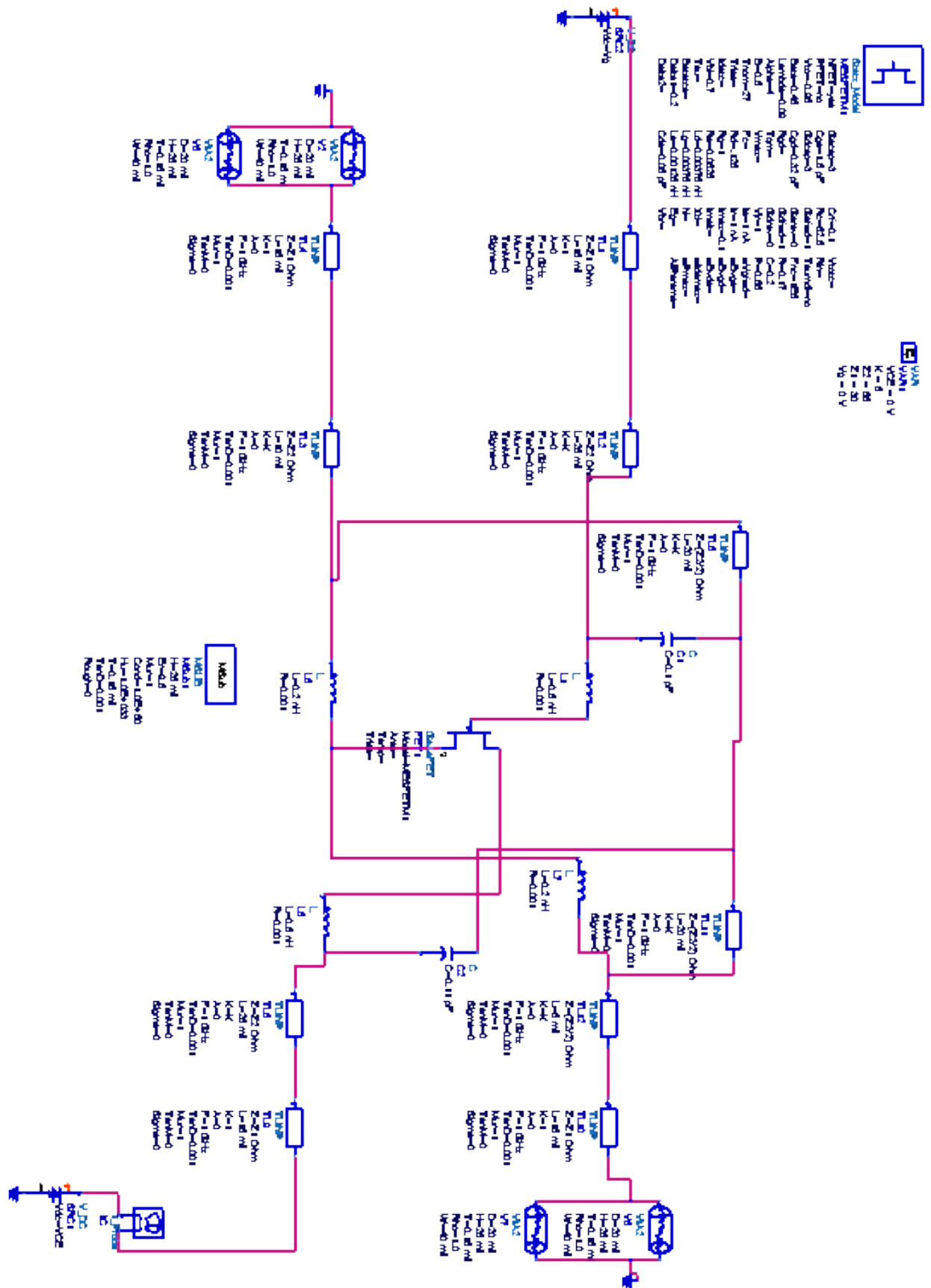
1. Define the representation (encoding-decoding),
2. Define “fitness” function F (incorporate constraints and objectives),
3. Define the genetic operators (initialization, selection, crossover, mutation, insertion),
4. Execute initial algorithm run (monitor average population fitness and identify best individual),

5. The random element of the GA is further enhanced by using a crossover process where a number of bits or genes of selected pairs of chromosomes are exchanged.

The iteration of the above process is run until a convergence is obtained to produce an optimum solution. The results obtained in the previous section will be used to ensure that the antenna has the required impedance at the design and harmonic frequencies. This will allow the antenna to be directly connected to the amplifier to realize the AIA having maximum efficiency.

In all of the above investigations selected antennas will be practically realized and tested to support the theoretical designs that have been used.

Appendix



Reference

- [1] K. Chang, R. A. York, P. S. Hall, and T. Itoh, "Active integrated antennas," *IEEE Transactions on Microwave Theory and Techniques*, vol. 50, pp. 937-944, Mar 2002.
- [2] J. S. Lin and T. Itoh, "Active Integrated Antennas," *IEEE Transactions on Microwave Theory and Techniques*, vol. 42, pp. 2186-2194, Dec 1994.
- [3] Y. X. Qian and T. Itoh, "Progress in active integrated antennas and their applications," *IEEE Transactions on Microwave Theory and Techniques*, vol. 46, pp. 1891-1900, Nov 1998.
- [4] R. A. Flynt, L. Fan, J. A. Navarro, and K. Chang, "Low cost and compact active integrated antenna transceiver for system applications," *IEEE Transactions on Microwave Theory and Techniques*, vol. 44, pp. 1642-1649, Oct 1996.
- [5] L. Wandinger and V. Nalbandian, "Millimeter-Wave Power Combiner Using Quasi-Optical Techniques," *IEEE Transactions on Microwave Theory and Techniques*, vol. 31, pp. 189-193, 1983.
- [6] J. W. Mink, "Quasi-Optical Power Combining of Solid-State Millimeter-Wave Sources," *IEEE Transactions on Microwave Theory and Techniques*, vol. 34, pp. 273-279, Feb 1986.
- [7] R. A. York and Z. B. Popović, *Active and quasi-optical arrays for solid-state power combining*: Wiley, 1997.
- [8] P. L. Sullivan and D. H. Schaubert, "Analysis of an Aperture Coupled Microstrip Antenna," *IEEE Transactions on Antennas and Propagation*, vol. 34, pp. 977-984, Aug 1986.
- [9] C. A. Balanis, *Antenna theory : analysis and design*, 3rd ed. Hoboken, N.J. ; Great Britain: Wiley-Interscience, 2005.
- [10] X. Ding and A. F. Jacob, "CPW-fed slot antenna with wide radiating apertures," *IEE Proceedings-Microwaves Antennas and Propagation*, vol. 145, pp. 104-108, Feb 1998.
- [11] T. Fujimoto, K. Tanaka, and M. Taguchi, "Analysis of elliptical microstrip antennas with and without a circular slot," *IEICE Transactions on Communications*, vol. E83b, pp. 386-393, Feb 2000.
- [12] S. H. Nam, K. M. Nam, C. U. Kim, and J. P. Kim, "Aperture-coupled cavity-fed back-to-back microstrip directional coupler," *Microwave and Optical Technology Letters*, vol. 50, pp. 551-555, Mar 2008.
- [13] D. M. Pozar, *Microwave and RF wireless systems*. New York: John Wiley, 2001.
- [14] D. M. Pozar, *Microwave engineering*, 3rd ed. Hoboken, NJ: J. Wiley, 2005.

- [15] D. M. Pozar, "Analysis of an Infinite Phased-Array of Aperture Coupled Microstrip Patches," *IEEE Transactions on Antennas and Propagation*, vol. 37, pp. 418-425, Apr 1989.
- [16] C. Wu, J. Wang, R. Fralich, and J. Litva, "Analysis of a Series-Fed Aperture-Coupled Patch Array Antenna," *Microwave and Optical Technology Letters*, vol. 4, pp. 110-113, Feb 1991.
- [17] M. G. Keller, D. Roscoe, Y. M. M. Antar, and A. Ittipiboon, "Active Millimeter-Wave Aperture-Coupled Microstrip Patch Antenna-Array," *Electronics Letters*, vol. 31, pp. 2-4, Jan 5 1995.
- [18] S. Kanamaluru, M. Y. Li, and K. Chang, "Analysis and design of aperture-coupled microstrip patch antennas and arrays fed by dielectric image line," *IEEE Transactions on Antennas and Propagation*, vol. 44, pp. 964-974, Jul 1996.
- [19] S. D. Targonski, R. B. Waterhouse, and D. M. Pozar, "Wideband aperture coupled microstrip patch array with backlobe reduction," *Electronics Letters*, vol. 33, pp. 2005-2006, Nov 20 1997.
- [20] F. Y. Kuo and H. T. Hsu, "Aperture-Coupled Patch Array Antenna for Microwave Band RFID Handheld Reader Applications," *2010 IEEE Antennas and Propagation Society International Symposium*, 2010.
- [21] M. M. Honari, A. Abdipour, and G. Moradi, "Aperture-coupled multi-layer broadband ring-patch antenna array," *IEICE Electronics Express*, vol. 9, pp. 250-255, Feb 25 2012.
- [22] C. Hua, X. Wu, and W. Wu, "A Cavity-Backed Aperture-Coupled Microstrip Patch Antenna Array with Sum/Difference Beams," *Journal of Electromagnetic Waves and Applications*, vol. 26, pp. 932-941, 2012.
- [23] M. D. Vose. (1998). *The simple genetic algorithm foundations and theory*. Available: <http://cognet.mit.edu/library/books/view?isbn=026222058X>
- [24] S. J. Najafabadi and K. Forooghi, "Genetic optimization of an aperture-coupled microstrip patch antenna," *2004 3rd International Conference on Computational Electromagnetics and Its Applications, Proceedings*, pp. 141-144581, 2004.
- [25] J. Namkung, E. L. Hines, R. J. Green, and M. S. Leeson, "Probe-fed microstrip antenna feed point optimization using a genetic algorithm and the method of moments," *Microwave and Optical Technology Letters*, vol. 49, pp. 325-329, Feb 2007.
- [26] O. Watanabe and T. Zeugmann. (2009). *Stochastic algorithms foundations and applications : 5th International Symposium, SAGA 2009, Sapporo, Japan, October 26-28, 2009, proceedings*. Available: <http://dx.doi.org/10.1007/978-3-642-04944-6>
- [27] S. Asmussen and P. W. Glynn, *Stochastic simulation : algorithms and analysis*. New York: Springer, 2007.
- [28] T. S. Fong and Birgenhe.Ra, "Method of Conjugate Gradients for Antenna Pattern Synthesis," *Radio Science*, vol. 6, pp. 1123-&, 1971.

- [29] J. K. Reid, "Use of Conjugate Gradients for Systems of Linear Equations Possessing Property," *Siam Journal on Numerical Analysis*, vol. 9, pp. 325-&, 1972.
- [30] P. Colantonio, F. Giannini, R. Giofre, and L. Piazzon, "Doherty Power Amplifier and GaN technology," *18th International Conference on Microwaves, Radar and Wireless Communications (Mikon-2010), Vol 1 and Vol 2*, 2010.
- [31] King, *Transmission-Line Theory*.
- [32] C. Caloz and T. Itoh, *Electromagnetic metamaterials transmission line theory and microwave applications : the engineering approach*. Hoboken, N.J.: John Wiley & Sons, 2006.
- [33] G. Golo, V. Talasila, and A. J. van der Schaft, "Approximation of the Telegrapher's equations," *Proceedings of the 41st IEEE Conference on Decision and Control, Vols 1-4*, pp. 4587-4592, 2002.
- [34] N. Weck, "Theory of Maxwell Equations," *Zeitschrift Fur Angewandte Mathematik Und Mechanik*, vol. 52, pp. T195-&, 1972.
- [35] M. S. Zhdanov, "Maxwell's Equations and Numerical Electromagnetic Modeling in the Context of the Theory of Differential Forms," *Active Geophysical Monitoring*, vol. 40, pp. 299-324, 2010.
- [36] A. G. Benedict, "Transmission-Line Model," *IEEE Spectrum*, vol. 7, pp. 6-&, 1970.
- [37] B. C. Wadell, *Transmission line design handbook*. Boston, Mass. ; Norwood, MA ; London: Artech House, 1991.
- [38] C. Christopoulos, *The transmission-line modeling method TLM*. New York, Oxford: Institute of Electrical and Electronics Engineers ;Oxford University Press, 1995.
- [39] S. F. Adam, *Microwave theory and applications*. Englewood Cliffs ; Hemel Hempstead: Prentice-Hall, 1969.
- [40] A. J. Baden Fuller, *Microwaves : an introduction to microwave theory and techniques*, 3rd ed. Oxford: Pergamon, 1990.
- [41] D. M. Pozar, *Microwave engineering*, 2nd ed. New York: Wiley, 1997.
- [42] E. J. Denlinger, "Losses of Microstrip Lines," *IEEE Transactions on Microwave Theory and Techniques*, vol. 28, pp. 513-522, 1980.
- [43] R. A. Rucel, D. J. Masse, and C. P. Hartwig, "Losses in Microstrip," *IEEE Transactions on Microwave Theory and Techniques*, vol. MTT-16, 1968.
- [44] B. G. Evans, *Satellite communication systems*, 3rd ed. London: Institution of Electrical Engineers, 1999.
- [45] L. C. Godara, *Handbook of antennas in wireless communications*. Boca Raton, Fla. ; London: CRC Press, 2002.
- [46] L. C. Yang, X. L. Zhou, H. J. Li, K. Fu, and B. S. Zhang, "Ultra-Wideband Multi-Frequency Terahertz Square Microstrip Patch Antenna on Hybrid Photonic Crystal

- Substrate," *Journal of Computational and Theoretical Nanoscience*, vol. 10, pp. 968-973, Apr 2013.
- [47] V. Nimbark, Q. Lu, E. Korolkiewicz, and L. Liu, "Design of a Three Port Feed Matching Network for a Dual- Band and Dual -Polarized Rectangular Patch Antenna," *The International Conference on Signal Processing and Communications - 2012*, India, 2012.
 - [48] J. P. Ma, A. B. Kouki, and R. Landry, "Wideband circularly polarized single probe-fed patch antenna," *Microwave and Optical Technology Letters*, vol. 54, pp. 1803-1808, Aug 2012.
 - [49] A. Buffi, R. Caso, M. R. Pino, P. Nepa, and G. Manara, "Circularly Polarized Square Ring Slot Patch Antennas," *2010 IEEE Antennas and Propagation Society International Symposium*, 2010.
 - [50] M. Albooyeh, N. Komjani, and M. S. Mahani, "A Circularly Polarized Element for Reflectarray Antennas," *IEEE Antennas and Wireless Propagation Letters*, vol. 8, pp. 319-322, 2009.
 - [51] V. Sharma, K. B. Sharma, V. K. Saxena, and D. Bhatnagar, "Radiation performance of Circularly Polarized Broadband Gap Coupled Elliptical Patch Antenna," *Frequenz*, vol. 66, pp. 69-74, 2012.
 - [52] P. Sekra, S. Shekhawat, D. Bhatnagar, J. S. Saini, and V. K. Saxena, "Stacked Arrangement of Edge Truncated Elliptical and Conventional Circular Patches for Modern Communication Systems," *Microwave and Optical Technology Letters*, vol. 53, pp. 947-952, Apr 2011.
 - [53] H. I. Jung and C. H. Seo, "Characteristics of circular polarization of elliptical microstrip antenna with full-wave analysis considering the attachment mode," *Microwave and Optical Technology Letters*, vol. 22, pp. 111-113, Jul 20 1999.
 - [54] R. Garg, *Microstrip antenna design handbook*. Boston, Mass. ; London: Artech House, 2001.
 - [55] M. I. Montrose and Institute of Electrical and Electronics Engineers., *Printed circuit board design techniques for EMC compliance : a handbook for designers*, 2nd ed. New York: Institute of Electrical and Electronics Engineers, 2000.
 - [56] N. Ellis, *Electrical interference handbook*, 2nd ed. Oxford: Newnes, 1998.
 - [57] R. S. Elliott and IEEE Antennas and Propagation Society., *Electromagnetics history, theory, and applications*. Piscataway, NJ: IEEE Press, 1993.
 - [58] J. R. Wait and Institution of Electrical Engineers., *Introduction to antennas & propagation*. London: Peregrinus on behalf of the Institution of Electrical Engineers, 1986.
 - [59] B. Y. Wu, "Aperture Coupled H Shape Miniature Patch Antenna," *2007 International Conference on Wireless Communications, Networking and Mobile Computing, Vols 1-15*, pp. 5816-5818, 2007.
 - [60] M. T. Islam, M. N. Shakib, and N. Misran, "Modified E-H shaped microstrip patch antenna," *IEICE Electronics Express*, vol. 6, pp. 1350-1354, Sep 25 2009.

- [61] M. T. Islam, M. N. Shakib, and N. Misran, "Broadband E-H Shaped Microstrip Patch Antenna for Wireless Systems," *Progress in Electromagnetics Research-Pier*, vol. 98, pp. 163-173, 2009.
- [62] R. Bakshi and S. K. Sharma, "A Wideband U-Slot Loaded Modified E-Shape Microstrip Patch Antenna and Frequency Agile Behavior by Employing Different Height Ground Plane and Ribbon Type Switches," *Applied Computational Electromagnetics Society Journal*, vol. 26, pp. 539-550, Jul 2011.
- [63] D. M. Ma, Z. C. Hong, T. H. Lee, and B. J. Chang, "Design of a micro-satellite constellation for communication," *Acta Astronautica*, vol. 82, pp. 54-59, Jan 2013.
- [64] Z. Xu and C. H. Liang, "Ka/S dual-band antenna for satellite communication," *Microwave and Optical Technology Letters*, vol. 54, pp. 1246-1251, May 2012.
- [65] S. Kawasaki, S. Kawai, T. Yamamoto, K. Takei, and H. Seita, "A 5.8GHz-Band Active Integrated Phased Array Antenna with Wireless Communication and Power Transmission Functions for Space and Satellite Use," *2008 China-Japan Joint Microwave Conference (Cjmw 2008), Vols 1 and 2*, pp. 393-396, 2008.
- [66] F. S. Chang and K. L. Wong, "Broadband patch antenna edge-fed by a coplanar probe feed," *Microwave and Optical Technology Letters*, vol. 31, pp. 287-289, Nov 20 2001.
- [67] H. T. Zhang, W. Wang, Z. H. Zhang, and X. P. Lu, "A Broadband Single Layer Edge-Fed Cavity-Backed Microstrip Antenna," *Microwave and Optical Technology Letters*, vol. 53, pp. 2831-2834, Dec 2011.
- [68] H. Moghadas and A. Tavakoli, "A Design Procedure for Defected Ground Structure in Antenna Arrays based on Genetic Algorithm," *2012 IEEE Antennas and Propagation Society International Symposium (Apsursi)*, 2012.
- [69] D. M. Pozar, "An overview of wireless systems and antennas," *IEEE Antennas and Propagation Society International Symposium, Vols 1-4*, pp. 566-569, 2000.
- [70] M. S. R. M. Shah, M. R. C. Rose, M. F. A. Kadir, D. Misman, M. Z. A. A. Aziz, M. K. Suaidi, A. S. Ja'afari, I. Ibrahim, M. Sidek, and M. K. A. Rahim, "Dual Polarization Inset-Fed Microstrip Patch Antenna," *2008 8th International Conference on Its Telecommunications, Proceedings*, pp. 29-32, 2008.
- [71] X. Zhao, "Inset-fed Patch Antenna for LTE Application," *Mechanical and Electronics Engineering Iii, Pts 1-5*, vol. 130-134, pp. 4020-4023, 2012.
- [72] S. Rawat and P. Pathak, "A Novel Inset Fed Patch Antenna Design for RFID at 2.4 GHz," *International Conference on Recent Advances in Microwave Theory and Applications, Proceedings*, pp. 748-749, 2008.
- [73] D. C. Nascimento, R. Schildberg, and J. C. D. Lacava, "Design of Probe-Fed Circularly-Polarized Rectangular-Patch Thick Microstrip Antenna Revisited," *2010 IEEE Antennas and Propagation Society International Symposium*, 2010.
- [74] H. Y. Zhou, N. W. Kefauver, and D. S. Filipovic, "A Wideband Patch Antenna With Dual-Cylindrical Probe Feed," *IEEE Antennas and Wireless Propagation Letters*, vol. 8, pp. 1321-1324, 2009.

- [75] H. L. Hu, Y. H. Tan, B. C. Zhu, and L. Z. Zhou, "Analysis of a Probe-fed Bow-tie Antenna Scattering by Using the Hybrid FE-BI Method," *Apmc: 2009 Asia Pacific Microwave Conference, Vols 1-5*, pp. 104-107, 2009.
- [76] Y. Ding and K. W. Leung, "L-Probe-Fed Fabry-Perot Resonator Antenna for Millimeter-Wave Applications," *2009 IEEE Antennas and Propagation Society International Symposium and Usnc/Ursi National Radio Science Meeting, Vols 1-6*, pp. 108-111, 2009.
- [77] E. Alanen, "Analysis of the Probe-Fed Annular Microstrip Antenna for Hyperthermic Applicators," *Annales Des Telecommunications-Annals of Telecommunications*, vol. 46, pp. 163-170, Mar-Apr 1991.
- [78] M. Veysi, M. Kamyab, and A. Jafargholi, "Single-Feed Dual-Band Dual-Linearly-Polarized Proximity-Coupled Patch Antenna," *IEEE Antennas and Propagation Magazine*, vol. 53, pp. 90-96, Feb 2011.
- [79] S. Gao and A. Sambell, "Broadband dual-polarized proximity coupled circular patch antenna," *Microwave and Optical Technology Letters*, vol. 47, pp. 298-302, Nov 5 2005.
- [80] D. M. Pozar, "Microstrip Antenna Aperture-Coupled to a Microstripline," *Electronics Letters*, vol. 21, pp. 49-50, 1985.
- [81] D. M. Pozar, "A Review of Aperture Coupled Microstrip Antennas: History, Operation, Development, and Applications," University of Massachusetts at Amherst, 1996.
- [82] M. Civerolo and D. Arakaki, "Aperture Coupled Patch Antenna Design Methods," *2011 IEEE International Symposium on Antennas and Propagation (Apsursi)*, pp. 876-879, 2011.
- [83] A. Buffi, R. Caso, M. R. Pino, P. Nepa, and G. Manara, "Single-feed circularly polarised aperture-coupled square ring slot microstrip antenna," *Electronics Letters*, vol. 46, pp. 268-269, Feb 18 2010.
- [84] L. Liu, E. Korolkiewicz, Z. Ghassemlooy, A. Sambell, S. Danaher, and K. Busawon, "Investigation of the Equivalent Circuit Parameters and Design of a Dual Polarised Dual Frequency Aperture Coupled Microstrip Antenna" *Antennas and Propagation, IEEE Transactions on*, vol. 61, pp. 2304-2308, 2013.
- [85] J. P. Bourgoin, E. Meyer-Scott, B. L. Higgins, B. Helou, C. Erven, H. Hubel, B. Kumar, D. Hudson, I. D'Souza, R. Girard, R. Laflamme, and T. Jennewein, "A comprehensive design and performance analysis of low Earth orbit satellite quantum communication," *New Journal of Physics*, vol. 15, Feb 5 2013.
- [86] A. Genc, T. Turpin, T. Yasin, and R. Baktur, "Active integrated meshed patch antennas for small satellites," *Microwave and Optical Technology Letters*, vol. 54, pp. 1593-1595, Jul 2012.
- [87] M. Sadek and S. Aissa, "Personal Satellite Communication: Technologies and Challenges," *IEEE Wireless Communications*, vol. 19, pp. 28-35, Dec 2012.

- [88] B. V. Ha, P. Pirinoli, R. E. Zich, M. Mussetta, and C. N. Dao, "Reflectarray antenna for X-band satellite communication," *2012 Fourth International Conference on Communications and Electronics (Icce)*, pp. 417-420, 2012.
- [89] T. N. Chang and J. M. Lin, "Serial Aperture-Coupled Dual Band Circularly Polarized Antenna," *IEEE Transactions on Antennas and Propagation*, vol. 59, pp. 2419-2423, Jun 2011.
- [90] L. Liu, Z. Ghassemloooy, A. Sambell, S. Danaher, Q. Lu, and E. Korolkiewicz, "Investigation of transformers' turn ratios and design procedure for an aperture coupled slot antenna," in *Active RF Devices, Circuits and Systems Seminar*, 2011, pp. 61-65.
- [91] K. J. Lee, T. H. Lee, and Y. S. Kim, "Dual-Band Aperture-Coupled Shorted-Patch Antenna with a U-Shaped Slot," *IEICE Transactions on Communications*, vol. E94b, pp. 1748-1751, Jun 2011.
- [92] R. Glogowski, J. F. Zurcher, J. R. Mosig, and C. Peixeiro, "Circularly Polarized Aperture Coupled Stacked Patch Antenna Element for Ka-Band," *2011 IEEE International Symposium on Antennas and Propagation (Apsursi)*, pp. 911-914, 2011.
- [93] R. Caso, A. Buffi, M. R. Pino, P. Nepa, and G. Manara, "A Novel Dual-Feed Slot-Coupling Feeding Technique for Circularly Polarized Patch Arrays," *IEEE Antennas and Wireless Propagation Letters*, vol. 9, pp. 183-186, 2010.
- [94] K. F. Tong, G. Lacotte, and J. Huang, "Wideband single-fed proximity coupled circularly polarised annular slot antenna," *IET Microwaves Antennas & Propagation*, vol. 4, pp. 1451-1455, Oct 2010.
- [95] S. D. Targonski and D. M. Pozar, "Design of Wide-Band Circularly Polarized Aperture-Coupled Microstrip Antennas," *IEEE Transactions on Antennas and Propagation*, vol. 41, pp. 214-220, Feb 1993.
- [96] F. Croq and D. M. Pozar, "Millimeter-Wave Design of Wide-Band Aperture-Coupled Stacked Microstrip Antennas," *IEEE Transactions on Antennas and Propagation*, vol. 39, pp. 1770-1776, Dec 1991.
- [97] S. D. Targonski, R. B. Waterhouse, and D. M. Pozar, "Wideband aperture coupled stacked patch antenna using thick substrates," *Electronics Letters*, vol. 32, pp. 1941-1942, Oct 10 1996.
- [98] N. Herscovici, B. Tomasic, J. Ginn, and T. Donisi, "A Wide-Band Single-Layer Aperture-Coupled Micro strip Antenna," *2009 3rd European Conference on Antennas and Propagation, Vols 1-6*, pp. 2268-2271, 2009.
- [99] D. H. Schaubert, D. M. Pozar, and A. Adrian, "Effect of Microstrip Antenna Substrate Thickness and Permittivity - Comparison of Theories with Experiment," *IEEE Transactions on Antennas and Propagation*, vol. 37, pp. 677-682, Jun 1989.
- [100] A. Adrian and D. H. Schaubert, "Dual Aperture-Coupled Microstrip Antenna for Dual or Circular-Polarization," *Electronics Letters*, vol. 23, pp. 1226-1228, Nov 5 1987.

- [101] J. Eichler, P. Hazdra, M. Capek, T. Korinck, and P. Hamouz, "Design of a Dual-Band Orthogonally Polarized L-Probe-Fed Fractal Patch Antenna Using Modal Methods," *IEEE Antennas and Wireless Propagation Letters*, vol. 10, pp. 1389-1392, 2011.
- [102] R. Caso, A. A. Serra, M. Rodriguez-Pino, P. Nepa, and G. Manara, "A Wideband Slot-Coupled Stacked-Patch Array for Wireless Communications," *IEEE Antennas and Wireless Propagation Letters*, vol. 9, pp. 986-989, 2010.
- [103] Y. Suzuki and T. Sugiyama, "Ground-Based Polarization-Forming Technique for Polarization-tracking-free Ku-band Mobile Satellite Communication Systems," *2012 IEEE Antennas and Propagation Society International Symposium (Apsursi)*, 2012.
- [104] F. Boeykens, Q. Doolaege, F. Declercq, and H. Rogier, "A Planar Aperture-Coupled Patch Antenna Implemented on Dashboard Foams for Intra-Vehicle Communication," *Microwave and Optical Technology Letters*, vol. 53, pp. 1186-1189, May 2011.
- [105] C. H. Tsao, Y. M. Hwang, F. Kilburg, and F. Dietrich, "Aperture-coupled patch antennas with wide-bandwidth and dual-polarization capabilities," in *Antennas and Propagation Society International Symposium, 1988. AP-S. Digest*, 1988, pp. 936-939 vol.3.
- [106] J. P. Daniel, G. Dubost, C. Terret, J. Citerne, and M. Drissi, "Research on planar antennas and arrays: 'structures Rayonnantes'," *Antennas and Propagation Magazine, IEEE*, vol. 35, pp. 14-38, 1993.
- [107] M. Edimo, P. Rigoland, and C. Terret, "Wide-Band Dual Polarized Aperture-Coupled Stacked Patch Antenna-Array Operating in C-Band," *Electronics Letters*, vol. 30, pp. 1196-1198, Jul 21 1994.
- [108] D. M. Pozar, "A Reciprocity Method of Analysis for Printed Slot and Slot-Coupled Microstrip Antennas," *IEEE Transactions on Antennas and Propagation*, vol. 34, pp. 1439-1446, Dec 1986.
- [109] Y. T. Lo, B. Engst, and R. Q. Lee, "Simple Design Formulas for Circularly Polarized Microstrip Antennas," *IEE Proceedings-H Microwaves Antennas and Propagation*, vol. 135, pp. 213-215, Jun 1988.
- [110] A. K. Bhattacharyya, Y. M. M. Antar, and A. Ittipiboon, "Spectral Domain Analysis of Aperture-Coupled Microstrip Patch Antennas," *IEE Proceedings-H Microwaves Antennas and Propagation*, vol. 139, pp. 459-464, Oct 1992.
- [111] B. Al-Jibouri, H. Evans, E. Korolkiewicz, E. G. Lim, A. Sambell, and T. Viasits, "Cavity model of circularly polarised cross-aperture-coupled microstrip antenna," *IEE Proceedings-Microwaves Antennas and Propagation*, vol. 148, pp. 147-152, Jun 2001.
- [112] D. Jaisson, "Transmission line model for the input impedance of a slot-coupleld rectangular patch antenna," *IEE Proceedings-Microwaves Antennas and Propagation*, vol. 153, pp. 461-468, Oct 2006.
- [113] S. B. Cohn, "Slotline on a Dielectric Substrate," *IEEE Transactions on Microwave Theory and Techniques*, vol. MTT-17, pp. 768-778, 1969.

- [114] J. B. Knorr and K. D. Kuchler, "Analysis of Coupled Slots and Coplanar Strips on Dielectric Substrate," *IEEE Transactions on Microwave Theory and Techniques*, vol. Mt23, pp. 541-548, 1975.
- [115] T. Itoh and R. Mittra, "Dispersion Characteristics of Slot Lines," *Electronics Letters*, vol. 7, pp. 364-&, 1971.
- [116] R. Janaswamy and D. H. Schaubert, "Dispersion Characteristics for Wide Slotlines on Low-Permittivity Substrates," *IEEE Transactions on Microwave Theory and Techniques*, vol. 33, pp. 723-726, 1985.
- [117] R. Janaswamy and D. H. Schaubert, "Characteristic Impedance of a Wide Slotline on Low-Permittivity Substrates," *IEEE Transactions on Microwave Theory and Techniques*, vol. 34, pp. 900-902, Aug 1986.
- [118] G. C. Liang, Y. W. Liu, and K. K. Mei, "Full-Wave Analysis of Coplanar Waveguide and Slotline Using the Time-Domain Finite-Difference Method," *IEEE Transactions on Microwave Theory and Techniques*, vol. 37, pp. 1949-1957, Dec 1989.
- [119] J. B. Knorr, "Slot-Line Transitions," *IEEE Transactions on Microwave Theory and Techniques*, vol. Mt22, pp. 548-554, 1974.
- [120] N. K. Das, "Generalized Multiport Reciprocity Analysis of Surface-to-Surface Transitions between Multiple Printed Transmission-Lines," *IEEE Transactions on Microwave Theory and Techniques*, vol. 41, pp. 1164-1177, Jun-Jul 1993.
- [121] O. Lafond, M. Himdi, and J. P. Daniel, "Cavity method for slot-fed patches: Inclined line, circular polarization," *15eme Colloque International Optique Hertzienne Et Dielectriques, Ohd'99*, pp. A9-A12288, 1999.
- [122] M. Sauzade, G. J. Elfring, and E. Lauga, "Taylor's swimming sheet: Analysis and improvement of the perturbation series," *Physica D-Nonlinear Phenomena*, vol. 240, pp. 1567-1573, Oct 1 2011.
- [123] A. A. Nahla, "Taylor's series method for solving the nonlinear point kinetics equations," *Nuclear Engineering and Design*, vol. 241, pp. 1592-1595, May 2011.
- [124] A. K. Bhattacharyya, Y. M. M. Antar, and A. Ittipiboon, "Full-Wave Analysis of an Aperture-Coupled Patch Antenna," *Electronics Letters*, vol. 27, pp. 153-155, Jan 17 1991.
- [125] R. H. Jansen, "Hybrid Mode Analysis of End Effects of Planar Microwave and Millimeterwave Transmission-Lines," *IEE Proceedings-H Microwaves Antennas and Propagation*, vol. 128, pp. 77-86, 1981.
- [126] H. Y. Yang and N. G. Alexopoulos, "A Dynamic-Model for Microstrip Slotline Transition and Related Structures," *IEEE Transactions on Microwave Theory and Techniques*, vol. 36, pp. 286-293, Feb 1988.
- [127] J. B. Knorr and J. Saenz, "End Effect in a Shorted Slot," *IEEE Transactions on Microwave Theory and Techniques*, vol. Mt21, pp. 579-580, 1973.
- [128] G. A. Kyriacou, O. Breinbjerg, and J. N. Sahalos, "Aperture Coupled Microstrip Antennas: A Design Approach," presented at the Seventh International Conference

on Advances in Communication and Control Proceedings, New York.Los Angeles, 1999.

- [129] H. Nakagaki, N. Amada, and S. Inoue, "A High-Efficiency Audio Power-Amplifier," *Journal of the Audio Engineering Society*, vol. 31, pp. 430-436, 1983.
- [130] P. J. Poggi, "Applications of high efficiency techniques to the design of RF Power Amplifier and amplifier control circuits in tactical radio equipment," *Milcom 95 - Conference Record, Vols 1-3*, pp. 743-747, 1995.
- [131] F. H. Raab, P. Asbeck, S. Cripp, P. B. Kenington, Z. B. Popovic, N. Potheary, J. F. Sevic, and N. O. Sokal, "Power amplifiers and transmitters for RF and microwave," *IEEE Transactions on Microwave Theory and Techniques*, vol. 50, pp. 814-826, Mar 2002.
- [132] A. Nagari, "Tutorial review: audio amplifiers in mobile platforms," *Analog Integrated Circuits and Signal Processing*, vol. 72, pp. 511-520, Sep 2012.
- [133] B. Zheng, J. P. Walder, H. von der Lippe, W. Moses, and M. Janecek, "A High-speed Adaptively-biased Current-to-current Front-end for SSPM Arrays," *Proceedings of the 2nd International Conference on Technology and Instrumentation in Particle Physics (Tipp 2011)*, vol. 37, pp. 1473-1479, 2012.
- [134] R. Sobot, "RF and IF Amplifiers," *Wireless Communication Electronics: Introduction to Rf Circuits and Design Techniques*, pp. 173-220, 2012.
- [135] M. Y. Ren, C. X. Zhang, and D. S. Sun, "Design of CMOS Instrumentation Amplifier," *2012 International Workshop on Information and Electronics Engineering*, vol. 29, pp. 4035-4039, 2012.
- [136] L. J. Kushner and Lincoln Laboratory., *Microwave power amplifier analysis and design*. Lexington, Mass.: Massachusetts Institute of Technology, Lincoln Laboratory, 1988.
- [137] J. Bardeen and W. H. Brattain, "The transistor, a semiconductor triode (Reprinted from Physical Review, vol 74, pg 230-231, 1948)," *Proceedings of the Ieee*, vol. 86, pp. 29-30, Jan 1998.
- [138] W. Shockley, "The Theory of p-n Junctions in Semiconductors and p-n Junction Transistors," *The Bell System Technical Journal*, vol. XXVIII, pp. 435-489, 1949.
- [139] B. Kattouf, Y. Ein-Eli, A. Siegmann, and G. L. Frey, "Hybrid mesostructured electrodes for fast-switching proton-based solid state electrochromic devices," *Journal of Materials Chemistry C*, vol. 1, pp. 151-159, 2013.
- [140] D. Medvedev, V. Maragou, E. Pikalova, A. Demin, and P. Tsiakaras, "Novel composite solid state electrolytes on the base of BaCeO3 and CeO2 for intermediate temperature electrochemical devices," *Journal of Power Sources*, vol. 221, pp. 217-227, Jan 1 2013.
- [141] J. Capmany, J. Mora, I. Gasulla, J. Sancho, J. Lloret, and S. Sales, "Microwave Photonic Signal Processing," *Journal of Lightwave Technology*, vol. 31, pp. 571-586, Feb 15 2013.

- [142] P. S. Lee, C. S. Lee, and J. H. Lee, "Development of FPGA-based digital signal processing system for radiation spectroscopy," *Radiation Measurements*, vol. 48, pp. 12-17, Jan 2013.
- [143] C. E. Weitzel, "RF power devices for wireless communications," *2002 IEEE Radio Frequency Integrated Circuits (RFIC) Symposium, Digest of Papers*, pp. 369-372, 2002.
- [144] Y. F. Wu, B. P. Keller, S. Keller, J. J. Xu, B. J. Thibeault, S. P. Denbaars, and U. K. Mishra, "GaN-based FETs for microwave power amplification," *IEICE Transactions on Electronics*, vol. E82c, pp. 1895-1905, Nov 1999.
- [145] H. L. Krauss, C. W. Bostian, and F. H. Raab, *Solid state radio engineering*. New York ; Chichester: Wiley, 1980.
- [146] A. Y. Goncharov, "High-Efficiency Power-Amplifier Design," *Telecommunications and Radio Engineering*, vol. 33-4, pp. 129-130, 1979.
- [147] M. K. Kazimierczuk and W. A. Tabisz, "Class C-E High-Efficiency Tuned Power-Amplifier," *IEEE Transactions on Circuits and Systems*, vol. 36, pp. 421-428, Mar 1989.
- [148] D. Self, *Audio power amplifier design handbook*, 4th ed. Amsterdam ; Boston: Newnes, 2006.
- [149] D. Y. C. Lie and C. K. Clive, "Special Topic: High Efficiency Supply-Modulated Rf Power Amplifier," *IEEE Microwave and Wireless Components Letters*, vol. 22, pp. 277-278, Jun 2012.
- [150] R. Darraji and F. M. Ghannouchi, "High Efficiency Harmonically-Tuned Gan Power Amplifier for 4g Applications," *2011 24th Canadian Conference on Electrical and Computer Engineering (Ccece)*, pp. 1264-1267, 2011.
- [151] R. B. H. Becker, "High-Power Audio Amplifier Design - Obtaining 100w and More from a Fully-Protected Class-B Circuit," *Wireless World*, vol. 78, pp. 79-&, 1972.
- [152] F. H. Raab, "Class Bd High-Efficiency Rf Power-Amplifier," *IEEE Journal of Solid-State Circuits*, vol. 12, pp. 291-298, 1977.
- [153] M. C. Tsai, "A Wide-Band Class-B Amplifier Using Tapered Interdigital Power Combiners," *Microwave and Optical Technology Letters*, vol. 4, pp. 455-459, Oct 1991.
- [154] M. Kazimierczuk, *RF power amplifiers*. Chichester, West Sussex, U.K.: Wiley, 2008.
- [155] R. C.-H. Li, *RF circuit design*. Hoboken, N.J.: Wiley, 2009.
- [156] R. Yalamanchili, Z. A. Qiu, and Y. C. Wang, "Review of Microwave Distributed Superconducting Vortex-Flow Transistor-Amplifiers," *International Journal of Electronics*, vol. 73, pp. 585-604, Sep 1992.
- [157] S. R. Mazumder, A. Azizi, and F. E. Gardiol, "Improvement of a Class-C Transistor Power-Amplifier by 2nd-Harmonic Tuning," *IEEE Transactions on Microwave Theory and Techniques*, vol. 27, pp. 430-433, 1979.

- [158] F. H. Raab, "Idealized Operation of Class-E Tuned Power-Amplifier," *IEEE Transactions on Circuits and Systems*, vol. 24, pp. 725-735, 1977.
- [159] N. O. Sokal, "Class-E switching-mode high-efficiency tuned RF/microwave power amplifier: Improved design equations," *2000 IEEE Mtt-S International Microwave Symposium Digest, Vols 1-3*, pp. 779-782
1976, 2000.
- [160] F. H. Raab, "Class-E, class-C, and class-F power amplifiers based upon a finite number of harmonics," *IEEE Transactions on Microwave Theory and Techniques*, vol. 49, pp. 1462-1468, Aug 2001.
- [161] F. H. Raab, "Maximum efficiency and output of class-F power amplifiers," *IEEE Transactions on Microwave Theory and Techniques*, vol. 49, pp. 1162-1166, Jun 2001.
- [162] S. A. Elhamamsy, "Design of High-Efficiency Rf Class-D Power-Amplifier," *IEEE Transactions on Power Electronics*, vol. 9, pp. 297-308, May 1994.
- [163] J. H. Jeong, H. H. Seong, J. H. Yi, and G. H. Cho, "A class D switching power amplifier with high efficiency and wide bandwidth by dual feedback loops," *IEEE 1995 International Conference on Consumer Electronics - Digest of Technical Papers*, pp. 428-429, 1995.
- [164] F. H. Raab and N. O. Sokal, "Transistor Power Losses in Class-E Tuned Power-Amplifier," *IEEE Journal of Solid-State Circuits*, vol. 13, pp. 912-914, 1978.
- [165] H. Koizumi, T. Suetsugu, M. Fujii, K. Shinoda, S. Mori, and K. Ikeda, "Class DE high-efficiency tuned power amplifier," *IEEE Transactions on Circuits and Systems I-Fundamental Theory and Applications*, vol. 43, pp. 51-60, Jan 1996.
- [166] N. O. Sokal, "Class-E switching-mode high-efficiency tuned RF/microwave power amplifier: Improved design equations," *2000 IEEE Mtt-S International Microwave Symposium Digest, Vols 1-3*, pp. 779-782, 2000.
- [167] F. H. Raab, "Class-F power amplifiers with maximally flat waveforms," *IEEE Transactions on Microwave Theory and Techniques*, vol. 45, pp. 2007-2012, Nov 1997.
- [168] V. J. Tyler, "A new high-efficiency high power amplifier," *Marconi Rev.*, vol. 21, pp. 96-109, 1958.
- [169] K. Chiba and N. Kanmuri, "Gaas-Fet Power-Amplifier Module with High-Efficiency," *Electronics Letters*, vol. 19, pp. 1025-1026, 1983.
- [170] T. Nojima, S. Nishiki, and K. Chiba, "High-Efficiency Quasimicrowave Gaas-Fet Power-Amplifier," *Electronics Letters*, vol. 23, pp. 512-513, May 7 1987.
- [171] S. Toyoda, "High-Efficiency Amplifiers," *1994 IEEE Mtt-S International Microwave Symposium Digest, Vols 1-3*, pp. 253-256, 1994.
- [172] J. D. Huang and D. Zhan, "High Efficiency Fet Power Amplifier with Very Low Drain Bias for Mobile Communication," *1995 IEEE Mtt-S Symposium on Technologies for Wireless Applications Digest*, pp. 123-126, 1995.

- [173] A. V. Grebennikov, "Circuit design technique for high efficiency class F amplifiers," *2000 IEEE Mtt-S International Microwave Symposium Digest, Vols 1-3*, pp. 771-774, 2000.
- [174] M. Wren and T. J. Brazil, "Experimental class-F power amplifier design using computationally efficient and accurate large-signal pHEMT model," *IEEE Transactions on Microwave Theory and Techniques*, vol. 53, pp. 1723-1731, May 2005.
- [175] F. H. Raab, R. Caverly, R. Campbell, M. Eron, J. B. Hecht, A. Mediano, D. P. Myer, and J. L. B. Walker, "HF, VHF, and UHF systems and technology," *IEEE Transactions on Microwave Theory and Techniques*, vol. 50, pp. 888-899, Mar 2002.
- [176] Y. Yang, J. Yi, Y. Y. Woo, and B. Kim, "Optimum design for linearity and efficiency of a microwave Doherty amplifier using a new load matching technique," *Microwave Journal*, vol. 44, pp. 20-+, Dec 2001.
- [177] S. F. Ooi, S. K. Lee, A. Sambell, E. Korolkiewicz, and P. Butterworth, "Design of a high efficiency power amplifier with input and output harmonic terminations," *Microwave and Optical Technology Letters*, vol. 49, pp. 391-395, Feb 2007.
- [178] A. Vanderziel and K. M. Vanvliet, "High-Injection Transmission-Line Model of P-N Diode and P-N-P Transistor Noise," *Solid-State Electronics*, vol. 21, pp. 1023-1024, 1978.
- [179] E. Abou-Allam and T. Manku, "An improved transmission-line model for MOS transistors," *IEEE Transactions on Circuits and Systems II-Analog and Digital Signal Processing*, vol. 46, pp. 1380-1387, Nov 1999.
- [180] A. Telegdy, B. Molnar, and N. O. Sokal, "Class-E-M switching-mode tuned power amplifier - High efficiency with slow-switching transistor," *IEEE Transactions on Microwave Theory and Techniques*, vol. 51, pp. 1662-1676, Jun 2003.
- [181] H. C. Park, G. H. Ahn, S. C. Jung, C. S. Park, W. S. Nah, B. S. Kim, and Y. G. Yang, "High-efficiency class-F amplifier design in the presence of internal parasitic components of transistors," *2006 European Microwave Conference, Vols 1-4*, pp. 1055-1058 1840, 2006.
- [182] Y. Y. Woo, Y. Yang, and B. Kim, "Analysis and experiments for high-efficiency class-F and inverse class-F power amplifiers," *IEEE Transactions on Microwave Theory and Techniques*, vol. 54, pp. 1969-1974, May 2006.
- [183] D. Kang, D. Yu, K. Min, K. Han, J. Choi, D. Kim, B. Jin, M. Jun, and B. Kim, "A highly efficient and linear Class-AB/F power amplifier for multimode operation," *IEEE Transactions on Microwave Theory and Techniques*, vol. 56, pp. 77-87, Jan 2008.
- [184] V. Meraftab and A. Abdipour, "Harmonic balance analysis of a microwave balanced power amplifier," *Canadian Conference on Electrical and Computer Engineering 2001, Vols I and II, Conference Proceedings*, pp. 901-905, 2001.

- [185] S. Asadi, A. Abdipour, A. Tavakoli, and G. Moradi, "Design and nonlinear analysis of high-gain and broad-band distributed power amplifier with traveling-wave gain stages by harmonic balance method," *2006 IEEE International Conference on Semiconductor Electronics, Proceedings*, pp. 835-837, 2006.
- [186] J. Kawata, T. Kinouchi, Y. Yamagami, Y. Nishio, and A. Ushida, "Envelope analysis of nonlinear electronic circuits based on harmonic balance method," *International Journal of Circuit Theory and Applications*, vol. 40, pp. 247-262, Mar 2012.
- [187] G. n. Kompa, *Practical microstrip design and applications*. Boston, Mass. ; London: Artech House, 2005.
- [188] M. Helaoui and F. M. Ghannouchi, "Optimizing Losses in Distributed Multiharmonic Matching Networks Applied to the Design of an RF GaN Power Amplifier With Higher Than 80% Power-Added Efficiency," *Ieee Transactions on Microwave Theory and Techniques*, vol. 57, pp. 314-322, Feb 2009.
- [189] O. Bengtsson, L. Vestling, and J. Olsson, "A computational load-pull method with harmonic loading for high-efficiency investigations," *Solid-State Electronics*, vol. 53, pp. 86-94, Jan 2009.
- [190] F. De Groote, J. Verspecht, D. Barataud, and J. P. Teyssier, "An improved coupling method for time domain Load-Pull measurements," *35th European Microwave Conference, Vols 1-3, Conference Proceedings*, pp. 601-604, 2005.
- [191] K. Ishida, H. Ikeda, H. Kosugi, M. Nishijima, and T. Uwano, "A high efficiency and low distortion GaAs power MMIC design in the wide load impedance range by extended use of load-pull method," *1999 IEEE Mtt-S International Microwave Symposium Digest, Vols 1-4*, pp. 775-778, 1999.
- [192] M. Jones and M. Dehaan, "A method for deriving large-signal input impedance of microwave devices using a modified source and load pull technique," *45th Arftg Conference Digest - Spring 1995*, pp. 97-104, 1995.
- [193] Y. Takayama, "New Load-Pull Characterization Method for Microwave-Power Transistors," *Nec Research & Development*, pp. 23-29, 1978.
- [194] S. Dudkiewicz, "Vector-Receiver Load Pull Measurements," *Microwave Journal*, vol. 54, pp. 88-+, Feb 2011.
- [195] D. M. Drury, D. C. Zimmermann, and W. A. Davis, "Large-Signal Characterization of Dual-Gate Field-Effect Transistors Using Load-Pull Measurements," *IEEE Transactions on Microwave Theory and Techniques*, vol. 41, pp. 183-189, Feb 1993.
- [196] R. Hajji, F. M. Ghannouchi, and R. G. Bosisio, "Large-Signal Microwave Transistor Modeling Using Multiharmonic Load-Pull Measurements," *Microwave and Optical Technology Letters*, vol. 5, pp. 580-585, Oct 1992.
- [197] D. Poulin, "Load-Pull Measurements Help You Meet Your Match," *Microwaves*, vol. 19, pp. 61-&, 1980.

- [198] S. Gao, P. Butterworth, S. Ooi, and A. Sambell, "High-efficiency power amplifier design including input harmonic termination," *IEEE Microwave and Wireless Components Letters*, vol. 16, pp. 81-83, Feb 2006.
- [199] S. Gao, P. Butterworth, A. Sambell, C. Sanabria, H. Xu, S. Heikman, U. Mishra, and R. A. York, "Microwave class-F and inverse class-F power amplifiers designs using GaN technology and GaAs pHEMT," *2006 European Microwave Conference, Vols 1-4*, pp. 1-4, 2006.
- [200] S. Gao, P. Butterworth, S. Ooi, and A. Sambell, "Microwave Class-F power amplifier design including input harmonic terminations," *2005 Asia-Pacific Microwave Conference Proceedings, Vols 1-5*, pp. 3360-3363, 2005.
- [201] M. Maeda, H. Takehara, M. Nakamura, Y. Ota, and O. Ishikawa, "A High Power and High Efficiency Amplifier with Controlled 2nd-Harmonic Source Impedance," *1995 IEEE Mtt-S International Microwave Symposium Digest, Vols 1-3*, pp. 579-582, 1995.
- [202] M. Maeda, H. Masato, H. Takehara, M. Nakamura, S. Morimoto, H. Fujimoto, Y. Ota, and O. Ishikawa, "Source second-harmonic control for high efficiency power amplifiers," *IEEE Transactions on Microwave Theory and Techniques*, vol. 43, pp. 2952-2958, Dec 1995.
- [203] P. M. White, "Effect of input harmonic terminations on high efficiency class-B and class-F operation of PHEMT devices," in *Microwave Symposium Digest, 1998 IEEE MTT-S International*, 1998, pp. 1611-1614 vol.3.
- [204] J. Kye-Ik, K. Young-Se, and H. Song-Cheol, "Input harmonics control using non-linear capacitor in GaAs FET power amplifier," in *Microwave Symposium Digest, 1997., IEEE MTT-S International*, 1997, pp. 817-820 vol.2.
- [205] P. Colantonio, F. Giannini, E. Limiti, and V. Teppati, "An approach to harmonic load- and source-pull measurements for high-efficiency PA design," *IEEE Transactions on Microwave Theory and Techniques*, vol. 52, pp. 191-198, Jan 2004.
- [206] A. Kheirkhahi, P. Naghshtabrizi, and L. E. Larson, "Stability Analysis of RF Power Amplifier Envelope Feedback," *Ieee Transactions on Circuits and Systems II-Express Briefs*, vol. 58, pp. 852-856, Dec 2011.
- [207] F. Cappelluti, F. L. Traversa, F. Bonani, S. D. Guerrieri, and G. Ghione, "Rigorous, HB-based nonlinear stability analysis of multi-device power amplifier," *2010 European Microwave Integrated Circuits Conference (Eumic)*, pp. 90-93, 2010.
- [208] A. Suarez, S. G. Jeon, and D. Rutledge, "Global Stability Analysis and Stabilization of Power Amplifier," *2008 Workshop on Integrated Nonlinear Microwave and Millimetre- Wave Circuits (Inmmic)*, pp. 76-79, 2008.
- [209] D. Elad, R. Shaulsky, and B. Mezhebovsky, "A novel method for even odd parametric oscillation stability analysis of a microwave power amplifier.," *2006 IEEE Mtt-S International Microwave Symposium Digest, Vols 1-5*, pp. 1850-1854, 2006.
- [210] G. Collinson and M. Jones, "A Novel Technique for Measuring Small-Signal S-Parameters of an Rf Microwave, Transistor, Power Amplifying Stage for Use in

- Power-Amplifier Stability Analysis," *1993 IEEE Mtt-S International Microwave Symposium Digest, Vols 1-3*, pp. 1255-1258, 1993.
- [211] H. A. Wheeler, "Small Antennas," *IEEE Transactions on Antennas and Propagation*, vol. Ap23, pp. 462-469, 1975.
 - [212] A. P. Anderson, W. S. Davies, M. M. Dawoud, and Galanaki.De, "Transistor-Fed Active-Array Antennas," *IEEE Transactions on Antennas and Propagation*, vol. Ap19, pp. 537-&, 1971.
 - [213] M. M. Dawoud and A. P. Anderson, "Calculations Showing Reduction in Frequency-Dependence of a 2-Element Array Antenna Fed by Microwave Transistors," *IEEE Transactions on Antennas and Propagation*, vol. Ap20, pp. 497-&, 1972.
 - [214] A. P. Anderson and M. M. Dawoud, "The performance of transistor fed monopoles in active antennas," *Antennas and Propagation, IEEE Transactions on*, vol. 21, pp. 371-374, 1973.
 - [215] M. I. Kontorovich and N. M. Lyapunova, "Active Antennas," *Radiotekhnika I Elektronika*, vol. 19, pp. 2616-2618, 1974.
 - [216] T. S. M. Maclean and P. A. Ramsdale, "Short Active Aerials for Transmission," *International Journal of Electronics*, vol. 36, pp. 261-269, 1974.
 - [217] M. M. Dawoud and A. P. Anderson, "Experimental Verification of Reduced Frequency-Dependence of Active Receiving Arrays," *IEEE Transactions on Antennas and Propagation*, vol. Ap22, pp. 342-344, 1974.
 - [218] P. K. Rangole and S. S. Midha, "Short Antenna with Active Inductance," *Electronics Letters*, vol. 10, pp. 462-463, 1974.
 - [219] *Active Integrated Antennas*. USA,, 1994.
 - [220] V. Radisic, S. T. Chew, Y. X. Qian, and T. Itoh, "High-efficiency power amplifier integrated with antenna," *IEEE Microwave and Guided Wave Letters*, vol. 7, pp. 39-41, Feb 1997.
 - [221] V. Radisic, Y. X. Qian, and T. Itoh, "Class F power amplifier integrated with circular sector microstrip antenna," *1997 IEEE Mtt-S International Microwave Symposium Digest, Vols I-Iii*, pp. 687-690, 1997.
 - [222] V. Radisic, Y. X. Qian, and T. Itoh, "Broad-band power amplifier using dielectric photonic bandgap structure," *IEEE Microwave and Guided Wave Letters*, vol. 8, pp. 13-14, Jan 1998.
 - [223] Y. K. Chung, C. Y. Hang, S. J. Cai, Y. X. Qian, C. P. Wen, K. L. Wang, and T. Itoh, "AlGaIn/GaN HFET power amplifier integrated with microstrip antenna for RF front-end applications," *IEEE Transactions on Microwave Theory and Techniques*, vol. 51, pp. 653-659, Feb 2003.
 - [224] Y. Chung, C. Y. Hang, S. J. Cai, Y. X. Qian, C. P. Wen, K. L. Wang, and T. Itoh, "Output harmonic termination techniques for AlGaIn/GaN HEMT power amplifiers using active integrated antenna approach," *2002 IEEE Mtt-S International Microwave Symposium Digest, Vols 1-3*, pp. 433-436, 2002.

- [225] H. Kim, I. J. Yoon, and Y. J. Yoon, "A novel fully integrated transmitter front-end with high power-added efficiency," *IEEE Transactions on Microwave Theory and Techniques*, vol. 53, pp. 3206-3214, Oct 2005.
- [226] G. A. Ellis and S. Liw, "Active planar inverted-F antennas for wireless applications," *IEEE Transactions on Antennas and Propagation*, vol. 51, pp. 2899-2906, Oct 2003.
- [227] M. D. Weiss and Z. Popovic, "A 10 GHz high-efficiency active antenna," *1999 IEEE Mtt-S International Microwave Symposium Digest, Vols 1-4*, pp. 663-666, 1999.
- [228] P. Colantonio, F. Giannini, and E. Limiti, "Nonlinear approaches to the design of microwave power amplifiers," *International Journal of Rf and Microwave Computer-Aided Engineering*, vol. 14, pp. 493-506, Nov 2004.
- [229] P. Colantonio, F. Giannini, and L. Sclicchia, "A method to design distributed harmonic matching networks," *2006 European Microwave Integrated Circuits Conference*, pp. 79-82, 2006.
- [230] S. Z. Fan and E. L. Tan, "A Low Cost Omnidirectional High Gain Active Integrated Antenna for WLAN Applications," *2012 IEEE Asia-Pacific Conference on Antennas and Propagation (Apcap)*, pp. 124-125, 2012.
- [231] F. Giuppi, A. Georgiadis, A. Collado, and M. Bozzi, "A Compact, Single-Layer Substrate Integrated Waveguide (SIW) Cavity-Backed Active Antenna Oscillator," *IEEE Antennas and Wireless Propagation Letters*, vol. 11, pp. 431-433, 2012.
- [232] B. A. Khawaja and M. J. Cryan, "Millimeter-wave photonic active integrated antennas using hybrid mode-locked lasers," *Microwave and Optical Technology Letters*, vol. 54, pp. 1200-1203, May 2012.
- [233] S. F. Ooi, S. K. Lee, A. Sambell, E. Korolkiewicz, and S. Scott, "A new approach to the design of a compact high efficiency active integrated antenna," *Microwave and Optical Technology Letters*, vol. 50, pp. 585-589, Mar 2008.
- [234] S. Kawasaki, "Development of 5.8GHz High Power Active Integrated Antenna Arrays," *2007 Asia Pacific Microwave Conference, Vols 1-5*, pp. 385-388, 2007.
- [235] E. Lee, K. M. Chan, P. Gardner, and T. E. Dodgson, "Active integrated antenna design using a contact-less, proximity coupled, differentially fed technique," *IEEE Transactions on Antennas and Propagation*, vol. 55, pp. 267-276, Feb 2007.
- [236] S. Gao, Y. Qin, and A. Sambell, "Circularly polarized broadband high-efficiency active integrated antenna," *Microwave and Optical Technology Letters*, vol. 48, pp. 2145-2148, Nov 2006.
- [237] C. Kai, "Integrated and active antennas for system applications," *Icmwfst '96 - 1996 4th International Conference on Millimeter Wave and Far Infrared Science and Technology, Proceedings*, pp. 35-38, 1996.
- [238] T. Itoh, "Recent progress in active integrated antennas," *27th European Microwave 97, Conference + Exhibition - Bridging the Gap between Industry and Academia, Vols I and II*, pp. 992-997, 1997.

- [239] M. Varasi, M. Signorazzi, M. Massani, and A. Vannucci, "Integrated Optical Coherent Architecture for Beam Forming in Phased-Array Active Antennas," *Optical Technology for Microwave Applications Vi and Optoelectronic Signal Processing for Phased-Array Antennas Iii*, vol. 1703, pp. 566-572, 1992.
- [240] W. K. Leverich, X. D. Wu, and K. Chang, "A 3x3 Quasi-Optical Power Combining Array Using Fet Active Notch Antennas," *Microwave and Optical Technology Letters*, vol. 9, pp. 196-198, Jul 1995.
- [241] A. Petosa, R. Larose, A. Ittipiboon, and M. Cuhaci, "Active phased array of dielectric resonator antennas," *IEEE Antennas and Propagation Society International Symposium 1997, Vols 1-4*, pp. 690-693, 1997.
- [242] S. Kawasaki, K. Hayata, and T. Goi, "Topology of laminated active integrated antenna arrays," *Icmmt'98: 1998 International Conference on Microwave and Millimeter Wave Technology Proceedings*, pp. 277-280, 1998.
- [243] N. M. K. Nguyen, M. Sasaki, and K. Asada, "A CMOS Fully Integrated Antenna Array Transmitter with On-chip Skew and Pulse-Delay Adjustment for Millimeter-Wave Active Imaging," *2012 IEEE 12th Topical Meeting on Silicon Monolithic Integrated Circuits in Rf Systems (Sirf)*, pp. 163-166, 2012.
- [244] C. E. Patterson, W. T. Khan, G. E. Ponchak, G. S. May, and J. Papapolymerou, "A 60-GHz Active Receiving Switched-Beam Antenna Array With Integrated Butler Matrix and GaAs Amplifiers," *IEEE Transactions on Microwave Theory and Techniques*, vol. 60, pp. 3599-3607, Nov 2012.
- [245] J. H. Holland, "Genetic Algorithms," *Scientific American*, vol. 267, pp. 66-72, Jul 1992.
- [246] C. R. M. Silva, H. W. C. Lins, S. R. Martins, E. L. F. Barreto, and A. G. d'Assuncao, "A multiobjective optimization of a UWB antenna using a self organizing genetic algorithm," *Microwave and Optical Technology Letters*, vol. 54, pp. 1824-1828, Aug 2012.
- [247] A. X. Chen, T. H. Jiang, Z. Z. Chen, and Y. J. Zhang, "A Genetic and Simulated Annealing Combined Algorithm for Optimization of Wideband Antenna Matching Networks," *International Journal of Antennas and Propagation*, 2012.
- [248] Y. Chen, X. Chen, and K. M. Huang, "Design of Microstrip Reflectarray Antenna Using a Genetic Algorithm Based Optimization Method," *Electromagnetics*, vol. 32, pp. 77-85, 2012.
- [249] F. Yaman and A. E. Yilmaz, "Impacts of Genetic Algorithm Parameters on the Solution Performance for the Uniform Circular Antenna Array Pattern Synthesis Problem," *Journal of Applied Research and Technology*, vol. 8, pp. 378-394, Dec 2010.
- [250] V. Sathi, S. Taherizadeh, A. Lotfi, and C. Ghobadi, "Optimisation of multi-frequency microstrip antenna using genetic algorithm coupled with method of moments," *IET Microwaves Antennas & Propagation*, vol. 4, pp. 477-483, Apr 2010.

- [251] M. Bousahla, B. Kadri, and F. T. Bendimerad, "Circular Antenna Array Synthesis Using Fuzzy Genetic Algorithm," *International Review of Electrical Engineering-Iree*, vol. 5, pp. 785-792, Mar-Apr 2010.
- [252] S. Y. Sun, Y. H. Lv, and J. L. Zhang, "The Application of Genetic Algorithm Optimization in Broadband Microstrip antenna Design," *2010 IEEE Antennas and Propagation Society International Symposium*, 2010.
- [253] T. L. Pu, K. M. Huang, B. Wang, and Y. Yang, "Application of Micro-Genetic Algorithm to the Design of Matched High Gain Patch Antenna with Zero-Refractive-Index Metamaterial Lens," *Journal of Electromagnetic Waves and Applications*, vol. 24, pp. 1207-1217, 2010.